CATHODE DURABILITY IN PEM FUEL CELLS

A Dissertation
Presented to
The Academic Faculty

by

Erin Leigh Redmond

In Partial Fulfillment
of the Requirements for the Degree
Doctor of Philosophy in the
School of Chemical & Biomolecular Engineering

Georgia Institute of Technology
December 2013

CATHODE DURABILITY IN PEM FUEL CELLS

Approved by:

Dr. Thomas F. Fuller, Advisor
School of Chemical & Biomolecular Engineering
Georgia Institute of Technology

Dr. Yoshiaki Kawajiri
School of Chemical & Biomolecular Engineering
Georgia Institute of Technology

Dr. Paul A. Kohl
School of Chemical & Biomolecular Engineering
Georgia Institute of Technology

Dr. Faisal Alamgir
School of Materials Science & Engineering
Georgia Institute of Technology

Dr. David S. Sholl
School of Chemical & Biomolecular Engineering
Georgia Institute of Technology

Date Approved: September 30, 2013

To James S. Schanck, Janice M. Gunther, and Arthur W. Redmond

ACKNOWLEDGEMENTS

I wish to thank Dr. Tom Fuller for his professional guidance and valuable thoughts, comments, and critiques of this research work. Committee member Dr. Faisal Alamgir is recognized for his collaborative efforts regarding the in operando X-ray absorption spectroscopy experiments presented in Chapter 6. Dr. Simon Billinge and Dr. Pavol Juhas of Columbia University and Brookhaven National Lab are thanked for their involvement with the pair distribution studies in Chapters 5 and 7. Technical support from Kaumudi Pandya at beamline X11A of the National Synchrotron Light Source and the Structural Science Group at beamline 11-ID-B of the Advanced Photon Source is acknowledged. Thanks to Toyota Motor Engineering & Manufacturing North America Inc. for supporting this work.

The advice given by previous Fuller Group members Cheng Chen, Kevin Gallagher, and Rajeswari Chandrasekaran has never been forgotten. Special recognition is given to current Fuller Group members Vyran George, Tapesh Joshi, Rajiv Jaini, and Dr. KwangSup Eom for their support and camaraderie. I am particularly grateful for the assistance and collective research efforts given by Brian Setzler.

Thanks are given to my entire extended family for their continuous encouragement. I would especially like to recognize my parents, Kevin and Eileen, brothers, Christopher and William, Nana, Aunt Sally, and Uncle Douglas for their love and optimism during my studies. Major gratitude is expressed to my grad-school friends Brian Setzler, Steph Didas, Justin Vaughn, T Rubin, Saujan Sivaram, Ismael Gomez, Katie Vermeersch, and Graham Wenz for their comfort and cheer throughout the years.

TABLE OF CONTENTS

LIST OF TABLES

LIST OF FIGURES

LIST OF ABBREVIATIONS

CV	Cyclic Voltammogram
ECA	Electrochemically Active Area
EIS	Electrochemical Impedance Spectroscopy
EXAFS	Extended X-ray Absorption Fine Structure
FCTS	Fuel Cell Test Stand
MEA	Membrane Electrode Assembly
PDF	Pair Distribution Function
PEM	Proton Exchange Membrane
PFSA	Perfluorosulfonic Acid
TEM	Transmission Electron Microscopy
UPL	Upper Potential Limit
XANES	X-ray Absorption Near Edge Structure
XAS	X-ray Absorption Spectroscopy
XPS	X-ray Photoelectron Spectroscopy
XRD	X-ray Diffraction

LIST OF SYMBOLS

A_{np}	Surface area of nanoparticle, cm^2
a	Lattice parameter, $0.392\ nm$
a_i	Activity of species i
b	Tafel slope, $mV/decade$
C	Pseudocapacitance, $mF/cm^2\ [=]\ mC/\left(mV \cdot cm^2\right)$
C_{dl}	Double layer capacitance, $0.25\ mF/cm^2_{Pt}$
d	Particle diameter, nm
$E, E^0, E_{\max}$	Potential, V
e_{s-c}	Sutton-Chen potential constant, $1.9833 \times 10^{-2}\ eV$
F	Faraday's constant, $96{,}487\ C/equivalent$
f	Surface stress, J/m^2
f	Ratio of Faraday's constant to ideal gas constant and temperature, V
G	Gibbs Energy, J/mol
i	Current density, A/cm^2
i_0	Exchange current density, A/cm^2
k	Reaction rate constant, $mol \cdot cm^{-2}_{Pt} s^{-1}$
L	Metal loading, g_{Pt}/cm^2_{geo}
m	Sutton-Chen potential constant, 8
MW	Molecular weight, $195\ g/mol$
N_{np}	Number of nanoparticles

n	Number of electrons passed per equivalent charge, $equivalents/mol$
n	Sutton-Chen potential constant, 10
p_{H_2O}	Partial pressure of water, atm
$p^*_{H_2O}$	Vapor pressure of water, atm
q	Charge, C
R	Ideal gas constant, $8.314\ J \cdot mol^{-1}K^{-1}$
R	Particle radius, nm
r	Bond distance, $\AA$
r_i	Kinetic reaction rate, $mol \cdot cm_{Pt}^{-2}s^{-1}$
s	Sutton-Chen potential constant, 34.408
SA	Geometric surface area of electrode, cm^2_{geo}
T	Temperature, K
U_i^θ	Standard potential of reaction i, V
u_j	Distance from atom within particle to center of j^{th} neighbor shell, $\AA$
X_{Edge}	Fraction of edge sites, 0.36
X_j	Fraction of j^{th} neighbor shell that lies within particle boundaries
α	Charge transfer coefficient
Γ, Γ_{Edge}	Concentration of active sites, mol/m^2_{Pt}
γ	Surface energy, J/m^2
ε	Strain
η	Overpotential, V
θ_i	Coverage of species i

κ	Compressibility, $4.35 \times 10^{-12}\ m^3/J$
ν	Scan rate, V/s
ρ	Density, $21 \times 10^3\ kg/m^3$
$\Phi(r)$	Interatomic potential, eV
Φ	Electrochemical potential, V
χ	Kinetic parameter
ω	Interaction energy, kJ/mol

SUMMARY

Proton exchange membrane (PEM) fuel cells are competitive with other emerging technologies that are being considered for automotive transportation. Commercialization of PEM fuel cells would decrease emissions of criteria pollutants and greenhouse gases and reduce US dependence on foreign oil. However, many challenges exist that prevent this technology from being realized, including power requirements, durability, on-board fuel storage, fuel distribution, and cost. This dissertation focuses on fuel-cell durability, or more specifically catalyst stability.

New techniques to comprehensively observe and pin-point degradation mechanisms are needed to identify stable catalysts. In this text, an in operando method to measure changes in catalyst particle size at the cathode of a PEM fuel cell is demonstrated. The pair distribution function analysis of X-ray diffraction patterns, generated from an operating fuel cell exposed to accelerated degradation conditions, was used to observe the growth of catalyst particles. The stability of Pt/C and PtCo/C electrodes, with different initial particle sizes, was monitored over 3000 potential cycles. The increase in particle size was fit to a linear trend as a function of cycle number for symmetric linear sweeps of potential. The most stable electrocatalyst was found to be alloyed PtCo with a larger initial particle size.

A better understanding of oxide growth kinetics and its role in platinum dissolution is needed to develop a comprehensive fuel-cell performance model. There is an ongoing debate present in the current literature regarding which oxide species are involved in the oxide growth mechanism. This dissertation discusses the results of in operando X-ray absorption spectroscopy studies, where it was found that PtO_2 is present at longer hold times. A new method to quantify EXAFS data is presented, and the extent of oxidation is directly compared to electrochemical data. This comparison indicated that PtO_2 was formed at the expense of an initial oxide species, and these steps were included in a proposed mechanism for platinum oxidation.

Simulations of platinum oxidation in literature have yet to fully replicate an experimental cyclic voltammogram. A modified Butler-Volmer rate equation is presented in this thesis. The effect of including an extra parameter, χ, in the rate equations was explored. It was found that while the χ-parameter allowed the cathodic peak width to be decoupled from the Tafel slope for the platinum-oxide reduction, its inclusion could not address all observed experimental characteristics. Exploration of this concept concluded that current is not a function of only potential and coverage. To that end, a heterogeneous oxide layer was introduced. In this model, place-exchanged PtO_2 structures of varying energy states are formed through a single transition state. This treatment allowed, for the first time, the simulation of the correct current-potential behavior under varying scan rates and upper potential limits.

Particle size plays a critical role in catalysts stability. The properties of nanoparticles can differ significantly from bulk values, yet few tools exist to measure these values at the nanoscale. Surface stress and surface energy are diagnostic criterion that can be used to differentiate nano from bulk properties. The pair distribution function technique was used to measure lattice strain and particle size of platinum nanoparticles supported on carbon. The effect of adsorbates on surface stress was examined and compared to previous literature studies. Furthermore, a methodology for measuring the surface energy of supported platinum nanoparticles has been developed.

While the results of this work are significant, many more challenges need to be addressed before fuel-cell vehicles are marketed. Recommendations for future work in the field of catalyst durability are addressed.

CHAPTER 1

INTRODUCTION

As the world population continues to increase and less developed countries become more industrialized, a large demand will be placed on the transportation sector of the economy (1). Many challenges are anticipated from the impending rise of global transport including traffic safety, greenhouse gas emissions, and dependence on petroleum. Burning of fossil fuels is the largest source of greenhouse gas emissions, and transportation accounts for approximately a quarter of world energy-related greenhouse gas emissions (1). Passenger cars and light duty trucks are responsible for over half of these emissions (1). Thus, automakers have assumed a responsibility to develop more fuel efficient and alternative fuel vehicles. Hydrogen fuel cell technology has appealed to automotive companies, as part of a long term solution, to decrease pollutants because hydrogen is an abundant source of clean burning fuel, with zero tail-pipe emissions.

1.1 Proton Exchange Membrane Fuel Cells

At the heart of proton exchange membrane (PEM) fuel cell technology is the perfluorosulfonic acid membrane, whereby only protons are transported (2). On either side of the membrane is an electrode, composed of a catalyst supported on electrically conductive, high surface area carbon and a thin coating of ionomer. One electrode, the anode, is supplied with hydrogen, and the hydrogen is oxidized to form protons and electrons. The protons are transferred through the membrane to the other side of the cell, and the electrons are transported through an external circuit, which would power an electric motor in a fuel-cell vehicle. Air is supplied to the cathode, and oxygen reacts with the protons and electrons to form water.

Though the chemistry is simple, there are many barriers that prevent the mass commercialization of these devices including power requirements, durability, on-board fuel storage, fuel distribution, and cost. This dissertation is focused on fuel cell durability, or more specifically catalyst stability.

1.2 Durability of PEM Fuel Cells

Degradation of the PEM fuel cell can be categorized into three topics: membrane degradation, carbon corrosion, and catalyst stability. A commonly used perfluorosulfonic acid polymer membrane is Nafion® since it possesses a relatively high chemical stability in fuel cell applications (3) and it is able to maintain high proton conductivity over a wide range of relative humidity conditions (4). Optimizing the performance of Nafion® requires fully humidified reactant streams and the use of thinner membranes to lower proton transfer resistance. Adversely, thinner membranes are more susceptible to degradation and increase gas permeability (2). Chemical degradation occurs when crossover hydrogen and oxygen react to form hydrogen peroxide, which then reacts with metal impurities of the catalyst forming harmful peroxide radicals *OH and *OOH. These radicals then attack the weak polymer chain resulting in membrane degradation, which has been identified as the primary degradation mechanism in Nafion® (2, 3). Research continues in membrane degradation focusing on mitigation techniques that aim to reduce trace metal contaminants, optimize relative humidity conditions and membrane thickness to decrease gas permeability, and minimize radical formation through the use of free radical scavengers, such as ceria (2, 5).

Carbon is used as a catalyst support due to its high surface area, electrical conductivity, low cost, and abundant supply. Carbon blacks, such as Vulcan XC-72, are typical catalyst supports used in PEM fuel cell applications (6, 7). Major contributors to carbon instability are oxidants and the high potentials reached during start-up/shut-down

or idle conditions of the fuel cell (6). The proposed path of degradation is described by the reverse-current mechanism in which crossover oxygen is reduced at the anode and, in the absence of hydrogen, protons are supplied from the cathode by either carbon oxidation or oxygen evolution from water (6, 7). Fuel starvation occurs due to blocked gas-flow channels. The electrode is significantly damaged after 5 to 10 percent carbon weight loss occurs (7). Graphitization of carbon reduces the rate of oxidation seen in fuel cells, but also reduces the surface area, which limits catalyst dispersion (6). Enhancing the oxygen evolution reaction by incorporating a selective catalyst on the carbon support is another approach to mitigate carbon oxidation. The reverse current is generated by the oxygen evolution reaction at less positive potentials in place of carbon oxidation (7). The economic viability of carbon will ensure continued progress in carbon corrosion mitigation research for use in fuel cell systems.

Platinum has a relatively high kinetic activity for the oxygen reduction reaction and is resistant to corrosion, both of which are desirable properties for a fuel cell catalyst. However, platinum is unstable during certain points of fuel cell operation resulting in catalyst loss. At high potentials, above 0.8 V (all potentials in this work are with respect to the reference hydrogen electrode), an oxide layer forms on the platinum surface, and as the layer becomes unstable, platinum and oxygen undergo a place exchange (8). Upon reduction, platinum ions are formed, which have a finite solubility at high potentials and low pH as shown in the platinum Pourbaix diagram (9), Figure 1.1.The Pourbaix diagram is a thermodynamic phase diagram that displays the possible equilibrium phases of an aqueous electrochemical system. Platinum ions are also released into solution on the anodic sweep.

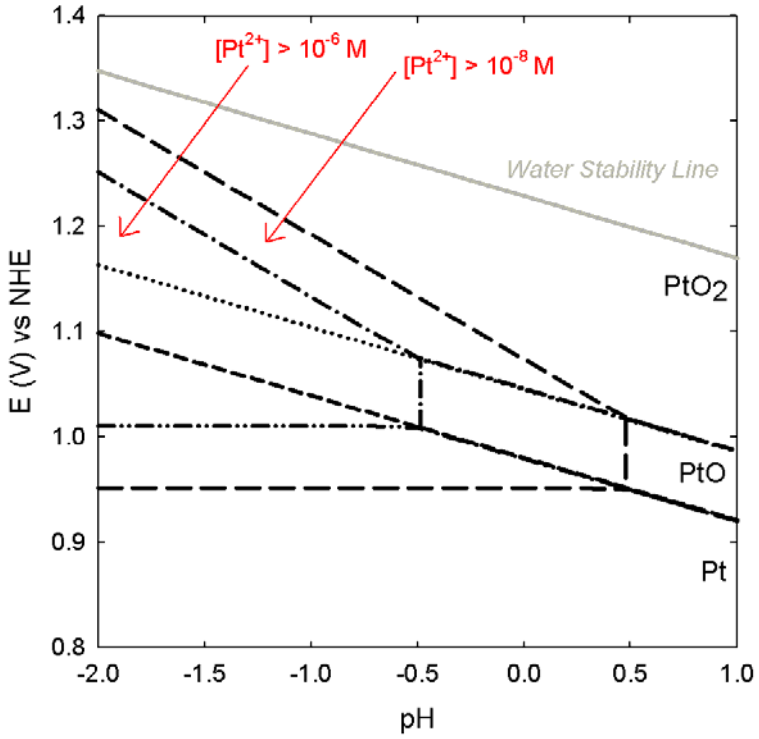

Figure 1.1 Pourbaix diagram (9) for platinum oxidation.

Both conditions exist in PEM fuel cells since high potentials are reached during start-up, shut-down, and idle periods of fuel cell operation, and the electrolyte, typically Nafion®, is highly acidic. Consequently, platinum dissolves into the electrolyte. Platinum can either recrystallize on larger particles, contributing to Ostwald ripening or diffuse into the membrane and precipitate, forming a platinum band. Both mechanisms contribute to reducing the electrochemically active area of the catalyst layer; thereby, reducing fuel cell efficiency (10). Additionally, the platinum band can generate high stress areas inside the membrane making it more susceptible to degradation (2).

Platinum nanoparticles are used to decrease the overall platinum loading on the electrode, while maintaining the necessary catalytic surface area to drive the reactions (11, 12). However, there is a lower limit on particle size as particles smaller than 5 nm have been shown to be more unstable and coarsen via a surface energy driven, Ostwald ripening process (11, 13). In addition to losing active catalyst area and reducing fuel cell

efficiency, this process necessitates the use of higher than desired platinum loadings corresponding to an increased manufacturing cost. This thesis focused on contributing to an enhanced fundamental understanding of catalyst stability in PEMFCs.

1.3 References

1. S. Kahn Ribeiro, S. Kobayashi, M. Beuthe, J. Gasca, D. Greene, D. S. Lee, Y. Muromachi, P. J. Newton, S. Plotkin, D. Sperling, R. Wit and P. J. Zhou, in *Climate Change 2007: Mitigation. Contribution of Working Group III to the Fourth Assessment Report of the Intergovernmental Panel on Climate Change* B. Metz, O. R. Davidson, P. R. Bosch, R. Dave and L. A. Meyer Editors, Cambridge University Press, New York (2007).

2. A. Collier, H. J. Wang, X. Z. Yuan, J. J. Zhang and D. P. Wilkinson, *International Journal of Hydrogen Energy*, **31**, 1838 (2006).

3. D. E. Curtin, R. D. Lousenberg, T. J. Henry, P. C. Tangeman and M. E. Tisack, *J Power Sources*, **131**, 41 (2004).

4. C. Chen and T. F. Fuller, *Polym Degrad Stabil*, **94**, 1436 (2009).

5. P. Trogadas, J. Parrondo and V. Ramani, *Electrochem Solid St*, **11**, B113 (2008).

6. K. Gallagher, R. M. Darling and T. F. Fuller, in *Handbook of Fuel Cells – Fundamentals, Technology and Applications*, W. Vielstich, H. Yokokawa and H. A. Gasteiger Editors, p. 819 John Wiley & Sons, West Sussex, United Kingdom (2009).

7. P. T. Yu, W. Gu, J. Zhang, R. Makharia, F. T. Wagner and H. A. Gasteiger, in *Polymer Electrolyte Fuel Cell Durability*, p. 29 Spring, New York, NY (2009).

8. G. Jerkiewicz, G. Vatankhah, J. Lessard, M. P. Soriaga and Y. S. Park, *Electrochim Acta*, **49**, 1451 (2004).

9. M. Pourbaix, *Atlas of Electrochemical Equilibria in Aqueous Solutions*, National Association of Corrosion Engineers, Houston, TX (1974).

10. W. Bi, G. E. Gray and T. F. Fuller, *Electrochem Solid St*, **10**, B101 (2007).

11. E. F. Holby, W. C. Sheng, Y. Shao-Horn and D. Morgan, *Energy & Environmental Science*, **2**, 865 (2009).

12. Z. M. Peng and H. Yang, *Nano Today*, **4**, 143 (2009).

13. A. S. Masadeh, E. S. Bozin, C. L. Farrow, G. Paglia, P. Juhas, S. J. L. Billinge, A. Karkamkar and M. G. Kanatzidis, *Phys Rev B*, **76**, 115413 (2007).

CHAPTER 2

PLATINUM DISSOLUTION AT THE CATHODE

Throughout the lifetime of a fuel cell the cathode loses a significant amount of electrochemically active surface area (ECA) due to platinum dissolution. The loss of platinum in acidic solutions was first observed by Tafel in 1905 (1), and further studied in phosphoric acid fuel cells in the 1970s (2, 3). The mechanisms governing platinum deterioration in phosphoric acid fuel cells (4, 5) are similar to those processes found in PEM fuel cells. The four mechanisms responsible for ECA loss are (i) Ostwald ripening, (ii) particle coalescence, (iii) particle detachment from the carbon support, and (iv) platinum diffusion into the electrolyte (6). Ostwald ripening refers to the growth of large particles at the expense of small particles via either ion diffusion through the ionomer (3D transport), Figure 2.1a (3, 4, 6), or surface-diffusion transport of platinum adatoms (2D transport) (7, 8). Due to the effects of surface energy and particle curvature, small particles have a higher solubility than large particles (9). As a result, ions or adatoms diffuse through the electrolyte or across the support from small to large particles, where reduction and/or redeposition occur. Coalescence may occur due to crystal migration Figure 2.1b where particles randomly collide and stick together (6). Both mechanisms are driven by a reduction in surface energy and can be distinguished by particle size distribution analysis (6). Ostwald ripening will exhibit a tail at smaller particles. Conversely, coalescence will have a distinctive tail at large ends (10, 11). Another distinctive factor between the two mechanisms is that particle coalescence is independent of voltage, yet 3D-Ostwald ripening is driven by the upper potential limit (10).

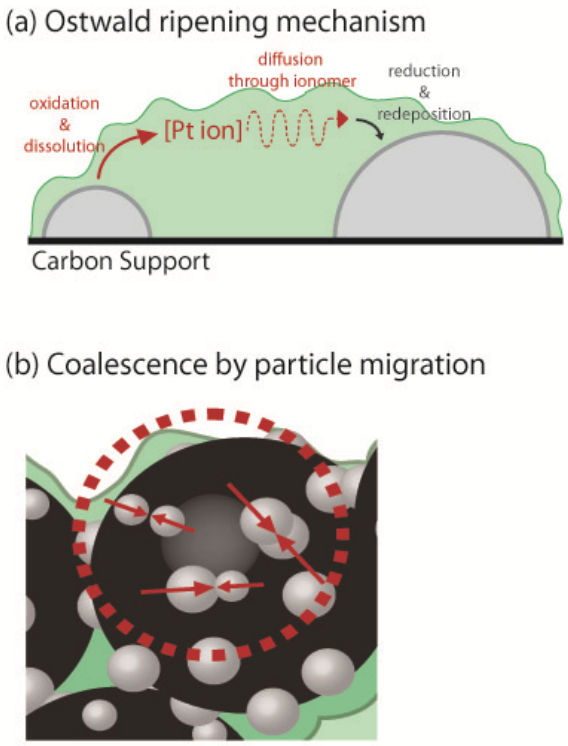

Figure 2.1 Illustration of mechanisms that contribute to particle growth, adapted from references (4) and (6).

Further degradation occurs at high potentials, where the carbon support is subject to corrosion (6, 12). Under these conditions, platinum detaches from the carbon, and it is no longer electrically connected. Platinum agglomerates have been found in the membrane as a result of this mechanism of ECA loss (10, 12). Loss of platinum also occurs through platinum diffusion and deposition in the membrane (6, 13, 14). This mechanism is supported by scanning electron microscopy images showing a platinum band in the membrane for hydrogen air cycles or at the membrane/cathode interface in the absence of oxygen (10, 13, 15). There is a need to characterize platinum losses and understand the mechanisms by which dissolution occurs for the development of mitigation strategies.

2.1 Cycling Conditions and Platinum Surface Area Loss

Fuel cells for automotive applications must be able to withstand demanding drive cycles. Platinum is most vulnerable to dissolution during start/stop transients or idle conditions, where the potentials are the highest. In the lab, real-world drive cycles are simulated with elementary cyclic potential sweeps that accelerate dissolution (2). Early dissolution studies were performed using 3-chamber, liquid electrolyte cells in de-aerated acid solution. Kinoshita and coworkers investigated the effect that different cyclic waveforms and electrode types had on platinum dissolution (2). Their findings suggested that increasing the upper potential limit of triangular waveforms up to 1.0V accelerated dissolution; thereafter, it became independent of the upper potential limit (2). Platinum sheet electrodes exhibited more platinum area loss and formation of (111) crystal faces under a triangular wave cycle than a square wave cycle. However, regardless of cycle type, the surface morphologies remained the same on unsupported platinum black and platinum supported on carbon due to the rapid establishment of equilibrium of atoms on the crystal faces to give the lowest surface energy (2). From these early studies it became apparent that the cycling conditions affect the driving forces of ECA loss. Patterson provided the first study of platinum dissolution in an MEA using cyclic voltammetry (16). In this case, a square wave cycle between 0.87 V and 1.2 V was used at varying frequencies and compared to a potential hold at 1.05 V for 300 hours. Cycling resulted in more severe ECA loss (16). Both studies show that the rate of dissolution approaches zero at long times(2, 16).

Since 2002, many cyclic voltammetry studies have been conducted under a wide range of operating conditions to determine the dominant modes of degradation, so that the system design of fuel cell vehicles can be optimized to minimize platinum loss during operation. Effects of the wave shape (triangular or square), frequency, sweep rate, and potential limits have all been investigated (7, 13, 17-21). Many studies have confirmed that high upper potential limits increase dissolution (13, 19, 22-24), though a short

cycling range in the high potential region results in less dissolution than a full cycling range (13, 18). This outcome is explained by the formation of a passivating oxide layer on the platinum surface at high potentials. As long as the lower potential limit is remains greater than 0.8 V, to prevent oxide reduction, the metal surface is protected (13, 18).

Mitsushima and coworkers measured the consumption rate of platinum through gravimetric analysis after 900,000 cycles of various potential profiles of a 1 cm^2, 0.3 mm diameter platinum wire submerged in 1 M sulfuric acid at 40 °C (17). The difference in anodic and cathodic charges per cycle was determined and plotted as a function of consumption rate for the potential profiles. The ratio of the change in weight to the difference in charge was converted to an electron transfer number. A profile with a slow cathodic sweep resulted in an electron transfer number of 2, and a symmetric wave profile or those with a fast cathodic sweep demonstrated a slope of 4. Thus, the mechanism of ion formation was determined as either $PtO_2 + 4H^+ + 2e^- \rightarrow Pt^{2+} + 2H_2O$ or $Pt \rightarrow Pt^{4+} + 4e^-$, depending on which profile was employed (17). While this study does lend some insight to the mechanism of platinum dissolution, it is not very relevant to PEM fuel cells in an automotive system. The upper potential limits were above 1.5 V in a liquid electrolyte cell, which is outside of the operable potential range in a fuel cell vehicle. Additionally, it appears that the voltages were not iR corrected, thus the voltage limits reached in the cell during the fast sweeping experiments may have been different than the targeted voltage range.

It was also found that an asymmetric profile with a slow cathodic sweep (0.5 V/s) resulted in 10 times more dissolution than symmetric potential profiles, regardless of the sweep rate (17), which was confirmed in other studies (18, 20). After the first full potential sweep to high potentials, there is an increase in the amount of uncoordinated atoms due to place exchange of the oxygen and platinum atoms (18). These uncoordinated atoms are less stable and subject to increased dissolution. If the anodic

sweep is fast, relative to the cathodic sweep, less oxide growth occurs resulting in an exposed metal surface. A large number of small islands are formed, but there is less time for ion or particle diffusion. On the other hand, a slow anodic sweep allows more time for diffusion from small to large particles and less platinum is dissolved upon reduction (18).

Other studies have focused on identifying the mechanism of dissolution at constant potential holds. Xu and coworkers applied in situ scanning tunneling microscopy to a platinum film held at varying potentials in acidic solution (7). No change of the platinum surface was observed after holding at either 0.25 V or 0.8 V for hours. However, surface diffusion of platinum adatoms was established as the dominant mechanism of dissolution at 0.5 V (7). This study suggested operation at high potentials for less ECA loss (7), though carbon corrosion was not considered. Through transmission electron microscopy, Ettingshausen and coworkers observed an increase in surface area loss due to carbon oxidation during high potential holds on an MEA (19).

In addition to probing the effects of potential profiles, many researchers have focused on the effects of relative humidity, and found that a lower relative humidity results in less platinum diffusion and deposition within the membrane (18, 25). Platinum band formation is mitigated at low humidity conditions because cation transport through the ionomer is slowed. Platinum dissolution is decreased, but the overall performance of the fuel cell is decreased because of increased proton transfer resistance (26). The position of the platinum band was simulated, by Bi and coworkers, as a function of the gas permeation rates across the membrane (15). In this study, platinum was found in the membrane after hydrogen/air cycling, but not after hydrogen/nitrogen cycling. Electrochemically active area losses for hydrogen/air cycles were 10% less than hydrogen/nitrogen cycles (15). In the absence of hydrogen, platinum diffuses from the cathode and redeposits at the anode (13). To mitigate platinum loss through micron scale platinum band formation in the membrane, hydrogen crossover should be eliminated. Thicker membranes limit hydrogen crossover, but also decrease the performance of the

cell; thus, these advances must occur through material development. Furthermore, if the mechanism of platinum ion diffusion through the ionomer is different than proton transport, the advancement of an electrolyte material that shuts off the platinum ion diffusion mechanism would decrease ECA loss (27).

2.2 Deconvoluting Surface Area Loss Processes

One collaborative goal of the research community is to establish the mechanism by which platinum dissolves into the ionomer (28), but various factors such as reactant types and electrochemical conditions make this determination very difficult. Platinum dissolution is the common first step for the Ostwald ripening mechanism and the platinum band mechanism, but coalescence and detachment proceed without dissolution, so the mitigation approach will vary with the loss mechanism. Thus, another objective regarding platinum stability in PEM fuel cells is to deconvolute the processes that contribute to ECA loss. Electron microscopy is widely used in conjunction with electrochemical cycling to study the extent of each platinum surface area loss process.

An extensive study was conducted by Ferreira and coworkers to investigate both nanometer (Ostwald ripening, migration) and micron (platinum band) scale mechanisms (10). Wet cell experiments were conducted to measure platinum ion concentration as a function of potential, where a proportional relationship was found. However, the observed potential dependence was approximately half that predicted by Nernstian behavior. This effect could be attributed to simultaneous chemical and electrochemical processes, surface morphologies, and particle size effects (6). Short stack experiments were performed, followed by post-mortem investigations by scanning electron microscopy, X-ray diffraction, and transmission electron microscopy (10). Larger particles were observed on the cathode after cycling, supporting the Ostwald ripening hypothesis (6, 10). Additionally, non-spherical platinum agglomerates separated from the

carbon support were detected close to the cathode/membrane interface. It was determined that nanometer scale dissolution and the micron scale mechanism each account for a loss of ⅓ of the total ECA (10). The experimental observations obtained by Ferreira support the theory that dissolution is limited to the under-coordinated surface atoms, which would contribute to extreme surface distortion in nanoparticles (6).

In 2011, application of transmission electron microscopy to an MEA identified platinum agglomerates off the carbon support which resulted from potential holds at relatively high values (19). Start/stop cycling procedures showed increased ECA loss and the dominant process was determined to be platinum dissolution (19). Prior to Perez-Alonso et al.'s study, the observation of dissolution had been limited to intermittent sampling of the liquid electrolyte in solution studies or post-mortem imaging of the MEA (22). Through identical location transmission electron microscopy, particle coalescence with time was identified as the major contributor to ECA loss (22). Using the same technique, Zana and coworkers concluded that when the potential is cycled from a bare metal surface to the oxide coverage regime, Ostwald ripening and coalescence are responsible for ECA loss (21). , if the potential is cycled to extreme values beyond 1.4 V or cycled in the oxide regime only, then carbon corrosion is the contributing factor to ECA loss (21). Using identical location scanning electron microscopy, Hodnik and coworkers observed particle growth in real time over 50,000 cycles from 0.2 to 1.4 V in a liquid electrolyte solution (29). Two distinguishable platinum area loss rates were identified around a critical cycle number. The first region was attributed to nanoparticle dissolution, whereas the second region was proposed as the deposition of the dissolved platinum onto the catalyst film (29). Identical location electron microscopy is extremely useful because dissolution can be observed in real time and evidence of all degradation modes can be identified (12). However, these studies are limited to working electrodes in liquid electrolyte solutions. For detailed mechanisms to be confirmed there is a need for the cell environment and cycling conditions to mimic real life (19). Scanning and

transmission electron microscopy studies through pre and post mortem analyses of MEAs have established that degradation is not always uniform through the thickness of the electrode due to local exposure to high interfacial potential and that particles less than 4 to 5 nm are extremely unstable (10, 30, 31). The accuracy of these techniques in determining particle size distributions has been called into to question due to the low detection limits (> 0.5 nm) of some instruments (32). These types of studies are also destructive and time-consuming.

Recently, Dhanushkodi and coworkers established a fingerprint for the performance loss due to carbon corrosion in an MEA (33). An empirical exponential expression was derived from performance loss as a function of carbon loss after a number of stress tests to accelerate carbon corrosion. This fingerprint can then be used to deconvolute the performance loss due to platinum dissolution and carbon corrosion (33). However, this technique has just been demonstrated and is not usable across all operating conditions (33).

2.3 Theoretical Studies

Modeling platinum dissolution has been adopted as an ancillary method for deconvoluting and attaining a better understanding of the processes behind ECA loss. Darling and Meyers were the first to simulate platinum dissolution in PEM fuel cells (34, 35). Platinum dissolution, assumed to be a single elementary step, electrochemical formation of platinum oxide, and chemical dissolution of platinum oxide were all considered, although chemical dissolution was given a very slow rate constant, which effectively eliminated it. The shift in electrochemical potential (ΔU) due to the size effect was modeled using the Kelvin equation,

$$|\Delta U| = \frac{1}{nF} \cdot \frac{\gamma_{Pt(111)} M_{Pt}}{\rho_{Pt} R}, \tag{2.1}$$

assuming a constant surface energy ($\gamma_{Pt(111)} = 2.37\, J/cm^2$) for all size (R) regimes (34). The platinum (111) surface has the lowest surface energy of all surface planes (34, 36). The molecular weight (M_{Pt}), the density of platinum (ρ_{Pt}), and Faraday's constant (F) are all equal to the respective standard reference values. The number of electrons (n) involved in the platinum dissolution reaction is 2, associated with the Pt^{2+} oxidation state. Kinetic and thermodynamic parameters were fit to data obtained by Bindra et al. and Kinoshita et al. (2, 34, 37). Overall, a good fit was achieved between the simulated and experimental CV. Some deviations were observed as shape changes in the CV curve; for example, the onset of oxide reduction was predicted to begin at a more positive potential (34). In 2005, Darling and Meyers expanded the model to a 1-D MEA model and allowed platinum to travel from the cathode to anode, but did not allow deposition in the membrane. A bimodal particle size distribution was incorporated to study the particle size effect. Variations between model and experimental studies were predicted to be due to the simplification of the Kelvin equation (35). Extending Darling and Meyer's model, Bi and coworkers incorporated platinum band formation in the membrane (38). Further treatment of the model involved dissolution and redeposition at the cathode, ion transport into matrix, and ion reduction by the hydrogen front present in the membrane (38).

In a 2009 study, Holby and coworkers studied the effect of various particle size distributions on Ostwald ripening and platinum band formation (39). It was found that after particles reached 4 nm to 5 nm in diameter rapid stability was achieved, and that coarsening was the dominant mechanism of surface area loss in the absence of hydrogen (39) or when the platinum sink was far away (14). Thus, it was recommended that hydrogen crossover be minimized and larger particle diameters used instead of the standard 2 nm to 3 nm range. However, larger particles may alter the platinum specific activity and result in an increased cost (39).

The most challenging issue when using models to predict platinum dissolution are the unknown kinetics and the fact that the individual mechanisms change based on

cycling conditions. In addition, platinum dissolution occurs concomitantly with platinum oxidation and oxide reduction. Thus, more in situ techniques would be beneficial to enable study of particle behavior during cycling conditions so that the processes of platinum surface area loss can be elucidated. Also, a comprehensive understanding of the role of platinum oxidation in surface area loss must be developed so that kinetic parameters can be identified.

2.4 References

1. J. Tafel and B. Emmert, *Z Phys Chem-Stoch Ve*, **52**, 349 (1905).

2. K. Kinoshita, J. T. Lundquist and P. Stonehart, *Electroanalytical Chemistry and Interfacial Electrochemistry*, **48**, 157 (1973).

3. J. A. S. Bett, K. Kinoshita and P. Stonehart, *J Catal*, **41**, 124 (1976).

4. P. N. Ross, in *Catalyst Deactivation*, E. E. Petersen and A. T. Bell Editors, p. 165 Marcel Dekker, Inc. , New York (1987).

5. J. Aragane, T. Murahashi and T. Odaka, *J Electrochem Soc*, **135**, 844 (1988).

6. Y. Shao-Horn, W. C. Sheng, S. Chen, P. J. Ferreira, E. F. Holby and D. Morgan, *Top Catal*, **46**, 285 (2007).

7. Q. Xu, E. Kreidler, D. O. Wipf and T. He, *J Electrochem Soc*, **155**, B228 (2008).

8. W. W. Mullins, *Metal surfaces: structure, energetics and kinetics: Papers presented at a joint seminar of the American Society for Metals and the Metallurgical Society of AIME*, American Society for Metals, Metals Park, Ohio (1963).

9. C. T. Campbell, S. C. Parker and D. E. Starr, *Science*, **298**, 811 (2002).

10. P. J. Ferreira, G. J. la O', Y. Shao-Horn, D. Morgan, R. Makharia, S. Kocha and H. A. Gasteiger, *J Electrochem Soc*, **152**, A2256 (2005).

11. P. Ascarelli, V. Contini and R. Giorgi, *J Appl Phys*, **91**, 4556 (2002).

12. J. C. Meier, C. Galeano, I. Katsounaros, A. A. Topalov, A. Kostka, F. Schuth and K. J. J. Mayrhofer, *Acs Catal*, **2**, 832 (2012).

13. K. Yasuda, A. Taniguchi, T. Akita, T. Ioroi and Z. Siroma, *Phys Chem Chem Phys*, **8**, 746 (2006).

14. E. F. Holby and D. Morgan, *J Electrochem Soc*, **159**, B578 (2012).

15. W. Bi, G. E. Gray and T. F. Fuller, *Electrochem Solid St*, **10**, B101 (2007).

16. T. Patterson, in *AIChE Spring National Meeting*, G. J. Igwe and D. Mah Editors, p. 313, Topical Conference Proceedings, New York (2002).

17. S. Mitsushima, S. Kawahara, K. I. Ota and N. Kamiya, *J Electrochem Soc*, **154**, B153 (2007).

18. M. Uchimura, S. Sugawara, Y. Suzuki, J. B. Zhang and S. S. Kocha, *ECS Transactions*, **16**, 225 (2008).

19. F. Ettingshausen, J. Kleemann, A. Marcu, G. Toth, H. Fuess and C. Roth, *Fuel Cells*, **11**, 238 (2011).

20. F. Hiraoka, K. Matsuzawa and S. Mitsushima, *Electrocatalysis-Us*, **4**, 10 (2013).

21. A. Zana, J. Speder, M. Roefzaad, L. Altmann, M. Baumer and M. Arenz, *J Electrochem Soc*, **160**, F608 (2013).

22. F. J. Perez-Alonso, C. F. Elkjaer, S. S. Shim, B. L. Abrams, I. E. L. Stephens and I. Chorkendorff, *J Power Sources*, **196**, 6085 (2011).

23. A. P. Yadav, T. Okayasu, Y. Sugawara, A. Nishikata and T. Tsuru, *J Electrochem Soc*, **159**, C190 (2012).

24. R. Chandrasekaran, W. Bi and T. F. Fuller, *J Power Sources*, **182**, 546 (2008).

25. S. Ohyagi, T. Matsuda, Y. Iseki, T. Sasaki and C. Kaito, *J Power Sources*, **196**, 3743 (2011).

26. W. Bi, Q. Sun, W. Deng and T. F. Fuller, *Electrochim Acta*, **54**, 1826 (2009).

27. P. Choi, N. H. Jalani and R. Datta, *J Electrochem Soc*, **152**, E123 (2005).

28. T. Sakurai, M. Shibata, R. Horiuchi, I. Yagi and T. Kondo, *Chem Lett*, **40**, 402 (2011).

29. N. Hodnik, M. Zorko, B. Jozinovic, M. Bele, G. Drazic, S. Hocevar and M. Gaberscek, *Electrochem Commun*, **30**, 75 (2013).

30. L. Guetaz, S. Escribano and O. Sicardy, *J Power Sources*, **212**, 169 (2012).

31. H. Gyoten, T. Hirayama, J. Kondo, A. Taomoto and M. Aizawa, *Electrochemistry*, **79**, 392 (2011).

32. W. C. Sheng, S. Chen, E. Vescovo and Y. Shao-Horn, *J Electrochem Soc*, **159**, B96 (2012).

33. S. R. Dhanushkodi, M. Tam, S. Kundu, M. W. Fowler and M. D. Pritzker, *J Power Sources*, **240**, 114 (2013).

34. R. M. Darling and J. P. Meyers, *J Electrochem Soc*, **150**, A1523 (2003).

35. R. M. Darling and J. P. Meyers, *J Electrochem Soc*, **152**, A242 (2005).

36. Z. M. Peng and H. Yang, *Nano Today*, **4**, 143 (2009).

37. P. Bindra, S. J. Clouser and E. Yeager, *J Electrochem Soc*, **126**, 1631 (1979).

38. W. Bi and T. F. Fuller, *J Power Sources*, **178**, 188 (2008).

39. E. F. Holby, W. C. Sheng, Y. Shao-Horn and D. Morgan, *Energy & Environmental Science*, **2**, 865 (2009).

CHAPTER 3

PLATINUM DISSOLUTION AND OXIDE GROWTH

The thermodynamics and kinetics of platinum dissolution are complicated by the simultaneous formation of an oxide layer on the platinum surface. This subject has been studied for decades, but there is no consensus on the exact mechanism of platinum oxidation and reduction. This chapter summarizes a collection of literature studies and highlights the missing details needed for the development of a comprehensive, physics-based model. The observed behavior of platinum oxidation and reduction in a cyclic voltammogram (CV) is discussed, followed by an examination of the proposed oxidation mechanisms in literature. Lastly, this chapter will include a discussion of the previous models and simulations that have been published in the field.

3.1 Platinum Dissolution and Oxide Growth

Thermodynamically, metallic dissolution of platinum $Pt \rightleftharpoons Pt^{2+} + 2e^-$ is a function of potential as determined from the Nernst equation (1),

$$E = E^0 + 2.303\frac{RT}{nF}\cdot\log\left[Pt^{2+}\right]. \tag{3.1}$$

The equilibrium potential, $E^0 = 1.188$ V, is a standard value at room temperature and was measured by Pourbaix (2). Experimentally, as seen in Figure 3.1, platinum solubility does increase with potential, but at a much slower rate than expected for a 2 or 4 electron process due to interactions with the oxide layer (3, 4). Based on Equation (3.1) platinum dissolution should increase tenfold for every 29 mV increase in potential at room temperature (n = 2). However, in the region from 0.85 V to 1.0 V, Wang et al. and Ahluwalia et al. show a tenfold increase in platinum ion concentration for every 105 mV increase in potential (3, 5).

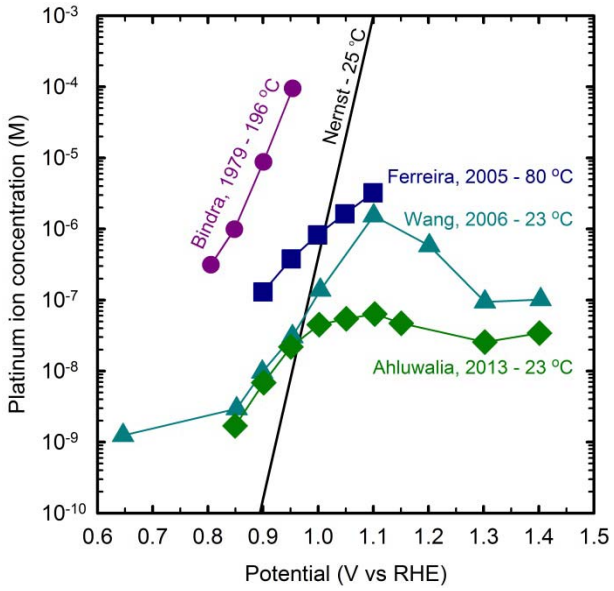

Figure 3.1 Dissolved platinum ion concentration as a function of potential (3-6).

Both experiments measured dissolution of platinum in 0.57 M perchloric acid solution under an argon atmosphere using inductively coupled plasma mass spectroscopy after 72 hour potential holds. Wang et al.'s experiment was performed on a platinum wire in solution with an electrochemically active surface area of 40 cm^2 (3). Contrarily, Ahluwalia and coworkers performed dissolution tests on platinum supported on carbon electrocatalysts that were deposited on carbon paper with a microporous layer (5). The electrocatalysts varied by average particle diameter, and the data shown in Figure 3.1 were taken from the sample with an average particle diameter of 3.2 nm. The deviation in the data seen for the two studies (3, 5) after 1.0 V, was attributed to the different catalyst types (5). Nanoparticles have an increased number of edge and corner sites that are higher in energy than planar sites. The more active sites have a higher affinity for oxide absorption, and the increased oxide coverage limits platinum dissolution at high potentials.

Ferreira and coworker's study displayed results for a 12.5 cm^2 electrode loaded with 0.67 mg_{Pt}/cm^2_{geo} of a platinum supported on carbon electrocatalyst with an average

particle diameter between 2 nm to 3 nm (4). This study was performed in 0.5 M sulfuric acid solution at 80 °C, and 20 mL samples of the electrolyte, taken between 50 and 100 hours, were analyzed using inductively coupled plasma mass spectroscopy (4). The results show a similar dependence on potential to the Ahluwalia study (5) as seen in Figure 3.1, but the solubility is greater as expected for the higher temperature.

At 196 °C, platinum dissolution is expected to increase by an order of magnitude every 46.5 mV increase in potential, which agrees very well the study conducted by Bindra and coworkers (6). Dissolution from a 25 cm^2 platinum foil in 96 % phosphoric acid solution at 176 °C and 196 °C was analyzed for varying potential holds after 1 hour using gravimetric analysis (6). Both data sets predicted the same dissolution trend, so only the data set at 196 °C is shown in Figure 3.1. At these temperatures, the data agree with the equilibrium relation due to relatively low overpotentials, more facile kinetics, and because a bulk platinum foil is used, which eliminates any effects due to surface energy.

Potential cycling greatly increases the rate of platinum dissolution, but the mechanism is not fully understood and is dependent upon cycling conditions (3, 4, 7-12), as discussed in Chapter 2. Dissolution is enhanced during the anodic potential sweep as less oxide is present than after a long hold (13, 14). At long times or high potentials the oxygen atoms penetrate the platinum lattice and it has been shown that platinum dissolution occurs concomitantly with the reduction of this place-exchanged oxide (15). The rate of platinum dissolution is increased for smaller particles due to the effects of curvature and surface energy, especially for diameters below 5 nm (16-18), which is a standard particle size due to the practice of maximizing the surface area to volume ratio.

As noted, the oxide layer strongly affects the dissolution equilibrium and is critical to the accelerated dissolution under potential cycling. Thus, to understand the dissolution of platinum under dynamic conditions, we must understand the kinetics of oxide growth on small platinum particles.

3.2 Current-Overpotential Behavior of Oxide Growth on Platinum

Cyclic voltammetry is a common technique (see Chapter 4) used to examine the electrochemical kinetics of oxide growth and reduction on platinum. Figure 3.2 displays several CVs measured at varying scan rates and upper potential limits (UPLs) on a commercial (Ion Power, Inc.) membrane electrode assembly (MEA). The working electrode consisted of platinum supported on carbon electrocatalyst with a loading of 0.3 mg_{Pt}/cm^2_{geo}. The peak and subsequent plateau on the anodic sweep results from platinum surface oxidation by the representative reaction

$$Pt + H_2O \leftrightarrow PtO + 2H^+ + 2e^- , \tag{3.2}$$

while the peaks on the cathodic sweep result from the reduction of this oxide. PtO is a representative oxide species, as there is no consensus on the exact structure of the surface oxides. For Pt/C catalysts, carbon corrosion is a process that contributes to the shape of the CV under certain conditions, but this process is not discussed in this dissertation. Furthermore, the CV is not noticeably affected by platinum dissolution currents, which are estimated to be at least two orders of magnitude less than platinum oxidation currents (19).

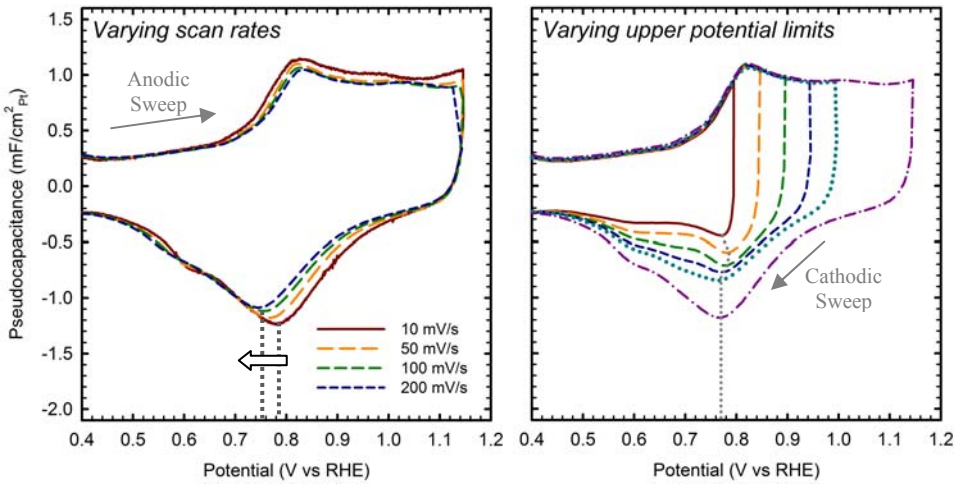

Figure 3.2 Experimental CVs for a commercial MEA with a Pt/C catalyst under dynamic conditions. Left: The effect of varying the scan rate from 10 to 200 mV/s. Right: The effect of varying the upper potential limit at a constant scan rate = 50 mV/s.

Several key experimental characteristics of CVs are observed in Figure 3.2. Notably, the oxidation peak at 0.82 V barely changes position, regardless of scan rate, indicating that a nearly reversible reaction is occurring. In contrast, the position of the reduction peak does shift with increasing scan rate. To probe kinetically irreversible systems, Tafel relationships can be used to describe the current-overpotential behavior (1). In the absence of mass-transfer effects the net reaction of the electron transfer process, $O + e^- \underset{k_b}{\overset{k_f}{\rightleftharpoons}} R$, is described by the Butler-Volmer equation

$$i = i_0 \left[e^{-\alpha f \eta} - e^{(1-\alpha) f \eta} \right], \tag{3.3}$$

which predicts the effect of overpotential (η) on current density (i). i_0 is the exchange current density, α is the transfer coefficient, and f is the ratio of Faraday's constant to the product of the ideal gas constant and temperature (1). The first exponential term in Equation (3.3) represents the forward or reduction reaction and the second term represents the backward or anodic process. At high overpotentials, greater than ca. 100 mV from the equilibrium potential, either the anodic or cathodic contributions to the net reaction become negligible (1). In this region, Tafel plots, where overpotential is plotted as a function of the logarithm of current density,

$$\eta = b \cdot \log\left(\frac{i}{i_0}\right) \tag{3.4}$$

are used to back out kinetic parameters such as the exchange current density and the transfer coefficient (1). This technique can be used when the current-overpotential relationship can be measured under steady-state conditions. For instance, the oxygen reduction reaction, $O_2 + 4H^+ + 4e^- \rightarrow 2H_2O$, on platinum can be studied in this way as long as enough oxygen is supplied to negate any mass-transfer effects. Conversely, the reduction of a platinum oxide film cannot be studied under steady-state conditions because it is impossible to maintain the amount of oxide on the surface while cathodically sweeping the potential. However, for oxide reduction during a CV, the peak current is

linearly proportional to scan rate (20), and the peak shape is largely unchanged with scan rate. The peak maximum represents a reproducible state of coverage, and the scan rate becomes a proxy for current. Thus, the Tafel slope is determined by measuring the change in peak position $\left(E_{\max}\right)$ with scan rate $\left(\nu\right)$,

$$b = \frac{dE_{\max}}{d\log\left(\nu/\nu_0\right)}. \tag{3.5}$$

Experimental values for the Tafel slope range from 20 to 50 mV/decade (20-24). The dotted gray lines and arrow on the left plot of Figure 3.2 mark the shift in peak position as the scan rate is increased from 10 mV/s to 100 mV/s, yielding the measured Tafel slope of 30 mV/decade. This value indicates that for every 30 mV decrease in potential, current should increase by an order of magnitude. If the current is assumed to be a function of only potential and coverage, as in Equation (3.3), then, at low overpotentials, the cathodic Tafel slope is

$$b = \frac{2.303}{f}\cdot\frac{1}{\alpha_C}, \tag{3.6}$$

where the factor 2.303 converts a natural logarithm to a base 10 logarithm. This relationship also determines the cathodic peak width. A Tafel slope of 30 mV/decade requires $\alpha_C = 2$, which results in a narrow reduction peak. Experimentally, the reduction peak is very wide, ca. 250 at full-width at half-max.

To summarize, we expect a very sharp leading edge during the initial stages of reduction; instead, a very shallow leading edge is observed. Because the coverage of oxide is nearly constant during the initial stages of reduction, the current-potential relationship is expected to follow Tafel kinetics. However, the Tafel slopes are not remotely consistent, which indicates that current is not only a function of potential and coverage. These seemingly contradictory facts pose a challenge for simulations.

It has been proposed in literature that after an initial submonolayer of oxide has chemisorbed onto the platinum surface, that a place exchange between the platinum

lattice atoms and oxygen atoms takes place; i.e., a surface phase transition occurs. Oxide growth past a monolayer occurs in this way and produces the anodic plateau region on the CV. Another characteristic is the nearly constant position of the reduction peak, regardless of the upper potential limit, which is marked by the dotted line in the right plot of Figure 3.2. Many of the above mentioned processes have been discussed in the literature (20, 22, 23, 25).

In addition to the potentiodynamic behavior described above, oxide growth can be studied under potentiostatic conditions to monitor growth with time. The initial oxidation of the platinum surface is very rapid, but the surface does not reach equilibrium over experimentally relevant timescales. Instead, the oxidation rate decreases proportionally to t^{-1}. This behavior gives rise to the observed logarithmic growth with time (26).

3.3 Oxide Growth Mechanisms

The initial chemisorbed oxide species has been debated for a long time. In the beginning, there was no direct chemical evidence of the chemisorbed species as OH. Instead, the OH species was assumed because it appeared to be consistent with the measured charge on the anodic sweep. Reddy, Genshaw, and Bockris used ellipsometry to characterize the thickness of the oxide film on platinum with time in 1968 and found a linear dependence of film thickness on potential (27). At 1 V the observed film was 1 Å thick, and at 1.6 V the film thickness increased to 8 Å. In the region from 0.7 to 0.95 V no oxide film was observed (27), in contrast to studies whereby the charge passed in forming the oxide was measured (28). Thus, a partial oxide layer, not observed by ellipsometry, was assumed, and a three-step mechanism

$$Pt + H_2O \rightleftharpoons PtOH + H^+ + e^-, \tag{3.7}$$

$$PtOH \rightarrow HOPt, \tag{3.8}$$

and

$$HOPt \rightarrow PtO + H^+ + e^- . \quad (3.9)$$

was proposed for oxide growth on platinum (27). The first step was proposed to follow a Temkin isotherm, where the adsorption enthalpy is a linear function of surface coverage (27). The second step represents the place exchange of OH molecules with platinum in the metal lattice and is considered the rate determining step (27). Place exchange has been found to be consistent with the kinetics of oxidation on other metals (29), and was proposed as the mechanism on platinum because deviation from Tafel kinetics is not observed (27). However, in other studies the discharge of water was confirmed as the rate determining step based on the analysis of anodic and cathodic Tafel slopes for the oxygen reduction reaction, stoichiometric numbers, overpotential as a function of acidity, and current density measured as a function of the partial pressure of oxygen (30). Under potential holds, the mechanism correctly predicts that charge increases with the logarithm of time (27). This mechanism was later disputed by Angerstein-Kozlowksa, Conway, and Sharp claiming that OH adsorbs as three geometrically distinguishable types of species, followed by further oxidation to PtO (20). This process was proposed by associating the charge under three peaks in the anodic profile of the CV (20). However, Conway's papers on this subject are the only studies where there are three observable anodic peaks (20, 31, 32). Furthermore, no physical evidence of OH was identified.

For the reduction of the oxide, Gilroy and Conway proposed a two-step mechanism

$$PtO + H^+ + e^- \overset{eqbm}{\rightleftharpoons} PtOH \quad (3.10)$$

$$PtOH + H^+ + e^- \rightarrow Pt + H_2O , \quad (3.11)$$

with the first step in equilibrium (24). A complex mechanism was proposed because the observed Tafel slope for oxide reduction was much less the theoretical value derived from theoretical Butler-Volmer rate equation. In this study the valency of PtO_2 ($4e^-$ per surface Pt atom) was reached at 1.8 V, if one ignores the place exchange concept.

However, 1.8 V is outside the range of interest if comparing the operation of a liquid electrolyte cell to fuel-cell operation in automotive applications (24). Tilak and coworkers confirm this reduction process, as the Tafel slope from 40 to 55 mV can be simulated under various conditions (32). Though, mathematically fitting the CV is very different than confirming the actual mechanism.

Thacker and coworkers analyzed the trace from a galvanic, cathodic stripping pulse to detect oxygen in the sublattice up to 2 atomic layers at low overpotentials and further absorbed oxygen atoms at high overpotentials (33). These researchers proposed the onset of oxidation to begin at 0.8 V and oxygen penetration into the metal lattice above 1.0 V (33).

In 2004, Jerkiewicz et al. performed a series of electrochemical and spectroscopic experiments on a platinum wire electrode in aqueous sulfuric acid solution (34). Contrary to previous studies (20, 35), the authors concluded that the chemisorbed species was oxide rather than hydroxide (34). Chemisorption was predicted to begin at 0.85 V. As the potential was increased, the dipole forces between the chemisorbed oxygen atoms continually increase with coverage. To minimize these interactions oxygen atoms begin to penetrate the platinum lattice, resulting in place exchange above 1.15 V (34, 36, 37).

In another study, in situ X-ray diffraction and real time energy dispersive X-ray absorption spectroscopy were carried out on Pt/C electrodes in an aqueous sulfuric acid solution (38). During the initial stages of a 1.4 V potential holds, bond lengths between Pt and oxygen containing molecules were identified. It was inconclusive whether the initial species was PtOH or PtO. However, the initial place-exchanged structure was detected as an α-PtO_2 phase. By 100 s of the potential hold, the oxide transitioned to a quasi-3D structure (β-PtO_2) (38). Holby and coworkers used DFT calculations and predicted a more stable hybrid structure involving platinum buckling and place exchange up to 1 monolayer of coverage (PtO basis, $2e^-$ per surface Pt atom) (39).

Most of the studies discussed thus far have been limited to those conducted in an atmosphere free from oxygen. In 2004, Paik and coworkers investigated the extent of surface oxidation under oxygen versus humidified inert gas streams using cyclic voltammetry. After holding an MEA at 0.85 V or 0.95 V under varying atmospheres they reduced the oxide and found that at 0.85 V a greater current was required as the partial pressure of oxygen was increased (40). However, this result can be traced back to the extremely low flow rate at the anode, 100 standard cubic centimeters per minute of 4 % hydrogen in balance nitrogen. This low flow rate only supports a maximum current density of ca. 18 mA/cm^2. At higher voltages, this limitation is not an issue, but at 0.85 V it is likely that near the outlet of the anode gas stream all the input hydrogen had been consumed. Therefore, the cathodic potential is increased to higher values, which would account for the observed increase in charge. A similar study by Liu and coworkers found no difference in the total oxygen reduction charge for varying partial pressures of oxygen (41). Kongkanand and Ziegelbauer conducted an investigation on platinum oxidation under oxygen-containing and pure nitrogen environments (42). Analysis of the X-ray absorption near edge structure revealed the presence of subsurface oxygen at 0.75 V under oxygen, about 0.25 V lower than subsurface oxygen detected under a nitrogen atmosphere (42). Thus, while the presence of oxygen may not affect the total amount absorbed, it may cause place exchange to occur much earlier than previously thought.

In summary, Jerkiewicz's extensive study established PtO as the initial chemisorbed oxide and contradicts previous literature investigations which favor PtOH. Additionally, these early works predicted PtO as the place-exchanged oxide, but recent works have detected evidence of PtO_2. Place exchange was thought to occur at potentials above 1 V in acidic solutions, though a recent study has shown place exchange to occur as early as 0.75 V in an oxygen containing atmosphere. Many researchers have tried to simulate the CV for oxide growth and reduction on platinum. However, there are many reactions and various conditions to consider, which complicate the modeling process.

3.4 Simulations

Many mathematical treatments have been provided for platinum oxide formation and reduction that are consistent with an experimental CV under certain conditions. However, developing a model that is physically consistent with the processes occurring on the platinum surface is a challenge. For instance, in an effort to understand the observed Tafel slope for oxide reduction, Srinivasan and Gileadi present a theoretical treatment of electrochemical adsorption and desorption steps on a metal surface (22). By mathematically analyzing a single charge-transfer step they proposed quantitative evaluation of rate constants, transfer coefficients, and charge (22). However, in this case Langmuirian conditions were assumed, where the activation energy (assumed to be related to adsorption enthalpy) is independent of coverage (22). This assumption is not acceptable for the oxidation of platinum because of the lateral interactions between adsorbed species and differing site activities on a polycrystalline surface (35).

Many times, Temkin kinetics, where the activation energy varies linearly with increasing coverage, are used to simulate oxide growth. The dependence between the two parameters is accounted for with an interaction parameter, ω, included in the Butler-Volmer rate equation

$$i = i_0 \left[e^{-\frac{\omega\theta}{RT}} e^{\alpha_A f\eta} - \theta e^{-\alpha_C f\eta} \right], \tag{3.12}$$

which allows for logarithmic growth with time (32, 43, 44). Physically, it represents the dipole interactions between adsorbed oxide species. As the interactions increase with coverage, the activation barrier for deposition of more oxygen atoms increases.

To evaluate the performance of different oxidation models, a handful of key experimentally observed characteristics have been identified in Table 3.1. The key characteristics identified are the Tafel slope and potentiostatic growth rate for the anodic process and the Tafel slope and reduction peak width for the cathodic process. For most

models, a simple combination of parameters can be derived that determine each characteristic, and these expressions are listed for the literature models described below.

Table 3.1 Summary of the important parameters that effect experimentally measurable quantities in various kinetic rate equations found in literature (13, 23).

Measurable Experimental Quantities		Anodic Tafel Slope *mV/decade*	Anodic Potentiostatic Growth Rate *ML/decade*	Cathodic Tafel Slope *mV/dec*	Cathodic Peak Width *mV*
MEA Experimental Values		12.5	0.26	35	320 (FWHM)
Appleby, 1973	**Symbolic Form**	$2.303\frac{RT}{\alpha_A F}$	$2.303\Big/\left(\frac{\alpha_A \omega}{RT}-\frac{1}{1-\theta}\right)$	$2.303\frac{RT}{\alpha_C F}$	$2.303\frac{RT}{\alpha_C F}+0.82\theta_{\max}\,\omega/F$
	Critical Parameters	α_A	α_A, ω	α_C	$\alpha_C, \omega, \theta_{\max}$
	Numeric Values[a]	39	0.25	39	$39+145\theta_{\max}$
Darling and Meyers, 2003	**Symbolic Form**	$2.303\frac{RT}{\alpha_A F}$	$2.303\frac{RT}{\omega}$	$2.303\frac{RT}{\alpha_C F}$	$2.303\frac{RT}{\alpha_C F}$
	Critical Parameters	α_A	ω	α_C	α_C
	Numeric Values[b]	84.5	0.19	197	197

a) T = 298 K, $\alpha_A = \alpha_C = 1.5$, ω = 17 095 mol/J, θ_0 = 0.10 (initial stages of growth)
b) T = 298 K, α_A = 0.70, α_C = 0.30, ω = 30 000 mol/J

One of the earliest attempts to simulate a full CV was made by Appleby (23). Appleby's work included a Temkin adsorption isotherm, and provided a way to decouple the cathodic Tafel slope and peak width by applying the adsorption isotherm effects equally to the anodic and cathodic reaction terms. Appleby showed that for a transfer coefficient of 1.5, the simulated Tafel slope would be 40 mV/decade (23). The figures generated in his work are presented as symmetric peaks. However, these shapes are not reproducible using the same equations and parameters given in his paper (23). The cause of inaccuracy is unknown, and the actual cathodic peak shapes generated by Appleby's mechanism are quite asymmetric with a steep leading edge, a sloped bottom, and a less steep trailing edge (23). This discrepancy is limited to peak shape, and the Tafel slope

and peak widths reported by Appleby are reproducible. Thus, the simulation of CVs depends on the mechanism and form of kinetic rate equations used and presents a challenge.

Darling and Meyers attempted to incorporate platinum dissolution and oxidation in a mathematical model (13, 14). They also included an interaction parameter, yet attributed the adsorption isotherm effects to the anodic term only as in Equation (3.12). To fit the reduction peak width on the CV, a symmetry coefficient of 0.15 (for a 2 electron reaction) was used, which broadened the shape of the simulated peak to match experimental results for a given scan rate, shown in figure 1 of reference (13). However, replicating their model and simulating under varying scan rates yielded a Tafel slope = 197 mV/decade, which is noted in Table 3.1. Because a single parameter, α_C, determines both characteristics, it is impossible to obtain the correct Tafel slope and peak width using the rate expression given by Equation (3.12). The results obtained for platinum dissolution versus potential (13) matched Nernstian experimental trends observed at 176 °C (6), rather than the weaker dependence observed at PEMFC operating temperatures (3-5). Additionally, when incorporated to a 1D model, no platinum dissolution is observed upon reduction of the oxide (14), despite experimental observation of this mechanism (15).

In a more general treatment of platinum oxidation, Hale and Greef were able to mathematically describe the observed curve shapes by choosing to express the interaction parameter as a Taylor series and varying the n^{th} order coefficients (44). If only the first order term is used, then the limiting case of Temkin kinetics is assumed. In the case of single peak analysis, the higher the coefficient, the broader the observed peaks (44). If the model is applied to describe multipeak behavior, Temkin kinetics is unrealistic because higher order interactions must be included. Thus, by varying the 1^{st} through 3^{rd} order coefficients of the Taylor series, double peaks can be generated with variable peak ratios and widths (44). This technique is in comparison to that first suggested by Breiter, where

a linear combination of 2 different Langmuir adsorption sites share the total surface area (45).

To summarize, the biggest obstacles for simulation of oxide growth and platinum dissolution are predicting the correct peak shape for varying scan rates and modeling the correct trends of platinum dissolution for various temperatures with respect to potential and reduction of the oxide. Many models have shown agreement in specific areas, but no models are comprehensive enough to describe the complicated processes. For this reason, more work is needed to better understand the interplay between platinum dissolution and oxide growth.

3.5 References

1. A. J. Bard and L. R. Faulkner, *Electrochemical methods: Fundamentals and applications*, John Wiley & Sons, USA (2001).

2. M. Pourbaix, *Atlas of Electrochemical Equilibria in Aqueous Solutions*, National Association of Corrosion Engineers, Houston, TX (1974).

3. X. P. Wang, R. Kumar and D. J. Myers, *Electrochem Solid St*, **9**, A225 (2006).

4. P. J. Ferreira, G. J. la O', Y. Shao-Horn, D. Morgan, R. Makharia, S. Kocha and H. A. Gasteiger, *J Electrochem Soc*, **152**, A2256 (2005).

5. R. K. Ahluwalia, S. Arisetty, X. P. Wang, X. H. Wang, R. Subbaraman, S. C. Ball, S. DeCrane and D. J. Myers, *J Electrochem Soc*, **160**, F447 (2013).

6. P. Bindra, S. J. Clouser and E. Yeager, *J Electrochem Soc*, **126**, 1631 (1979).

7. K. Kinoshita, J. T. Lundquist and P. Stonehart, *Electroanalytical Chemistry and Interfacial Electrochemistry*, **48**, 157 (1973).

8. K. Yasuda, A. Taniguchi, T. Akita, T. Ioroi and Z. Siroma, *Phys Chem Chem Phys*, **8**, 746 (2006).

9. S. Mitsushima, S. Kawahara, K. I. Ota and N. Kamiya, *J Electrochem Soc*, **154**, B153 (2007).

10. M. Uchimura, S. Sugawara, Y. Suzuki, J. B. Zhang and S. S. Kocha, *ECS Transactions*, **16**, 225 (2008).

11. F. Ettingshausen, J. Kleemann, A. Marcu, G. Toth, H. Fuess and C. Roth, *Fuel Cells*, **11**, 238 (2011).

12. T. Patterson, in *AIChE Spring National Meeting*, G. J. Igwe and D. Mah Editors, p. 313, Topical Conference Proceedings, New York (2002).

13. R. M. Darling and J. P. Meyers, *J Electrochem Soc*, **150**, A1523 (2003).

14. R. M. Darling and J. P. Meyers, *J Electrochem Soc*, **152**, A242 (2005).

15. D. C. Johnson, D. T. Napp and Buckenst.S, *Electrochim Acta*, **15**, 1493 (1970).

16. E. F. Holby, W. C. Sheng, Y. Shao-Horn and D. Morgan, *Energy & Environmental Science*, **2**, 865 (2009).

17. H. Akbarzadeh, H. Abroshan and G. A. Parsafar, *Solid State Commun*, **150**, 254 (2010).

18. D. J. Myers, X. Wang, N. Kariuki, T. Nowicki, S. DeCrane, R. Subbaraman, R. Ahluwalia and S. Arisetty, Polymer Electrolyte Fuel Cell Lifetime Limitations: The Role of Electrocatalyst Degradation, in *DOE Hydrogen and Fuel Cells Program: FY 2012 Annual Progress Report*, p. 168 (2012).

19. W. Bi and T. F. Fuller, *J Power Sources*, **178**, 188 (2008).

20. Angerstein-Kozlowska.H, B. E. Conway and W. B. A. Sharp, *J Electroanal Chem*, **43**, 9 (1973).

21. F. G. Will and C. A. Knorr, *Z Elektrochem*, **64**, 258 (1960).

22. S. Srinivasan and E. Gileadi, *Electrochim Acta*, **11**, 321 (1966).

23. A. J. Appleby, *J Electrochem Soc*, **120**, 1205 (1973).

24. D. Gilroy and B. E. Conway, *Can J Chemistry*, **46**, 875 (1968).

25. F. G. Will and C. A. Knorr, *Z Elektrochem*, **64**, 258 (1960).

26. M. Alsabet, M. Grden and G. Jerkiewicz, *J Electroanal Chem*, **589**, 120 (2006).

27. A. K. N. Reddy, M. A. Genshaw and J. O. Bockris, *J Chem Phys*, **48**, 671 (1968).

28. A. Damjanovic and V. Brusic, *Electrochim Acta*, **12**, 615 (1967).

29. M. A. H. Lanyon and B. M. W. Trapnell, *Proc R Soc Lon Ser-A*, **227**, 387 (1955).

30. A. Damjanovic, A. Dey and J. O. Bockris, *Electrochim Acta*, **11**, 791 (1966).

31. B. E. Conway and S. Gottesfeld, *J Chem Soc Farad T 1*, **69**, 1090 (1973).

32. B. V. Tilak, B. E. Conway and H. Angerstein-Kozlowska, *J Electroanal Chem*, **48**, 1 (1973).

33. R. Thacker and J. P. Hoare, *J Electroanal Chem*, **30**, 1 (1971).

34. G. Jerkiewicz, G. Vatankhah, J. Lessard, M. P. Soriaga and Y. S. Park, *Electrochim Acta*, **49**, 1451 (2004).

35. P. Stonehart, H. A. Kozlowska and B. E. Conway, *Proc R Soc Lon Ser-A*, **310**, 541 (1969).

36. B. E. Conway, B. Barnett, H. Angersteinkozlowska and B. V. Tilak, *J Chem Phys*, **93**, 8361 (1990).

37. B. E. Conway, *Prog Surf Sci*, **49**, 331 (1995).

38. H. Imai, K. Izumi, M. Matsumoto, Y. Kubo, K. Kato and Y. Imai, *J Am Chem Soc*, **131**, 6293 (2009).

39. E. F. Holby, J. Greeley and D. Morgan, *J Phys Chem C*, **116**, 9942 (2012).

40. C. H. Paik, T. D. Jarvi and W. E. O'Grady, *Electrochem Solid St*, **7**, A82 (2004).

41. Y. X. Liu, M. Mathias and J. L. Zhang, *Electrochem Solid St*, **13**, B1 (2010).

42. A. Kongkanand and J. M. Ziegelbauer, *J Phys Chem C*, **116**, 3684 (2012).

43. D. V. Heyd and D. A. Harrington, *J Electroanal Chem*, **335**, 19 (1992).

44. J. M. Hale and R. Greef, *Electrochim Acta*, **12**, 1409 (1967).

45. M. W. Breiter, *T Faraday Soc*, **62**, 2887 (1966).

CHAPTER 4

EXPERIMENTAL PROCEDURES AND ANALYTICAL TECHNIQUES

The following text describes the equipment, procedures, and techniques used to collect data presented in the later chapters. Details are provided for equipment and procedures that are used widely in the field of fuel cell research, so that the novice reader can follow the data collection and analysis present in this dissertation. Also, tips are provided for those who are working on projects of a similar nature. Background information is also provided for techniques requiring synchrotron radiation sources, since many people may not have direct experience in this area. References are given for widely used procedures across all disciplines.

4.1 Fuel Cell Test Station and Potentiostat

The fuel cell test station (FCTS) and potentiostat are central to characterizing fuel cell performance and analyzing the behavior of the working electrode. Measuring and manipulating the experimental variables of time, potential or current, reactant types or concentrations, and temperature allows one to observe cell performance, reaction kinetics, active surface area, and oxide growth on the platinum surface. This section provides a brief explanation of equipment operation and the procedures that can be carried out on each system. The FCTS provides a complete system that controls the reactant types, gas flow, gas line temperature, humidifier temperature and cell temperature. Figure 4.1 shows a schematic of the flow paths inside the system.

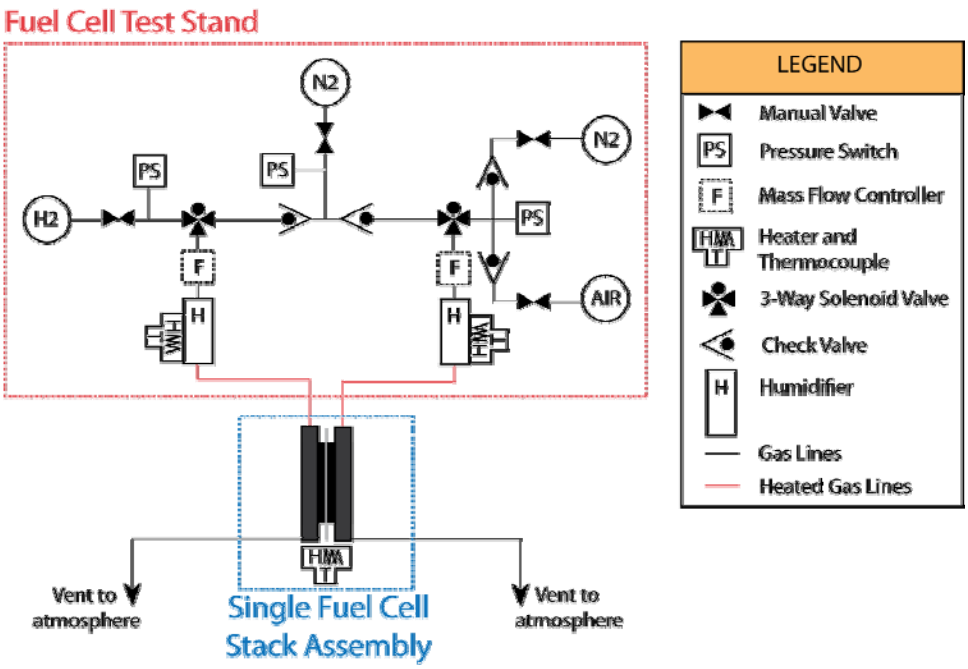

Figure 4.1 A diagram of the plumbing inside a FCTS. Adapted from reference (1), figure in Chapter 4, page 28.

To purge the cell, nitrogen flows through both gas lines leading to the fuel cell stack. When in operation hydrogen fuel flows to the anode of the fuel cell, while either nitrogen or air flows to the cathode, depending on which experiments were being performed. The dry gas flow rates were regulated with mass flow controllers. The FCTSs in this work had varying minimum and maximum flow rates, depending on which model was used. All gases were humidified by bubbling dry gases through two separately controlled water reservoirs. The gas lines from the humidifiers to the cell assembly were wrapped in heat tape set an additional 5 °C above the humidifier temperature to prevent water condensation. The relative humidity was controlled by varying the temperature of the humidifiers and the temperature of the cell,

$$\text{Relative humidity} = \frac{p_{H_2O}}{p^*_{H_2O}\left(T_{cell}\right)} = \frac{p^*_{H_2O}\left(T_{humidifier}\right)}{p^*_{H_2O}\left(T_{cell}\right)}, \tag{4.1}$$

where the partial pressure of water, p_{H_2O}, is equal to the vapor pressure of water, $p^*_{H_2O}$, at the temperature of the humidifier, $T_{humidifier}$. The denominator is the vapor pressure of water at the temperature of the cell, T_{cell}. Excess gas and reaction products were safely vented under a hood to atmosphere. The fuel cell stack assembly is explained in Chapter 4.2.

The FCTS is also used to apply an electric load to the fuel cell stack assembly, which allows for conditioning procedures and characterization tests to be performed. The wet-up procedure for conditioning the cell and an explanation of polarization curves can be found in Chapter 4.4. The FCTSs were either controlled by FuelCell software by Scriber Associates, Inc. or with a LabVIEW program by Fuel Cell Technologies, depending on which model was used.

The potentiostat regulates the potential difference between the reference electrode and the working electrode, and the current response is measured through the counter electrode and the working electrode as shown in Figure 4.2. The input voltage, E_{in}, is set through communication with a software program. The amplifier controls the potential difference between the working electrode and the reference electrode by varying the output current, which is measured between the counter and working electrodes. In the case of a fuel cell stack, the reference and the counter electrodes are the same. The schematic below shows the components of a potentiostat.

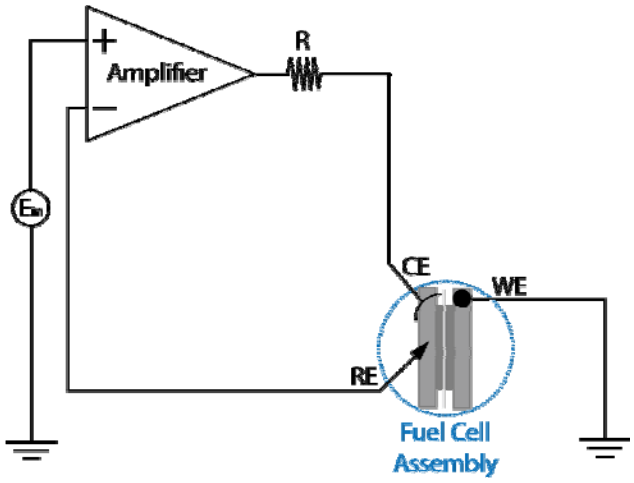

Figure 4.2 Electrical components for a simple potentiostat with connections to a single fuel cell stack.

A potentiostat can either act as an electric load on the cell or as a power source. FCTSs are only equipped to operate as a load. The components inside the potentiostat limit the maximum current, which is specific to the particular model of potentiostat. The Autolab PGSTAT302N has a 2 A limit and the Princeton Applied Research 263 has a 200 mA limit. For comparison, the FCTS can handle currents up to 50 A. Under air, the huge oxygen reduction current covers up contributions from cross over hydrogen, double layer capacitance, and any surface reactions, such as platinum oxidation or hydrogen adsorption. Humidified nitrogen is used at the cathode for experiments where these processes are under investigation, and the potentiostat is used to control the voltage or current. On the other hand, air is the cathode gas for most tests on the FCTSs, where cell performance is considered. The potentiostat was used for cyclic voltammetry, potential holds, and electrochemical impedance spectroscopy (Chapter 4.4).

4.2 Single PEM Fuel Cell Stack Assembly

The fuel cell stack assembly refers to the hardware encasing the membrane electrode assembly (MEA) and the MEA itself. The hardware is compressed by 8

$1/4" \times 20$ bolts tighted to 4.5 N-m (40 in-lbs) torque, which prevents air from coming into the cell and reactants from leaking out. The hardware forces gases through the cell, and contains the heaters and thermocouple for monitoring the cell temperature. Additionally, metal plates are used as the current collectors. Two hardware types were used in the following studies. The first hardware type is standard amongst fuel cell labs, and the second was specifically designed for synchrotron radiation experiments.

4.2.1 Standard Hardware

Standard hardware consists of two aluminum end plates (each ~18.5 mm thick), which are used to deliver the incoming gases from the FCTS and remove excess gases. Eight threaded screws are used to compress the end plates, and the symmetrical pattern of holes observed in Figure 4.3a ensures uniform compression. A thin insulating silicon mesh material (0.35 mm) separates the end plate from the current collector to prevent the cell from short circuiting. Electrical connections are made at the current collectors (1.4 mm) to complete the circuit. The current collectors are gold-coated to prevent surface oxidation and minimize lead resistance. A graphite flow field (12.9 mm) with a triple serpentine pattern was used to ensure uniform distribution of the reactants. The flow pattern was designed for a 25 cm^2 electrode. A PTFE gasket (0.16 mm) is used to seal around the electrode on either side of the MEA. Gas diffusion layers (0.19 mm) were made from PTFE treated Toray Carbon Paper (TGP-H-060, FuelCellStore.com).

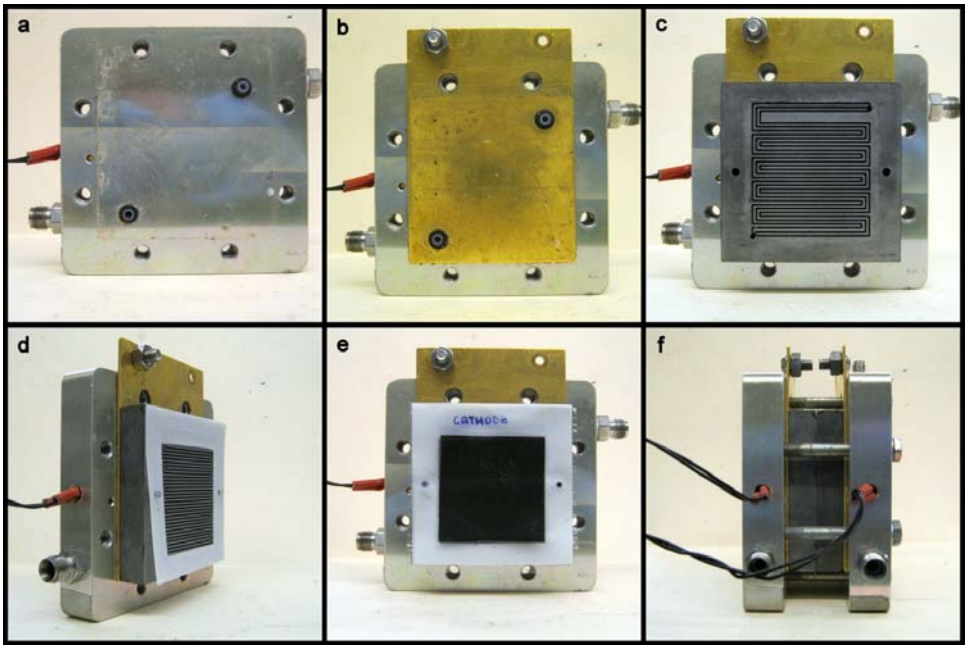

Figure 4.3 Images of standard fuel cell hardware components (a) Aluminum end plate with 8 threaded holes for uniform compression of the MEA (b) Gold plated current collector, separated from endplate by insulating material (not shown) (c) Graphite flow field with ser serpentine pattern for uniform gas delivery (d) Teflon gasket used to seal around electrode (e) MEA assembly (GDLs not shown) (f) Fully assembled hardware.

4.2.2 Custom Hardware

Custom hardware was designed for synchrotron experiments, such that the hardware would not interfere with the incident X-ray. The main difference compared to the standard hardware is that the custom hardware had holes cut through the end plates, current collectors, and flow fields. Initially, the cell hardware was designed for pair distribution function experiments, which required an incident X-ray energy of 58 keV. The beam size was very focused, approximately 0.5 mm × 0.5 mm. The original holes cut into the anode end plate and current collector had a diameter of 4 mm. Later, this hardware was modified for X-ray Absorption Spectroscopy experiments, where the beam is less focused, and the holes were widened to 10 mm. However, the holes in the flow fields were not altered because the graphite signal interfered less with the incoming beam of 10 keV. The holes in the flow field were sealed with Kapton®, a material that has

negligible interaction with X-rays. Additionally, Kapton® (0.12 mm) was used as the insulting material between the aluminum end plates (12.6 mm) and stainless steel (Type 420) current collectors (1.53 mm). The oxide layer formed on stainless steel resulted in an increased lead resistance, which was measured periodically, so that it could be accounted for in the data analysis. This effect was also minimized by sanding the current collectors with silicon carbide (1200 grit) between samples. The metal components were manufactured in the Georgia Tech ChBE Machine Shop. The graphite plates were machined by Fuel Cell Technologies. The single-serpentine flow field was designed for a 4.8 cm^2 electrode. Figure 4.4 shows the individual components and fully assembled hardware. The front view of the cathode side is shown in Figure 4.4f, where the hole was made larger than the anode side to enable collection of the diffracted X-rays. The conical step design was implemented to give a maximum scattering angle of 61° and allow a uniform pressure gradient across the MEA. For complete dimensions and design of hardware see APPENDIX B.

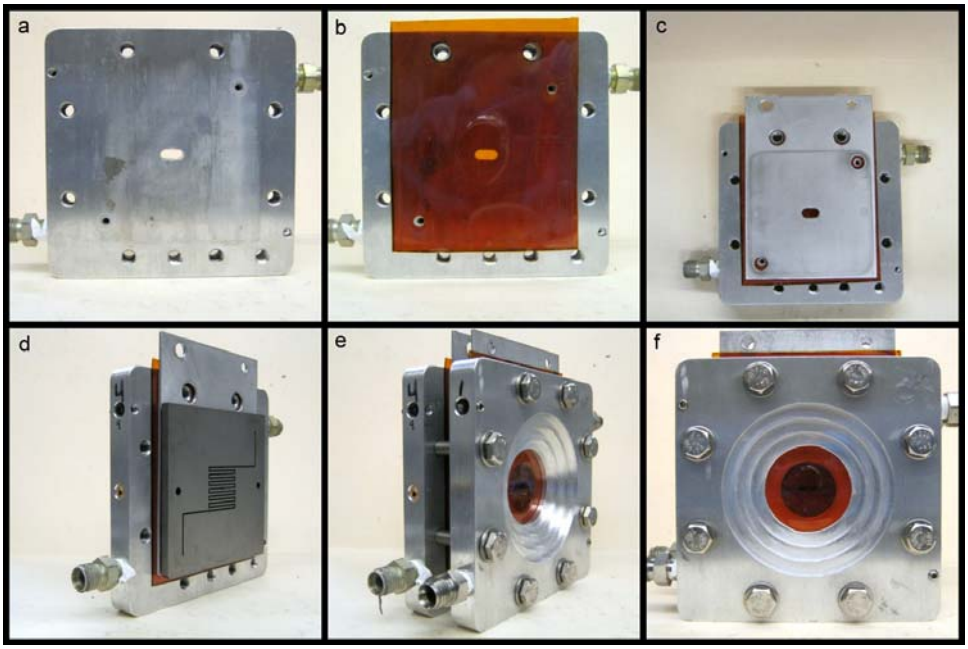

Figure 4.4 Images of custom fuel cell hardware components (a) Anodic aluminum end plate with 8 threaded holes for uniform compression of the MEA and 2 extra holes for attachment to a sample stage (b) Kapton® insulator (c) Anodic stainless steel current collector (d) Graphite flow field with serpentine pattern for uniform gas delivery (e) Fully assembled hardware (e) Front view of cathode side.

4.3 Fabrication of Membrane Electrode Assemblies

Membrane electrode assemblies (MEAs) can be fabricated through a variety of methods and experimental conditions (2-10). The first step to any process is to mix the catalyst ink and prep the membranes. The fabrication techniques used for this research were either direct spray coating of the membrane or the decal method. The following text explains the manufacturing steps in detail.

4.3.1 Catalyst Ink Preparation and Membrane Pretreatment

In order to achieve high catalyst utilization, platinum must be in contact with both the ionomer and the carbon. The ionomer conducts protons, and the high surface area carbon support conducts electrons. An ionomer that is too thick creates an increased resistance to gas transport. Alternatively, if the catalyst is not in contact with the ionomer

then no reaction occurs. An efficient catalyst ink will increase the contact between the platinum surface and the ionomer. In this work, two catalyst inks were used. The first was an aqueous mixture of alcohol, ionomer, and catalyst powder which formed a solution. The second was a colloid created by the addition of an organic solvent that caused the ionomer to absorb catalyst particles and form larger aggregates leading to the creation of a more connected network (11, 12).

In the aqueous mixture the mass ratio of Nafion® to deionized water to isopropyl alcohol to carbon was 0.8:5:20:1. First, a small amount of deionized water was added to a small 25 mL vial to wet the bottom and prevent the catalyst powder from sticking. Next, the catalyst powder was added, where the type of catalyst was specific to each experiment. The remaining deionized water was added and the mixture was sonicated in a bath for 10 minutes. After sonication, the correct amount of Nafion® was added in the form of a 5 % (w/w) Nafion® solution (45 % (w/w) water, 50 % (w/w) isopropyl alcohol (Ion Power D520)). The mixture was sonicated in a bath for 10 minutes. Last, the isopropyl alcohol was added before sonicating (Misonix Sonicator 3000) with a solid titanium microtip, 3.2 mm in diameter, for 2 hours (1 minute sonication on, 1 minute sonication off). The vial was kept in an ice bath during microtip sonication to prevent the solution from overheating.

To prepare the colloid ink (11) a 5 % (w/w) Nafion® solution was added drop-by-drop to n-butyl-acetate and stirred. The platinum based catalyst supported on carbon was immediately added to form a colloid based ink, which was then sonicated. The final ratio of the ink was 0.8 g of dry Nafion® per 50 g n-butyl-acetate per 1 g of carbon for all samples.

All membranes were hot pressed or spray coated in the H^+ form. The as-received membrane material was cut to size and pretreated to remove organic impurities by boiling in 3 % (v/v) aqueous hydrogen peroxide solution for 1 hour. Next, the membranes were rinsed with deionized water and boiled in deionized water for an additional hour.

Nafion® was then boiled in 0.5 M aqueous sulfuric acid solution for 1 hour to remove trace metal impurities, followed by a rinse and boiling in deionized water for the last hour. Membranes were stored in sealable plastic bags with a damp cloth to prevent them from drying out.

4.3.2 Direct Spray Coating

One of the goals when fabricating membranes is to determine an accurate catalyst loading, which is essential to measuring the electrochemically active area. Through direct spray coating the weight change of the membrane is monitored as the catalyst ink is deposited, and a catalyst loading can be calculated. The initial membrane weight was recorded, a stencil of the appropriate electrode area was overlaid on the membrane, and clamped to a sturdy support using binder clips as shown in Figure 4.5.

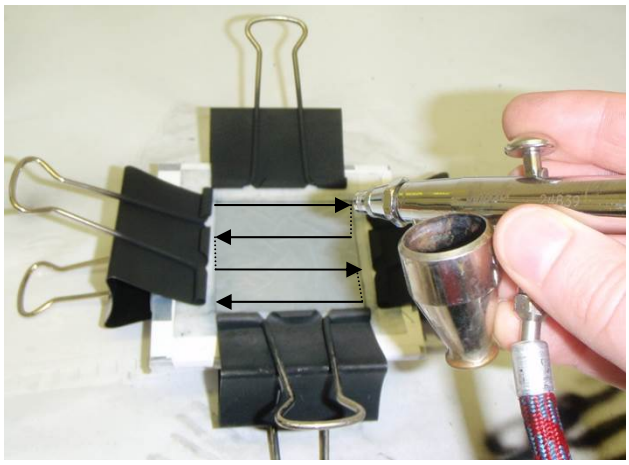

Figure 4.5 Demonstration of the direct spray coating set-up.

The membrane was then dried over a hot plate at 80 °C for 10 minutes, removed from the clamps, and the weight was measured again. This process was repeated until a stable weight was established. A small amount of the well-mixed catalyst ink was poured into the ink cup of the airbrush (Iwata Eclipse HP-CS), and the ink was sprayed directly onto

the membrane by applying medium pressure to the air release valve of the airbrush. It is best to spray in an alternating direction, denoted in Figure 4.5 by the arrows, to achieve a uniform coating. After a few coatings were applied, the membrane was placed over the hot plate and dried for 10 min at 80 °C. The membrane was then removed from the binder clips and weighed. The process was repeated until a stable weight was recorded. The ink would be sprayed again and the drying process repeated until the desired weight was realized.

The direct spray coating method is a simple procedure, though there are some limitations. For instance, electrode cracking is an issue and can be unpredictable. The MEAs fabricated by direct spray coatings in this work were made using the alternate 10 min drying process. However, others in the Fuller lab have recently found that a faster ink depositing method results in less cracking. In this case, the deposited layer is dried at room temperature for 1 minute or less between coatings. The key is never letting the catalyst layer dry out while spraying. Many coatings are applied before the membrane is dried over heat for longer times and removed from the clamps to monitor the weight change. Thus, the likelihood of overshooting the desired loading is increased. However, the faster procedure is thought to produce less cracking because the electrode is no longer subject to drying/wetting cycles. Also, better performance is measured because the ionomer and catalyst mixture remain well-mixed through the thickness of the electrode. Having a person controlling the airbrush results in a great variability of the uniformity of the electrode for each MEA, this can affect the utilization and performance of the fuel cells. Other groups have focused on automating the spray coating process to produce precise uniformity for all electrodes (13-15).

The catalyst ink is corrosive to the coating of the airbrush ink cup, which may introduce some impurities on the electrode area. At one point, a custom glass ink cup was used for several MEAs, but the glass was fragile and did not last very long. However, no

electrochemical inconsistencies were observed between the fuel cells. Care was taken to not leave the ink in the cup for long and to rinse the cup well between uses.

Nafion® absorbs water from the atmosphere, which makes obtaining a consistent weight challenging, especially in a lab environment where the humidity varies throughout the day. Compared to Nafion® 117, Nafion® 112 is better suited for drying over the hot plate because it absorbs less water. If a consistent weight cannot be recorded, then the catalyst loading is impossible to measure gravimetrically, which is why the decal method was employed.

4.3.3 Decal Method

In the decal method, the catalyst ink was applied to PTFE (0.30 mm) templates using an airbrush, and a membrane was sandwiched between two decals and hot pressed. The measured weight of PTFE will vary with time because it accumulates a static charge. To stabilize the weight measurements, aluminum foil was wrapped around the PTFE decals to act as a ground for the static charge, as demonstrated in Figure 4.6. The catalyst ink was directly sprayed onto a stenciled PTFE square following the procedure from the direct spray coating method. After the desired weight was achieved, the decals were dried overnight before hot pressing. The electrodes were centered on the membrane using small pin holes in the decals, Figure 4.6, where flattened wires were used as anchors. The assembly was then placed between two thick rubber pieces before being put on the hot press (Carver, Inc.; Kohl Lab, Georgia Tech) at 155 °C. Pressure of 1.807×10^6 N/m^2 (2600 lbs total per 9.92 in^2 of rubber area – the equipment is label in English units) was applied for 8 minutes. The assembly was then removed from the hot press and cooled before disassembling. Each decal was weighed before and after hot pressing and the percent of the electrode weight transferred was calculated. The procedure for hot pressing was adapted from Saha and coworker's 2010 study (16). The biggest issue observed with

the decal method is the incomplete transfer of the electrode from the decal to the membrane, as shown in Figure 4.7.

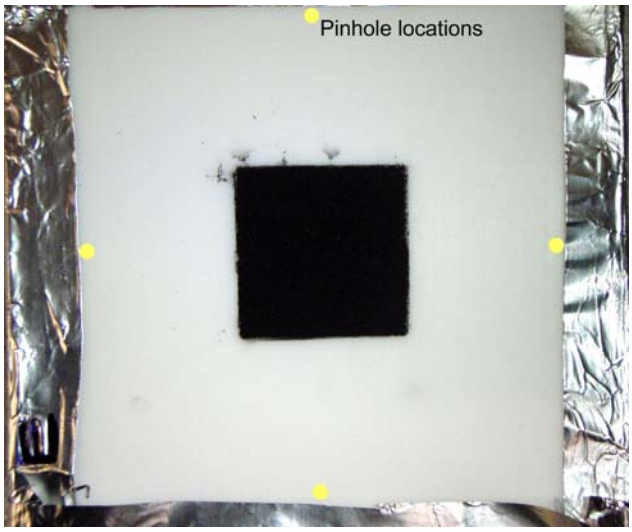

Figure 4.6 An example of an electrode decal is shown. The PTFE sheet was wrapped in aluminum foil to stabilize the weight measurements. When sandwiching two decals, thin wire was threaded through the pinholes and flattened to anchor the assembly for hot pressing. The approximate locations for the pinholes are highlighted in yellow.

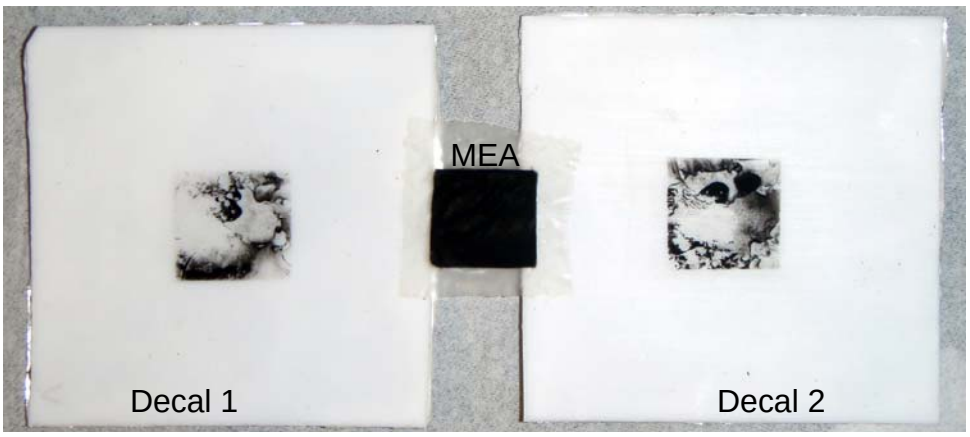

Figure 4.7 Decals and the MEA after hot pressing. Notice that while the MEA catalyst layer appears uniform, the decals were not 100 % transferred.

Many samples were made and those with the best transference were used in the experiments. When these samples are referred to, the percent transfer is noted. Furthermore, the performances of all fuel cells are reported in Appendix A.

4.4 Analytical Techniques

A unique set of tools were used to collect and analyze the data presented in this work. Electrochemical methods were used to collect information on cell performance, electrochemically active area, and oxide coverage on platinum at different conditions. Many times these experiments were combined with techniques requiring synchrotron radiation to help understand the surface chemistry that occurs on the electrode, such as platinum coarsening or oxide growth on platinum. In the following section, the necessary background for each technique is provided for one to understand the experiments presented in later chapters.

4.4.1 Fuel Cell Conditioning Procedure

Before use, all MEAs were preconditioned, or wet-up, to fully hydrate the ionomer, which allowed the fuel cell to reach its maximum performance. The cell was hydrated by cycling between high and low current densities. Once the cell has been hooked up to the FCTS, humidified nitrogen purged both sides of the cell at 0.5 L/min for at least 30 min. Then, the cell and humidifiers are slowly ramped, to prevent dry-out, to 85°C. At the set point, pure hydrogen and filtered air are supplied to the anode and cathode at a base flow rate of 0.2 L/min with a stoichiometric ratio of 6. No backpressure was applied to the MEAs in this work. Then, a slightly modified protocol, released by DuPont (17), was used for the wet-up and shown in Table 4.1.

Table 4.1 The cycling profile used for cell wet-up.

Protocol	Time *(min)*	Current Density *(A)*	Total Time *(min)*
Repeat 12 times	10	40	126
	0.5	0	
Repeat 2 times	20	30	280
	20	25	
	20	20	
	20	10	
	20	5	
	20	2.5	

4.4.2 Polarization Curves

After cell conditioning, several characterization tests were performed. Polarization curves, displayed as cell voltage as a function of current, are used to measure the internal resistances of the MEA that limit the overall performance of the fuel cell. The 3 major causations that contribute to the shape of an observed performance curve, Figure 4.8, are activation losses, ohmic losses, and mass transport losses (18).

The standard potential (E^0) for the oxygen reduction reaction is 1.223 V (19), which can be shifted from equilibrium, represented by the Nernst equation (20), due to changes in temperature and/or the activities of the oxidized (a_O) or reduced (a_R)

$$E = E^0 + \frac{RT}{nF} \ln\left(\frac{a_O}{a_R}\right). \tag{4.2}$$

An additional drop from the equilibrium potential is observed and caused by the activation losses due to the slow kinetics of the oxygen reduction reaction. Furthermore, some hydrogen molecules diffuse through the membrane and react at the positive electrode, generating electrons which lead to a lower open circuit potential.

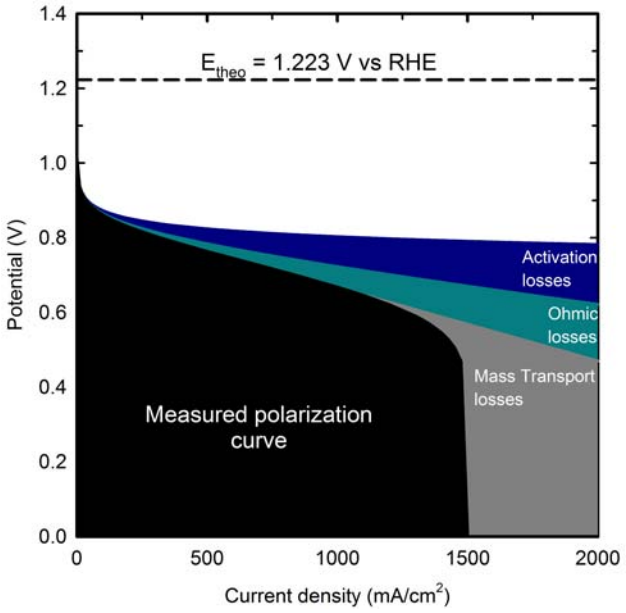

Figure 4.8 A simulated performance curve that includes the main source of performance loss with increasing current density.

Ohmic losses are due to the resistance of proton transport through the ionomer, resistance of electron transport through the electrode, and contact resistances within the fuel cell. This region is governed by Ohm's Law, V = IR, and is not affected by the concentration of reactants.

Mass transport losses occur when significant oxygen concentration gradients exist. The gasses must diffuse through the gas diffusion layers, the porous electrode structure, and the ionomer to reach the catalyst surface. The large concentration gradient causes a sharp decrease in cell performance at high current densities. All of the sources of performance loss can be minimized through optimum design of the cell components and experimental conditions.

The polarization curve was used to monitor the performance of the cells before and after cycling or potential hold experiments. Different temperatures were used for the experiment, but higher temperatures will minimize activation losses. The curve was always collected under a relative humidity of 100 % to minimize Ohmic losses.

Hydrogen and air were supplied to the anode and cathode at 0.2 L/min with a stoichiometric ratio of 6 to minimize mass transport losses. The voltage was held at 0.7 V for 30 minutes before running the polarization test, to give the temperature time to adjust if the previous step was at a different temperature. A scan current procedure was used in the FuelCell software to program the polarization curve to scan from high currents to low currents. The test was separated into 3 regions, and data were collected for 15 min/point to ensure a steady-state reading. The first region scans from 40 A to 10 A at 5 A/point, followed by 7.5 A to 5 A at 2.5 A/point, and the Tafel region is scanned from 3 A to 0 A at 0.5 A/point. There are a number of ways to program polarization currents (scan voltage, low to high current densities, etc.), so a number of methods were used in collecting the data. However, over the course of years, the above outlined procedure has been established as a standard method for collecting the polarization curve and was adapted from reference (21), though there a many ways to collect a quality polarization curve. Even though high cell performance is desired, optimizing MEAs was not a major goal of this thesis. For this reason, the polarization curves for the MEAs are presented in Appendix A.

4.4.3 Cyclic Voltammetry

Cyclic voltammetry, whereby the potential is swept in a triangular waveform at varying rates and the current response is measured, is a very flexible technique. It can be used as an initial characterization method to determine the electrochemically active area and test for impurities. The repetition of the procedure is used to simulate drive cycles for fuel-cell vehicles to accelerate the degradation of the working electrode. The effects that significantly contribute to the current are

$$2H^+ + 2e^- \rightleftharpoons H_2, \tag{4.3}$$

$$i = C \cdot \frac{dE}{dt}, \tag{4.4}$$

$$H^+ + e^- \rightleftharpoons H_{ads}, \tag{4.5}$$

and

$$PtO + 2H^+ + 2e^- \rightleftharpoons Pt + H_2O. \tag{4.6}$$

The resulting plot is called as cyclic voltammogram (CV) and is shown in Figure 4.9 as the shaded region, the major contributions to the 4 regions of peaks are labeled. The CV was measured under 1.0 L/min hydrogen and 0.05 L/min nitrogen at a scan rate of 10 mV/s. The other lines were sketched onto the measured CV to illustrate the contributing effects.

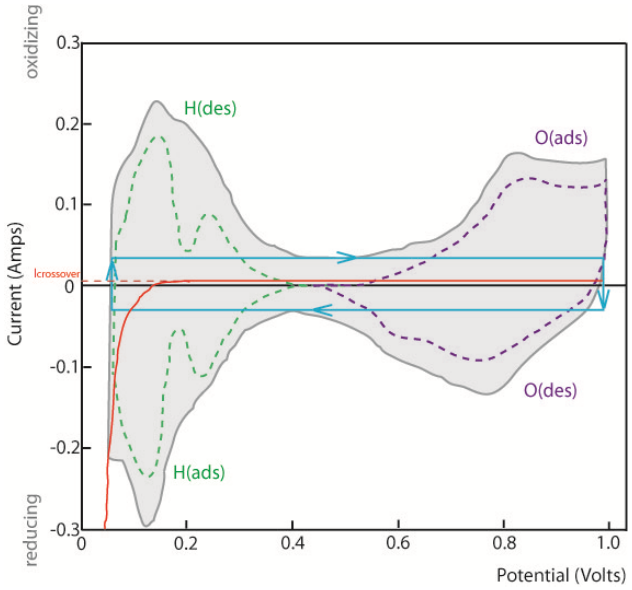

Figure 4.9 A measured CV (shaded region) includes contributions from many different processes: crossover hydrogen (red), double layer capacitance (blue), hydrogen adsorption and desorption (green), oxide formation and reduction (purple) that contribute to the measured CV (shaded region). The individual processes are illustrations, not an actual deconvolution of the data.

The red line corresponds to crossover hydrogen, process (4.3), which creates a small partial pressure of hydrogen at the cathode. At some low potential, hydrogen evolution is at equilibrium (I = 0 A). As the potential is increased, a shift from equilibrium occurs, causing the present hydrogen gas to immediately oxidize to protons. Once all the hydrogen is consumed, a limiting hydrogen crossover current is established

(red dashed line), even as the potential is taken to higher values. When the potential is below the equilibrium value hydrogen gas is evolved, causing a sharp increase in the absolute value of the observed current. A high nitrogen flow rate at the cathode will sweep away excess H_2 and the curve will shift to the right, which can mask the details seen in the hydrogen adsorption (green dashed line) region of the CV. For this reason, it is best to keep the nitrogen flow rate as low as possible.

CVs can be used to determine the electrochemically active area (ECA) of the electrode, which can be used to monitor degradation of the electrode with time and infer information about the utilization of the catalyst. As expressed in process (4.5) and shown in Figure 4.9, hydrogen adsorbs on platinum under reducing conditions and desorbs under oxidizing conditions at low potentials. Hydrogen only adsorbs up to a monolayer, and it has been established that approximately 210 μC of charge are passed per cm^2 of platinum surface area (Γ) (22, 23). Thus, the amount of charge (q_H) passed when either adsorbing or desorbing hydrogen can be used to determine the electrochemically active area in units of m^2_{Pt}/g_{Pt},

$$ECA = \frac{q_H / L}{\Gamma \cdot SA}, \tag{4.7}$$

when the catalyst loading, L (mg_{Pt}/cm^2_{geo}), and the geometric surface area, SA (cm^2_{geo}), are known. There are few things to consider when measuring q_H; which is determined by directly integrating the area under the current versus time profile, or by dividing the area of the current-potential region (0.4 V to 0.05 V) with the scan rate. First, the charge passed from double layer charging must be subtracted out, shown as the blue rectangle in Figure 4.9. Additionally, determining the lower potential bound is subjective, especially if there is significant hydrogen evolution in this region. In this work, the lower bound was chosen as the plateau, appearing to the left of the largest hydrogen adsorption peak. The values obtained for q_H in the hydrogen adsorption region and the hydrogen desorption region were within 5 % of each other.

At high potentials, a multilayer oxide can form on the platinum surface, this region is shown in Figure 4.9 as the dashed purple line. The current observed in the adsorption region can be convoluted by carbon oxidation, depending on experimental conditions. Therefore, the charge associated with the oxide, q_O, was measured in the oxide reduction region. The amount of oxide coverage is calculated as q_O/q_H.

The CVs presented in this work were recorded under humidified hydrogen and nitrogen, 1.0 L/min and 0.05 L/min. Sometimes, deionized water was used to flood the cathode, which resulted in an augmented ECA since all of the catalyst material was ionically connected. The most defined CVs are measured at room temperature, though many different temperatures were used throughout this work. Depending on the study, various linear scan rates were used ranging from 10 to 100 mV/s.

4.4.4 Potential Holds

Potential holds are essentially a square-wave version of cyclic voltammetry. The voltage is cycled up and down, but held at the given potential limits for a certain period of time while the current is being recorded. These experiments are able to probe the extent of oxidation by observing the growth rate at different potentials. The potential hold profile used in this dissertation, Figure 4.10, began with a hold at 0.4 V for 5 min to ensure a clean metal surface. Then, the potential was stepped up to the hold value and held for a certain amount of time. A linear sweep from the potential hold value to 0.4 V was used to reduce the oxide and held at 0.4 V for 5 minutes to ensure that all the oxide had been reduced. Last, linear sweep cyclic voltammetry was performed to monitor q_H with time as well. The oxide growth rate was determined for various potentials based on the measured q_O. Potential hold experiments were combined with X-ray absorption spectroscopy to gain insight to the oxide growth mechanism on platinum.

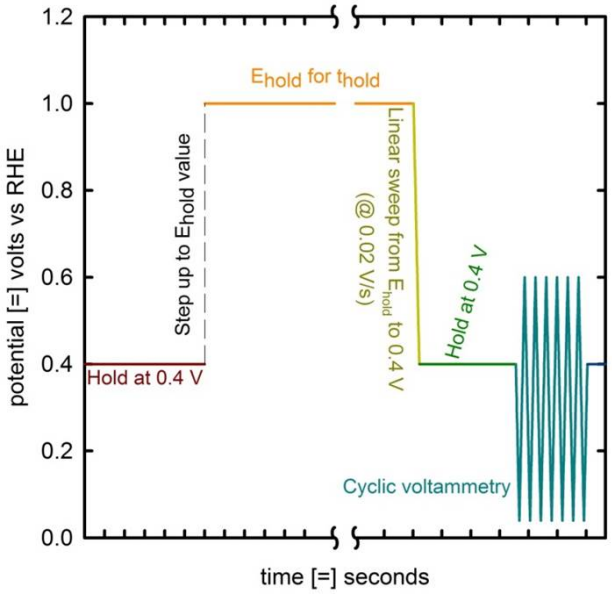

Figure 4.10 The potential profile used for a potential hold experiments.

4.4.5 Electrochemical Impedance Spectroscopy

Electrochemical impedance spectroscopy is a powerful technique used to probe and distinguish processes occurring at the electrode surface. Impedance is the alternating current analogue of resistance, the ability of a circuit to suppress the flow of electrons. Impedance is frequency dependent and is calculated from complex voltage and current (incorporating magnitude and phase) using Ohm's law. In general, a sinusoidal wave with a small amplitude is applied around a steady input current (or potential). The frequency of the perturbation is varied from high to low values, which allows for complex processes to be decoupled, such as the membrane and charge transfer resistance in a fuel cell. The measured impedance is a complex number that can be broken into real and imaginary parts. A Nyquist plot, imaginary versus real, is commonly used to analyze resistances in a fuel cell. The higher frequency intercept is interpreted as the membrane resistance and lower frequency intercept is the sum of the membrane resistance and charge transfer resistance. They theory behind impedance is beyond the scope of this dissertation, but for

more detailed explanations and further applications to fuel cells please see references (20, 24).

In this work impedance spectroscopy was used to determine the membrane resistance of the fuel cells, as a means of characterization. A galvanostatic procedure was used for measuring impedance, where the input current was set to -0.5 A. The amplitude of the curve was 0.025 A (5 % of the DC current). Fifty data points were collected over the frequency range of 0.05 to 1000 Hz. Impedance was measured at varying temperatures, but the fuel was always 1.0 L/min of hydrogen and the oxidant was 2.0 L/min of air. Nyquist plots for the MEAs can be found in Appendix A.

4.4.6 Synchrotron Radiation Techniques

While electrochemical methods are essential to the study of fuel cells, other complementary techniques are necessary to confirm hypotheses and further define the complex nature of the PEM fuel cell cathode. Synchrotron radiation sources offer a wide array of analyses that can be used to gain insight to particle morphology and surface species present at the working electrode in fuel cells. Synchrotron radiation is produced by accelerating charged particles radially by using a magnetic field. Frequencies spanning the entire electromagnetic spectrum are generated, which allows users to select the desired wavelength. To gain access to a synchrotron beam line, one must submit a proposal to a team of scientists at the synchrotron lab. If the proposal is given a high enough rating, then time is allotted for the experiments to be performed. Two synchrotron techniques were used in this work: (1) the pair distribution function method, applied to high energy X-ray diffraction data, and (2) X-ray absorption spectroscopy.

The pair distribution function (PDF) is a bond length distribution that reveals the average local atomic structure, in comparison to standard crystallographic technique of X-ray diffraction which gives information regarding the average bulk structure (25). Use of the PDF does not require the assumption of crystal periodicity, which is a key

requirement for crystallographic methods (26). The PDF, *G(r)*, is obtained by the Fourier sine transform of the total scattering pattern, *S(Q)*, recorded from powder diffraction data; the mathematical representation is

$$G(r) = 4\pi r[\rho(r) - \rho_0] = \frac{2}{\pi}\int_0^\infty Q[S(Q) - 1]\sin(Qr)dQ\,. \tag{4.8}$$

The microscopic pair density and average number density are respectively represented by $\rho(r)$ and ρ_0. The magnitude of the scatter vector is labeled Q (25). The benefit of viewing the data in real space is that it can accurately identify nearest neighbor distances; thereby revealing bond strain between atoms, chemical species present, and particle sizes (27).

The PDF reveals the short and long range order of the sample. The short range order is represented by sharp peaks in the low regions of real space. Weak broad peaks are observed at higher atomic distances whereby atomic interactions are less likely, depending on the size of the sample particles (28). To obtain accurate PDF data, high energy sources are required, which is a reason the PDF technique is not a dominant structure analysis tool. Generally, the measurements are carried out at synchrotron x-ray sources or pulsed neutron sources (27).

X-ray absorption spectroscopy is an element specific technique that allows the study of local atomic and electronic structure of a material (29, 30). X-ray absorption spectroscopy uses a tunable X-ray to excite a core electron to an unfilled state. The principal quantum numbers n = 1, 2, or 3 correspond to K-, L-, and M-edges. In the case of the platinum L_3 edge, 2p electrons are excited to the 5d orbital, as shown in Figure 4.11.

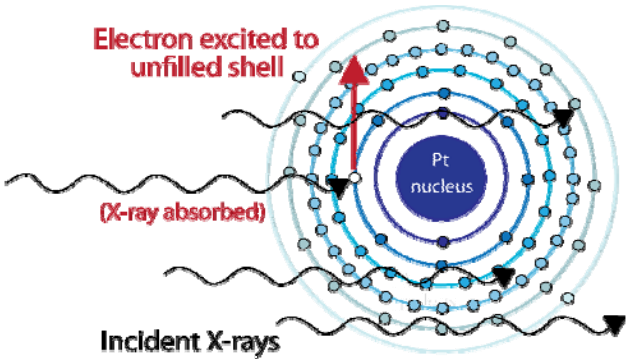

Figure 4.11 Cartoon demonstrating theory behind X-ray absorption spectroscopy.

An X-ray absorption spectra will have a characteristic rising edge, which is known as the X-ray Absorption Near Edge Structure. This steep increase in energy corresponds to the excitation of the core electron. The Extended X-ray Absorption Fine Structure region, at higher energies, is caused by the interactions of the ejected photon with neighboring atoms. Typically, X-ray absorption is combined with ab initio calculations to determine coordination parameters (31).

Other techniques used in these hereafter presented studies are X-ray diffraction (32, 33) and transmission electron microscopy (34). Both approaches were used to compliment the analysis of particle diameters from the pair distribution function.

4.5 References

1. I. Scribner Associates, Fuel Cell Test System Scibner Associates Model 890CL Operating Manual, in, Scribner Associates, Southern Pines, NC (2003).

2. K. Shah, W. C. Shin and R. S. Besser, *J Power Sources*, **123**, 172 (2003).

3. V. Mehta and J. S. Cooper, *J Power Sources*, **114**, 32 (2003).

4. S. Litster and G. McLean, *J Power Sources*, **130**, 61 (2004).

5. A. Therdthianwong, P. Saenwiset and S. Therdthianwong, *Fuel*, **91**, 192 (2012).

6. D. C. Huang, P. J. Yu, F. J. Liu, S. L. Huang, K. L. Hsueh, Y. C. Chen, C. H. Wu, W. C. Chang and F. H. Tsau, *Int J Electrochem Sc*, **6**, 2551 (2011).

7. M. Uchida, Y. Fukuoka, Y. Sugawara, H. Ohara and A. Ohta, *J Electrochem Soc*, **145**, 3708 (1998).

8. Y. G. Chun, C. S. Kim, D. H. Peck and D. R. Shin, *J Power Sources*, **71**, 174 (1998).

9. A. Barrio, J. Parrondo, J. I. Lombrana, M. Uresandi and F. Mijangos, *Int J Chem React Eng*, **6** (2008).

10. J. H. Wee, K. Y. Lee and S. H. Kim, *J Power Sources*, **165**, 667 (2007).

11. M. Uchida, Y. Aoyama, N. Eda and A. Ohta, *J Electrochem Soc*, **142**, 463 (1995).

12. S. J. Shin, J. K. Lee, H. Y. Ha, S. A. Hong, H. S. Chun and I. H. Oh, *J Power Sources*, **106**, 146 (2002).

13. E. J. J. Wang, M. F. R. Lee and C. H. K. Ko, *J Chin Inst Eng*, **33**, 89 (2010).

14. D. Wang, L. Wang, J. Liang and C. Liu, *Rev Sci Instrum*, **83** (2012).

15. H. R. Jhong, F. R. Brushett and P. J. A. Kenis, *Adv Energy Mater*, **3**, 589 (2013).

16. M. S. Saha, D. K. Paul, B. A. Peppley and K. Karan, *Electrochem Commun*, **12**, 410 (2010).

17. DuPont, DuPont Fuel Cells: MEA Preconditioning and Qualification Protocol, in, http://9gfgw.qdok6.servertrust.com/v/Meapreconditioningqualificationprotocol.PDF Editor (2008).

18. M. M. Mench, *Fuel cell engines*, John Wiley & Sons, Inc., Hoboken, NJ (2008).

19. M. Pourbaix, *Atlas of Electrochemical Equilibria in Aqueous Solutions*, National Association of Corrosion Engineers, Houston, TX (1974).

20. A. J. Bard and L. R. Faulkner, *Electrochemical methods: Fundamentals and applications*, John Wiley & Sons, USA (2001).

21. K. C. Neyerlin, W. B. Gu, J. Jorne and H. A. Gasteiger, *J Electrochem Soc*, **154**, B631 (2007).

22. S. Gilman, *J Phys Chem-Us*, **67**, 78 (1963).

23. S. B. Brummer, *The Journal of Physical Chemistry*, **69**, 562 (1965).

24. T. E. Springer, T. A. Zawodzinski, M. S. Wilson and S. Gottesfeld, *J Electrochem Soc*, **143**, 587 (1996).

25. T. Proffen, S. J. L. Billinge, T. Egami and D. Louca, *Z. Kristallogr.*, **218**, 132 (2003).

26. A. S. Masadeh, E. S. Bozin, C. L. Farrow, G. Paglia, P. Juhas, S. J. L. Billinge, A. Karkamkar and M. G. Kanatzidis, *Phys Rev B*, **76**, 115413 (2007).

27. S. J. L. Billinge and M. G. Kanatzidis, *Chem Commun*, 749 (2004).

28. T. Egami and S. J. L. Billinge, *Underneath the Bragg peaks: Structural analysis of complex materials*, Pergamon Press Elsevier, Oxford England (2003).

29. J. Yano and V. K. Yachandra, *Photosynth Res*, **102**, 241 (2009).

30. D. C. Kongingsberger and R. Prins, *X-ray absorption: Principles, applications, techniques of EXAFS, SEXAFS, and XANES*, Wiley, New York (1988).

31. B. Ravel and M. Newville, *J Synchrotron Radiat*, **12**, 537 (2005).

32. H. M. Rietveld, *J Appl Crystallogr*, **2**, 65 (1969).

33. B. E. Warren, *X-ray diffraction*, Addison-Wesley Publication Company, Reading, MA (1969).

34. R. D. Heidenreich, *Fundamentals of transmission electron microscopy*, Interscience Publishers, New York (1964).

CHAPTER 5

IN SITU MONITORING OF PARTICLE GROWTH AT PEMFC CATHODE UNDER ACCELERATED CYCLING CONDITIONS

In situ methods to measure particle growth of supported catalysts in proton exchange membrane (PEM) fuel cells under realistic operating environments are needed to better understand the mechanisms of platinum degradation. Further information is needed regarding the forces behind catalyst degradation to enable development of a detailed, physics-based model of platinum dissolution. In-situ techniques are valuable since real time data can be recorded and compared to theoretical models.

In situ X-ray techniques have been previously employed to study molecular structure changes within the catalyst layer using liquid electrolyte cells (1-7). Other researchers have focused their efforts on the design of fuel-cell hardware for use in X-ray absorption spectroscopy investigations such that oxidation states could be monitored in operando (8-12). The atomic pair distribution function (PDF) analysis compliments other X-ray techniques by yielding information about electrocatalyst morphology such as atomic bond lengths and average spherical particle diameter (13-15).

Previous studies have been employed to examine platinum nanoparticle formation and in situ growth using the PDF method (16, 17). In this study we apply a similar method of analysis; and for the first time, the PDF method was used to measure growth of catalyst particle size in an operating fuel cell. Although the Scherrer method (18),

$$d = \frac{\lambda}{\beta \cdot \cos\theta}, \tag{5.1}$$

is simpler than the PDF method and is often used to estimate crystallite size (d) from the full width of Bragg peaks at half the maximum intensity (β), it is less accurate in small nanoparticles due to the increasing disorder. The shape factor is assumed to be 1 in the

equation above and λ is the X-ray wavelength and θ is the Bragg angle. Crystallite size is different than particle size since a particle can consist of several crystallites. The particle size can be greater than the crystallite size, but never the other way around. To monitor particle size changes in operando using the PDF analysis, the experiment required rapid data collection, but at an expense of low angular resolution that adds more inaccuracy to the width of the Bragg peaks. Thus, high X-ray intensity was required to decrease data collection time. Custom fuel-cell hardware was designed, based upon cells found in literature (8, 10, 19), to monitor changes in cathode morphology. To demonstrate the utility of the technique, different catalyst types and sizes were studied. PDF analysis of the diffraction data allowed for spherical particle size changes to be tracked simultaneously with accelerated degradation experiments (13, 14), and the results were compared with pre and post mortem XRD and TEM analyses. It was found that the alloyed PtCo electrocatalyst with an initial particle diameter of 3.8 nm exhibited the greatest stability. Furthermore, an approach to examine the mechanism of platinum dissolution is presented.

5.1 Experimental

MEAs were made in-house to enable control over the catalytic loading. In addition to monitoring particle growth using the PDF technique, the ink solutions were subject to XRD and TEM to obtain the initial average particle diameters of the samples. After cycling, sections of the cathode layer were scraped off and subjected to XRD measurements directly or suspended in an aqueous solution and deposited on a copper grid for TEM imaging. The following section explains the experimental protocol in detail.

5.1.1 Materials and Membrane Electrode Assembly Preparation

MEAs were fabricated by the decal method (20) using 4 different electrocatalyst samples at the cathode: 50 % Pt/C, 50 % – HT Pt/C (heat treated), 30 % PtCo/C, and 51 % PtCo/C. The catalysts were obtained from Tanaka Kikinzoku Kogyo (Tokyo, Japan), and the different weight percentages are correlated with varying average particle diameters. The catalyst ink was prepared using the colloid method (21), which is introduced in Chapter 5. Briefly, a 5 weight percent Nafion® solution in a mixture of water and isopropanol (Ion Power D520) was added drop-by-drop to n-butyl-acetate. The platinum based catalyst supported on carbon was immediately added to form a colloid based ink. The final ratio of the ink was 0.8 g of dry Nafion® per 50 g n-butyl-acetate per 1 g of carbon for all samples. All samples were sprayed coated onto 0.30 mm Teflon® sheets and transferred to the membrane via hot pressing at 155 °C and 1.8 MPa for 8 minutes. Anodes were made from 46% Pt/C with a loading of 0.1 mg_{Pt}/cm^2 and the cathodes were loaded with about 1 mg_{Pt}/cm^2. Any changes observed in the diffraction pattern were dominated by the electrocatalyst at the cathode since the anode only accounted for 10% of the platinum X-ray signal. Additionally, platinum is more stable at low potentials (22) and undergoes negligible changes at the anode. Nafion® 117 was used as the electrolyte in all samples to minimize hydrogen crossover, and gas diffusion layers made of Toray carbon paper (TGP-H-060) were placed between the catalyst layers and flow fields. Multiple MEAs were made with the same electrocatalyst at the cathode, and only one MEA was subject to degradation in operando. The other MEAs underwent accelerated cycling experiments at Georgia Tech for electrochemical comparison.

5.1.2 Cell Hardware Design

The fuel-cell hardware was designed to enable X-ray collection in transmission mode of the cathode catalyst layer with minimum interference from the cell hardware. A 4 mm hole was drilled through the anode end plate, current collector, and all but 1.3 mm

of the 5.1 mm thick flow field for the incident beam to enter. On the cathode side, a conical window was cut down to the last 1.3 mm of the flow field (using a series of steps) to collect the scattering pattern up to an angle of 61 degrees. A 1 mm hole (large enough for the beam with slight misalignment) was drilled through the center of both flow channels to minimize graphite background, and the holes were sealed with a 0.130 mm Kapton® liner to prevent gas leakage. A Kapton® sheet was used as the insulator between the current collector and end plate to minimize interference with X-rays. The experimental design and set-up is shown in the Figure 5.1 below, and detailed information can be found in Chapter 5 and Appendix B.

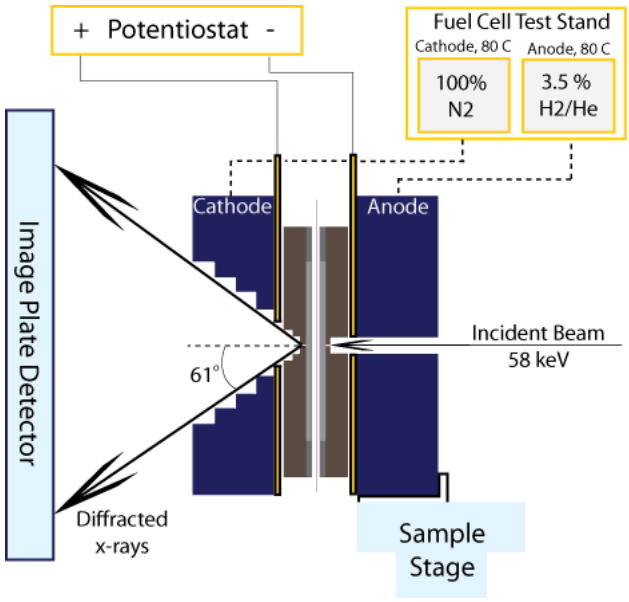

Figure 5.1 Schematic of the custom fuel cell hardware and experimental set-up inside the hutch at beam line 11-ID-B at the Advanced Photon Source.

5.1.3 Pair Distribution Function Technique

Powder X-ray diffraction data were collected every 5 minutes for the duration of the cycling tests. The raw detector images were converted to standard powder patterns with the fit2d program (23) and the PDFgetX2 software (24) was used to correct the data

for experimental effects, apply Fourier transforms, and produce the experimental PDFs (25). The observed PDFs were fit with an fcc platinum structure using PDFgui (26). The refinements included a spherical shape damping correction to obtain a particle diameter as outlined in Masadeh et al. (14). Briefly, the application assumes that a nanoparticle is formed by cutting a spherical particle from the bulk lattice, whereby it is attenuated by an envelope function (14, 27). The effect of particle size distribution is not taken into account. The PDF technique is introduced in Chapter 5.

5.1.4 Electrochemical Cycling

The experiment was conducted at the Advanced Photon Source Beam Line 11-ID-B with a collimated beam of size 0.5 × 0.5 mm and energy 58 keV. X-rays were collected with a Perkin-Elmer amorphous silicon area detector, total area 0.168 m^2 and pixel size 200 μm, placed 171.5 mm from the sample. Each MEA was subject to an accelerated degradation test by cycling 3000 times from 0.60 to 1.2 volts versus the reversible hydrogen electrode (V_{RHE}) at a scan rate 100 mV/s with a Metrohm Autolab potentiostat PGSTAT302N. For safety reasons 3.5% hydrogen with balance helium, 500 mL/min, was used as the anode gas. High purity nitrogen flowed through the cathode at 100 mL/min. The cell temperature was maintained at 80 °C and 100% relative humidity using a fuel-cell test stand. A schematic of the experimental set up is shown in Figure 5.1.

5.1.5 Pre and Post Mortem Analysis Through XRD and TEM

XRD patterns were recorded using a PANalytical X'Pert Pro Alpha-1 configured with a 1.8 kW ceramic copper tube as the X-ray source (45 kV, 40 mA). The instrument was configured with a 1/2° primary slit and 1° secondary slit which help control the width of the beam size from left to right and, as a result, reduce the amount of background noise in the data. Additionally, a 10 mm mask was used to filter the beam from front to back, and an anti-scatter filter of 5.5 mm was used. A continuous scan rate

of 0.2° per minute from 32° to 130° of 2θ was used for all samples. Pristine catalyst powder or the cycled cathode powder, scraped from the MEA using a razor blade, was spread onto 1 cm^2 piece of double sided-tape that was supported on a plastic sample holder. Using putty, the sample holder was placed on a circular metal support in the path of the beam. The crystallite sizes for both the pristine catalyst powders and the cycled cathode catalysts were obtained from the $\{111\}_{Pt}$, $\{200\}_{Pt}$, $\{220\}_{Pt}$, and $\{311\}_{Pt}$ peaks using the Scherrer analysis (18) in MDI JADE software. The average particle size was estimated as the average of the crystallite sizes.

TEM images were obtained at the Clemson University Electron Microscopy Laboratory using a Hitachi 7600 at 120 keV. The pristine catalyst ink solutions were diluted to a light gray color using isopropyl alcohol and deionized water. The cycled cathode powders were scraped away and dissolved in an equal mixture of isopropyl alcohol and deionized water. These mixtures were also diluted to a light gray color and sonicated in a water bath to ensure a well-mixed solution. The diluted solutions were deposited on lacey carbon, 300 mesh copper grid support films (Ted Pella, Inc., product no. 01890-F) and dried at room temperature for at least 48 hours. Particle size distributions were obtained by manually measuring and counting the observed platinum particles; over 500 particles per sample were counted.

5.2 Results and Discussion

Representative PDFs are shown for 50 % Pt/C with an initial PDF average particle diameter of 3.2 nm in Figure 5.2. The simulated PDF (dark red) is plotted over the experimental data (dark cyan), and the difference function is shown underneath (dark blue). The goal of the experiment was to track the change in particle size as the catalyst was cycled, which can be achieved by observing the long-range order in the PDF. Small nanoparticles show less long-range order than large nanoparticles, which is observed by

the rate of damping in the figure below. The damping of the signal in the high-r region of the PDF increases as particle size decreases because atomic interactions do not exist beyond the diameter of a particle. Thus, the damping of the PDF signal corresponds to the particle size.

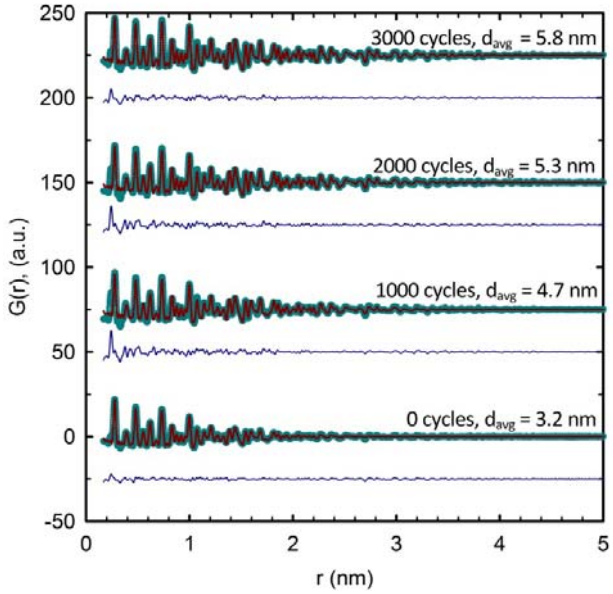

Figure 5.2 (○) Experimental PDF data, (–) Calculated PDF for *fcc* platinum, (—) Difference curve offset below. PDFs for 50 % Pt/C are shown at 0, 1000, 2000, and 3000 cycles to demonstrate how particle size changes with time. The PDF extends to longer distances with increasing cycle number, indicating a larger particle size.

An fcc platinum structure describes the experimental PDF well with the exception of peaks at 1.4 Å and 2.4 Å, which can be attributed to the first and second nearest-neighbor distances between carbon atoms in a graphite structure. The strong graphite signal is due to X-ray scattering from the Toray carbon paper gas diffusion layers. Because X-rays interact with the nucleus of atoms, the PDF is more sensitive to more dense nuclei. Thus, longer range signals from the graphite are not observed since the X-ray signal from platinum is stronger. The model dampens more quickly than the experimental data because of the relatively large particle size distribution of our catalyst

powders. For this reason, the particle size obtained from PDF measurements should be considered as a lower bound.

PDFs were measured continuously during potential cycling. Two of the catalyst samples were 50 weight percent platinum on carbon. One of these samples was heat treated, prior to being received, and had a larger particle diameter. The effect of initial particle size on catalyst stability was monitored, and all results are displayed in Figure 5.3 and summarized in Table 5.1.

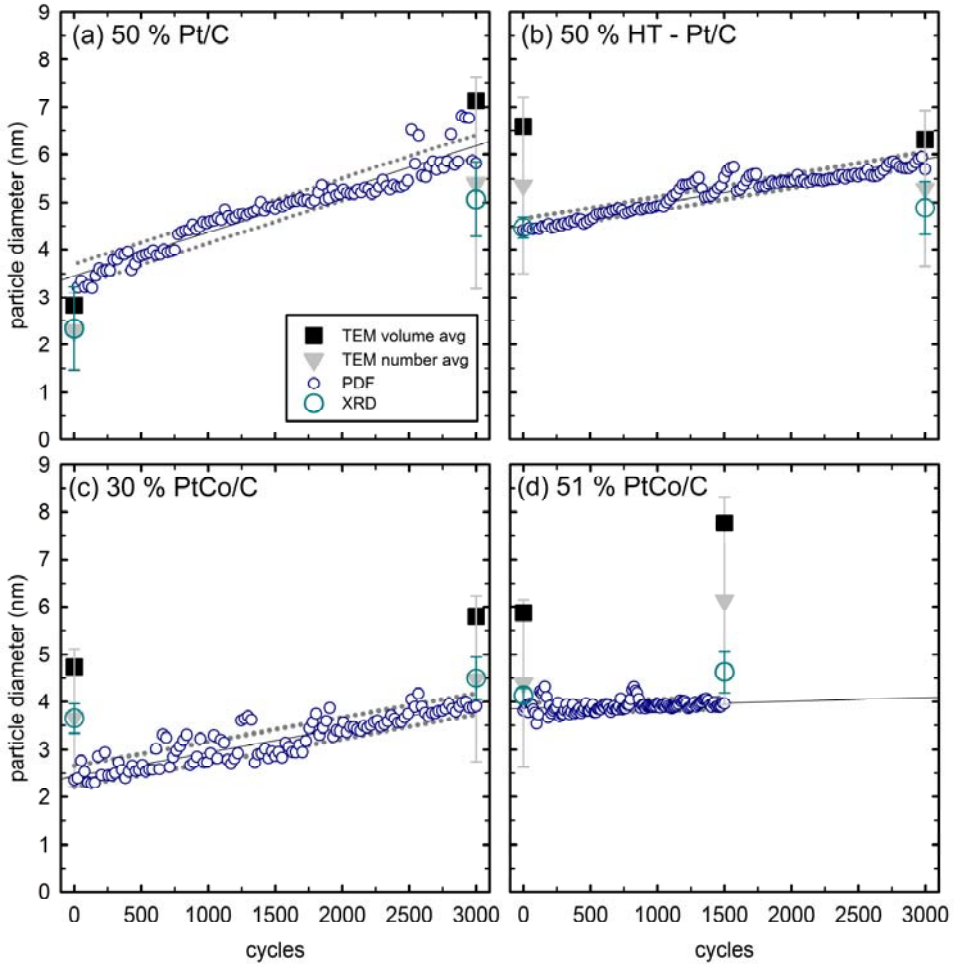

Figure 5.3 Experimental PDF particle diameters (○) are shown as a function of cycles for all samples. The data are fit to a linear trend line, and the dotted lines represent the standard deviation of the difference between the experimental diameter and the predicted diameter. Average particle sizes determined through XRD and TEM analyses is also shown for comparison before and after cycling.

Table 5.1 Summary of average particle diameters obtained by PDF measurements and total ECA values before and after cycling. The reported growth rate assumes a linear trend for particle growth.

Sample	Initial d_{PDF} *(nm)*	Final d_{PDF} *(nm)*	Growth rate *(nm/cycle)*	Initial ECA (m^2_{Pt}/g_{Pt})	Final ECA (m^2_{Pt}/g_{Pt})
50% Pt/C	3.2	5.8	8.7×10^{-4}	27.3	11.6
50% – HT Pt/C	4.4	5.6	4.0×10^{-4}	19.3	18.9
30% PtCo/C	2.4	3.9	5.0×10^{-4}	21.7	14.4
51% PtCo/C	3.8	4.0*	1.3×10^{-4}	19.7	14.2

The dotted lines in Figure 5.3 represent the standard deviation of the data relative to the linear; however, due to outliers in the data, there is no straight-forward method to determine the uncertainties of PDF diameters. As the particle size increases, the driving force for ripening decreases; thus, an initial rapid change in particle size followed by more slow growth was anticipated. A linear trend is the lowest order fit consistent with the data; however, given the quality of data, we cannot rule out different power-law dependencies.

A lower initial particle diameter, sample 50% Pt/C, resulted in an 81% increase of average particle diameter. Whereas, the 50% – HT Pt/C sample had a larger initial average particle diameter of 4.4 nm and resulted in a 27% increase of particle diameter. The sample labeled 30% PtCo/C showed a 62.5% increase in particle diameter from the initial diameter of 2.4 nm. For sample 51% PtCo/C a software malfunction cut the experiment short after 1500 cycles, and at this time particle size had increased by 5% from 3.8 nm. Assuming linear growth and extrapolating, the expected increase in particle size at 3000 cycles is 10%. At 1500 cycles the particle size of sample 30% PtCo/C had already increased by 21%, indicating that the smaller electrocatalyst was less stable.

The PDF measurements are also compared to XRD and TEM data. The initial and final average particle sizes agree relatively well with XRD measurements for all samples.

During the PDF studies, the X-ray was focused on a small part of the cathode, while the XRD samples were constructed without regard to location on the MEA, which may explain the variability between the two measurements. In the case of the alloyed samples, the diameter determined from PDF fitting does hold as a lower bound. For the platinum only samples the uncertainties of both the PDF measurements and XRD data overlap each other to some extent. The uncertainties of the XRD measurements were calculated by taking the standard deviation amongst the different crystallite sizes, summarized in Table 5.2, measured for the first four peaks of the XRD pattern, Figure 5.4.

Table 5.2 Summary of the crystallite sizes for all samples determined using the Scherrer analysis in MDI Jade software.

Sample	Pre/Post	d_{111} *nm*	d_{200} *nm*	d_{220} *nm*	d_{311} *nm*	d_{avg} *nm*	d_{avg} *nm*	Standard deviation
50 % Pt/C	Pre	2	2	2	1	1.8	2.34	0.88
	Pre	2.9	3.4	1.8	3.6	2.9		
	Post	5.7	5.4	3.8	4.7	4.9	5.06	0.78
	Post	5.2	4.4	5	6.3	5.2		
50 % HT – Pt/C	Pre	4.4	4.6	4.7	4.8	4.6	4.46	0.22
	Pre	4.2	4.4	4.4	4.2	4.3		
	Post	5	4	5	5	4.8	4.88	0.56
	Post	4.9	4.2	5.1	5.8	5.0		
30 % PtCo/C	Pre	4	3.5	3.7	3.5	3.7	3.65	0.31
	Pre	4	3.2	x	x	3.6		
	Post	4	4	4	5	4.3	4.50	0.45
	Post	4.8	5	4.4	4.8	4.8		
51 % PtCo/C	Pre	4.4	4.2	4.1	4.3	4.3	4.13	0.16
	Pre	4	4	4	4	4.0		
	Post	5	5	4	4	4.5	4.63	0.44
	Post	5	4.9	4.4	4.7	4.8		

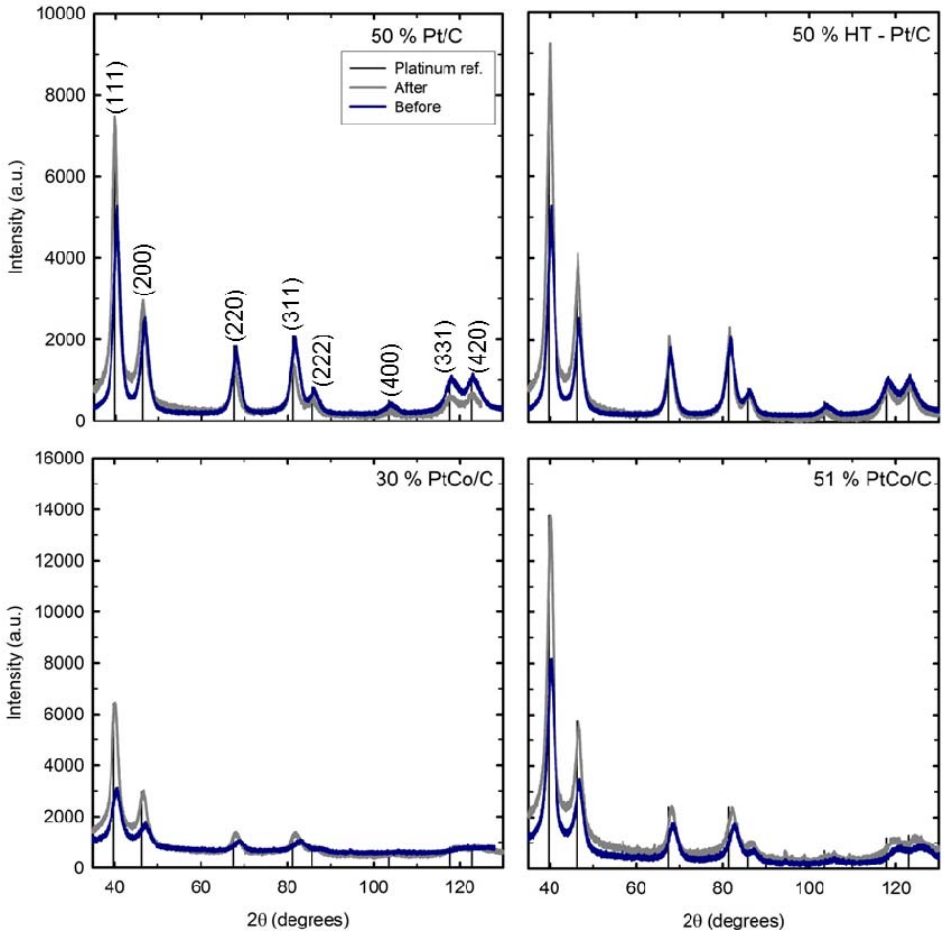

Figure 5.4 XRD patterns of catalyst samples before and after cycling.

Typically, the volume averaged TEM data is compared to XRD measurements, since XRD is a volume average technique. However, the diffraction data is in better agreement with the number average TEM data as shown in Figure 5.3. A probable justification is that some particle aggregates were counted as individual particles. Thus, the volume average would be weighted more strongly to the larger sizes than the number average. PSDs before and after cycling were obtained from TEM images and are presented in Figure 5.5. The expected behavior for a particle smaller than 5 nm in diameter is observed for the 50 % Pt/C sample, whereby the PSD broadens after cycling, and the amount of large particles is increased at the expense of the smaller particles. The volume average TEM diameter increases from 3.1 nm to 8 nm. However, the heat treated

Pt/C catalyst shows little change in the PSD and volume average TEM diameter over time. The 30 % PtCo/C sample shows a small shift in the PSD due to the ripening of particles and a growth from 5.2 nm to 6.4 nm. Lastly, the larger alloy sample shows a slight broadening of the initial PSD, though initially the PSD is larger than that of 50 % Pt/C. Particle size increases from 6.8 nm to 8.7 nm after cycling.

Overall, the larger alloyed electrocatalyst was less subject to ripening over time, but the HT Pt/C catalyst showed less ECA loss. Thus, to obtain a comprehensive understanding of platinum stability, degradation must be characterized by changes in particle size and ECA loss. The initial and final ECA values are reported in Table 5.1. Sample 50% - HT Pt/C showed the lowest ECA loss (5 %), but had the second slowest growth rate. Alloyed sample 51% PtCo/C showed the second lowest ECA loss (33%), yet had the slowest growth rate. The ECA loss and growth rate for samples 50% Pt/C and 30% PtCo/C are consistent. The measured ECA values are lower than expected based on the measured particle sizes, which is attributed to the low utilization of the catalyst layer from the in-house MEA fabrication method.

The measured ECA loss is shown in Figure 5.6 and compared to the predicted loss rate. The predicted ECA loss was determined using the measured particle diameters for each sample and the surface area to volume ratio,

$$\mathrm{ECA} = \frac{6}{d \cdot \rho}. \tag{5.2}$$

The utilization factors were picked such that the initial measured ECA was the same as the predicted ECA value.

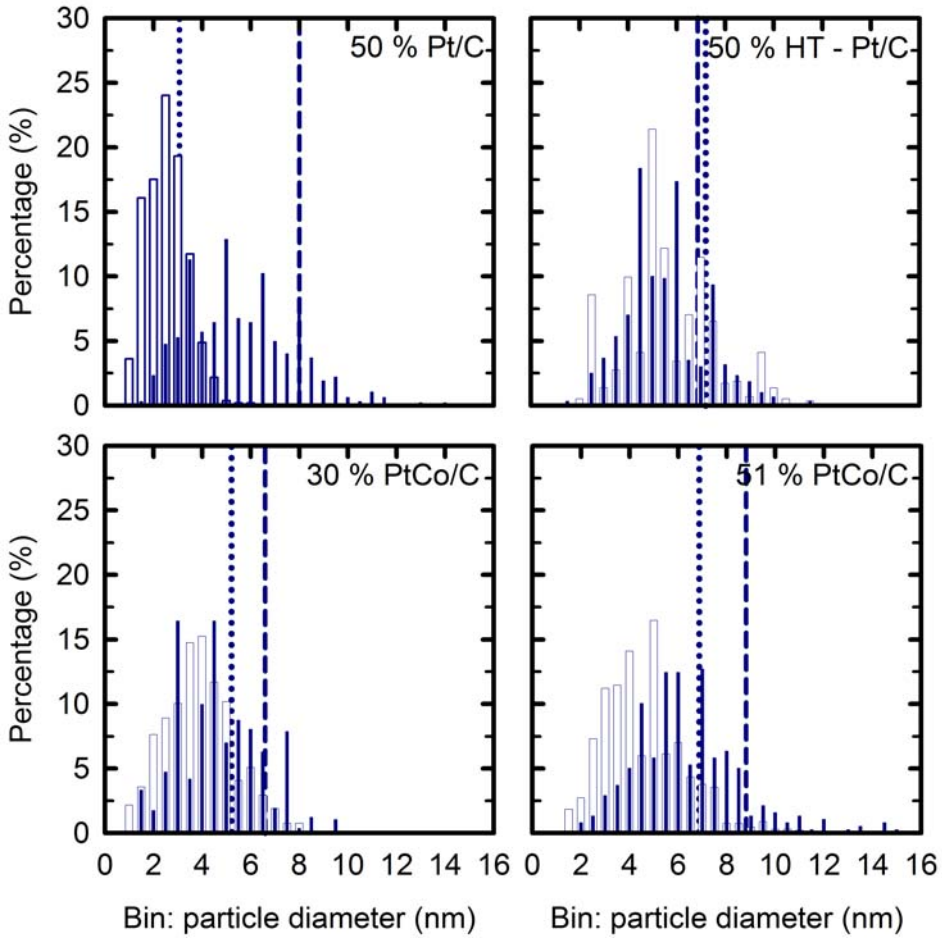

Figure 5.5 Particles size distributions for all samples before (unfilled) and after (filled) cycling. The dotted line represents the volume average diameter before cycling and the dashed line is the volume average diameter after cycling.

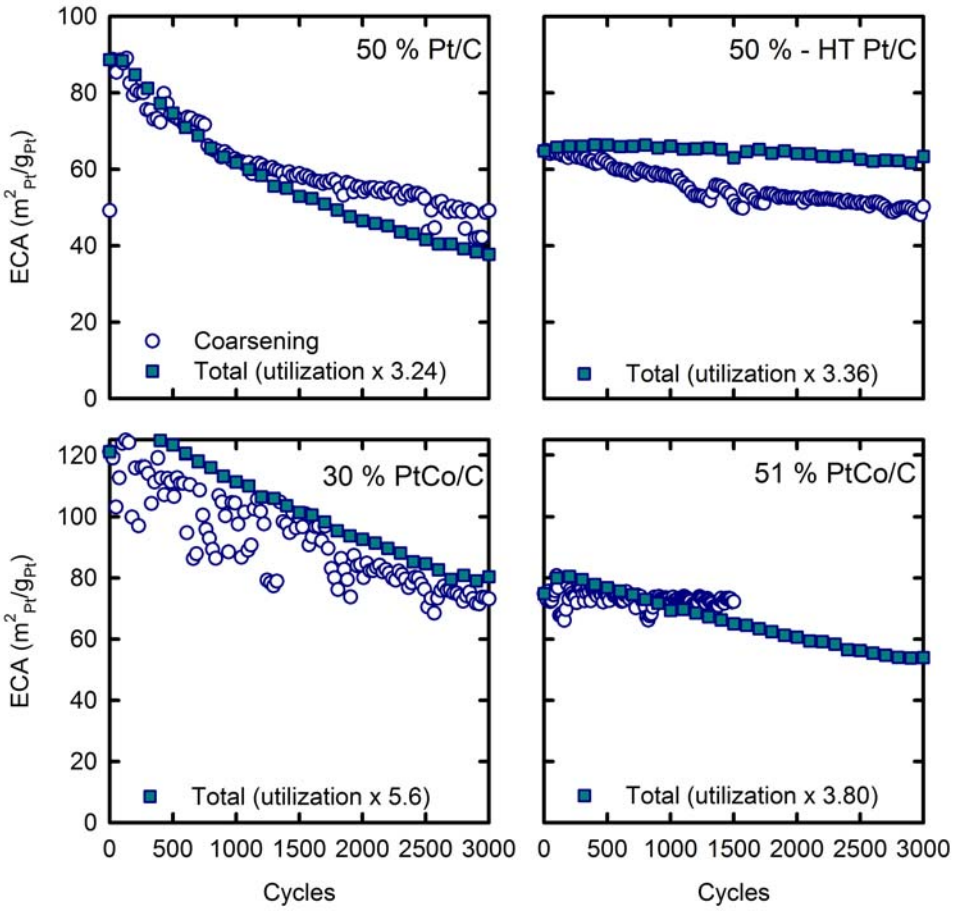

Figure 5.6 Comparison of the ECA loss estimated due to particle coarsening and the total ECA loss measured electrochemically.

In the case of 50 % Pt/C, 45 % of the total ECA loss can be explained by particle coalescence, while the additional 13 % loss is attributed to other mechanisms, such as carbon corrosion. Interestingly, the heat treated sample measures less ECA loss than predicted from particle coarsening. A possible explanation is that the catalyst was initially underutilized, and overtime the catalyst became more active; due to wetting of the electrode or particle movement. Thus, even though the particles are still subject to growth, the measured ECA would essentially remain unchanged. Comparison of the total and predicted ECA values for the smaller alloy sample shows that coarsening is the

dominant ECA loss mechanism. While the large alloy shows that the catalyst itself is stable, other mechanisms are contributing to total ECA loss.

5.3 Conclusions

For the first time the PDF method was used to measure particle size growth in an operating fuel cell. The ability to track particle size changes over time will allow for better understanding of catalyst degradation mechanisms and provide better data for comparison with physics-based models of platinum dissolution. Particularly, the detailed growth rate can be monitored with time rather than just two endpoints. This technique is valuable because the mechanism of platinum dissolution is dependent upon the applied potential cycling conditions. By comparing the predicted ECA loss determined from the PDF diameters and the total ECA loss measured electrochemically the dominant degradation mechanism can be established and used in the design of novel materials for increased catalyst stability. The PtCo/C alloy catalyst with the larger particle size proved to be the most resistant to particle growth. The HT Pt/C sample offered interesting results whereby the utilization of the electrocatalyst increased with time. The method of in situ PDF analysis on operating fuel cells offers a complementary technique to post-mortem analyses.

5.4 References

1. H. Imai, K. Izumi, M. Matsumoto, Y. Kubo, K. Kato and Y. Imai, *J Am Chem Soc*, **131**, 6293 (2009).

2. M. C. Smith, J. A. Gilbert, J. R. Mawdsley, S. Seifert and D. J. Myers, *J Am Chem Soc*, **130**, 8112 (2008).

3. A. Teliska, W. E. O'Grady and D. E. Ramaker, *J Phys Chem B*, **109**, 8076 (2005).

4. N. Guo, B. R. Fingland, W. D. Williams, V. F. Kispersky, J. Jelic, W. N. Delgass, F. H. Ribeiro, R. J. Meyer and J. T. Miller, *Phys Chem Chem Phys*, **12**, 5678 (2010).

5. Y. Lei, J. Jelic, L. C. Nitsche, R. Meyer and J. Miller, *Top Catal*, **54**, 334 (2011).

6. A. Kongkanand and J. M. Ziegelbauer, *J Phys Chem C*, **116**, 3684 (2012).

7. D. Friebel, D. J. Miller, C. P. O'Grady, T. Anniyev, J. Bargar, U. Bergmann, H. Ogasawara, K. T. Wikfeldt, L. G. M. Pettersson and A. Nilsson, *Phys Chem Chem Phys*, **13**, 262 (2011).

8. R. J. K. Wiltshire, C. R. King, A. Rose, P. P. Wells, M. P. Hogarth, D. Thompsett and A. E. Russell, *Electrochim Acta*, **50**, 5208 (2005).

9. C. Roth, N. Benker, M. Mazurek, F. Scheiba and H. Fuess, *Adv Eng Mater*, **7**, 952 (2005).

10. E. Principi, A. Di Cicco, A. Witkowska and R. Marassi, *J Synchrotron Radiat*, **14**, 276 (2007).

11. V. Croze, F. Ettingshausen, J. Melke, M. Soehn, D. Stuermer and C. Roth, *J Appl Electrochem*, **40**, 877 (2010).

12. M. Tada, S. Murata, T. Asakoka, K. Hiroshima, K. Okumura, H. Tanida, T. Uruga, H. Nakanishi, S. Matsumoto, Y. Inada, M. Nomura and Y. Iwasawa, *Angew Chem Int Edit*, **46**, 4310 (2007).

13. S. J. L. Billinge and M. G. Kanatzidis, *Chem Commun*, 749 (2004).

14. A. S. Masadeh, E. S. Bozin, C. L. Farrow, G. Paglia, P. Juhas, S. J. L. Billinge, A. Karkamkar and M. G. Kanatzidis, *Phys Rev B*, **76**, 115413 (2007).

15. T. Egami and S. J. L. Billinge, *Underneath the Bragg peaks: Structural analysis of complex materials*, Pergamon Press Elsevier, Oxford England (2003).

16. P. J. Chupas, K. W. Chapman, G. Jennings, P. L. Lee and C. P. Grey, *J Am Chem Soc*, **129**, 13822 (2007).

17. P. J. Chupas, K. W. Chapman, H. L. Chen and C. P. Grey, *Catal Today*, **145**, 213 (2009).

18. Y. Waseda, E. Matsubara and K. Shinoda, *X-ray diffraction crystallography: Introduction, examples, and solved problems*, Springer, New York, NY (2011).

19. R. Viswanathan, R. Liu and E. S. Smotkin, *Rev Sci Instrum*, **73**, 2124 (2002).

20. M. S. Saha, D. K. Paul, B. A. Peppley and K. Karan, *Electrochem Commun*, **12**, 410 (2010).

21. M. Uchida, Y. Fukuoka, Y. Sugawara, H. Ohara and A. Ohta, *J Electrochem Soc*, **145**, 3708 (1998).

22. M. Pourbaix, *Atlas of Electrochemical Equilibria in Aqueous Solutions*, National Association of Corrosion Engineers, Houston, TX (1974).

23. A. P. Hammersley, Fit2D V9.129 Reference Manual V3.1, in *ESRF Internal Report* p. 1 (1998).

24. X. Qiu, J. W. Thompson and S. J. L. Billinge, *J Appl Crystallogr*, **37**, 678 (2004).

25. T. Proffen, S. J. L. Billinge, T. Egami and D. Louca, *Z. Kristallogr.*, **218**, 132 (2003).

26. C. L. Farrow, P. Juhas, J. W. Liu, D. Bryndin, E. S. Bozin, J. Bloch, T. Proffen and S. J. L. Billinge, *J Phys-Condens Mat*, **19**, 335219 (2007).

27. K. Kodama, S. Iikubo, T. Taguchi and S. Shamoto, *Acta Crystallogr A*, **62**, 444 (2006).

CHAPTER 6

ELUCIDATING THE OXIDE GROWTH MECHANISM

As discussed previously, to understand the interplay between platinum dissolution and oxide growth a better understanding of the kinetics of platinum oxidation is needed. Experimentally, there is a need to determine what oxygen-containing species adsorb to the platinum surface under varying conditions. Additionally, it is challenging to capture the behavior of experimental cyclic voltammograms (CVs) through simulations. This chapter addresses both objectives.

6.1 Literature Review

X-ray absorption spectroscopy (XAS) is an element specific technique used to probe the local atomic structure of a sample, and it can be used to monitor changes in the sample under varying conditions when used simultaneously with electrochemical measurements (1, 2). Many researchers have implemented this technique to investigate which oxygen-containing species are involved in the platinum oxidation mechanism at varying potentials. For example, Imai and coworkers found evidence of an α-PtO_2 layer that is transformed to a quasi-3D structure (β-PtO_2) during later states of oxide growth (3). Teliska and coworkers applied the $\Delta\mu$ technique to X-ray absorption near edge structure (XANES) spectra and found that place-exchanged oxides are not directly observed before 1.1 V. However, changes in platinum coordination numbers, calculated through ab initio fits of the extended X-ray absorption fine structure (EXAFS), suggested that place exchange occurs at much lower potentials (4). In the presence of oxygen, Kongkanand and Ziegelbauer applied $\Delta\mu$ analysis to the XANES spectra and found that place exchange occurred as early 0.75 V (5), which has been of interest in the electrochemical community (6, 7). Friebel and coworkers qualitatively demonstrate

through in situ XAS studies that coverage of oxide is low below 1 V (8). Additionally, the authors rule out formation of a PtO_2 layer (8), which is seen in other studies (3, 9).

All experiments in the aforementioned in situ XAS studies have been limited to the analysis of the platinum catalyst in liquid electrolyte cells. Other XAS studies have placed emphasis on the importance of in operando experiments, requiring the optimization of specialty hardware to hold membrane electrode assemblies (MEAs). In the past, many works have placed emphasis on hardware design to decrease background adsorption and achieve good quality data (10-12). These developments have enabled researchers to collect data in a working fuel cell and estimate coordination parameters under different conditions (13-16). The use of ab initio calculations to fit experimental data and estimate the coordination parameters is a valuable technique with its own merits. However, to have confidence in these calculations, clean, consistent data are required. This task is difficult to accomplish in an operating fuel cell where many processes are occurring.

In this chapter, in operando XAS was used to identify evidence of PtO_2 at increasing hold times and potentials. The extent of oxidation was quantified and compared to electrochemical data. A mechanism for oxide formation was proposed based on the results of this study and used in the development of a model.

The experimental characteristics that are challenging to capture in a simulation have been discussed in Chapter 3. To summarize, a nearly reversible oxidation peak is observed with increasing scan rate, while the position of the reduction peak shifts according to Equation (3.5). A shallow leading edge to the reduction peak is observed, and the reduction peak is wide, ca. 250 mV at full-width at half-max. The position of the reduction peak remains nearly constant with increasing upper potential limit (UPL). Furthermore, it is proposed that the small reduction peak/shoulder at 0.6 V (see Figure 3.2) is due to platinum oxide reduction on the edge sites of nanoparticles. Some researchers have suggested that this peak is a result of the hydroquinone/quinone redox

couple of the carbon support (17-19). However, the data put forth in these studies can be interpreted in a different way. Degradation studies, either through potential cycling or potential holds, are known to result in particle growth, hence, a decrease in the percentage of edge sites. If the cathodic peak at 0.6 V is due to oxide reduction on edge sites, then one would expect the peak to diminish as particle size increases. Ball and coworkers degraded the cathode through potential hold experiments and found that the platinum particles grew in diameter from 2 nm to 8 nm, while the reduction peak at 0.6 V practically disappeared (17). Additionally, it was found that the anodic peak signal at 0.58 V increased with increasing degradation (17), but we do not observe an anodic peak in this potential range in our study. In Ball's study, the fact that the anodic peak grows and the cathodic peak shrinks with time may suggest two different processes (17). In the absence of carbon, Hu and Liu found that cycling platinum electrodes resulted in a decrease of the amplitude of the reduction peak at 0.58 V, as well as a shift to more positive potentials (20). Similarly, Shao, Peles, and Shoemaker found that larger catalyst samples resulted in a shift of the reduction peak to more positive potentials by 0.2 V (21). Komanicky and coworkers investigated platinum dissolution with regard to single-crystal surfaces, and the Pt(110) CV displays a small shoulder at 0.6 V (see ref.(22) figure 3). It is an interesting observation because the surface atoms of a Pt(110) surface have the same coordination number as the edge sites in a truncated cuboctahedron (21). Though we cannot rule out electrochemical contributions from carbon, based on observations in literature studies, the shoulder at 0.6 V was modeled as platinum oxide reduction on edge sites in this study.

6.2 Experimental

6.2.1 Experimental Methods

A custom MEA was fabricated, to enable control over the electrode materials, through direct spray coating of the catalyst ink onto the membrane (23). A 5 wt% Nafion® dispersion in 45 % water and 50 % isopropanol was obtained from Ion Power, Inc. The ink ratio used was 0.8 g of Nafion® and 20 g DI H_2O per 1 g of carbon. The anode was made from 30 % Pd/C (Sigma-Aldrich) with a loading of 0.18 mg_{Pd}/cm^2. Palladium was used instead of platinum so that the signal from the counter electrode would not interfere with the platinum absorption edge. This electrode also served as the reference. The cathode was loaded with approximately 0.33 mg_{Pt}/cm^2 of 30 % Pt/C. The average particle diameter was about 2 nm as determined by X-ray diffraction. The electrode area was 4.8 cm^2, and Nafion® 117 was used as the membrane in all samples. Although the performance is poor with this thick membrane, our principal objective was to minimize hydrogen crossover. Teflon treated carbon fiber paper (TGP-H-060, Fuel Cell Store) was used as the gas diffusion layer. The fuel-cell hardware was machined to enable X-ray collection in transmission mode, which is explained in greater detail in the authors' previous work involving high energy X-rays (24, 25). A slight modification was made to widen the opening to 1 cm where the incident beam enters for the XAS experiments. The experiment was conducted at beam line X11A at the National Synchrotron Light Source, Brookhaven National Laboratory. The energy range for XAS measurements covered the Pt-L_3 edge. Powder PtO_2 and a metal platinum foil were used as references for Pt(IV) and Pt(0) oxidations states. Transforming the spectra can result in a phase shift. Because reference spectra are transformed the same way as the experimental data, peak shifts can be distinguished as real or an artifact of data processing.

A series of potential hold experiments were performed on the MEA under 0.2 L/min of 4 % H_2/N_2 at the anode and 0.2 L/min of pure N_2 at the cathode. The cell was

maintained at 100 % relative humidity, and a temperature of 60 °C (rather than 80 °C) was chosen to mitigate condensation at the cathode window. Gas flow rates and all temperatures were controlled with a Scribner Fuel Cell Test System model 850e. The procedure began with a 400 mV potential hold for 10 minutes to ensure that the platinum surface was free from adsorbates. Then the potential was increased to oxidizing conditions (800 to 1200 mV) and held for 1200, 3600, or 10,800 seconds. During the potential hold XAS scans were measured continuously every 15 minutes. The oxide layer was reduced by sweeping from the UPL to 400 mV, followed by a 5 minute hold at 400 mV to ensure complete reduction. The charge associated with oxide reduction was recorded, and the electrochemically active surface area was measured by a CV (26) over the range 50 to 600 mV. Each potential sweep had a scan rate of 20 mV/s, and the potential was monitored and controlled by a Metrohm Autolab potentiostat PGSTAT302N. Electrochemical experiments were repeated for 3 additional MEAs with a wider range of hold times, and the oxide coverage trends presented in this paper are averaged between all 4 samples.

Cyclic voltammetry was performed on a commercial MEA under 1 L/min pure hydrogen at the anode and 0.05 L/min pure N_2 at the cathode. The cell was maintained at 100 % relative humidity and 25 °C. Gas flow rates and all temperatures were controlled with a Teledyne Medusa® Fuel Cell Test Stand equipped with a Scribner electronic load (model 890CL). The MEA (Ion Power Inc.) was loaded with 0.3 mg/cm^2_{geo} of platinum at each electrode separated by Nafion® 212. The electrode area was 25 cm^2. The scan rate was varied between 10 and 200 mV/s and the UPL was varied between 0.80 V and 1.15 V, and all experiments were performed in a random order. All potentials were controlled and recorded with the Autolab potentiostat.

6.2.2 Experimental Results and Discussion

XAS scans were processed using the Athena software (part of the IFEFFIT package (27, 28)) where the k-space data was truncated by a Hanning function before Fourier transforming to real space. Real space spectra, $\chi(R)$, were obtained from the extended fine structure of the Pt-L_3 edge, which displayed a characteristic metallic peak at 3 Å and a peak indicative of PtO_2 at 1.6 Å. Since both platinum and PtO_2 have significant structure in the 2 to 2.5 Å region, the peaks at 2.2 Å were not used as unique structural markers. Furthermore, the peaks at 1.6 and 3 Å can become convoluted for in operando studies, where many processes are taking place on the metallic surface. Typically, ab initio calculations are used with the experimental data to draw conclusions about various coordination parameters, which may lead to over-interpreting a particular data set. In this study, we offer an alternative way to quantify the extent of oxidation directly from the EXAFS data.

The extent of oxidation was quantified by inverse Fourier transforming the data in characteristic R-ranges for metallic or oxide structures, 2.7 to 3.4 Å and 1 to 2 Å, respectively, to q-space. Comparing the resulting q-space spectra in Figure 6.1 for the metallic foil and PtO_2 reference samples, it is seen in the range from 5 to 9 $Å^{-1}$ that the structural information is incongruent, showing differences in both phase and amplitude. In other words, using this truncated region of the reciprocal space, rather than the full k-space bandwidth, allows us to mutually filter out as much of the metallic platinum information from the platinum oxide information and vice versa. The integrated magnitude of the EXAFS function over the narrow q-space region between 5 and 9 $Å^{-1}$ was used to provide Fourier filtered metallic and oxide information.

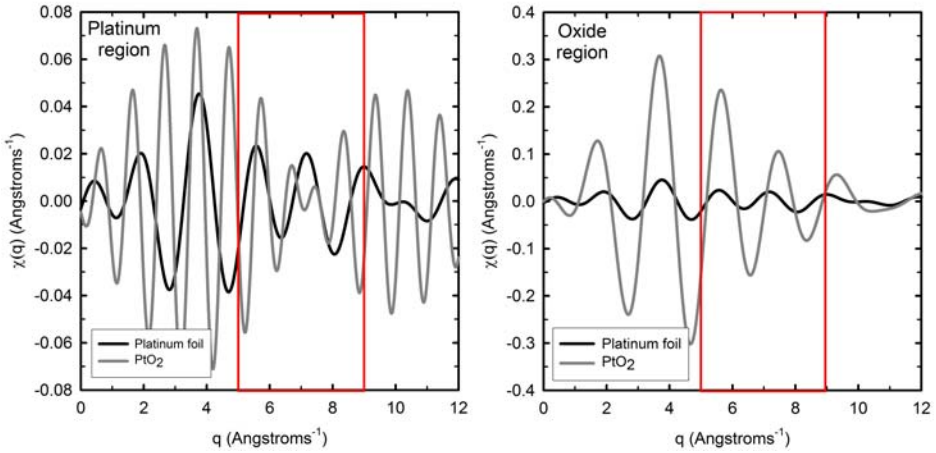

Figure 6.1 Inverse Fourier transforms of data in the metallic region from 2.7 to 3.4 Å and the oxide region from 1 to 2.2 Å. For both the platinum foil and PtO_2 reference powder, the q-range from 5 to 9 $Å^{-1}$ (boxed region) shows distinguishable characteristics.

The effect of filtering, for the different regions, is seen Figure 6.2 and the signal is compared at various potentials for a 1200 second hold. The unfiltered data are shown in Figure 6.2(a) and the peak at 3 Å decreases in amplitude with increasing potential. The long-range order of platinum is preserved until higher potentials, where peaks positioned above 3 Å no longer resemble those of the platinum foil. The loss of the higher order metallic structure indicates that oxygen atoms are penetrating the metal lattice. The overall trend seen at 1.6 Å is an increase in peak amplitude with potential. Thus, as potential is increased the nanoparticles become less metallic and begin to show characteristics of the PtO_2 reference powder.

As an alternative way to visualize the filtering process, the filtered q-space signal, which was integrated to quantify oxide and metallic structure, was transformed back to real space using only the data from 5 to 9 $Å^{-1}$. The result of this forward transform for the metallic region is shown in Figure 6.2(b), which displays a clear trend of decreasing amplitude for higher potentials. At 1200 mV the peak is shifted to the left, which indicates that a change in the platinum structure is occurring. In Figure 6.2(a) there is an unclear distinction between the 800 mV and 950 mV spectra at 1.6 Å. Upon inverse

Fourier transforming the oxide region and subsequent k-filtering, the peak at 1.6 Å becomes uncompromised by the effects of the signal around 2.2 Å. Figure 6.2(c) shows and increase in the amplitude from 800 mV to 950 mV, as well as a peak shift to more positive values. Changes in the oxide structure are seen at lower potentials, compared to the metallic structure, and another peak shift is observed when increasing the potential from 950 mV to 1200 mV. The process of inverse Fourier transforming the data in a specific region of interest and filtering in dissimilar regions magnifies the respective domain signals and yields the particular trends. Furthermore, the integrated filtered data can be compared to directly estimate the oxide coverage.

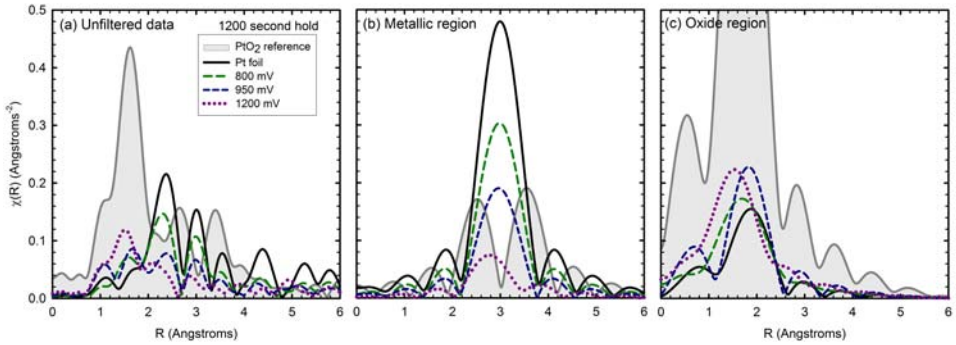

Figure 6.2 (a) Unfiltered EXAFS data (b) Data that has been inverse Fourier transformed in the metallic peak region from 2.7 to 3.4 Å followed by filtering from 5 to 9 $Å^{-1}$, (c) R-space spectra for data that has been inverse Fourier transformed in the oxide peak region from 1 to 2 Å and filtered from 5 to 9 $Å^{-1}$.

To quantify the extent of oxidation of the catalyst observed in EXAFS, the oxide and metallic responses were first normalized to the responses for the PtO_2 and platinum foil reference samples, respectively. The fraction of the particle that was oxidized was calculated by dividing the normalized oxide area by the total normalized metallic and oxide areas. The extent of oxidation was then converted to an equivalent surface oxide coverage by multiplying by the coverage value corresponding to a fully oxidized particle (complete conversion to PtO_2). The fully oxidized coverage was calculated using the

ECA to determine the fraction of surface atoms, and accounting for the oxidation state of PtO_2,

$$\frac{4F}{ECA \cdot 2.1 \cdot MW_{Pt}}, \tag{6.1}$$

where 4 electrons are transferred per Pt atom in PtO_2, ECA is measured in m^2/g, 2.1 C of electric charge are passed per m^2 (210 $\mu C/cm^2$ (29)), and MW is the molecular weight of platinum. Based on the ECA of the MEA in the XAS experiments, a fully oxidized particle corresponds to 16.5 MLs of coverage (PtOH basis).

The oxide coverage calculated from the XAS data (unfilled points) is compared to the electrochemical data in Figure 6.3. The electrochemical oxide coverage was measured as the ratio of charge required to reduce the oxide and the charge associated with hydrogen desorption. Growth is logarithmic with time, which is in agreement with literature findings (30-32). The nanoparticles are expected to oxidize at a faster rate than the platinum wires reported in the literature due to the increased percentage of edge sites. For shorter potential holds, the XAS data under-predicts the amount of coverage compared to electrochemical measurements. At longer times, above 3000 s, the XAS coverage begins to converge with the electrochemical coverage values. There are two possible interpretations of these data. Electrochemically, we cannot distinguish between various oxide species, but the XAS data reveal the extent of oxidation with respect to PtO_2. The difference in rates of formation of the total oxide and place-exchanged PtO_2 oxide indicates that PtO_2 is forming at the expense of the chemisorbed oxide species. Alternatively, the oxide may initially be amorphous, which would not be picked up well by the EXAFS. However, once the oxide layer becomes more structured, the signal would sharpen.

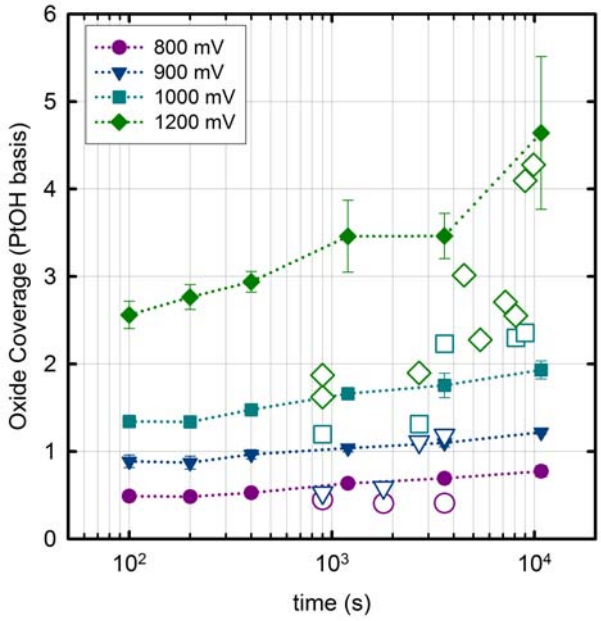

Figure 6.3 Oxide coverage measured electrochemically (filled points) and through XAS (unfilled points).

In addition to the EXAFS spectra produced through XAS studies, X-ray absorption near edge spectroscopy (XANES) can reveal the nature of the oxidation state of platinum. The XANES region directly refers to the energies surrounding the absorption edge. Increased intensity corresponds to d-orbital vacancies, where electrons have been transferred from the metal surface. Qualitatively, we observed an increase in oxidation with potential, as shown in Figure 6.4. While the trends here are expected, the only way to glean more specific information from the near-edge fine structure would be to amplify the differences (such as with the $\Delta\mu$ method) and fingerprint the rendered features against calculated spectra based on adsorption models. Although this model-based approach has its own merits, it is ultimately only as good as the chosen models – not an easy proposition with the multitude of moieties possible in nanoparticle ensembles. The treatment applied to the extended fine structure instead treats the operando data using filtering methods that are quantifiable while remaining independent of structural models.

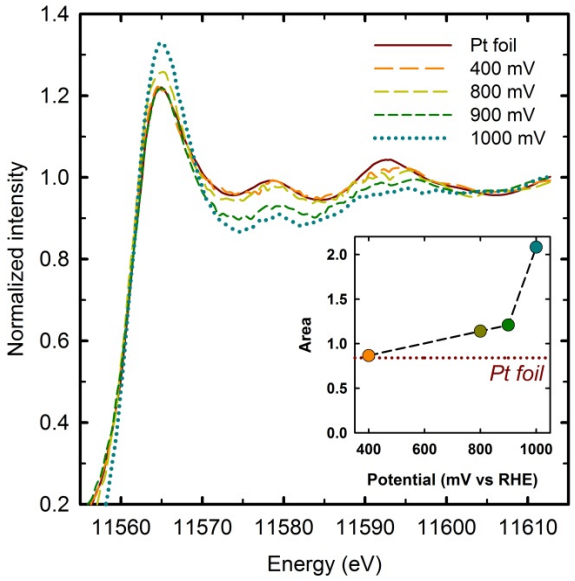

Figure 6.4 X-ray absorption near edge spectra shown as a function of potential. Inset: The area under the peaks were integrated to demonstrate a qualitative rise in platinum oxidation with increasing potential.

6.3 Theoretical Considerations

The main platinum oxidation simulation studies discussed in Chapter 3 were conducted by Darling and Meyers (33) and Appleby (34). Both studies use a Temkin adsorption isotherm to describe the thermodynamics of the oxide layer. Darling and Meyers allocated the Temkin effects to the anodic portion only, and Appleby equally allocated these effects to both parts of the reaction. In response to these two extremes, a new parameter was introduced as an extension of that concept in this study. After exploring the implications of the χ-parameter, it was found that introducing a single parameter is not enough to fully simulate an experimental CV. An extra variable, in addition to potential and coverage, is needed to accurately model platinum oxide reduction under many conditions. Thus, the concept of a heterogeneous oxide layer is introduced and discussed.

6.3.1 The χ-parameter

Before introducing the new parameter, the meaning of the symmetry factor, β, and the interaction parameter, ω, is discussed. The symmetry factor is the fraction of overpotential that is applied to the anodic or cathodic reaction and is reflected in the symmetry of the energy barrier (35, 36). In general, the transfer coefficient (α) is related to the symmetry factor by the number of electrons (n) as $\alpha = n\beta$. Interaction parameters represent how the heat of adsorption changes with increasing coverage and were originally incorporated into rate equations to ensure logarithmic growth of the oxide layer (33, 34, 37). Analogous to the purpose of the symmetry factor, the χ-parameter allocates the adsorption isotherm effects to anodic and cathodic rates,

$$r = k\left[e^{\left(-\frac{\chi\omega\theta}{RT}\right)}e^{\left(\frac{\alpha_A F}{RT}\left(\Phi - U^{\theta}\right)\right)} - \theta e^{\left(\frac{(1-\chi)\omega\theta}{RT}\right)}e^{\left(-\frac{\alpha_C F}{RT}\left(\Phi - U^{\theta}\right)\right)}\right]. \tag{6.2}$$

The derivation of Equation (6.2) is further discussed in the following section and Appendix C. Factoring out the $e^{\left(\frac{(1-\chi)\omega\theta}{RT}\right)}$ term of Equation (6.2) offers another way to interpret the χ-parameter, where the rate constant is coverage dependent. In this way, the rate at which an oxide is formed or reduced can be adjusted. Inclusion of the χ-parameter allows the cathodic peak width to be decoupled from the Tafel slope, and the theoretical equations used to generate these values are shown in Table 6.1.

Table 6.1 Key parameters that effect experimentally measurable quantities in χ-modified Butler-Volmer kinetic rate equation.

Measurable Experimental Quantities	Anodic Tafel Slope *(mV/decade)*	Anodic Potentiostatic Growth Rate *(ML/decade)*	Cathodic Tafel Slope *(mV/decade)*	Cathodic Peak Width *(mV)*
Symbolic Form	$2.303\frac{RT}{\alpha_A F}$	$2.303\frac{RT}{\chi\omega}$	$2.303\frac{RT}{\alpha_C F}$	$2.303\frac{RT}{\alpha_C F}+0.82\theta_{\max}\frac{(1-\chi)\omega}{\alpha_C F}$
Critical Parameters	α_A	χ,ω	α_C	$\chi,\omega,\alpha_C,\theta_{\max}$
Numeric Values*	39	0.25	39	$39+42\,\theta_{\max}$

*T = 298K, $\alpha_A=\alpha_C=1.5, \omega=30$ kJ/mol, $\chi=0.75$

The χ-parameter is already inherent to oxide growth models found in literature, though no studies have explicitly identified or explained the significance of including this extra parameter. For example, a χ-parameter of 0.5 reduces Equation (6.2) to the form used in Appleby's work, thereby equally distributing the considered Temkin adsorption isotherm effects between the anodic and cathodic rates (34). Darling and Meyers present a case where the χ-parameter equals 1 (33), meaning that the adsorption isotherm effects were only applied to the anodic rate. In the following section a mechanism for oxide growth is proposed, utilizing the χ-parameter, to describe the effects seen in CVs at varying scan rates and UPLs.

6.3.1.1 The Mechanism

The anodic peak seen in our experimental CVs was treated as a reversible chemisorbed oxide, denoted in Reaction I by 'eqbm'. As the potential increases, the mechanism favors the growth of a kinetically irreversible oxide, Reaction II, which is responsible for the plateau on the CV. Upon reduction, the small shoulder around 0.6 V is proposed as oxide reduction on edge sites, Reaction III, and this oxide reduction happens in parallel with Reaction II.

In summary, the electrochemical equations that significantly contribute to the simulated CV are

$$Pt + H_2O \overset{eqbm}{\rightleftharpoons} PtO + H^+ + e^-, \quad \text{(I)}$$

$$Pt + 2H_2O \rightleftarrows PtO_2 + 4H^+ + 4e^-, \quad \text{(II)}$$

and

$$Pt + 2H_2O \underset{Sites}{\overset{Edge}{\rightleftharpoons}} PtO_2 + 4H^+ + 4e^-. \quad \text{(III)}$$

All reactions are treated independently, and there is no interaction between adsorbed intermediates. Various studies have provided evidence for which oxide species are involved in the mechanism (3, 38-40). The focus of this theoretical discussion is on the kinetic and thermodynamic behavior of the oxide species with increasing coverage (or upper potential limit), scan rate, and time.

6.3.1.2 Mass Balances

Three concentration variables are defined to represent each of the oxide species. The chemisorbed oxide, place-exchanged oxide, and the oxide formed on edge sites are all described by surface coverages θ_O, θ_{PtO_2}, and θ_{Edge}. The concentration of surface sites (Γ) for planar surface sites is $2.1/F \ \ mol \cdot m_{Pt}^{-2}$ (29). The concentration of surface edge sites is estimated to be 1/3 of the planar amount, which is geometrically calculated in Appendix C. The following differential equations describe how the coverage of each oxide species changes with time:

$$\frac{d\theta_O}{dt} = \frac{r_1}{\Gamma}, \quad (6.3)$$

$$\frac{d\theta_{PtO_2}}{dt} = \frac{r_2}{\Gamma}, \quad (6.4)$$

and

$$\frac{d\theta_{Edge}}{dt} = \frac{r_3}{\Gamma_{Edge}}. \quad (6.5)$$

6.3.1.3 Rate Equations and Equilibrium Expressions

The initial adsorbed oxide species is denoted as PtO, which is easily deposited on the platinum surface at low potentials and up to a limiting coverage of 2/3 ML. Additionally, a modified adsorption isotherm was incorporated where the heat of adsorption increases with coverage squared. The equilibrium expression for Reaction I is

$$e^{\left(\frac{F}{RT}\left(\Phi-U_1^{\theta}\right)-\frac{\omega_{OH}\theta_O^2}{RT}\right)}=\frac{\theta_O}{\theta_V}=\frac{\theta_O}{2/3-\theta_O}, \tag{6.6}$$

where U_1^{θ} is the standard potential and ω_O is the interaction parameter between adsorbed O species. The coverage of O is determined from the equilibrium expression in Equation (6.6), and the rate is determined from the material balance in Equation (6.3).

A list of all parameters can be found in Table 6.2. The full derivation of Equation (6.6) can be found in Appendix C.

The rate of place exchange on a planar surface is expressed as

$$r_2=k_2\left[e^{-\frac{\chi_2\omega_{PtO_2}}{RT}\left(\sqrt{\theta_{PtO_2}}+0.1\cdot\theta_{PtO_2}\right)}e^{\frac{\alpha_{A2}F}{RT}\left(\Phi-U_2^{\theta}\right)}-\theta_{PtO_2}e^{-\frac{(1-\chi_2)\omega_{PtO_2}}{RT}\left(\sqrt{\theta_{PtO_2}}+0.1\cdot\theta_{PtO_2}\right)}e^{-\frac{\alpha_{C2}F}{RT}\left(\Phi-U_2^{\theta}\right)}\right], \tag{6.7}$$

taking the form of Equation (6.2) but with a modified adsorption isotherm chosen to fit experimental cyclic voltammetry curves (see Appendix C). The adsorption isotherm term that is first-order in coverage produces a plateau on the anodic CV sweep. The square root term causes current to increase linearly with potential, making the onset of place exchange more gradual. The constant, 0.1, in front of the first-order coverage term was manually fit to experimental data with a scan rate of 50 mV/s and an UPL of 1.15 V. This representation of the adsorption isotherm gives a logarithmic growth rate with time.

The higher energy edge sites quickly adsorb oxygen species leading to the formation of a stabilized, place-exchanged oxide structure, PtO_2, as shown in Reaction III. The kinetic rate expression,

$$r_3 = k_3\left[e^{-\frac{\chi_3\omega_{PtO_2}}{RT}\left(\sqrt{\theta_{PtO_2}}+2\cdot\theta_{PtO_2}\right)}e^{\frac{\alpha_{A3}F}{RT}\left(\Phi-U_3^{\theta}\right)} - \theta_{PtO_2}e^{-\frac{(1-\chi_3)\omega_{PtO_2}}{RT}\left(\sqrt{\theta_{PtO_2}}+2\cdot\theta_{PtO_2}\right)}e^{-\frac{\alpha_{C3}F}{RT}\left(\Phi-U_3^{\theta}\right)}\right] \quad (6.8)$$

is derived in the appendix. Equation (6.8) is similar in form to Equation (6.7), but the constant of 2 instead of 0.1 causes growth to reach a plateau quickly during the anodic sweep. This assumption was based on fitting a simulated CV to an experimental CV. A lower standard potential is justified in this case as the under-coordinated edge sites have a higher affinity for oxygen.

The above equations fully describe the system, but other variables are introduced to simplify the analysis with experimental results. The pseudo-capacitance, C, is the total current divided by the scan rate. The total current is the sum of all rates multiplied by nF where n=2, 4, 4 for Reactions I, II, III respectively. Equation (6.9) expresses the normalized current density in $\mu C/V\cdot cm_{Pt}^2$ with an added double-layer capacitance, C_{dl},

$$C = \frac{1}{\nu}\left(\left(F\sum_{i=1}^{3} n_i\cdot r_i\right) + C_{dl}\frac{d\Phi}{dt}\right). \quad (6.9)$$

The total coverage is the sum of all coverages calculated on a PtOH (1 e^- transfer per Pt surface atom) basis

$$\theta_{total} = 2\theta_O + 4\theta_{PtO_2} + 4\left(\frac{\Gamma_{Edge}}{\Gamma}\right)\theta_{Edge}. \quad (6.10)$$

There is no limit on total coverage. All equations were solved using gPROMS software version 3.3.1, and the code can be found in Appendix D. Parameters were fit manually to an experimental CV with a scan rate of 50 mV/s and UPL of 1.15 V.

6.3.1.4 Assumptions

The following assumptions were made in the derivation of the presented model:

- The limiting coverage of O is limited to 2/3 ML, which is an arbitrary assignment. It is likely that chemisorbed O will not reach a full monolayer before being place exchanged due to lateral interactions of the adsorbed species (41).
- The active sites available for reaction on the edge sites are 1/3 the amount available on planar surfaces, which is a geometrical calculation outlined in detail in Appendix C for assuming a cubooctahedral particle occupying the same volume as a sphere 3 nm in diameter.
- The heat of adsorption for place-exchanged oxide initially increases with the square root of coverage and at higher coverage values a linear term dominates. The factors in front of the first-order coverage term in both Equations (6.7) and (6.8) are related to the rate of oxidation, and were fit to yield good agreement with experimental data. For the chemisorbed hydroxide, heat of adsorption increases with the square of coverage, and for the chemisorbed oxide, heat of adsorption increases with the one-fourth power of coverage. We cannot say whether the modified adsorption isotherms for each reaction are accurate, but the overall contribution is able to fit experimental data well.

The χ-parameter allows the Tafel slope to be decoupled from the cathodic peak width to an extent, but there are still limitations to the model. For a given symmetry factor, when $\chi < 1$ the Tafel slope increases from the expected amount. At high UPLs the simulated peak shape is characterized by a steep leading edge and asymmetric bottom. The proposed mechanism allows too much chemisorption, which results in a misfit to the experimental reduction curve on the CV at high potentials.

6.3.1.5 Results and Discussion

The parameters in Table 6.2 were fit to an experimental CV at 50 mV/s and UPL of 1.15 V. The simulated and experimental CVs are compared in Figure 6.5 and the characteristic features are labeled 1 – 7. The simulated version follows the anodic portion of the CV very closely. Experimentally, we observe that the charge associated with oxide reduction is 57 % to 84 % of the charge associated with oxidation, depending on the scan rate and UPL. A greater difference between the measured charges is seen at higher UPLs and lower scan rates, which suggests that carbon oxidation is contributing to the measured anodic current. The CV is not noticeably affected by platinum dissolution currents, which are estimated to be at least two orders of magnitude less than platinum oxidation currents (42). The simulation does not account for carbon corrosion so the anodic and cathodic charges will always balance, which partially explains the increased area observed for the simulated cathodic current. The slight increase in the overall rate, labeled as feature 1 in Figure 6.5, is achieved by the early onset of oxidation, $U_3^\theta = 0.595$ V at the edge sites. The edge sites are less stable than planar sites due to the lower coordination number. Therefore, it seems plausible that these sites are first to develop the oxide. The oxide formed is very stable and requires a lower potential to reduce. The reduction of this oxide is labeled as the 7th feature in Figure 6.5.

Table 6.2 List of parameters and values used in χ-parameter simulations.

Symbol	Meaning	Values	Units
F	Faraday's constant	96,487	$C \cdot mol^{-1}$
R	Ideal Gas constant	8.314	$J \cdot mol^{-1}K^{-1}$
T	Temperature	298	K
Γ Γ_{Edge}	Concentration of active sites	$2.1/F$ $2.1/3F$	$mol \cdot m_{Pt}^{-2}$
C_{dl}	Double layer current	0.25	$mF \cdot cm_{Pt}^{-2}$
U_1^θ U_2^θ U_3^θ	Standard potentials	0.860 0.860 0.595	V
ω_O ω_{PtO_2} ω_{Edge}	Interaction parameters	45 235 72	$kJ \cdot mol^{-1}$
α_{A2}, α_{C2} α_{A3}, α_{C3}	Transfer coefficients	1.5, 1.5 1.5, 1.5	*dimensionless*
χ_2 χ_3	χ-parameters	0.735 0.750	*dimensionless*
k_2 k_3	Rate constants	5×10^{-12} 5×10^{-10}	$mol \cdot cm_{Pt}^{-2}s^{-1}$

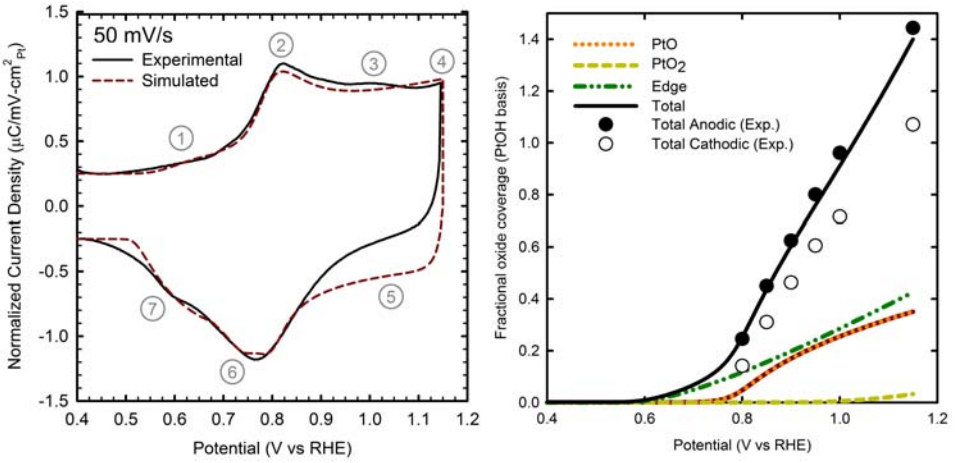

Figure 6.5 Left: Comparison between the experimental CV and simulated version with optimized parameters listed in Table 6.2 and scan rate = 50 mV/s. Right: The simulated coverage of various oxide species during the anodic branch of the CV. The experimental oxide coverage values are included.

The anodic peaks (features 2 and 3) are a result of the equilibrated, chemisorbed oxides of Equations 8 and 9. The initial chemisorbed oxide has a relatively low interaction parameter = 45 $kJ \cdot mol^{-1}$, indicating that it is fairly easy to deposit 2/3 monolayers (MLs) of oxide on the platinum surface. The 4^{th} feature is the place-exchanged oxide that is formed at the expense of chemisorption sites. During the initial stages of reduction, feature 5, the reversible chemisorbed oxide is reduced. The main reduction peak, feature 6, is the reduction of the surface place exchanged oxide and the remaining chemisorbed oxide. The simulated oxide coverage (PtOH basis) for the anodic sweep is also shown in Figure 6.5, and the values agree very well with the experimental oxide coverage values (filled data points).

By incorporating an additional parameter, we are able to widen the reduction peak as well as obtain a Tafel slope closer to experimental values. Figure 6.6 demonstrates how scan rate changes certain features in the CV both experimentally and in simulated versions. The 1^{st} and 2^{nd} features are related to the oxidation of edge sites and amount of chemisorbed oxide. Less oxide is adsorbed at faster scan rates, which can be seen in both the experimental results and simulated CV at larger potential ranges. The initial slopes of the chemisorbed peaks fall on top of one another in the model, but are offset to the right from each other experimentally when the scan rate is increased. Another difference is seen at feature 3, where the leading edges of the experimental reduction peaks are offset to the left with increasing scan rates, indicating an irreversible oxide. In the model, the reversible chemisorbed oxide is reduced in this region with little contribution from the irreversible place-exchanged oxides. Because this process is in equilibrium, it is unaffected by a change in scan rate resulting in the same reduction path.

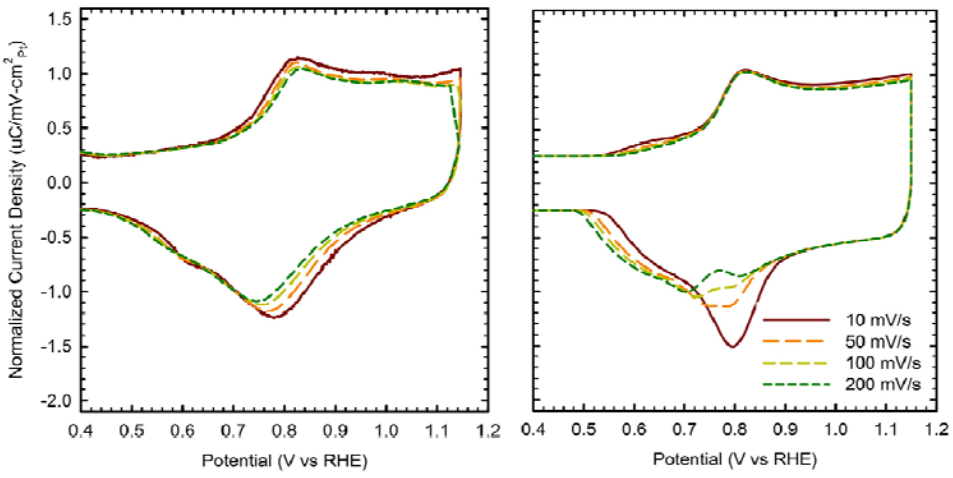

Figure 6.6 Comparison between experimental (left) and simulated (right) CVs at different scan rates.

The experimental Tafel slope is 30 mV/decade, and the simulated Tafel slope is 70 mV/decade. The reason for the difference is the maximum peak position in the model is not determined by one peak alone, instead there are three reduction processes to consider. The chemisorbed oxide is equilibrated, and its reduction peak does not shift with scan rate. The other two processes are irreversible place exchanged oxides, with transfer coefficient values of 1.5 in Equations 10 and 11. The maxima of these reduction peaks are shifted to the left 39 mV/decade with increasing scan rate; therefore, less overlap occurs between chemisorbed and place exchanged peaks. At low scan rates, the expected position of the peak maximum is shifted to the right due to overlap. As scan rate increases, a larger than expected Tafel slope is generated due to peak separation. Including the χ-parameter amplifies this effect as well since its inclusion causes peaks to move right with increasing oxide coverage (an effect of low scan rates). To reiterate, if we considered only Equation (6.2) and began each reduction sweep with the same initial oxide coverage, we would expect a Tafel slope of 39 mV/decade when the transfer coefficient had a value of 1.5. However, accounting for the varying maximum coverage due to the varying anodic scan rate causes the Tafel slope to increase (for $\chi = 0.73$, Tafel

slope = 53 mV/decade). The additional 17 mV difference in the Tafel slope observed in the overall simulation is due to the varying degree of overlap with the chemisorption peak. Tafel kinetics force the trailing edges of the simulated reduction peak to be offset from one another. This effect is seen experimentally in platinum wire data (38), but it is not seen in the experimental MEA data of Figure 6.6.

When examining the effects of the UPL on the CV with a constant scan rate of 10 mV/s, there are three characteristic features seen on the reduction sweep. The 1st feature in the experimental graph of Figure 6.7 is offset to the right at higher UPLs and is an attribute of an irreversible process. As mentioned previously, the largest contribution to current when reducing from the UPL to 0.9 V during the simulation is the reversible chemisorption, so we observe the same reduction pathway. At 0.8 V, the main peak is nearly reversible and as the UPL is increased the main reduction peak becomes more irreversible. This overall trend is also seen in the simulated curves, where the peak positions at lower UPLs are shifted more to the right than the peak for UPL = 1.15 V. However, the simulated plots show peak separation for UPLs less than 1.15 V. This effect is due to too much chemisorption taking place and not enough place exchange at lower potentials.

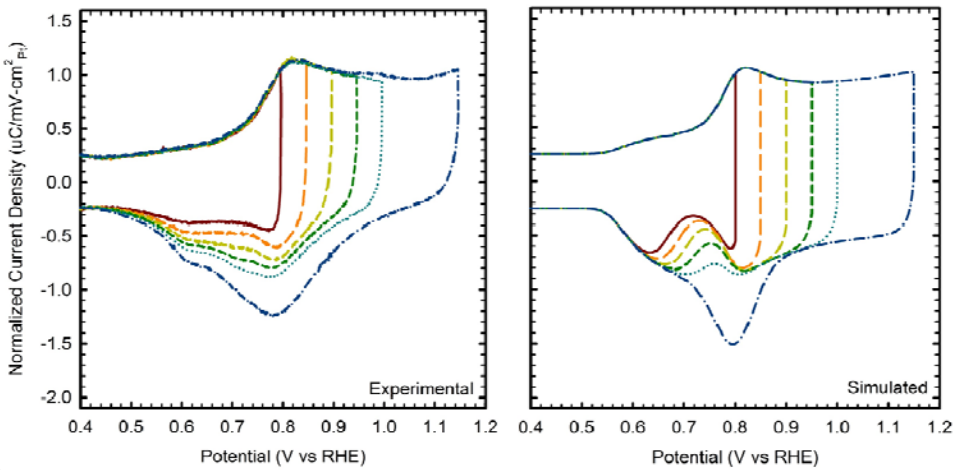

Figure 6.7 The effect of varying the UPL on experimental and simulated CVs with a scan rate of 10 mV/s.

Lastly, the shoulder seen at 0.6 V has been attributed to oxide reduction on the edge sites, and it is seen experimentally that the peak shrinks with decreasing UPL, though the position remains the same. The simulated version shows smaller peaks as well, but also a shift in position to more positive potentials. The change in position is due to the overlapping of the edge site reduction current and the planar site reduction current. The edge sites are oxidized very quickly, so that peak is relevant even at 0.8 V. The planar site oxidation happens more slowly and requires higher potentials. At low potentials, only a small planar site place exchange current contributes to the overall peak shape.

From this study, many experimental CV characteristics are successfully simulated. However, we are unable to simulate the correct Tafel slope and nearly constant reduction peak potential (with varying UPL) by introducing a single parameter. This study shows that the rate is not only a function of coverage and potential. Thus, we propose to include the addition of a heterogeneous oxide layer.

6.3.2 Heterogeneous Oxide Layer

Various stable platinum oxide structures have been predicted and found experimentally. We are proposing that a single oxide "layer" contains many different oxide structures, as shown in Figure 6.8(a). This heterogeneous oxide layer has a distribution of formation energies. Early studies detected subsurface oxygen in a platinum lattice through X-ray scattering (43) and low-energy electron diffraction (44), and simplistic place-exchanged structures, such as Figure 6.8(b) were proposed. In 2008, platinum oxide chain structures were directly observed using scanning tunneling microscopy (45). Following this observation, DFT was used to predict the structure of the chain, classifying them as PtO_2 stripes, whereby the platinum surface atoms 'buckle' into the oxide layer (46) as shown in Figure 6.8(c). Other DFT studies predicted full fcc hollow site occupation of oxygen atoms (47), an α-PtO_2 oxide layer (48, 49), or a simple place-exchange structure (50) as shown in Figure 6.8(d).

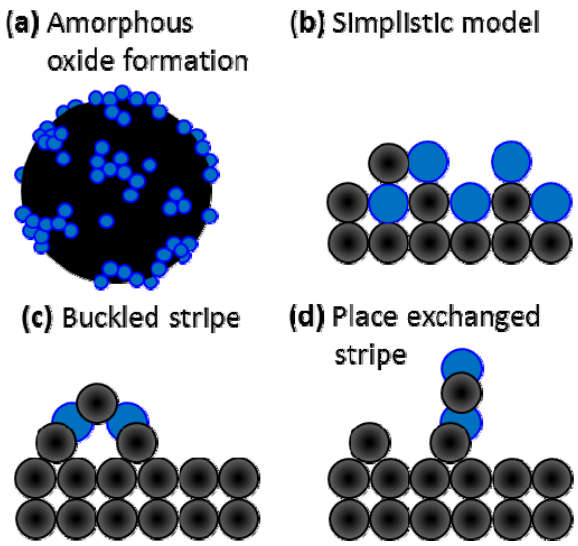

Figure 6.8 It is proposed that the oxide (blue) forms as an (a) amorphous layer on the platinum surface (black). Different sites lead to different structure types such as (b) simplistic subsurface oxygen models (43), (c) buckled PtO_2 (45, 46), and (d) simple place-exchanged stripes (50).

Considering all possible stable structures presented in the DFT literature, Holby and coworkers predicted a more stable place-exchanged hybrid structure that combines the buckled stripe and place exchanged stripe (41). The hybrid structure is stable at 1 ML on a Pt(111) surface and offers a low energy barrier mechanism for forming subsurface oxygen through chain rotation (41).

The model presented in this section does not distinguish between various surface planes. It is reasonable that many stable place-exchanged structures are present on a polycrystalline surface. We assume the different place-exchanged structures are formed by the oxidation of PtOH through a single transition state as illustrated in Figure 6.9, but the products assume a PtO_2 state of varying energies. Thus, during the anodic branch of the CV, as potential is increased, the energy states of the various PtO_2 structures are filled evenly as shown in Figure 6.10. However, upon reduction the higher energy (or less stable) states are reduced at higher potentials. Figure 6.10 also illustrates the occupancies of the PtO_2 states at discrete points during the anodic and cathodic sweep.

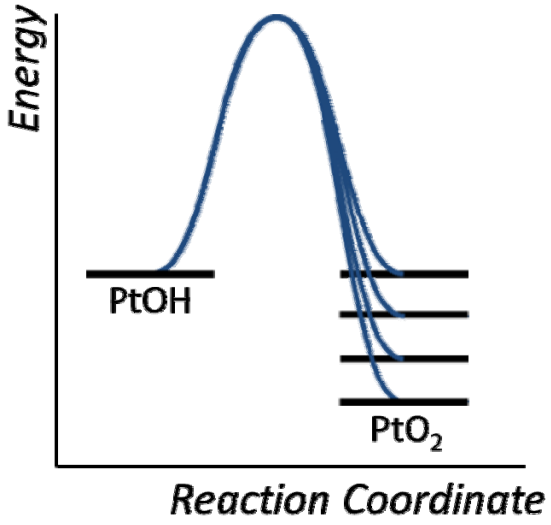

Figure 6.9 Sketch of proposed energy coordination diagram where the place-exchanged oxides form through a single transition state.

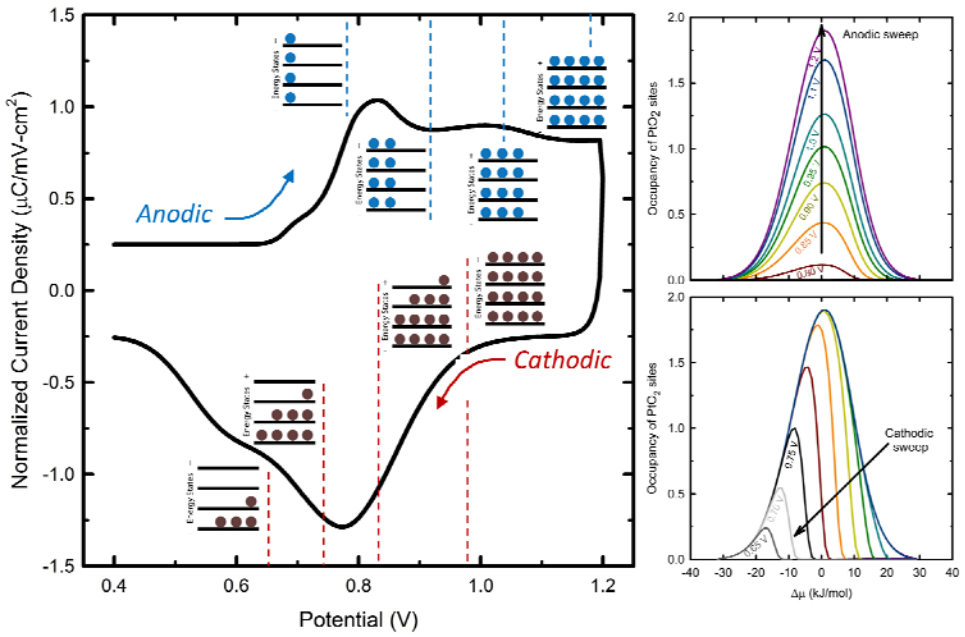

Figure 6.10 The CV shows the filling/unfilling of the PtO_2 energy states upon oxidation/reduction. PtO_2 forms evenly around a standard chemical potential as shown by the occupancy of PtO_2 sites during the anodic sweep. Cathodically, the high energy states are reduced first.

6.3.2.1 The Mechanism

Following the interpretation of the XAS results, the mechanism of platinum oxidation on planar sites was taken to be a two-step process. As discussed previously, edge sites may show different behavior and were treated separately. On planar sites, platinum is first oxidized to PtOH, and this process is treated at equilibrium. Then, the place-exchange process converts PtOH to PtO_2. Because edge sites are much higher in energy than planar sites, the formation of a place-exchanged PtO_2 species from the metallic edge sites was chosen as a direct process. In summary, the following chemical reactions are considered for platinum oxidation:

$$Pt + H_2O \overset{eqbm}{\rightleftharpoons} PtOH + H^+ + e^- , \qquad \text{(I)}$$

$$PtOH + H_2O \rightleftharpoons PtO_2 + 3H^+ + 3e^- , \qquad \text{(II)}$$

and

$$Pt + 2H_2O \underset{Sites}{\overset{Edge}{\rightleftharpoons}} PtO_2 + 4H^+ + 4e^- \quad \text{(III)}$$

Each of the three oxide species needs a concentration variable. The chemisorbed oxide is described by a surface coverage θ_{OH}. The surface and edge place exchanged oxides have many possible configurations distinguished by a chemical potential shift, $\Delta\mu$. The total coverage of PtO_2 is distributed over this range of chemical potentials, and the coverage of PtO_2 at a given chemical potential on planar or edge sites is $x(\Delta\mu)$ and $x_{Edge}(\Delta\mu)$, respectively. The total coverage is calculated by integrating the coverage of each oxide configuration

$$\theta_{PtO_2} = \int_{-3\sigma}^{3\sigma} x(\Delta\mu) \cdot d\Delta\mu \quad (6.11)$$

and

$$\theta_{Edge} = \int_{-3\sigma}^{3\sigma} x_{Edge}(\Delta\mu) \cdot d\Delta\mu \quad (6.12)$$

The limits of integration should be ±∞, but the numerical simulation was truncated at 3 standard deviations (±3σ) for practical reasons.

The number of active sites for each species must also be specified. The total number of active sites available on a platinum surface is $\Gamma = 2.1/F \;\; C/m_{Pt}{}^2$ (29), where F is Faraday's constant of 96,487 $C/equivalent$. A fraction, X_{Edge}, of these sites is edge sites, and the remainder is planar sites. Assuming a cuboctohedral particle of ca. 3 nm diameter, X_{Edge} is calculated to be exactly 0.36, as shown in Appendix C. Thus, the basis for θ_{PtO_2} is

$$\Gamma_{planar} = (1 - X_{Edge})\Gamma, \quad (6.13)$$

and the basis for θ_{Edge} is

$$\Gamma_{Edge} = X_{Edge}\Gamma. \quad (6.14)$$

The number of sites available for chemisorption is initially equal to the number of planar sites, but decreases as place-exchanged oxide is formed according to an empirical relationship,

$$\Gamma_{OH} = e^{-8\theta_{PtO_2}} \Gamma_{planar} . \tag{6.15}$$

This relationship specifies that the first units of PtO_2 formed inhibit the adsorption of eight OH sites, but as more PtO_2 is deposited, fewer additional sites are inhibited due to overlap. The sites for chemisorption are never completely eliminated.

6.3.2.2 Mass Balances

With the coverage variables properly defined, mass balances can be written for each oxide species. For chemisorbed oxide, the mass balance is written as

$$\frac{d\theta_{OH}}{dt} = \frac{\bar{r}_1 - \bar{r}_2}{\Gamma_{OH}} - \frac{\theta_{OH}}{\Gamma_{OH}} \frac{d\Gamma_{OH}}{dt} , \tag{6.16}$$

where the first term on the right side describes the net rate of formation of PtOH, and the second term describes changes in coverage due to changes in the number of surface sites. The planar and edge site PtO_2 mass balances are

$$\frac{dx(\Delta\mu)}{dt} = \frac{r_2(\Delta\mu)}{\Gamma_{planar}} \tag{6.17}$$

and

$$\frac{dx_{Edge}(\Delta\mu)}{dt} = \frac{r_3(\Delta\mu)}{\Gamma_{Edge}} \tag{6.18}$$

A distinction must be made between two types of rates. The term $r_i(\Delta\mu)$ refers to the specific rate of reaction *i*, where i = 1, 2, or 3, involving a heterogeneous oxide layer at a given chemical potential shift, $\Delta\mu$. The term $\bar{r}_i$ is the overall rate of reaction *i* considering all oxide configurations. This overall rate can be calculated by integrating the specific rate over all chemical potential shifts,

$$\overline{r_i} = \int_{-3\sigma}^{3\sigma} r_i\left(\Delta\mu\right) d\Delta\mu \,. \tag{6.19}$$

6.3.2.3 Rate Equations and Equilibrium Expressions

For every reaction rate introduced in the mass balances, either an equilibrium expression or a kinetic rate equation must be specified. Rate 1 is at equilibrium

$$\theta_{OH} = \left(1-\theta_{OH}\right) e^{\left(\frac{F}{RT}\left(\Phi-U_1^{\theta}\right)-\frac{\omega_{OH}\theta_{OH}^2}{RT}\right)}, \tag{6.20}$$

where Φ is the electrode potential and U_1^{θ} is the standard potential of Reaction I. The heat of adsorption for the deposition of OH species is modeled as a nonlinear isotherm, whereby the heat of adsorption increases with coverage squared. The interaction parameter, ω_{OH}, accounts for the rate of increase.

Rate 2 is written as

$$r_2\left(\Delta\mu\right) = k_2\left[\theta_{OH}\Gamma_{OH}\psi\left(\Delta\mu\right) e^{\left(-\frac{\omega_{PtO_2}\theta_{PtO_2}-\omega_{OH}\theta_{OH}^2}{RT}\right)} e^{\left(\frac{\alpha_{A2}F}{RT}\left(\Phi-U_2^{\theta}\right)\right)} - \Gamma_{planar}x\left(\Delta\mu\right) e^{\left(\frac{\Delta\mu}{RT}\right)} e^{\left(-\frac{\alpha_{C2}F}{RT}\left(\Phi-U_2^{\theta}\right)\right)}\right]. \tag{6.21}$$

The forward rate is first order in PtOH and includes effects due to the changing enthalpy of the reaction as a function of the two coverages, θ_{OH} and θ_{PtO_2}. The tendency of the various oxide configurations to form from the transition state is described by the function,

$$\psi\left(\Delta\mu\right) = \frac{1}{\sigma\sqrt{2\pi}} e^{\left(-\frac{\Delta\mu^2}{2\sigma^2}\right)} \tag{6.22}$$

which is a Gaussian distribution with a standard deviation, σ, of 14.5 kJ/mol. The reverse rate is first order in planar site PtO_2 and includes the heterogeneity effects of the chemical potential shift, $\Delta\mu$.

Finally, rate 3 is

$$r_3\left(\Delta\mu\right) = k_3\Gamma_{Edge}\left[\psi_{Edge}\left(\Delta\mu\right) e^{\left(-\frac{\omega_{Edge}\theta_{Edge}}{RT}\right)} e^{\left(\frac{\alpha_{A3}F}{RT}\left(\Phi-U_3^{\theta}\right)\right)} - x_{Edge}\left(\Delta\mu\right) e^{\left(\frac{\Delta\mu}{RT}\right)} e^{\left(-\frac{\alpha_{C3}F}{RT}\left(\Phi-U_3^{\theta}\right)\right)}\right]. \tag{6.23}$$

Conceptually, this rate equation is very similar to Equation (6.21), except that the formation of PtOH on edge sites is not considered. The tendency to form various oxide configurations is also a Gaussian distribution,

$$\psi_{Edge}\left(\Delta\mu\right)=\frac{1}{\sigma_{Edge}\sqrt{2\pi}}e^{\left(-\frac{\Delta\mu^2}{2\sigma_{Edge}^2}\right)} \tag{6.24}$$

with a standard deviation, σ_{Edge}, of 8.7 kJ/mol.

Equations (6.11) - (6.24) fully define the model, but additional variables are introduced for convenient interpretation of the results. Total oxide coverage was calculated on a PtOH or 1 electron transfer basis as

$$\theta_{Total}=\frac{\Gamma_{OH}\theta_{OH}+4\Gamma_{planar}\theta_{PtO_2}+4\Gamma_{Edge}\theta_{Edge}}{\Gamma} \tag{6.25}$$

Pseudo-capacitance, *C*, is a more convenient way of looking at current density for varying scan rates and is calculated by dividing the total current density by the scan rate, ν. The pseudo-capacitance is calculated from the overall reaction rates $\left(\bar{r}_i\right)$, adding in a double layer capacitance, C_{dl}, according to

$$C=\frac{F\left(\bar{r}_1+3\bar{r}_2+4\bar{r}_3+\left(C_{dl}/F\right)\cdot d\Phi/dt\right)}{\nu} \tag{6.26}$$

All equations were solved using gPROMS software version 3.3.1. Parameters were fit manually to an experimental CV with a scan rate of 50 mV/s and UPL of 1.15 V.

6.3.2.4 Assumptions

The assumptions are discussed in detail in the above section. Here, we summarize the major assumptions that were made in the derivation of the presented model:

- A continuous distribution of oxides is formed through a single transition state.
- The transfer coefficients are effective transfer coefficients, and do not represent elementary steps.

- Isotherms for the heat of adsorption are assumed.
- Place exchange sites destroy chemisorption sites.
- Edge sites behave differently than planar sites.
- The active sites available for reaction on the edge sites are 36% the amount available on planar surfaces for a cuboctahedron (an established shape for platinum particles supported on carbon (51-55)) with the volume equivalent to a sphere 3 nm in diameter.

6.3.2.5 Theoretical Results

The parameters listed in Table 6.3 were fit to an experimental CV at 50 mV/s and UPL of 1.15 V. The simulated and experimental CVs are compared in Figure 6.11, and the simulated version follows the experimental CV very closely. The parameters F, R, T, and Γ are standard values. The double layer capacitance was measured from experimental data, and the fraction of edge sites value was estimated geometrically and explained in Appendix C. The standard reaction potentials were fit to the experimental CV at 50 mV/s. Place exchange occurring on the edge sites has a lower standard potential because the edge sites are more active, which is consistent with a higher interaction parameter. The effective transfer coefficients for Reaction II are 1.5, which are consistent with an elementary mechanism with equilibrated steps before and after the rate determining step with a symmetry factor of 0.5. The stable oxide species on planar sites are PtOH and PtO_2 and possible intermediate oxide species are PtO and HO-Pt-O. Reaction II has an anodic transfer coefficient of 2.5 and a cathodic transfer coefficient of 1.5. These values are consistent with an elementary mechanism with 2 pre-equilibrated steps before the rate determining step (symmetry factor of 0.5) and an equilibrated step after. In this case, all oxides, except PtO_2, are considered intermediates, and this assumption is consistent with the higher energy edge sites. The rate constants are reasonable values compared to those found in literature (33, 56-58).

Table 6.3 List of parameters and values used in heterogeneous oxide layer simulations.

Symbols	Name	Values	Units
F	Faraday's constant	96,487	$C \cdot mol^{-1}$
R	Ideal gas constant	8.314	$J \cdot mol^{-1}K^{-1}$
T	Temperature	298	K
Γ	Concentration of active sites	$2.1/F$	$mol \cdot m_{Pt}^{-2}$
C_{dl}	Double layer capacitance	0.25	$mF \cdot cm_{Pt}^{-2}$
X_{Edge}	Fraction of edge sites	0.36	*dimensionless*
U_1^θ U_2^θ U_3^θ	Standard reaction potentials	0.83 0.83 0.67	V
ω_{OH} ω_{PtO_2} ω_{Edge}	Interaction parameters	15 140 667	$kJ \cdot mol^{-1}$
α_{A2} α_{C2} α_{A3} α_{C3}	Effective transfer coefficients	1.5 1.5 2.5 1.5	*dimensionless*
k_2 k_3	Rate constants	7.4×10^{-2} 7.8×10^{-3}	s^{-1}

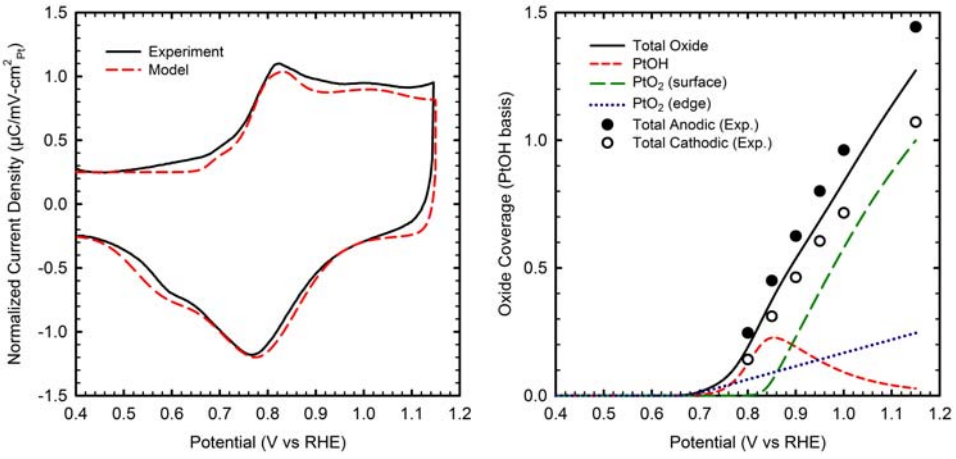

Figure 6.11 Left: CV comparisons between experimental and model results at 50 mV/s. Right: Experimental (anodic and cathodic) and theoretical comparison of oxide coverage values with potential. The individual coverage values for each oxide species considered are shown.

The plot on the right of Figure 6.11 compares the oxide coverage values measured experimentally, both anodically and cathodically, and those simulated. The simulated total coverage splits the difference between the experimentally measured oxide coverage values. Additionally, the oxide coverage values for each oxide species are shown in Figure 6.11.

The model yielded the correct results when the scan rate or UPL was varied, as shown in Figure 6.12. When the scan rate is varied, the simulated anodic peak is reversible, and the correct Tafel slope of 30 mV/decade, for platinum oxide reduction, is achieved. Furthermore, a reduction peak with a shallow leading edge is also observed. Therefore, the introduction of a heterogeneous oxide layer allows for a strong Tafel relationship and a broad reduction peak. Above an UPL of 0.8 V, the position of the reduction peak is nearly constant, which is observed experimentally.

Features observed in Figure 6.12, but not observed experimentally are the shifting of the edge peak with scan rate and nearly complete reversibility at UPL = 0.8 V. Additionally, it was found that the potentiostatic growth rate was much lower than experimental values, which was also the case for the χ-parameter studies. The experimental and simulated growth rates are compared in Table 6.4. Therefore, some challenges still exist, but all of the experimental characteristics previously discussed have been achieved through the incorporation of a heterogeneous oxide layer.

Table 6.4 Comparison of experimental and simulated growth rates.

Study	Growth Rate (ML/dec)
Literature (31, 32)	0.08 (experimental)
Nanoparticles	0.3 (experimental)
χ-parameter	0.1 (simulation)
Heterogeneous oxide layer	0.1 (simulation)

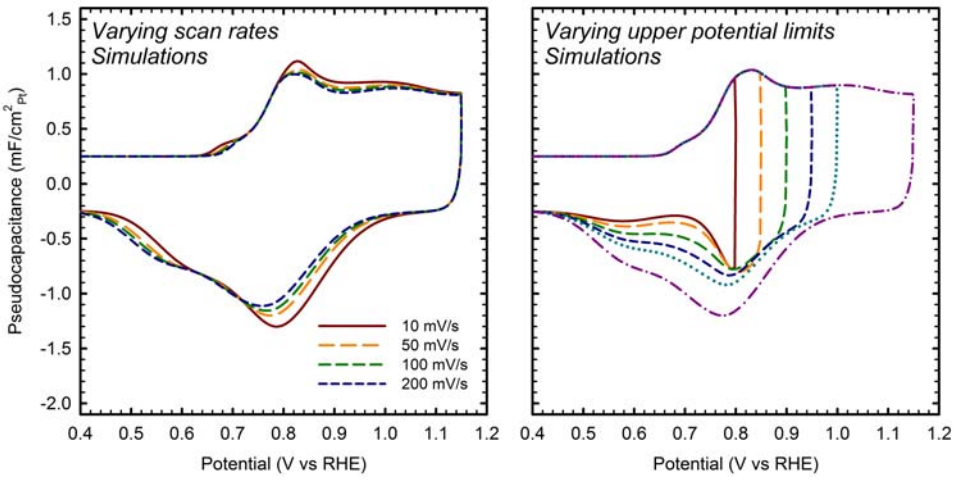

Figure 6.12 Simulation results under varying scan rates (left) and UPLs (right).

6.4 Conclusions

A technique to measure oxide coverage directly from EXAFS data was presented. First, the data is inverse Fourier transformed in a specific region of interest and then Fourier transformed where the reference spectra are out of phase. This process allows the specific signals (oxide or metallic) to be amplified and elucidates the peaks in each region. Then, the relative areas were normalized to give the total oxidation of the platinum particle, which was converted to a surface coverage and compared to electrochemical data. This technique is complementary to ab initio calculations used to determine coordination parameters because it allows for the direct comparison between EXAFS and electrochemical measurements. EXAFS results indicated PtO_2 was present on the platinum surface during potential holds. Comparison of the measured oxide coverages to the calculated equivalent EXAFS coverages, indicated the place-exchanged PtO_2 species was being formed at the expense of a chemisorbed oxide species. These results were used in two different simulation studies.

Previously, literature simulations have not been able to fully reproduce the behavior observed in a CV of the cathode in a PEM fuel cell. As a first attempt in understanding the kinetics of oxide growth on platinum, the χ-parameter was introduced into kinetic equations. The χ-parameter allocated the adsorption isotherm effects to the anodic and cathodic portions of the rate equation, and allowed the Tafel slope to be decoupled from the peak width for the reduction peak. A mechanism was proposed for platinum oxidation with an initial chemisorbed oxide in equilibrium with the platinum surface and irreversible place exchanged oxides representing surface and edge sites. The second reduction peak at lower potentials observed in the CV was attributed to oxidation on the edge sites of platinum particles. Although the parameters can be adjusted to achieve a good fit with experimental data, peak separation occurs at lower UPLs and higher scan rates. Thus, the rate is not only a function of potential and coverage, and a heterogeneous oxide layer was proposed.

Place-exchanged oxide species with different chemical potentials were allowed to form through a single transition state. The mechanism was changed to reflect the results of the EXAFS study, whereby place exchange on the planar surface destroys active sites for chemisorption. This heterogeneity allowed, for the first time, the simulation of the correct current-potential behavior under varying scan rates and UPLs.

6.5 References

1. N. Guo, B. R. Fingland, W. D. Williams, V. F. Kispersky, J. Jelic, W. N. Delgass, F. H. Ribeiro, R. J. Meyer and J. T. Miller, *Phys Chem Chem Phys*, **12**, 5678 (2010).

2. Y. Lei, J. Jelic, L. C. Nitsche, R. Meyer and J. Miller, *Top Catal*, **54**, 334 (2011).

3. H. Imai, K. Izumi, M. Matsumoto, Y. Kubo, K. Kato and Y. Imai, *J Am Chem Soc*, **131**, 6293 (2009).

4. A. Teliska, W. E. O'Grady and D. E. Ramaker, *J Phys Chem B*, **109**, 8076 (2005).

5. A. Kongkanand and J. M. Ziegelbauer, *J Phys Chem C*, **116**, 3684 (2012).

6. C. H. Paik, T. D. Jarvi and W. E. O'Grady, *Electrochem Solid St*, **7**, A82 (2004).

7. Y. X. Liu, M. Mathias and J. L. Zhang, *Electrochem Solid St*, **13**, B1 (2010).

8. D. Friebel, D. J. Miller, C. P. O'Grady, T. Anniyev, J. Bargar, U. Bergmann, H. Ogasawara, K. T. Wikfeldt, L. G. M. Pettersson and A. Nilsson, *Phys Chem Chem Phys*, **13**, 262 (2011).

9. S. Mitsushima, S. Kawahara, K. I. Ota and N. Kamiya, *J Electrochem Soc*, **154**, B153 (2007).

10. R. J. K. Wiltshire, C. R. King, A. Rose, P. P. Wells, M. P. Hogarth, D. Thompsett and A. E. Russell, *Electrochim Acta*, **50**, 5208 (2005).

11. R. Viswanathan, R. Liu and E. S. Smotkin, *Rev Sci Instrum*, **73**, 2124 (2002).

12. E. Principi, A. Di Cicco, A. Witkowska and R. Marassi, *J Synchrotron Radiat*, **14**, 276 (2007).

13. C. Roth, N. Benker, T. Buhrmester, M. Mazurek, M. Loster, H. Fuess, D. C. Koningsberger and D. E. Ramaker, *J Am Chem Soc*, **127**, 14607 (2005).

14. E. Principi, A. Witkowska, S. Dsoke, R. Marassi and A. Di Cicco, *Phys Chem Chem Phys*, **11**, 9987 (2009).

15. V. Croze, F. Ettingshausen, J. Melke, M. Soehn, D. Stuermer and C. Roth, *J Appl Electrochem*, **40**, 877 (2010).

16. M. Tada, S. Murata, T. Asakoka, K. Hiroshima, K. Okumura, H. Tanida, T. Uruga, H. Nakanishi, S. Matsumoto, Y. Inada, M. Nomura and Y. Iwasawa, *Angew Chem Int Edit*, **46**, 4310 (2007).

17. S. C. Ball, S. L. Hudson, D. Thompsett and B. Theobald, *J Power Sources*, **171**, 18 (2007).

18. D. R. Lowde, J. O. Williams and B. D. McNicol, *Applications of Surface Science*, **1**, 215 (1978).

19. K. Kinoshita and J. A. S. Bett, *Carbon*, **11**, 403 (1973).

20. C. C. Hu and K. Y. Liu, *Electrochim Acta*, **44**, 2727 (1999).

21. M. H. Shao, A. Peles and K. Shoemaker, *Nano Lett*, **11**, 3714 (2011).

22. V. Komanicky, K. C. Chang, A. Menzel, N. M. Markovic, H. You, X. Wang and D. Myers, *J Electrochem Soc*, **153**, B446 (2006).

23. E. L. Redmond, P. Trogadas, F. Alamgir and T. F. Fuller, *ECS Transactions*, **50**, 1369 (2012).

24. E. L. Redmond, B. P. Setzler, P. Juhas, S. J. L. Billinge and T. F. Fuller, *Electrochem Solid St*, **15**, B72 (2012).

25. E. L. Redmond, B. P. Setzler, P. Juhas, S. J. L. Billinge and T. F. Fuller, *ECS Transactions*, **41**, 751 (2011).

26. S. Gilman, *J Phys Chem-Us*, **67**, 78 (1963).

27. M. Newville, *J Synchrotron Radiat*, **8**, 322 (2001).

28. B. Ravel and M. Newville, *J Synchrotron Radiat*, **12**, 537 (2005).

29. S. B. Brummer, *The Journal of Physical Chemistry*, **69**, 562 (1965).

30. B. E. Conway and G. Jerkiewicz, *J Electroanal Chem*, **339**, 123 (1992).

31. M. Alsabet, M. Grden and G. Jerkiewicz, *J Electroanal Chem*, **589**, 120 (2006).

32. G. Jerkiewicz, M. Alsabet, M. Grden, H. Varela and G. Tremiliosi, *J Electroanal Chem*, **625**, 172 (2009).

33. R. M. Darling and J. P. Meyers, *J Electrochem Soc*, **150**, A1523 (2003).

34. A. J. Appleby, *J Electrochem Soc*, **120**, 1205 (1973).

35. A. J. Bard and L. R. Faulkner, *Electrochemical methods: Fundamentals and applications*, John Wiley & Sons, USA (2001).

36. J. Newman and K. E. Thomas-Alyea, *Electrochemical Systems*, John Wiley & Sons, Inc., Hoboken, NJ (2004).

37. R. M. Darling and J. P. Meyers, *J Electrochem Soc*, **152**, A242 (2005).

38. Angerstein-Kozlowska.H, B. E. Conway and W. B. A. Sharp, *J Electroanal Chem*, **43**, 9 (1973).

39. B. E. Conway, *Prog Surf Sci*, **49**, 331 (1995).

40. G. Jerkiewicz, G. Vatankhah, J. Lessard, M. P. Soriaga and Y. S. Park, *Electrochim Acta*, **49**, 1451 (2004).

41. E. F. Holby, J. Greeley and D. Morgan, *J Phys Chem C*, **116**, 9942 (2012).

42. W. Bi and T. F. Fuller, *J Power Sources*, **178**, 188 (2008).

43. Z. Nagy and H. You, *Electrochim Acta*, **47**, 3037 (2002).

44. F. T. Wagner and P. N. Ross, *Surf Sci*, **160**, 305 (1985).

45. S. P. Devarajan, J. A. Hinojosa and J. F. Weaver, *Surf Sci*, **602**, 3116 (2008).

46. J. M. Hawkins, J. F. Weaver and A. Asthagiri, *Phys Rev B*, **79** (2009).

47. H. R. Tang, A. Van der Ven and B. L. Trout, *Phys Rev B*, **70** (2004).

48. N. Seriani, Z. Jin, W. Pompe and L. C. Ciacchi, *Phys Rev B*, **76** (2007).

49. R. B. Getman, Y. Xu and W. F. Schneider, *J Phys Chem C*, **112**, 9559 (2008).

50. Z. H. Gu and P. B. Balbuena, *J Phys Chem C*, **111**, 17388 (2007).

51. M. Cabie, S. Giorgio, C. R. Henry, M. R. Axet, K. Philippot and B. Chaudret, *J Phys Chem C*, **114**, 2160 (2010).

52. V. L. Nguyen, D. C. Nguyen, T. Hayakawa, H. Hirata, G. Lakshminarayana and M. Nogami, *Nanotechnology*, **21** (2010).

53. A. I. Frenkel, C. W. Hills and R. G. Nuzzo, *J Phys Chem B*, **105**, 12689 (2001).

54. M. B. Gordon, F. Cyrotlackmann and M. C. Desjonqueres, *Surf Sci*, **68**, 359 (1977).

55. S. Mukerjee and J. McBreen, *J Electroanal Chem*, **448**, 163 (1998).

56. D. V. Heyd and D. A. Harrington, *J Electroanal Chem*, **335**, 19 (1992).

57. S. G. Rinaldo, J. Stumper and M. Eikerling, *J Phys Chem C*, **114**, 5773 (2010).

58. A. A. Franco and M. Tembely, *J Electrochem Soc*, **154**, B712 (2007).

CHAPTER 7

EFFECT OF CURVATURE AND SAMPLE ENVIRONMENT ON SURFACE STRESS OF PLATINUM NANOPARTICLES SUPPORTED ON CARBON

Recent improvements in electrochemical energy conversion and storage devices have been in large part due to progress in fabrication of structures at the nanoscale. For example, highly dispersed platinum nanoparticles are used to facilitate the oxygen reduction reaction that takes place at the cathode of proton exchange membrane (PEM) fuel cells. The use of particle diameters between 2 nm to 5 nm increases the utilization of platinum. Thus, the cost of the device, a key barrier to commercialization, is lowered while maintaining an acceptable level of performance. However, as discussed in earlier chapters, high potentials and acidic conditions present at the cathode result in platinum instability, and the electrochemically active surface area decreases over time (1). The loss of active catalyst area reduces fuel cell efficiency (2). Platinum area loss mechanisms are accelerated in the case of small particle sizes (3). Ostwald ripening is driven by surface energy, where large particles grow at the expense of small particles (4, 5). In platinum dissolution simulations, the Gibbs-Thomson (or Kelvin) equation is used to account for the effect of surface energy, γ, and particle size, R, on the platinum dissolution rate (6). The increase in the Gibbs energy, ΔG, of a spherical platinum nanoparticle, compared to the bulk, due to the surface energy is given by

$$\Delta G = \frac{\gamma}{R}\frac{MW_{Pt}}{\rho_{Pt}}, \tag{7.1}$$

where MW_{Pt} and ρ_{Pt} are the molecular weight (195 g/mol) and density (21 x 10^3 kg/m^3), respectively. The increase in Gibbs energy results in a higher chemical potential and increased dissolution. In previous modeling studies of platinum stability (7-12), the surface energy is treated as a constant and equal to that of bulk platinum, 2.37 J/m^2.

Qualitatively, this approach yields the correct behavior, but no data exist to support this relationship. Ripening depends strongly on the thermodynamic driving forces and little is known about the values of these forces for nanoparticles. It is important to understand the physical forces driving platinum dissolution at the nanoscale, so that simulations are able to better predict the behavior of promising electrocatalyst materials. Methods to measure the surface energy of solid metal nanoparticles are needed to model the effects of this parameter on fuel-cell catalyst stability. One possible way to obtain surface energy is through the relation of surface stress and lattice strain, which are measurable quantities. Surface stress is an additional force that affects the chemical and electronic properties of catalysts and contributes to surface reconstruction (13).

For solid particles, surface stress and surface energy are separate quantities. Surface stress is the reversible work per unit area needed to elastically stretch a surface, such that no new surface atoms are created (14, 15). Surface energy is the reversible work per unit area required to form a new surface (14, 15). The term surface tension is assumed to be a direct reference to liquid matter, where the surface stress and surface energy are equal. This chapter specifically considers a metallic solid, where surface stress and surface energy are not equal, and the use of surface 'tension' is purposely avoided to prevent confusion.

Surface energy is the parameter that affects platinum dissolution in Equation (7.1). Surface stress, f, is related to surface energy, γ, by the thermodynamic relationship (15-17)

$$f_{ij} = \delta_{ij}\gamma_{ij} + \frac{\delta\gamma}{\delta\varepsilon_{ij}}, \tag{7.2}$$

where δ_{ij} is the Kronecker delta and ε_{ij} is the lattice strain. Assuming isotropic properties, the relationship simplifies to

$$f = \gamma + \frac{1}{2}\frac{\delta\gamma}{\delta\varepsilon}, \tag{7.3}$$

where the factor ½ enters because of the distinction between strain in a single direction and isotropic strain. For crystals, surface stress is expected to be less than surface energy because the long range repulsive forces acting on the surface atoms are less than the short range repulsive forces at the surface (15). Surface stress causes lattice strain in small particles. Lattice strain, ε, is contained in the information about the change in average atomic bond length, r_p, which can be measured with precision from electron or X-ray diffraction data (18-20). In detail,

$$\varepsilon = \frac{r_p(R) - r_p\big|_{R=\infty}}{r_p\big|_{R=\infty}} \tag{7.4}$$

where $r_p\big|_{R=\infty}$ is the bulk atomic bond length, for platinum $r_p\big|_{R=\infty}$ = 2.77 Å at room temperature. Surface stress can be calculated as a function of particle size and strain using the equation

$$f = -\frac{3}{2}\frac{\varepsilon R}{\kappa}, \tag{7.5}$$

where κ represents the compressibility, or inverse bulk modulus, of the metal (19, 21). For platinum, $\kappa = 4.35 \times 10^{-12}$ m^3/J (22).

Many studies have investigated the effect of surface stress on lattice contraction for solids (18, 19, 23-25). Wasserman and Vermaak first measured the surface stress of platinum by measuring the change in lattice parameter with particle curvature ($1/R$), assuming a constant compressibility (18). Platinum films, ranging from 3 nm in diameter to continuous, were deposited on a carbon substrate and annealed at 450 °C under ultra-high vacuum (18). Lattice constants were measured at 65 °C using the (111) and (220) diffraction patterns from transmission electron microscopy (18). A plot of lattice parameter versus curvature yielded a surface stress of 2.574±0.400 J/m^2 based on the (220) diffraction peak. A theoretical surface energy for platinum was extrapolated from the liquid state using Eötvös' rule, and was estimated to be 2.767 J/m^2 (18). The

difference between the measured surface stress and the theoretical surface energy was -0.193 J/m^2.

In 1985, Solliard and Flueli investigated lattice contraction of platinum nanoparticles as a function of temperature and size using scanning high energy electron diffraction (19). Reduced platinum particles were prepared by vacuum evaporation and condensation on a carbon substrate. Samples were annealed for 4 hours at 850 °C, and particle size was determined from electron microscopy (19). A nitrogen gas heat exchanger was used to control the temperature of the samples, and diffraction patterns were recorded every 50 K from 130 to 623 K. Lattice parameters were measured from the diffraction patterns of planes (220) and (422) because minimal background interference from carbon was observed (19). Temperature scans were used to determine the thermal expansion coefficient at the nanoscale. The nanoscale thermal expansion coefficient was calculated to be between 7.8 and 9 x 10^{-6} K^{-1}, which is lower than the bulk coefficient, 9.2 x 10^{-6} K^{-1} at 400 K. However, no dependence between the thermal expansion coefficient and particle size was found (19). The surface stress derived from the X-ray diffraction of the (220) and (422) planes was determined to be 3.86 J/m^2 and 4.44 J/m^2, respectively. The general trend of a lattice contraction with decreasing particle size agreed with the results of Wasserman and Vermaak's study. However, in contrast to Wasserman and Vermaak's study, these values of surface stress are greater than the theoretical values cited for surface energy. This conclusion is in agreement with the theoretical work of Khanna (26).

Qi and Wang developed a mechanical model to describe the elastic deformation caused by surface stress in nanoparticles with homogeneous strain (25). Lattice strain was predicted as a function of particle size for both spherical and non-spherical geometries, assuming that surface stress is independent of particle size. The model was used to predict the behavior of several fcc metals. The data used from previous experimental studies on lattice contraction (18, 21, 27-29) contained a significant amount of scatter,

which complicates the analysis of their model (25). Additionally, surface stress was considered to be the value of the bulk constant, which may not be true for particles with a diameter of 2 nm or less (25). Huang and co-workers modified Qi and Wang's model to include a surface stress that is dependent on particle size using Tolman's equation (24, 30). The model showed a significant change in predicted lattice strain for particles around 2 nm in diameter and below. Yet, this consideration did not describe the palladium lattice contraction data (31) any better than a constant bulk surface stress (24).

These fundamental studies regarding surface stress, lattice strain, and particle size are valuable because they set the groundwork for a better understanding of the surface properties of nanoparticles versus the bulk counterparts. However, in this manuscript we show that the surface stress values measured in references (18, 19) are not the intrinsic surface stress of platinum. Instead the surface stress measured was in reference to platinum oxide. Therefore, a fourth variable 'adsorbate type' is important when considering surface effects.

Many electro- and hetero- catalytic processes involve adsorbates which affect the local charge density at the surface and induce a surface stress. In 2011, Lei and coworkers investigated the effect of platinum particle size and adsorbates using X-ray absorption spectroscopy (32). The bond distance between platinum atoms was obtained from fits of the extended X-ray absorption fine structure spectra. Reduced catalysts showed a contraction of the bond distance, indicating that the d-band center moves away from Fermi level due to the hybridization of the metal bonds as the particle reconstructs to minimize its surface energy (32). The reduced catalyst samples show the same trend in lattice parameters as early studies such as Wasserman (18) and Solliard (19). Adsorption of carbon monoxide and hydrogen expanded the platinum bond distance, whereby the d-band center moves toward the Fermi level (32). Early studies attributed the expansion of the platinum lattice under hydrogen adsorption to the donation of electron density from hydrogen to platinum. Lei and coworkers show that antibonding orbitals are created

above the Fermi level (32). Platinum bond distances are dynamic and change with surface coverage, and in the study it was shown that lattice contraction is independent of the support (32).

A group in France used in situ environmental TEM to observe the effect that hydrogen and oxygen adsorbates have on platinum catalyst morphology (33). Under reducing conditions, the nanoparticles assume the equilibrium shape, truncated octahedron of an fcc platinum crystal. Upon oxide adsorption, it was observed that the (001) faces increased and the (111) faces decreased (33). Oxygen adsorbed more strongly on (100) surface planes. The morphological changes were found to be reversible. Discrepancies with ex situ studies were attributed to contamination of the literature samples with air, as exposure can be hard to avoid (33).

Alloy catalysts have shown increased stability in fuel-cell systems; however, lattice mismatch between alloying metals complicates the analysis of surface stress and the effect it has on the physical properties of nanoparticles. For example, Strasser and coworkers found that enhanced catalytic activity for the oxygen reduction reaction on core-shell particles can be explained by the compressive strain found between shell atoms (34). Particles were synthesized by de-alloying PtCu particles to form a PtCu core and a platinum rich shell, 0.6 nm to 1.0 nm thick. It was assumed that strain induced by particle curvature was insignificant, and the lattice mismatch between the alloyed core and platinum shell caused lattice strain (34). The induced strain caused the overlapping of electronic states between metal atoms, shifting the d-band orbitals below the Fermi level. X-ray diffraction was used to determine the average lattice parameter and chemical composition (34). A two phase core-shell model predicted that the shell lattice parameter was smaller than bulk platinum, indicating a compressive strain in the shell. The shell lattice parameter was found to decrease as the copper percentage or annealing temperature increased (34). Next, an electronic band structure model was used to explain the relationship between strain and surface reactivity. The model used layers of platinum

grown on top of Cu(111) to approximate the core-shell geometry (34). Finally, DFT was used to look at the Pt – O bond energy for strained Pt(111). A volcano relation was found: at first compressive strain lowers the binding energy, increasing the reactivity (34), and once a critical strain is reached, the binding energy becomes too weak for the reaction to occur (34). Experimental evidence did not support this relation, possibly due to the difference between the measured average strain and the predicted surface strain. No mention of measures to prevent oxidation of the surface was noted. If the particles were oxidized then adsorbate-induced strain could affect the reaction activity.

In summary, surface energy is a critical parameter used in predicting the stability of electrocatalysts, and it is possible that surface energy may be a function of curvature. There is no direct way to measure the surface energy of a solid, but surface stress can be measured. In studies of platinum it has been shown that smaller particles exhibit a lattice contraction from the bulk value (18, 19). When considering these particles in catalysis applications, the effect of adsorbates on surface stress must be considered. Adsorbates induce strain on the particle, thereby affecting the electronic properties. These properties differ between nanoparticles and the bulk. Thus, an understanding of adsorbates, strain, surface stress, and electronic bonding is needed to develop tools for catalyst screening. The situation becomes further complicated when lattice mismatch between alloys are introduced. In this chapter, the average lattice strain of platinum nanoparticles supported on carbon is measured as a function of curvature under hydrogen and oxygen containing environments using pair distribution function (PDF) analysis of high energy X-ray diffraction patterns. PDF analysis (35) has proven effective for determining the structure, average size and strain of nanoparticles with high accuracy (20, 36-38). We observe a significant particle size dependent compressive strain under air, with the platinum bonds shortening most for the smallest particles. A constant surface stress is unable to describe these data. Further analysis to quantify the extent of surface oxidation was completed using X-ray photoelectron spectroscopy. Under hydrogen, the particles show increased

expansion for larger particles, and a constant, negative surface stress is able to describe the data. Furthermore, a theoretical treatment for determining the surface energy of reduced metal particles is proposed.

7.1 Experimental

PDF experiments were performed at two separate times. The original experiment was performed in 2009 at Argonne National Lab with the metal particles exposed to air. The second experiment was conducted using a flow cell to control the sample environment at Brookhaven National Lab. In 2009, four carbon supported platinum catalyst samples of varying weight percentages were obtained from Tanaka Kikinzoku Group, Japan. Catalyst samples were loaded into Kapton capillaries, and the ends were sealed with epoxy. Rapid acquisition PDF data (39) were acquired at the Advanced Photon Source, beamline 11-ID-B configured with a Perkin Elmer image plate detector as shown schematically in Figure 7.1. Data were collected at 296 K for all samples using a flowing nitrogen cryocooler for temperature control. PDFgetX2 (40) was used to correct and normalize the diffraction data and Fourier transform the data to obtain the PDF using a $Q_{max} = 23$ Å^{-1}. Modeling was carried out using the PDF refinement program PDFgui (41) to extract a size-dependent bond strain with higher precision than just measuring the position of the nearest neighbor peak. An fcc bulk platinum structural model, modified to account for the finite size of the nanoparticles, was used to fit the experimental data. Structural parameters refined were lattice parameter and platinum isotropic atomic displacement factors. Experimental parameters $Q_{damp} = 0.037218$ and $Q_{broad} = 0.017329$ were determined from a crystalline nickel calibration standard and fixed in the nanoparticle refinements, and the lattice parameter was found to be within 0.05 % of the literature value. This procedure allowed the nanoparticle size parameter, spdiameter, to be separated from the instrument resolution effects and refined to yield the crystallite size

for the nanoparticles. Note that for well-ordered nanoparticles this also yields the nanoparticle size (20), but in the presence of certain kinds of disorder the range of structural coherence, or crystallite size, is less than the physical size of the nanoparticle (36). In this case it places a lower bound on the nanoparticle size. PDF fits were carried out over different ranges, but spdiameter was only refined when the fit was carried out over a wide r-range.

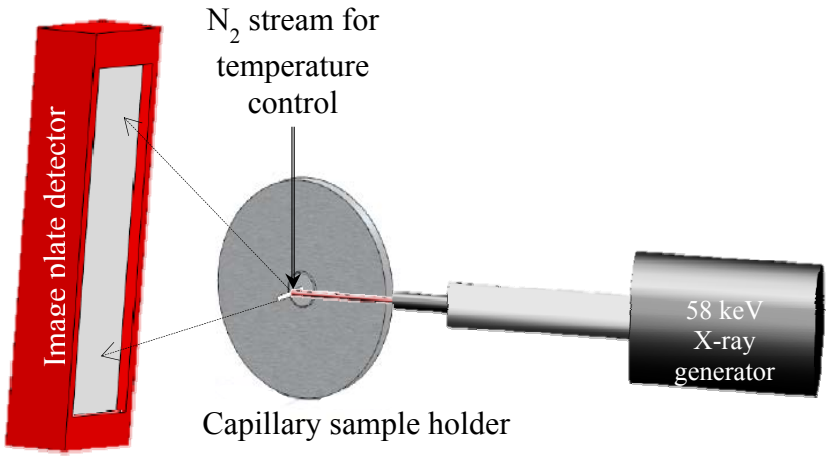

Figure 7.1 Experimental set up at beam line 11-ID-B, Argonne National Lab.

In 2012, the experiment was performed at the National Synchrotron Light Source, beamline X7B configured with a Perkin Elmer Area Detector on the original four catalyst samples, as well as four additional samples of varying platinum weight percentages and particle diameters. The flow cell is property of the beamline and pictured in Figure 7.2. The samples were prepared as previously described, except that glass wool was used to secure the powder inside the capillary instead of glue.

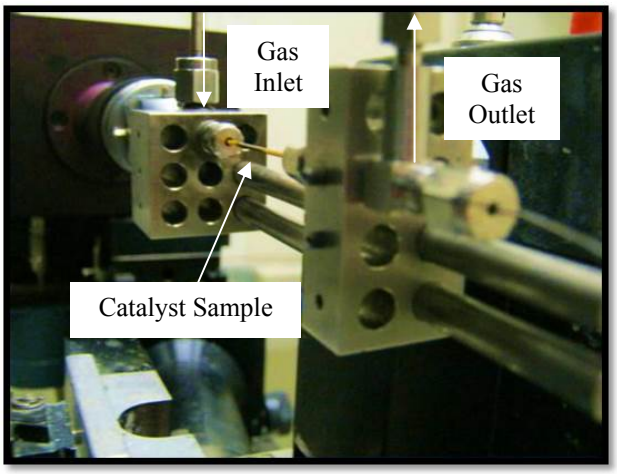

Figure 7.2 Sample holder at beamline X7B, Brookhaven National Lab.

All scans were performed at room temperature. First, the diffraction pattern of the catalyst with the native oxide was measured. No gas was flowing over the catalyst bed, and 3 to 5 PDF scans were taken. Then, 5 cubic centimeters per minute of 4 % hydrogen in balance nitrogen was introduced to the flow cell. After 5 minutes, 5 to 8 PDF scans were taken with 4 second exposures. The data were calibrated with a LaB_6 reference material where $Q_{damp} = 0.029383$ and $Q_{broad} = 0.000032508$. The experimental lattice parameter was found to be within 0.04% of the NIST value. The data were rapidly processed using python scripts, see Appendix E.

The samples were also analyzed using X-ray photoelectron spectroscopy to determine if surface coverage of the native oxide layer increased for smaller particles. The data were collected with a Thermo K-Alpha spectrometer with a monochromatized Al X-ray source. A Shirley background subtraction was applied to the data in XPSPeak 4.1 software. The photoemission spectra of Pt 4f were fit with three species, Pt(0), Pt(II), and Pt(IV), which is in agreement with previous literature studies (42-44). The doublet separation between $Pt_{7/2}$ and $Pt_{5/2}$ was constrained to be 3.4 eV, and the peak area ratio was constrained to be 4:3. The full-width at half-maximum values were constrained to be equal for each species, and the peaks were fit with a Gaussian profile.

7.2 Results and Discussion

Representative PDFs from 2009 are shown in Figure 7.3 for each sample, where the PDF, $G(r)$, is plotted versus atomic distance r. The PDFs for all samples exhibited comparable peak sharpness and a high signal to noise ratio, indicating high quality PDFs. Figure 7.3a shows that a standard fcc platinum model fits well to both bulk and nanoparticle samples, as can be observed by the green difference curves, implying that the bulk sample and nanoparticle sample are of similar structure. Smaller nanoparticles exhibit a higher residual function, Rw, an agreement factor for structure refinement, and more features in the difference curve, which means that the structural model does not fit as well. The largest contributions come from the carbon support. However, additional causes include disorder or static structural modifications in the smallest nanoparticles. Nonetheless, the fits are used primarily to extract the platinum nanoparticle lattice strain, which comes from the positions of the peaks. These peak positions are well matched by the fcc structural model in all samples, and the measured strains are accurate.

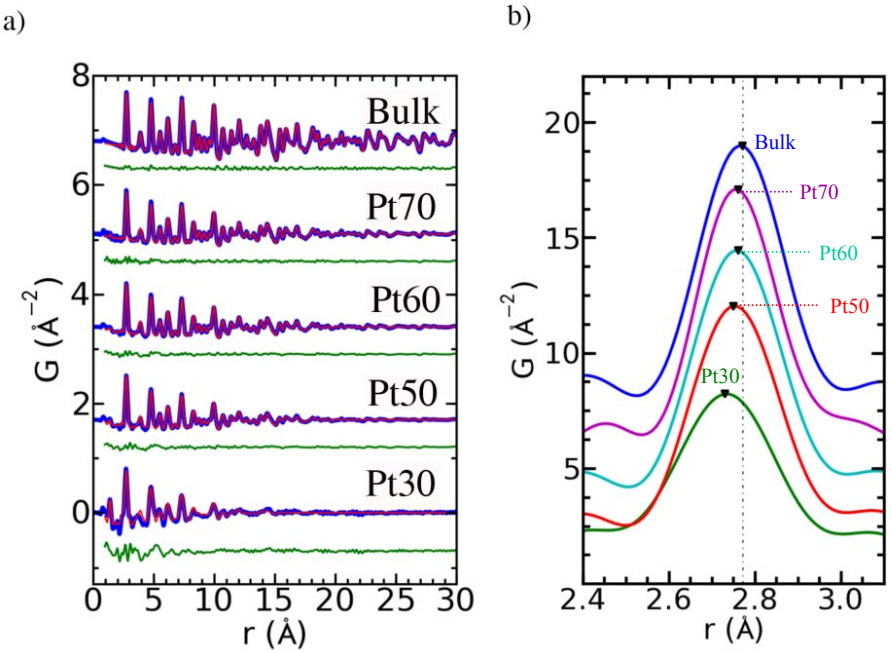

Figure 7.3 (a) Representative PDF scans of 2009 samples: (blue) experimental PDF, (red) fit PDF, and (green) difference. (b) Zoomed in image of the nearest-neighbor (first) peak.

As observed in Figure 7.3a, features in the bulk PDF extend over the whole plotted range. In the G(r) function, PDF peaks persist indefinitely in bulk crystalline materials, damped only by instrumental resolution effects (35). In nanoparticles there is an additional fall-off in the amplitude of features in the PDF due to their finite size. For spherical nanoparticles the attenuation is given by the auto-correlation of the shape function for the sphere (20), allowing us to make a determination of the crystallite size of the nanoparticle directly from the PDF data. As is evident in Figure 7.3a, the r-range of the PDF features diminishes as we go from Pt70 to Pt30. By fitting the characteristic function we obtain crystallite diameters of Pt70 = 3.56 nm, Pt60 = 2.99 nm, Pt50 =2.46 nm, and Pt30 = 1.82 nm for our supported platinum nanoparticles. These agree well with independent TEM characterizations of size, as shown in Figure 7.4, suggesting that these nanoparticles are well ordered and the crystallite size gives a good estimate of the average particle size.

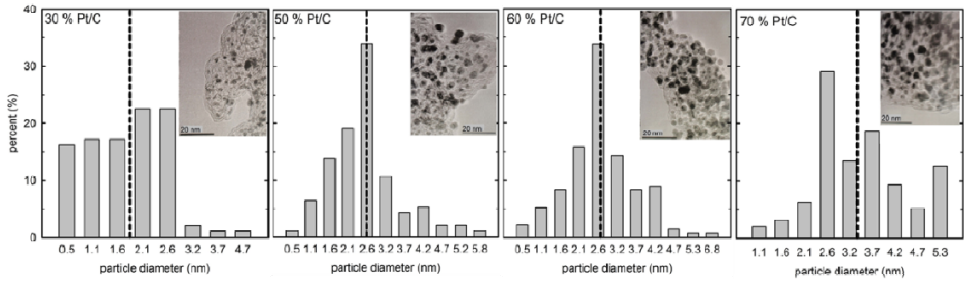

Figure 7.4 TEM results for catalyst samples measured in 2009 (45).

Figure 7.3b shows the first nearest neighbor peak for platinum is located around 2.77 Å. The peak shifts to the left as nanoparticle size decreases, indicating a compressive strain. This peak position can be determined directly from the data, or from fitting. Here, an fcc platinum model was fit to the first peak, refining only the lattice parameter to get an accurate determination of the peak position with varying particle sizes, $r_p\left(R\right)$. Similarly, in 2012, particle sizes and lattice parameters were obtained using the PDF technique. Particle size was refined over the entire r-range, and the lattice parameter was determined from fitting the nearest neighbor peaks. The particle diameter reported in Table 7.1 is the average of the diameter determined under hydrogen and oxygen for each sample in 2012. The three larger particle diameters determined from PDF fits in 2009 are within 5 % of the recalculated 2012 value; while the smallest particle is within 15 %.

Table 7.1 Summary of PDF fits, 2009 and 2012.

Sample *% Pt/C*	2012 Average diameter *(nm)*	2009 Oxidized lattice parameter *(nm)*	2012 Oxidized lattice parameter *(nm)*	2012 Hydrogen lattice parameter *(nm)*	Structural Model *(Fit range 0.22 to 0.33 nm)*
50 HT	4.34		0.39244	0.39313	Pt (fcc)
70	3.42	0.39113	0.39182	0.39303	Pt (fcc)
60	2.94	0.39078	0.39147	0.39295	Pt (fcc)
50	2.44	0.39003	0.39081	0.39373	Pt (fcc)
46	2.22		0.39154	0.39363	Pt (fcc)
05	2.04		0.38881	0.39395	Pt (fcc) + Graphite
30	1.95	0.38707	0.38802	0.39371	Pt (fcc)
10	1.77		0.39035	0.39428	Pt (fcc) + Graphite

The lattice parameter was determined by fitting the first peak with a single phase platinum fcc structure file. The samples with the lowest amount of platinum required a multiphase fit of platinum fcc and graphite hcp. The lattice parameters for each sample and adsorbate are listed in Table 7.1.

According to Equation (7.5), surface stress causes a lattice strain that is inversely proportional to particle radius. A plot of lattice parameter versus inverse particle radius (curvature) is shown in Figure 7.5 for the 2009, 2012, and literature (18, 19) data sets. The oxidized particles from 2009 and 2012, filled and unfilled circles, show offset from each other, which is attributed to the uncertainty in Q_{damp} and Q_{broad} and the two different instruments involved. Overall, the oxidized particles show a lattice contraction with decreasing particle size, which is the same trend observed for the metal particles in previous literature studies (18, 19). However, when reduced with hydrogen, the particles show lattice expansion with decreasing particle size.

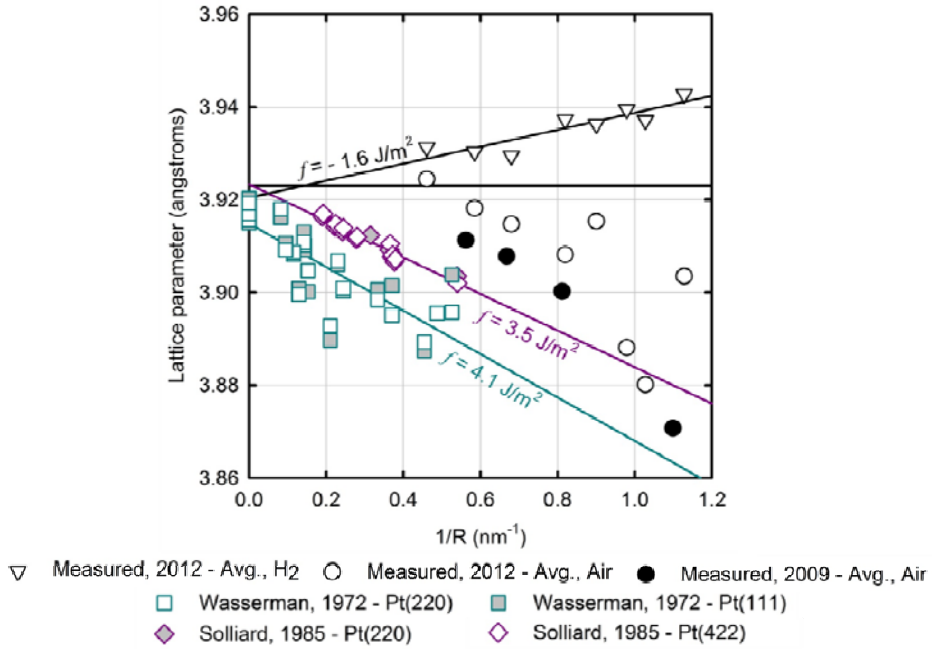

Figure 7.5 Comparison of experimental data with previous literature studies (18, 19). The thick solid line is the standard value of the platinum lattice parameter 3.9231Å. Surface stress values were calculated based on a compressibility of 4.35×10^{-12} m^3/J.

Neither air nor hydrogen environments represent a clean metal surface with no adsorbates. Thus, while surface stress can be estimated with hydrogen or oxygen adsorbates, the intrinsic surface stress of platinum cannot be separated from the stress caused by these adsorbates. The literature studies claim to measure this parameter, but the films were grown and analyzed in separate vacuum chambers, and the authors mention no precautions to prevent exposure to air while transferring samples (18, 19). Therefore, the presence of a native oxide layer can be assumed.

The adsorbate-induced surface stress can be studied by varying the extent of adsorption with time. In electrochemical systems the oxide layer on platinum grows logarithmically with time (46) and similar continuous growth behavior is expected for oxidation by air. The oxidized results presented in Table 7.1 and Figure 7.5 are for the native oxide that built up on the catalysts over years of lab storage. This oxide layer was reduced by the flow of hydrogen, and a new oxide layer formed once the samples were

returned to an air environment. Figure 7.6 shows the effect of oxidation time on the PDF nearest-neighbor peak for two samples that were analyzed at multiple times. The first sample, Pt30, was analyzed under air, reduced under hydrogen, then analyzed under air 12 hours later. The second sample, Pt46, was analyzed under air, reduced, analyzed under air after 21 hours, reduced, and analyzed a final time five minutes after exposure to air. For both samples, compressive strain increased with oxidation time, indicating that oxygen adsorbate-induced surface stress was positive (compressive). This observation provides further evidence that the previous literature studies involved an oxidized surface, as the derived surface stress values are more positive than expected for a metal surface. It is interesting that the models of Jiang et al. (23) and Qi and Wang (25) show good agreement with the experimental results of Wasserman and Vermaak (18) and Solliard and Flueli (19), though none of the models considered an oxide on the particle.

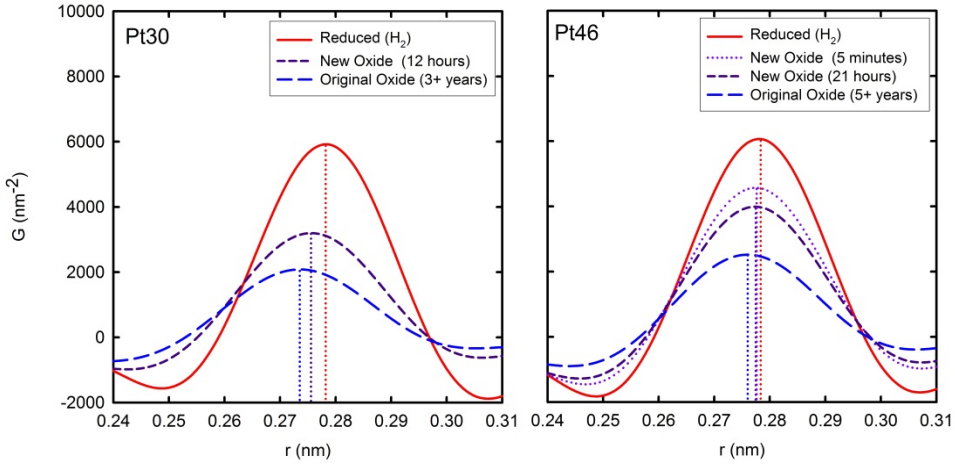

Figure 7.6 Shift in nearest-neighbor peak observed for varying air exposure times on 30 % Pt/C and 46 % Pt/C samples.

Figure 7.5 includes fits for each data set based on the elastic model of Equation (7.5) assuming a constant surface stress and compressibility. The fits of the literature data sets do not agree exactly with the authors' reported values, but neither author provides the value used for compressibility. Under hydrogen, a constant surface stress of -1.6 J/m^2 provides a good fit to the data with a y-intercept value of 3.92 Å, which is in agreement

with the bulk lattice parameter of platinum. It is challenging to fit the data collected under air with any trend. A linear fit of lattice strain versus curvature produces a y-intercept value much greater than the bulk lattice parameter. Yet, the exact dependence on curvature is difficult to determine due to uncertainty in the strain values of the smallest data points.

Previous literature studies are fit well with a constant surface stress, with a lower diameter limit of 3.3 nm. The non-linear trend in the present study could be due to increased oxide coverage on the smallest particles due to an abundance of undercoordinated edge sites. Chepulskii and Curtarolo used theoretical variational and ab initio calculations and predict a non-linear trend, where strain increased as particle size decreased with a greater than 1/R dependence (47). This effect was only observed below 1.6 nm, but provides an alternative explanation without adsorbate effects.

X-ray photoelectron spectroscopy was used to determine if differences in coverage of surface oxide could be responsible for the increased strain of small nanoparticles. The XPS data are plotted in Figure 7.7 and labeled with the corresponding sample name. The 5 % Pt/C sample was too noisy to fit. The experimental data were fit with three platinum species: Pt(0) (red curves), Pt(II) (light blue curves), and Pt(IV) (dark blue curves). The fraction of total peak area for each species is plotted at the bottom-right of Figure 7.7, where the smallest particles show that only 10 % of the particle is metallic platinum, while the other 90 % is cationic. Larger particles show an increase in metallic platinum to 30 %, though there is still a large amount of native oxide on the platinum surface. Sheng and coworkers show a similar trend where the metallic fraction increases with larger particles (42). However, the particles in that study show 60 to 90 % metallic character, despite covering a similar range of diameters as the present study (42). Real differences are seen in the XPS spectra between Sheng et al. and the current study, and the discrepancy cannot be attributed solely to the fitting procedure.

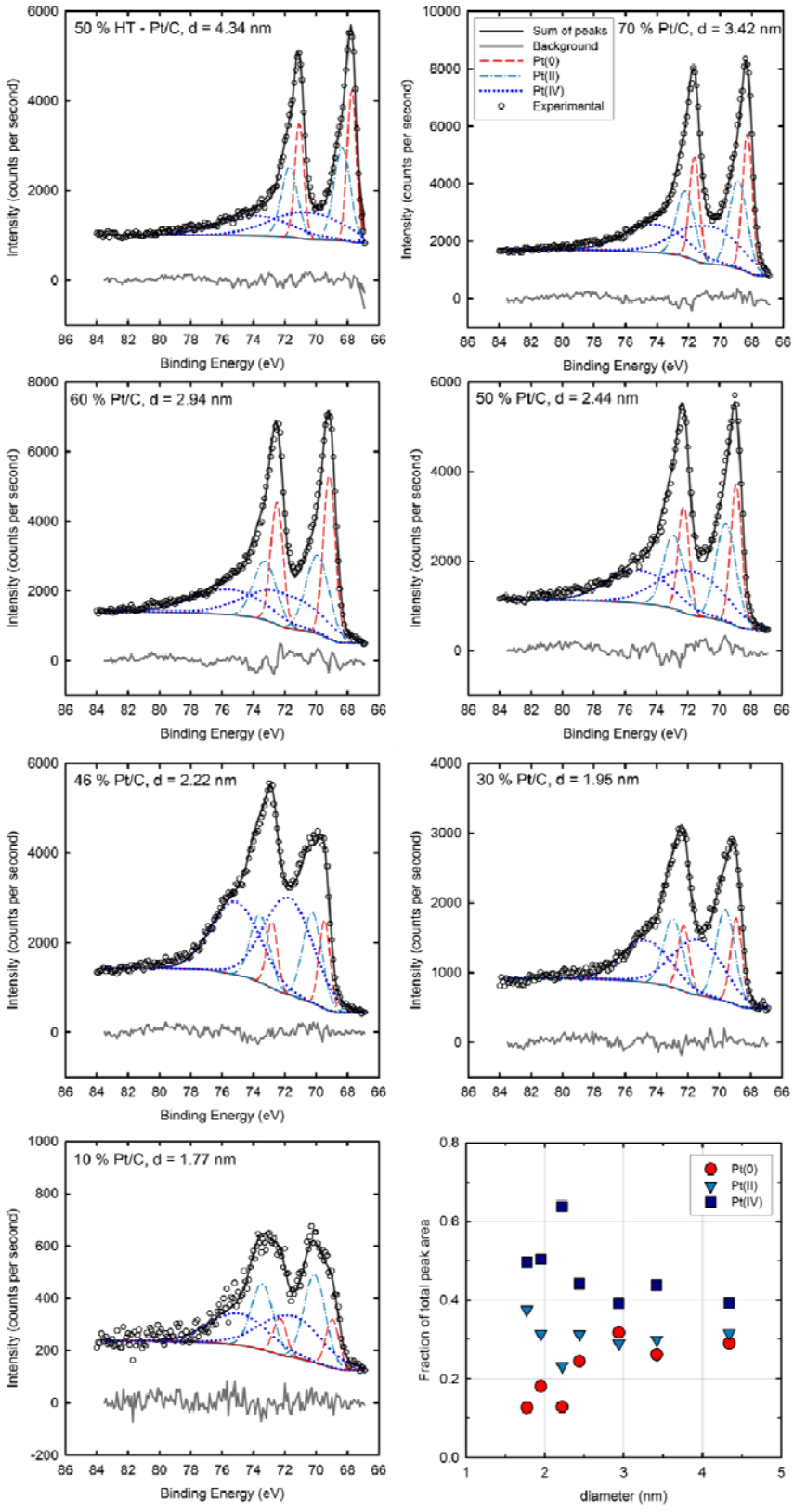

Figure 7.7 X-ray photoelectron spectra and observed trends.

XPS is considered a surface technique, because photoelectrons cannot travel far within the metal without losing energy. However, if the particle radius is smaller than the inelastic mean free path of electrons, XPS becomes a bulk technique. Various correlations estimate the inelastic mean free path in platinum to be 1.27 – 4.14 nm for an Al-Kα source. In searching for a particle size effect on native oxide coverage, the null hypothesis is that oxide coverage is independent of particle size. For a surface technique, this implies that the Pt(0), Pt(II), and Pt(IV) fractions should be constant with particle size. For a bulk technique, a 1/R dependence is implied to account for the surface to volume ratio. The small observed metallic signal is not consistent with the bulk platinum structure observed by PDF, which indicates that XPS is primarily sampling the surface. Assuming a surface technique, the increased fraction of oxide seen for small particles indicates increased coverage of oxides, and not just a surface to volume ratio effect. One possible explanation for the increased oxide compared to Sheng et al. (42) is the age of the catalysts. The catalysts involved in the present study were exposed to air for a minimum of 5 years, while the catalysts in Sheng et al. may have been newer and may have been reduced through high temperature annealing prior to XPS analysis.

As shown in Figure 7.6, the oxide layer adds a positive surface stress. XPS analysis indicated higher oxide coverage on smaller nanoparticles. Therefore, a possible explanation for the non-linearity observed in Figure 7.5 for oxidized particles is the adsorbate-induced strain. Figure 7.8 shows two possible fits of the lattice strain based on a constant surface stress and a surface stress proportional to 1/R. Constraining the fits to agree with the bulk lattice parameter of platinum yields a poor fit based on constant surface stress and an improved fit for the variable surface stress.

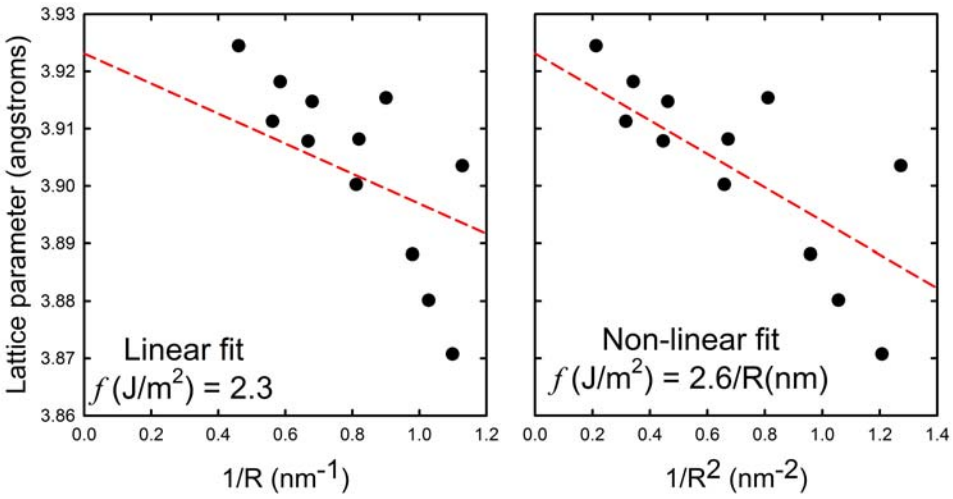

Figure 7.8 Comparison of 1/R and $1/R^2$ fits of lattice parameter for oxidized platinum nanoparticles.

7.3 Quantifying Surface Energy

Currently, the surface energy of metals is estimated using DFT or through other theoretical considerations. The original goal of this work was to measure the surface energy as a function of particle size through the relationship of surface energy, surface stress, and strain. All experiments included adsorbates on the platinum metal surface. Thus, no definitive conclusions can be stated about the effect of particle size on surface energy. However, if one was able to measure the intrinsic stress of platinum, an initial treatment of the data has been developed.

The following theoretical considerations were used to predict the surface energy of a reduced metal surface from lattice strain and curvature. The total energy of platinum nanoparticles was estimated using a potential function to model the interactions between atoms. Surface energy is the additional energy in the presence of a surface relative to the energy of the equivalent number of bulk atoms,

$$\gamma A_{np} = G_{np} - N_{np}\hat{G}_{bulk} \tag{7.6}$$

In Equation (7.6) the Gibbs energy of a nanoparticle of radius R containing N_{np} atoms is G_{np}, the Gibbs energy of the bulk containing the same number of atoms is $N_{np}\hat{G}_{bulk}$, and the surface area of the nanoparticle is A_{np}. At the nanoscale, it is still reasonable to define surface area by the number of active sites available on the surface.

A continuous model of a spherical particle of radius R was used to simplify the calculation of Gibbs energy by eliminating the effects of particle shape. In this approximation, discrete atoms were eliminated in favor of a volumetric integration of interatomic potential $\Phi(r)$ multiplied by the atomic density $\left(4/a^3\right)$ for an fcc lattice, where a is the lattice parameter. Spherical symmetry allowed the problem to be reduced to one dimension,

$$G_{np} = \frac{4}{a^3}\int_0^R \Phi(r)\cdot 4\pi r^2 dr. \tag{7.7}$$

The Sutton-Chen potential has been used to approximate fcc metal properties (16). For our calculation we used a modified Sutton-Chen potential to represent atomic interactions within a platinum particle,

$$\Phi(r) = e_{S-C}\left\{\sum_j\left[n_j X_j(r)\right]\cdot\frac{1}{2}\left(\frac{a}{u_j}\right)^n - s\sqrt{\rho(r)}\right\}, \tag{7.8}$$

where

$$\rho(r) = \sum_j\left[n_j X_j(r)\right]\cdot\left(\frac{a}{u_j}\right)^m \tag{7.9}$$

is the Sutton-Chen density at position r in the nanoparticle. The summation was over nearest neighbor shells instead of individual atoms, and the existence of a surface was considered. It should be noted that a model treating discrete atom positions yielded the same results. Every atom within a particle of radius R was located by a position vector **r** originating from the center, as shown in Figure 7.9. In turn, each atom has partially filled

j^{th} nearest neighbor shells located at a distance u_j from that atom. For each shell, the energy of interaction with one atom at distance u_j was multiplied by the number of atoms in shell *j* at position **r**. Values for the Sutton-Chen potential constants (s, $e_{s\text{-}c}$, m, n) for platinum can be found in the literature (48).

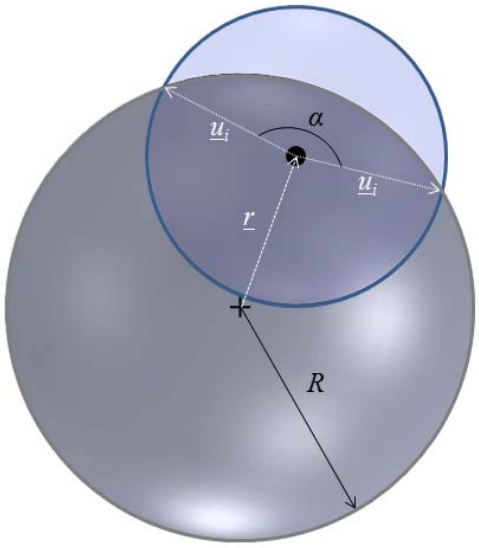

Figure 7.9 Illustration of model.

The total number of atoms in an fcc nearest neighbor shell *j* is denoted as n_j, and the fraction of the shell that lies within the boundaries of the particle is $X_j(r)$. For an atom within the particle of radius R, there is a spherical j^{th} nearest neighbor shell with radius u_j. The centers of these two spheres are separated by distance r, and it can be shown that the fraction of the surface of the sphere, defined by radius u_j, that lies inside the particle of radius R is

$$X_j(r) = \frac{1}{2} + \frac{R^2 - r^2 - u_j^2}{4ru_j}. \tag{7.10}$$

The energy of a bulk atom $\hat{G}_{bulk}$ was calculated by setting X_j to 1 for all shells to represent a full fcc crystal with no surfaces. Calculations were limited to the first 50

nearest neighbor shells. Results were identical to several decimal places even when considering only the first 12 nearest neighbor shells. This model does not account for surface relaxation or deviation from the ideal lattice positions. Calculations were carried out at absolute zero temperature and zero pressure such that Gibbs energy and internal energy are equivalent. Simulations were performed with MATLAB® version R2010b, by The MathWorks, Inc.

If lattice strain data could be collected on a reduced, adsorbate-free metal surface, testing the hypothesis that surface stress and surface energy have the same dependence on curvature could be conducted. If true, surface energy would be shown to increase with decreasing nanoparticle size, with significant ramifications for factors such as Ostwald ripening.

First, the observed size dependence of surface stress and its relationship to surface energy must be considered. Assuming there is curvature dependence to the surface energy as well as strain dependence, a Taylor expansion, truncating with linear terms, around the parameters 1/R and lattice strain yields the relationship,

$$\gamma = \gamma_0 + c_1\varepsilon + \frac{c_2}{R}. \tag{7.11}$$

Substituting Equation (7.11) into the surface stress-surface energy relationship, Equation (7.3), and rearranging yields

$$f = \left(\gamma_0 + \frac{c_1}{2}\right) + \frac{c_2}{R} \tag{7.12}$$

where strain is mathematically negligible (< 0.02). Equation (7.12) can be directly compared to measured strain data. First, a size dependent surface stress must be determined directly from the lattice strain data using the elastic model, Equation (7.5). Then Equation (7.12) can be used to fit the data, using a bulk value of surface energy. If the data follow a linear trend, then parameters c_1 and c_2 can be obtained. Accordingly,

these results would lead to the conclusion that surface stress and surface energy have the same linear dependence on curvature.

7.4 Conclusions

Lattice parameters were determined for platinum nanoparticle samples of varying size under air and hydrogen environments. Under air, a constant surface stress is unable to describe the full range of data, in contrast to previously literature studies on larger particles. Oxygen adsorption was shown to add a compressive surface stress, and XPS analysis suggested that the smallest particles had higher oxide coverage. Thus, the increased curvature dependence for nanoparticles less than 2.5 nm in diameter can be explained by a larger surface stress due to increased oxygen adsorption. In contrast, the lattice strain under hydrogen can be described by a constant, negative surface stress of -1.6 J/m^2. While the nanoparticle surfaces were reduced in a hydrogen environment, it is unclear how large an effect hydrogen adsorption has on the measured surface stress. Therefore, a high-temperature, vacuum system should be developed so that high energy X-ray diffraction and PDF analysis can applied to a reduced metal surface without adsorbates. Then, the effect of curvature, adsorbates, and the support on surface stress could be studied and decoupled. An initial theoretical consideration of how to determine surface energy from surface stress was presented in this chapter; however, measurements on a bare metal surface are needed to apply the theory.

7.5 References

1. M. Pourbaix, *Atlas of Electrochemical Equilibria in Aqueous Solutions*, National Association of Corrosion Engineers, Houston, TX (1974).

2. R. Borup, J. Meyers, B. Pivovar, Y. S. Kim, R. Mukundan, N. Garland, D. Myers, M. Wilson, F. Garzon, D. Wood, P. Zelenay, K. More, K. Stroh, T. Zawodzinski, J. Boncella, J. E. McGrath, M. Inaba, K. Miyatake, M. Hori, K. Ota, Z. Ogumi, S. Miyata, A. Nishikata, Z. Siroma, Y. Uchimoto, K. Yasuda, K. I. Kimijima and N. Iwashita, *Chem Rev*, **107**, 3904 (2007).

3. Y. Shao-Horn, W. C. Sheng, S. Chen, P. J. Ferreira, E. F. Holby and D. Morgan, *Top Catal*, **46**, 285 (2007).

4. P. N. Ross, in *Catalyst Deactivation*, E. E. Petersen and A. T. Bell Editors, p. 165 Marcel Dekker, Inc. , New York (1987).

5. J. Aragane, T. Murahashi and T. Odaka, *J Electrochem Soc*, **135**, 844 (1988).

6. C. T. Campbell, S. C. Parker and D. E. Starr, *Science*, **298**, 811 (2002).

7. R. M. Darling and J. P. Meyers, *J Electrochem Soc*, **150**, A1523 (2003).

8. R. M. Darling and J. P. Meyers, *J Electrochem Soc*, **152**, A242 (2005).

9. W. Bi and T. F. Fuller, *J Power Sources*, **178**, 188 (2008).

10. A. A. Franco and M. Tembely, *J Electrochem Soc*, **154**, B712 (2007).

11. E. F. Holby, W. C. Sheng, Y. Shao-Horn and D. Morgan, *Energy & Environmental Science*, **2**, 865 (2009).

12. S. G. Rinaldo, J. Stumper and M. Eikerling, *J Phys Chem C*, **114**, 5773 (2010).

13. M. C. Lafouresse, U. Bertocci and G. R. Stafford, *J Electrochem Soc*, **160**, H636 (2013).

14. R. C. Cammarata and K. Sieradzki, *Annu Rev Mater Sci*, **24**, 215 (1994).

15. J. S. Vermaak, C. W. Mays and Kuhlmann.D, *Surf Sci*, **12**, 128 (1968).

16. H. Akbarzadeh, H. Abroshan and G. A. Parsafar, *Solid State Commun*, **150**, 254 (2010).

17. R. C. Cammarata, *Prog Surf Sci*, **46**, 1 (1994).

18. H. J. Wasserman and J. S. Vermaak, *Surf Sci*, **32**, 168 (1972).

19. C. Solliard and M. Flueli, *Surf Sci*, **156**, 487 (1985).

20. A. S. Masadeh, E. S. Bozin, C. L. Farrow, G. Paglia, P. Juhas, S. J. L. Billinge, A. Karkamkar and M. G. Kanatzidis, *Phys Rev B*, **76**, 115413 (2007).

21. C. W. Mays, J. S. Vermaak and Kuhlmann.D, *Surf Sci*, **12**, 134 (1968).

22. Technical data for the element Platinum in the Periodic Table, in (2010).

23. Q. Jiang, L. H. Liang and D. S. Zhao, *J Phys Chem B*, **105**, 6275 (2001).

24. Z. X. Huang, P. Thomson and S. L. Di, *J Phys Chem Solids*, **68**, 530 (2007).

25. W. H. Qi and M. P. Wang, *J Nanopart Res*, **7**, 51 (2005).

26. S. N. Khanna, J. P. Bucher, J. Buttet and F. Cyrotlackmann, *Surf Sci*, **127**, 165 (1983).

27. H. J. Wasserman and J. S. Vermaak, *Surf Sci*, **22**, 164 (1970).

28. G. Apai, J. F. Hamilton, J. Stohr and A. Thompson, *Phys Rev Lett*, **43**, 165 (1979).

29. J. Woltersdorf, A. S. Nepijko and E. Pippel, *Surf Sci*, **106**, 64 (1981).

30. R. C. Tolman, *J Chem Phys*, **17**, 333 (1949).

31. R. Lamber, S. Wetjen and N. I. Jaeger, *Phys Rev B*, **51**, 10968 (1995).

32. Y. Lei, J. Jelic, L. C. Nitsche, R. Meyer and J. Miller, *Top Catal*, **54**, 334 (2011).

33. M. Cabie, S. Giorgio, C. R. Henry, M. R. Axet, K. Philippot and B. Chaudret, *J Phys Chem C*, **114**, 2160 (2010).

34. P. Strasser, S. Koh, T. Anniyev, J. Greeley, K. More, C. F. Yu, Z. C. Liu, S. Kaya, D. Nordlund, H. Ogasawara, M. F. Toney and A. Nilsson, *Nat Chem*, **2**, 454 (2010).

35. T. Egami and S. J. L. Billinge, *Underneath the Bragg peaks: Structural analysis of complex materials*, Pergamon Press Elsevier, Oxford England (2003).

36. B. Gilbert, F. Huang, H. Z. Zhang, G. A. Waychunas and J. F. Banfield, *Science*, **305**, 651 (2004).

37. C. Kumpf, R. B. Neder, F. Niederdraenk, P. Luczak, A. Stahl, M. Scheuermann, S. Joshi, S. K. Kulkarni, C. Barglik-Chory, C. Heske and E. Umbach, *J Chem Phys*, **123** (2005).

38. K. Page, T. Proffen, H. Terrones, M. Terrones, L. Lee, Y. Yang, S. Stemmer, R. Seshadri and A. K. Cheetham, *Chem Phys Lett*, **393**, 385 (2004).

39. P. J. Chupas, X. Y. Qiu, J. C. Hanson, P. L. Lee, C. P. Grey and S. J. L. Billinge, *J Appl Crystallogr*, **36**, 1342 (2003).

40. X. Qiu, J. W. Thompson and S. J. L. Billinge, *J Appl Crystallogr*, **37**, 678 (2004).

41. C. L. Farrow, P. Juhas, J. W. Liu, D. Bryndin, E. S. Bozin, J. Bloch, T. Proffen and S. J. L. Billinge, *J Phys-Condens Mat*, **19**, 335219 (2007).

42. W. C. Sheng, S. Chen, E. Vescovo and Y. Shao-Horn, *J Electrochem Soc*, **159**, B96 (2012).

43. Z. L. Liu, L. M. Gan, L. Hong, W. X. Chen and J. Y. Lee, *J Power Sources*, **139**, 73 (2005).

44. M. H. Lin, H. L. Huang, Y. J. Liu, C. J. Liang, S. D. Fei, X. F. Chen and C. L. Ni, *Nanotechnology*, **24** (2013).

45. C. Y. Shi, E. L. Redmond, A. Mazaheripour, P. Juhas, T. F. Fuller and S. J. L. Billinge, *J Phys Chem C*, **117**, 7226 (2013).

46. M. Alsabet, M. Grden and G. Jerkiewicz, *J Electroanal Chem*, **589**, 120 (2006).

47. R. V. Chepulskii and S. Curtarolo, *Acs Nano*, **5**, 247 (2011).

48. Y. H. Chui and K. Y. Chan, *Phys Chem Chem Phys*, **5**, 2869 (2003).

CHAPTER 8

RECOMMENDATIONS

This dissertation represents a significant advance in understanding the physical processes that are involved in platinum durability losses at the cathode in PEM fuel cells. Future work is needed in this field to improve the lifetime of fuel cells for automotive applications, which will result in reduced costs and push fuel-cell vehicles closer to the market.

Chapter 5 presented the application of the pair distribution function analysis to in operando fuel cell X-ray diffraction data to monitor particle size with time. The technique can be improved to decouple the various electrochemically active area loss mechanisms present at the cathode under varying potential cycles. This tool is extremely useful for testing the durability of new catalysts.

In operando X-ray absorption spectroscopy (XAS) was applied to fuel cells in order to observe the molecular processes occurring with increasing potentials and hold times. Results of this technique are especially useful for informing the mechanism of oxide formation and growth on platinum. The study presented in Chapter 6 outlined a way to directly relate the extended X-ray absorption fine structure spectra to a surface coverage for comparison with electrochemical data. This novel treatment of the data monitors the formation of PtO_2, which formed at a much faster rate than the electrochemically detected total oxide. The difference in rates implied that PtO_2 is formed at the expense of a chemisorbed oxide. The original experiment was not detailed enough to speculate on the nature of the chemisorbed oxide species. Rapid acquisition XAS is recommended so that a better understanding of the initial, time sensitive processes of oxide growth can be determined. Additionally, the cell hardware design needs to be improved to limit water condensation within the cell under realistic operating conditions, which proved to be a barrier in collecting clean and definite scans. An initial idea is to

incorporate moisture wicking strips into the flow field design to prevent the water droplet from falling into the path of the beam. Better insulation techniques at the cathode window would also minimize condensation. Additionally, more oxide types could be detected/monitored if stable PtOH and PtO references could be synthesized.

The proposed oxide growth mechanism was used in a kinetic model to describe platinum oxidation and reduction by simulating CVs and surface coverage in Chapter 6. A new parameter was introduced to the Butler-Volmer type kinetic rate equations that allowed the peak width to be decoupled from the Tafel slope. The extent of adsorption changes the energy of the products, which in turn changes the heat of reaction. The χ-parameter allocated the change to the forward of reverse activation energies. However, the χ-parameter does not address the coupling of peak width and the upper potential limit. Introducing the concept of a heterogeneous oxide layer allowed for the correct current-potential simulation of oxide growth on platinum. The model can be further improved to address the shifting of the edge site reduction peak with scan rate. Experimental CVs suggest that an irreversible change in the platinum surface occurs at 0.8 V, and this process could be included in a future model.

Chapter 7 outlines some of the issues to be considered when measuring the lattice strain of very small nanoparticles, particularly those particles less than 2.5 nm in diameter. A treatment for relating lattice strain to surface energy was presented, but data from a clean metal surface are needed to test the hypothesis. Thus, a system needs to be designed to allow for high energy X-ray data collection at high-temperatures and under a vacuum to drive off any adsorbates. A wider range of sample sizes should also be considered, including some in the subnanometer range. Small platinum samples could be synthesized in lab using electrodeposition and galvanic replacement reactions (1). These studies are relevant for developing models to screen catalysts for many applications as adsorbates, curvature, and the catalyst support can all affect the electronic properties of materials.

8.1 References

1. R. E. Rettew, J. W. Guthrie and F. M. Alamgir, *J Electrochem Soc*, **156**, D513 (2009).

APPENDIX A

ELECTROCHEMICAL DATA OF SAMPLES

This appendix reports fabrication methods and performance characterization data for MEAs (both in-house and commercial) used in the experiments presented in this dissertation. Table A.1 reports the source of each MEA and what studies it was used for. Detailed formulations and characterization data follow.

Table A.1 Comprehensive list of samples and fabrication methods.

Date	Membrane Type	Anode				Cathode				Electrode Area (cm^2)	Experiments
		Fabrication Method	Catalyst Type	Ink Preparation	Loading (mg_{Pt}/cm^2)	Fabrication Method	Catalyst Type	Ink Preparation	Loading (mg_{Pt}/cm^2)		
04.09.2011	N117	DM	46.1 % Pt/C	Colloid	0.080	DM	47.7 % Pt/C	Colloid	1.30	4.8	CT.2, ANL 2011 - Cycling
04.09.2011	N117	DM	46.1 % Pt/C	Colloid	0.165	DM	51 % PtCo/C	Colloid	1.39	4.8	CN51.1, ANL 2011 - Cycling
04.09.2011	N117	DM	46.1 % Pt/C	Colloid	0.145	DM	50 % - HT Pt/C	Colloid	1.035	4.8	CN50.1, ANL 2011 - Cycling
04.09.2011	N117	DM	46.1 % Pt/C	Colloid	0.090	DM	30 % PtCo/C	Colloid	1.21	4.8	CN30.2, ANL 2011 - Cycling
04.09.2011	N117	DM	46.1 % Pt/C	Colloid	0.090	DM	47.7 % Pt/C	Colloid	0.99	4.8	CT.1, TF 2011 - Re-Cycling (July)
04.09.2011	N117	DM	46.1 % Pt/C	Colloid	0.150	DM	51 % PtCo/C	Colloid	1.76	4.8	CN51.2, TF 2011 - Re-Cycling (July)
04.09.2011	N117	DM	46.1 % Pt/C	Colloid	0.125	DM	50 % - HT Pt/C	Colloid	1.30	4.8	CN50.2, TF 2011 - Re-Cycling (July)
04.09.2011	N117	DM	46.1 % Pt/C	Colloid	0.090	DM	30 % PtCo/C	Colloid	1.07	4.8	CN30.1, TF 2011 - Re-Cycling (July)
04.09.2011	N117	DM	46.1 % Pt/C	Colloid	0.170	DM	47.7 % Pt/C	Colloid	1.21	4.8	CT.3
04.09.2011	N117	DM	46.1 % Pt/C	Colloid	0.225	DM	50 % - HT Pt/C	Colloid	1.49	4.8	CN50.3
10.17.2011	N117	DSS	46.1 % Pt/C	IPA/H2O	0.270	DSS	30 % Pt/C	IPA/H2O	0.63	4.8	C30, BNL October 2011 - Oxide Growth
10.17.2011	N117	DSS	46.1 % Pt/C	IPA/H2O	0.300	DSS	47.7 % Pt/C	IPA/H2O	0.76	4.8	C50, BNL October 2011 - Oxide Growth
10.17.2011	N117	DSS	46.1 % Pt/C	IPA/H2O	0.240	DSS	67.1 % Pt/C	IPA/H2O	1.72	4.8	C70, BNL October 2011 - Oxide Growth
03.04.2012	N117	DSS	30 % Pd/C	IPA/H2O	0.190	DSS	46.1 % Pt/C	IPA/H2O	0.35	4.8	MEA6_9
03.09.2012	N117	DSS	30 % Pd/C	IPA/H2O	0.200	DSS	30 % Pt/C	IPA/H2O	0.37	4.8	MEA 11-12, TF May & July 2012 - Oxide Growth
03.09.2012	N117	DSS	30 % Pd/C	IPA/H2O	0.180	DSS	30 % Pt/C	IPA/H2O	0.33	4.8	MEA 15-14, BNL March 2012 - Oxide Growth
08.14.2012	N117	Commercial	Pt/C	NA	0.300	Commercial	Pt/C	NA	0.30	25.0	CMEA_117_A03_C03-20120814, Oxide Growth
09.10.2012	N212	Commercial	Pt/C	NA	0.300	Commercial	Pt/C	NA	0.30	25.0	CMEA-N212 (I), Oxide Growth
09.10.2013	N212	Commercial	Pt/C	NA	1.300	Commercial	Pt/C	NA	0.30	25.0	CMEA-N212 (II), Cycling - diff T

Legend: DM – Decal Method; DSS: Direct Spray Stencil

A.1 MEAs for monitoring particle growth

The following samples were made in-house for use in accelerated degradation experiments to study the effects of particle size with time. Cathodes varied by platinum percentage and alloy type, and all anodes were made with 46.1 % Pt/C. The general procedure consisted of fabricating the catalyst ink, details are reported in Table A.2, and sonicating for 30 minutes before directly spray coating onto a PTFE sheet using an airbrush. A stencil was used to limit the electrode area to 4.8 cm^2. After the anode and cathode decals were made, a pretreated Nafion 117 membrane was sandwiched between them and centered using small pin holes in the PTFE decals and flattened wire as anchors. The assembly was then placed between two thick rubber pieces before placing in the hot press at 155 °C. Pressure of 1807 kPa (2600 lbs total per 9.92 in^2 of hot plate area) was applied for 8 minutes. The assembly was then removed from the hot press and cooled before disassembling. Each decal was weighed before and after hot pressing and the percent of weight transferred was calculated, which is reported in Table A.3. The electrode loading was calculated from the weight transferred off the decal. Consecutive listings of the cathode and anode are the electrodes for an MEA sample.

Table A.2 Real ink ratios for electrode fabrication.

Sample name *Sample type*	Catalyst powder *g*	5 wt % PFSA solution *g*	n-butyl acetate *g*	Ratio *PFSA:n-butyl acetate:C*
CT.x ***47. 7 % Pt/C***	0.2032	1.7028	5.1070	0.80:48:1
CN50.x ***50 % HT Pt/C***	0.1939	1.5505	4.6518	0.80:48:1
CN30.x ***27.3 % Pt – 1.7 % Co /C***	0.1616	1.8605	5.4285	0.81:47:1
CN51.x ***48.7 % Pt – 2.8 % Co/C***	0.1901	1.5112	4.4805	0.82:49:1
Anodes ***46.1 % Pt/C***	0.1049	0.9252	2.7346	0.82:48:1

Table A.3 Summary of the decal transference and electrode loading calculations.

Sample	Decal loading *g*	Percent of catalyst layer transferred *%*	MEA loading mg_{Pt}/cm^2_{geo}
CT.1	0.0181	74	0.99
A.5	0.0019	74	0.09
CT.2	0.0187	98	1.3
A.1	0.0015	80	0.08
CT.3	0.0178	98	1.21
A.11	0.0031	84	0.17
CN50.1	0.0152	92	1.04
A.2	0.0022	100	0.15
CN50.2	0.0182	97	1.3
A.7	0.002	95	0.13
CN50.3	0.0202	100	1.49
A.4	0.0034	100	0.23
CN30.1	0.0318	94	1.07
A.9	0.0018	78	0.09
CN30.2	0.0344	98	1.21
A.10	0.0015	93	0.09
CN51.1	0.0196	99	1.4
A.12	0.0025	100	0.17
CN51.2	0.0247	100	1.8
A.08	0.0029	79	0.15

The MEAs are referred to by the cathode naming scheme. Samples CT.2, CN50.1, CN30.2, and CN51.1 were used for the accelerated cycling experiments at Argonne National Lab, beamline 11-ID-B. It was from these samples that particle size versus cycle number is reported in Chapter 5. To test the repeatability of the results obtained at the beamline, the remaining samples were used for identical accelerated cycling experiments in the laboratory at Georgia Tech (they were not exposed to X-rays).

Prior to cycling experiments, the cells were characterized in the custom made hardware, presented in Chapter 4 and Appendix B. The wet-up procedure recommended by Dupont and described in detail in Chapter 4 was used. After wet-up, a polarization curve was measured whereby the voltage was scanned from 0.1 V to 1.0 V at a rate of 0.1

V/point and collected at 10 min/point. The temperature was held at 80 °C and 100 % relative humidity. Hydrogen was delivered to the anode at 0.5 L/min and air was delivered to the cathode at 1 L/min. The performance curves for all samples are shown in Figure A.1.

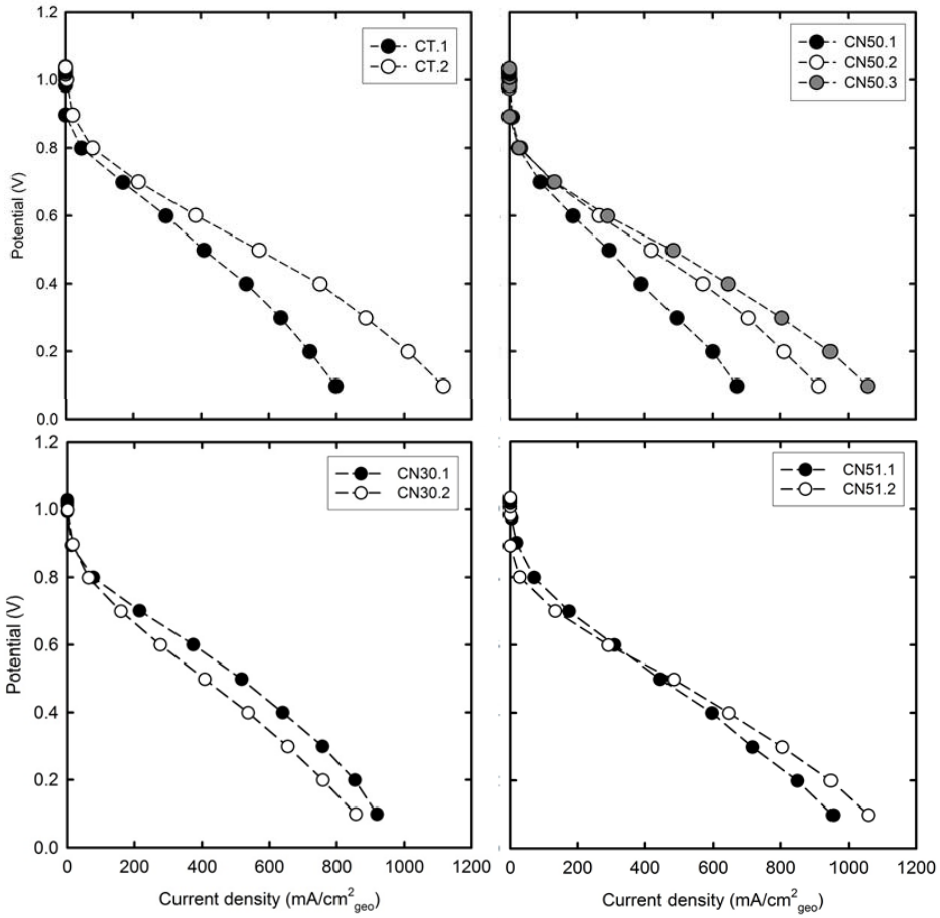

Figure A.1 Polarization curves of all samples. All cells suffer from extreme ohmic losses.

Overall, samples of the same type have similar performance behavior. The contact hardware resistance contributed to the extreme ohmic losses observed in the performance curves. The contact hardware resistance was measured at intermediate points and determined to be 18 mΩ, 47 mΩ, 55 mΩ, and 30 mΩ when testing samples CT.2, CN50.1, CN30.2, and CN51.1, respectively. The resistance can be reduced by sanding

the stainless steel plates before use, but the resistance builds over time due to the growing oxide layer.

Initial CVs were collected for samples prior to X-ray exposure at 50 mV/s, 80 °C, and 100 % relative humidity under hydrogen and nitrogen. A final CV was collected for sample CN30.2. The CVs are presented in Figure A.2. Advice for taking better CVs is given in Chapter 4.

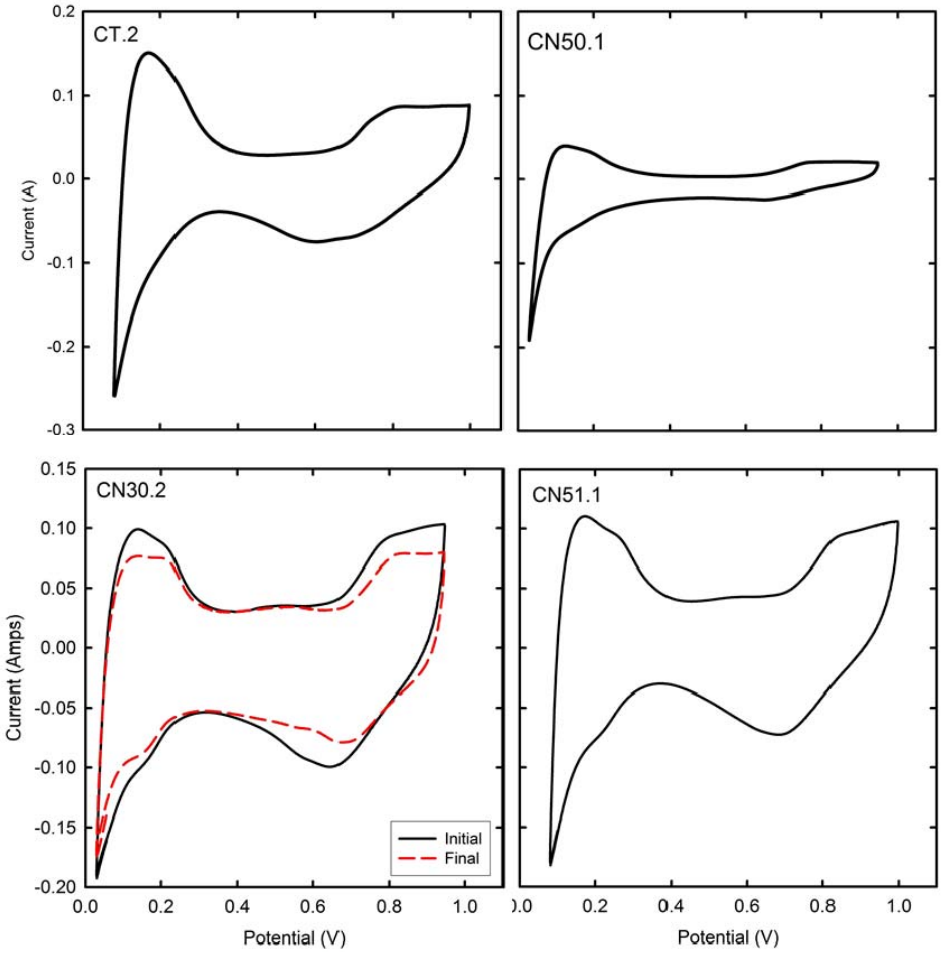

Figure A.2 Initial CVs for ANL cycled samples taken at 50 mV/s and 80 °C.

The initial impedance was measured for samples CN50.1 and CN30.2, and the spectra are shown in Figure A.3. Impedance was measured at 80 °C, 100 % relative humidity under 1 L/min hydrogen and 2 L/min air. The input current was -0.5 A, and the input sine wave had an amplitude of 0.025 A. Frequency was scanned from 1000 Hz to

0.05 Hz, and 50 data points were collected. The heat treated 50 % Pt/C sample (CN50.1) showed extreme resistances compared to the CN30.2 sample.

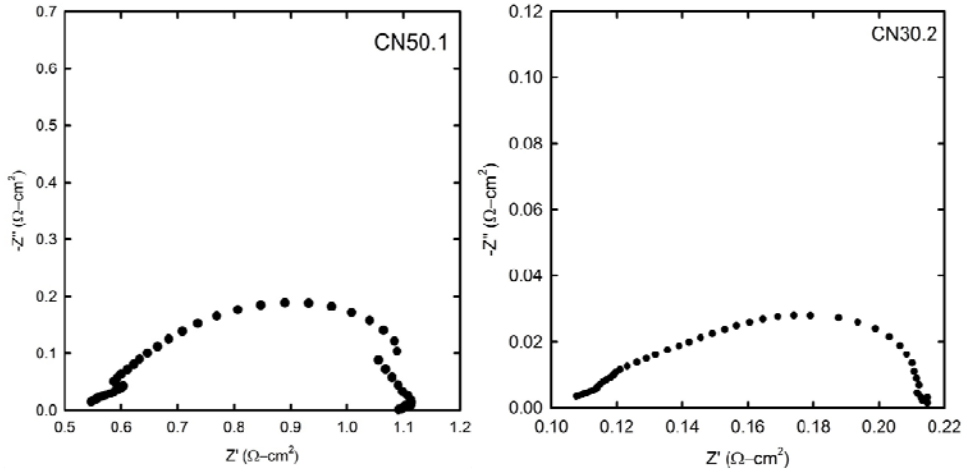

Figure A.3 Electrochemical impedance spectra for samples CN50.1(left) and CN30.2 (right).

After wet-up and initial characterization, the MEAs were held at 80 °C and cycled 3000 times from 0.6 to 1.2 V at 100 mV/s. The ECA loss was measured every 100 cycles, and the data is presented in Figure A.4. At Argonne National Lab, a Fuel Cell Technologies University Test Stand was used to deliver the reactants and control the temperature. The anode humidifier drained and filled abruptly causing the temperature to drop and introducing air into the system. This effect was reflected in the ECA data, Figure A.4, as a disturbance in the measured potential/current. To minimize this disturbance the humidifier was disconnected from the automatic refill switch and was manually refilled before each experiment. However, the cells were still subject to dryout with time, which limited the accuracy and precision of the measured ECA. Our ECA data for cycling at Georgia Tech are more accurate and precise and also displayed in Figure A.4. Intermediate ECA and accelerated cycling data are shown in Figure A.5. Table A.4lists the initial and final ECA for all samples and includes particle size information from XRD, TEM, and PDF studies before and after cycling.

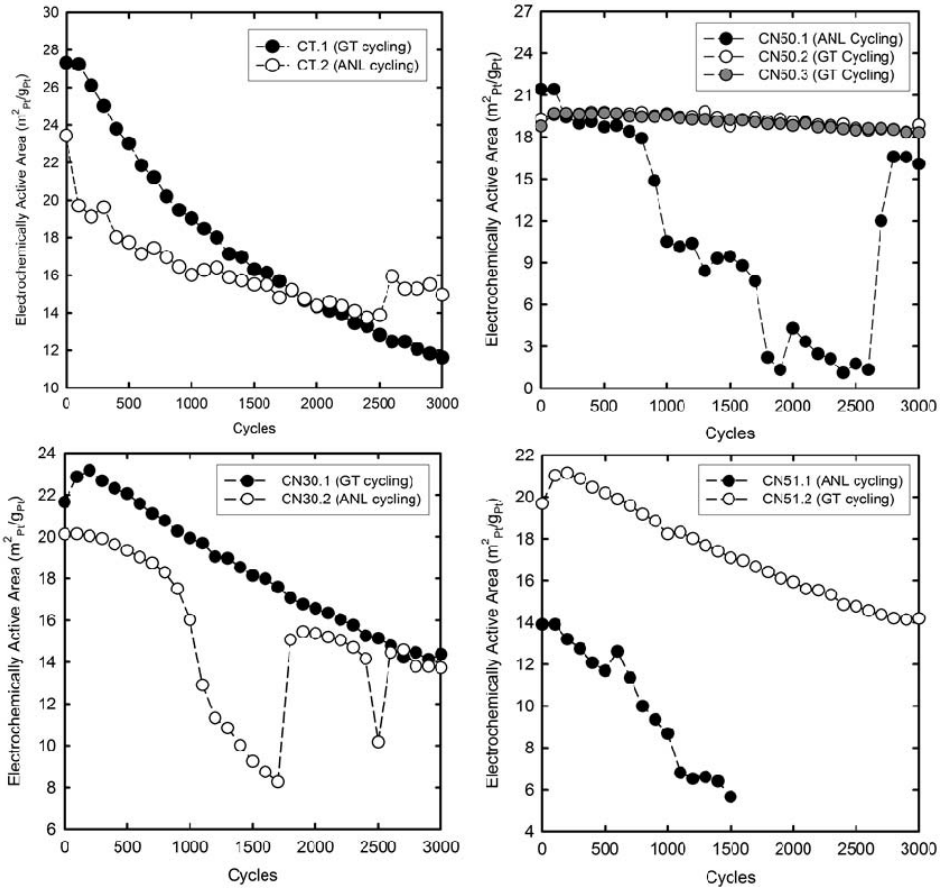

Figure A.4 ECA loss with time for all MEAs. The cells cycled at Argonne were subject to dryout due to fuel cell test stand malfunctions.

Table A.4 Summary of ECA and particle size before and after cycling for all samples..

Sample	Initial ECA (m^2_{Pt}/g_{Pt})	Final ECA (m^2_{Pt}/g_{Pt})	Initial diameter (nm)				Final diameter (nm)			
			XRD	TEM vol	TEM num	PDF	XRD	TEM vol	TEM num	PDF
CT.1	27.3	11.6	2.3	2.8	2.3	×	5.1	—	—	×
CT.2	28.0	15.0				3.2	NA	7.1	5.4	5.8
CT.3	*Never used*									
CN50.1	21.4	16.1	4.5	6.6	5.4	4.4	4.9	6.3	5.3	5.7
CN50.2	19.3	18.9				×	NA	—	—	×
CN50.3	18.8	18.3				×	NA	—	—	×
CN30.1	21.7	14.4	3.7	4.7	3.7	×	4.5	—	—	×
CN30.2	20.1	13.7				2.4	NA	5.8	4.5	3.9
CN51.1	13.9	5.6	4.1	5.9	4.4	3.8	4.6	7.8	6.1	4.0
CN51.2	19.7	14.2				×	NA	—	—	×

— Have TEM images, but not counted × Not exposed to X-rays

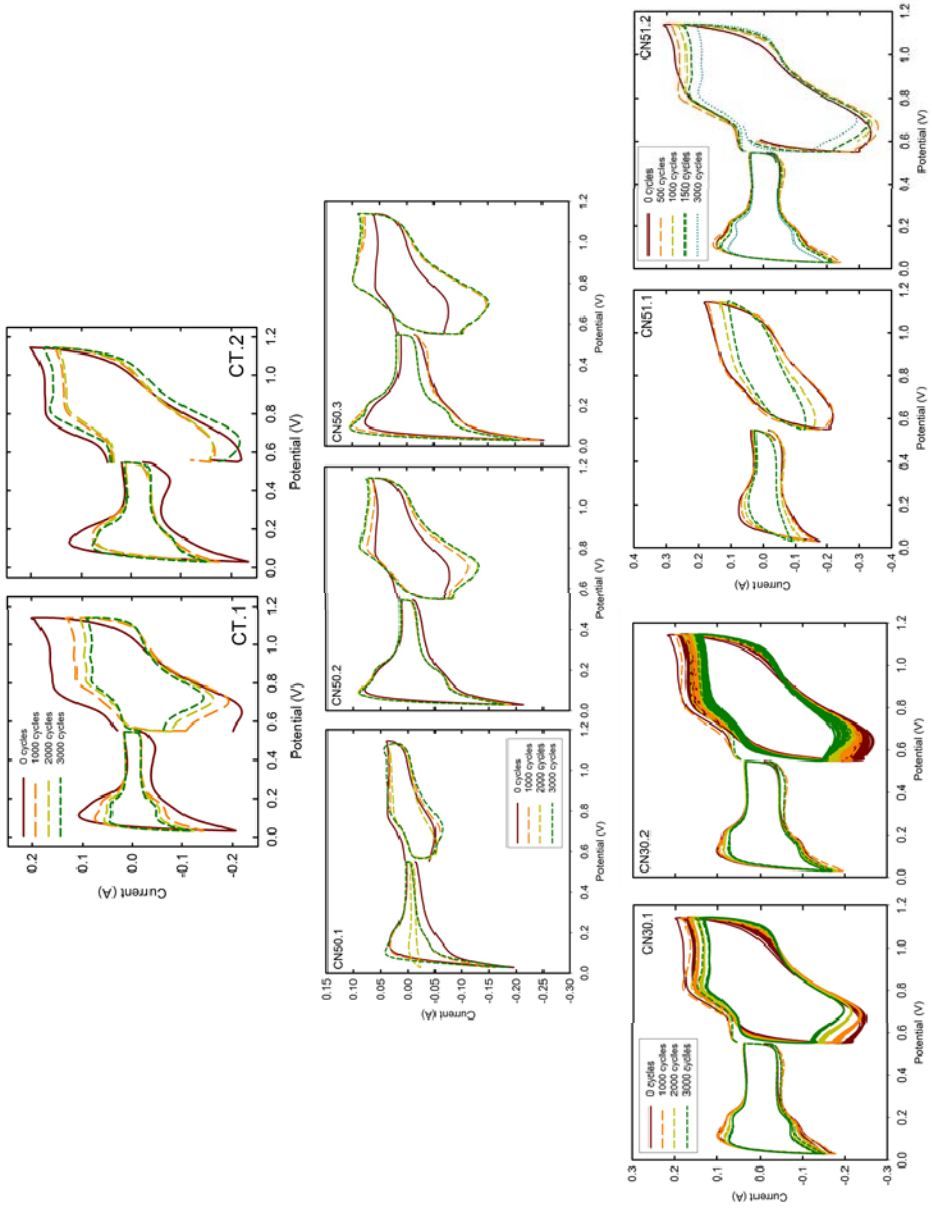

Figure A.5 Intermediate ECA and cycling data for all samples.

A.2 MEAs for monitoring oxide growth

The following MEAs were used in studying oxide growth on platinum at the cathode in PEM fuel cells. The in-house MEAs were fabricated by direct spray coating onto the membrane using a PTFE template wrapped in aluminum (discussed in Chapter 4). Samples C30, C50, and C70 were made using the respective catalyst powders of 30 % Pt/C, 46.1% Pt/C, and 70 % Pt/C. MEA 11 – 12 and MEA 14 – 15 were made with 30 % Pt/C, and MEA 6 – 9 was made with 46.1 % Pt/C. The goal ink ratio was 0.75:20:1 of PFSA:IPA:C for all samples. The actual ink formulations are listed in Table A.5. All samples were wet-up under 100 % hydrogen, and the performance curves are shown in Figure A.6.

Table A.5 Ink formulations of in-house MEAs made for oxide growth studies.

Sample name *Sample type*	Catalyst powder *g*	5 wt % PFSA solution *g*	IPA *g*	Ratio *PFSA:IPA:C*
C30	0.707	6.317	15.759	0.64:38:1
C50	1.060	8.353	6.932	0.79:21:1
C70	1.507	7.444	6.575	0.82:23:1
MEA 11 – 12	0.288	3.3310	2.5028	0.83:21:1
MEA 14 – 15	0.2892	3.3634	2.4936	0.83:21:1
MEA 6 – 9	0.1748	0.1490	1.1898	0.08:14:1

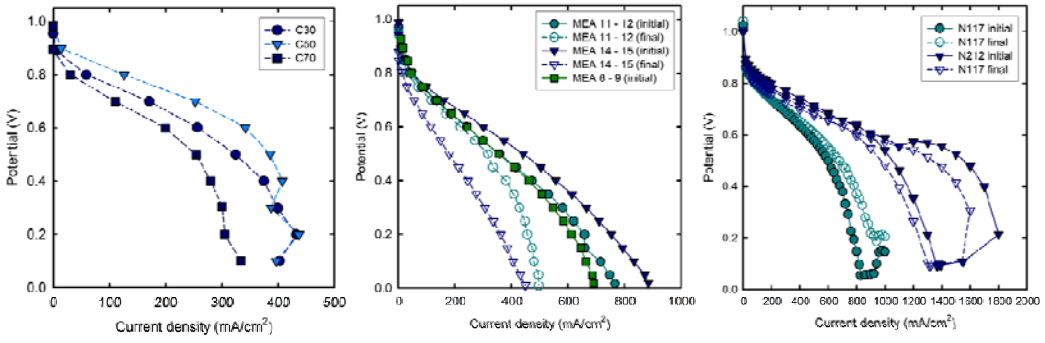

Figure A.6 Performance curves for all samples measured at 80 °C.

In some cases, final performance curves were measured after potential hold experiments, and those are also shown in Figure A.6. The in-house MEAs suffer from severe ohmic losses, similar to the samples presented in Section A.1. Commercial cell N212 (thinnest membrane) performs the best. Samples C30, C50, C70, and MEA 14 – 15 were exposed to synchrotron X-rays. Initial and final (if measured) CVs are presented in Figure A.7. C30, C50, and C70 were measured at room temperature with a scan rate of 10 mV/s under 100 % hydrogen at the anode and nitrogen at the cathode. MEAs 11 – 12 and 14 – 15 were measured under similar conditions as listed previous, except with a scan rate of 20 mV/s. Sample MEA 6 – 9 was measured using DI water at the cathode and a scan rate of 10 mV/s. CVs for commercial samples were measured using DI water at the cathode and a scan rate of 20 mV/s.

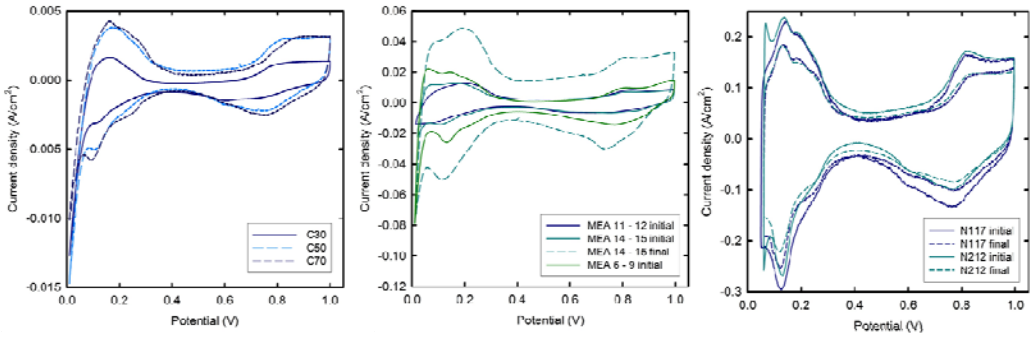

Figure A.7 Initial and final CVs for all samples before and after potential holds.

The impedance of the commercial samples was measured at 60 °C before and after potential hold testing, see Figure A.8. It is observed that the thinner membrane sample, N212, has increased membrane resistance after testing.

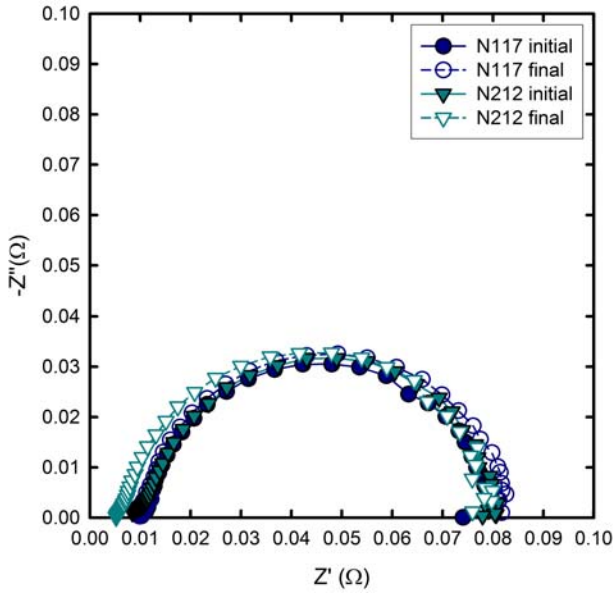

Figure A.8 EIS spectra for commercial samples before and after potential holds.

The ECA was characterized for all samples prior to testing, and it was measured for half the samples after testing as shown in Table A.6. ECA loss is observed after potential hold experiments.

Table A.6 ECA characterization for all samples.

Sample	Initial ECA (m^2_{Pt}/g_{Pt})	Final ECA (m^2_{Pt}/g_{Pt})
C30	15.6	X
C50	55.5	X
C70	30.1	X
MEA 11 – 12	103	103
MEA 14 – 15	101	82.6
MEA 6 – 9	115	X
Commercial N117	113	89.2
Commercial N212	97.3	75.1

The oxide coverage values presented in Chapter 6 are average between 4 samples. Figure A.9 overlays the oxide coverage values with time for samples MEA 14 – 15 (exposed to X-rays), MEA 11 – 12, N117, and N212.

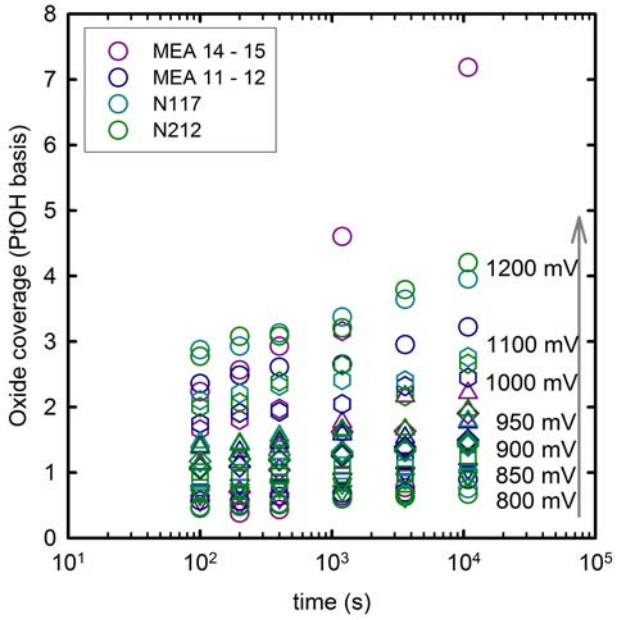

Figure A.9 Individual oxide coverage values for different samples.

A.3 Commercial MEA N212 cycled under varying scan rates and UPLs

A commercial MEA was obtained from Ion Power, Inc. and used to obtain experimental CVs under different scan rates and upper potential limits at 25 °C. These CVs were compared with the simulated CVs discussed in Chapter 6. The 25 cm^2 electrodes were made with a Pt/C catalyst powder with a loading of 0.3 mg_{Pt}/cm^2_{geo}. The membrane was Nafion 212. The fuel cell was wet-up using the Dupont procedure outlined in Chapter 4. The initial performance curve, CV, and EIS spectra are presented in Figure A.10.

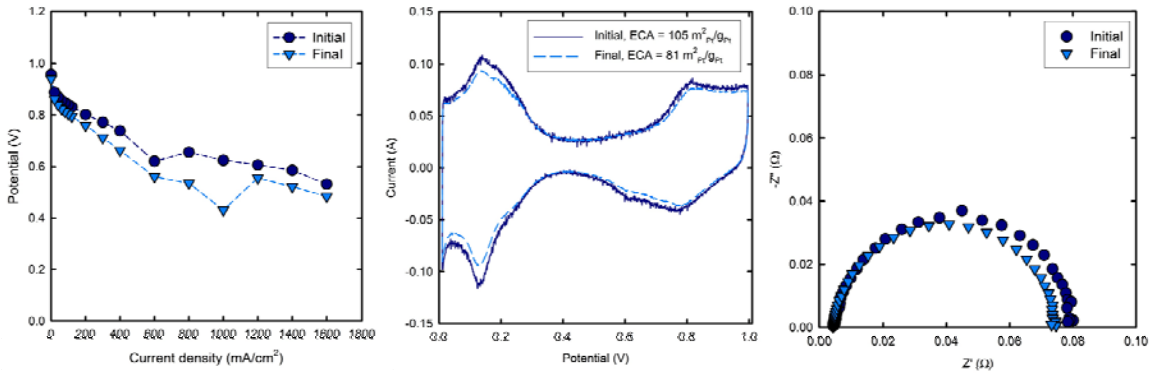

Figure A.10 The performance curve, CV, and EIS spectra before and after cycling experiments.

Following the initial characterization procedures the fuel cell was cycled in a random order with vary scan rates 10, 50, 100, or 200 mV/s and varying upper potential limits 0.8, 0.85, 0.90, 0.95, 1.0, or 1.15 V. The procedure was repeated twice with two different lower potential limits of 0.05 or 0.5 V. The data presented in this dissertation had a lower potential limit of 0.05 V. The final characterization data are also present in Figure A.10. The experimental curves with varying upper potential limits are shown in Figure A.11 and the effect of scan rate on the CV is shown in Figure A.12.

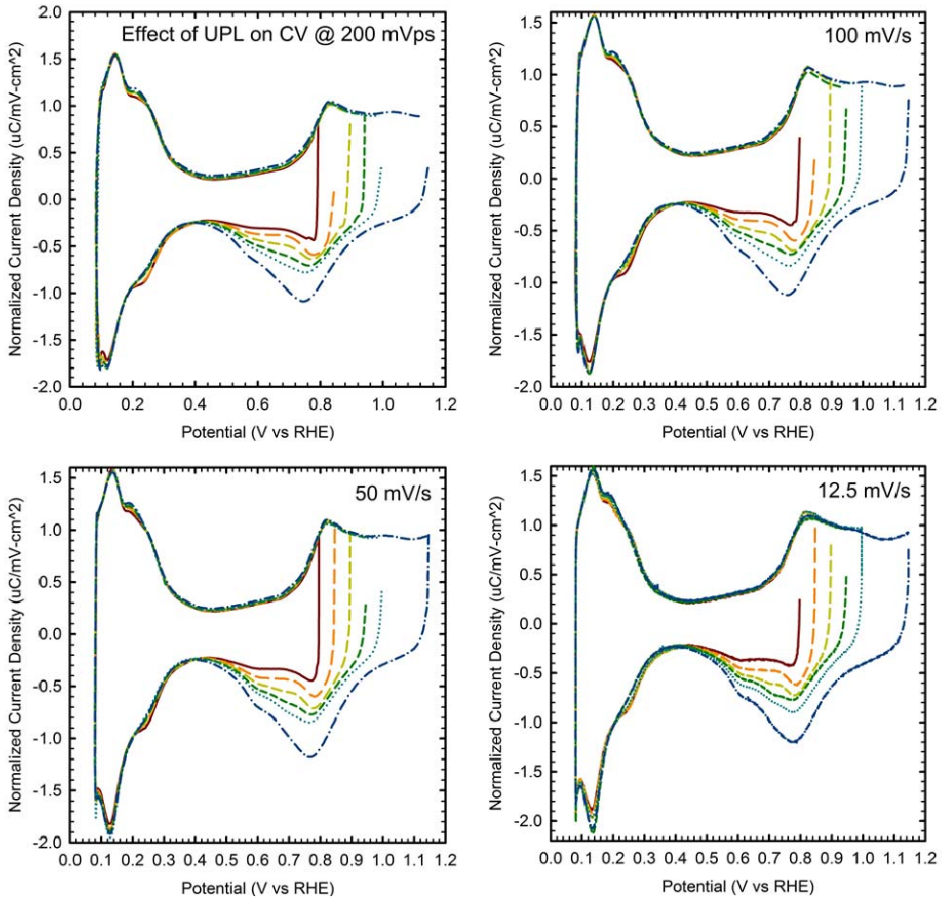

Figure A.11 Experimental curves showing the effect of varying upper potential limits for different scan rates.

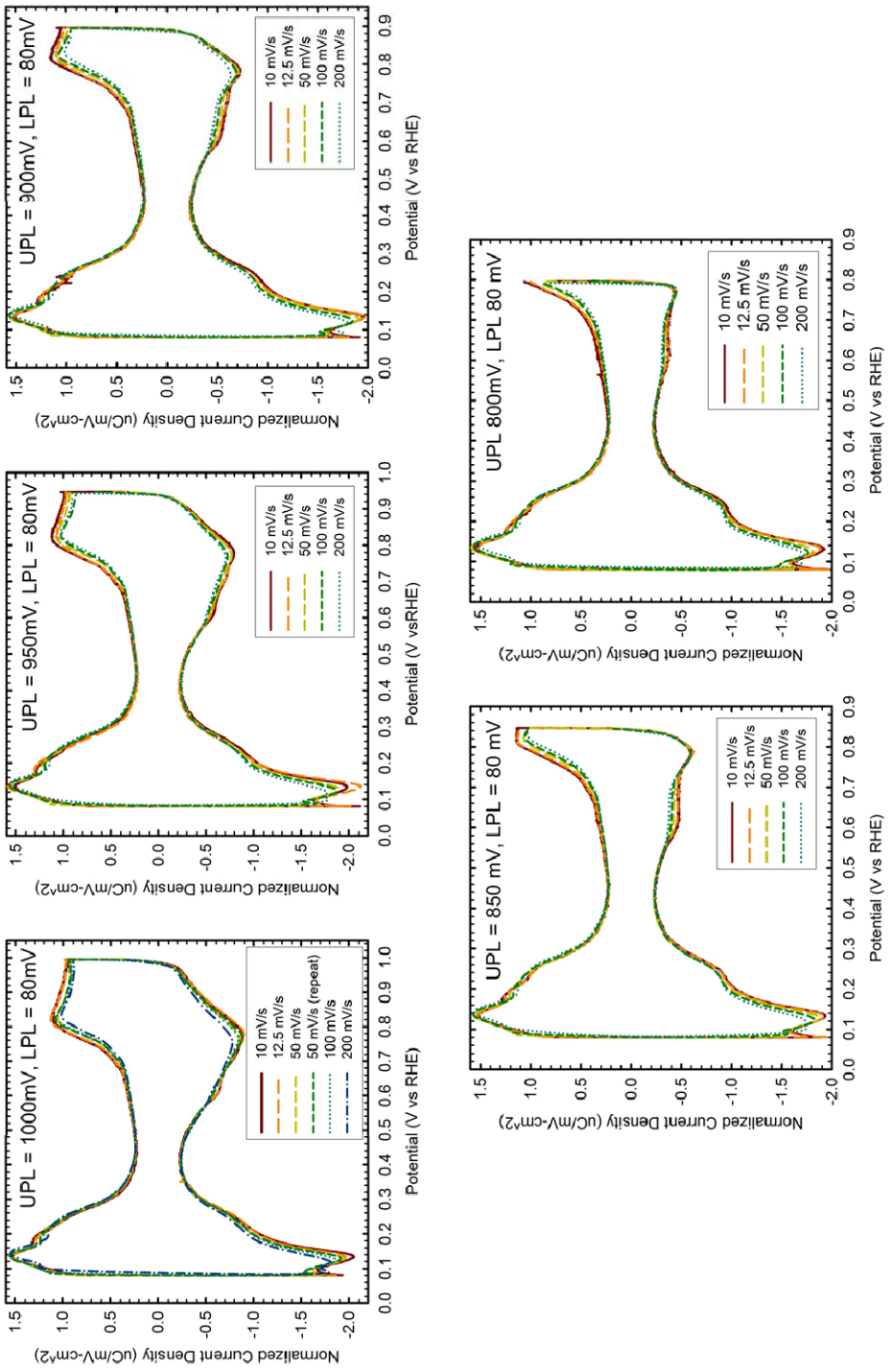

Figure A.12 Experimental CVs showing the effect of varying scan rates at different upper potential limits.

APPENDIX B

DETAILED DRAWINGS OF CUSTOM FUEL CELL HARDWARE

The following pages show the original drawings for the custom fuel cell hardware. All dimensions are reported as inches because that is the standard for manufacturing and machining the equipment.

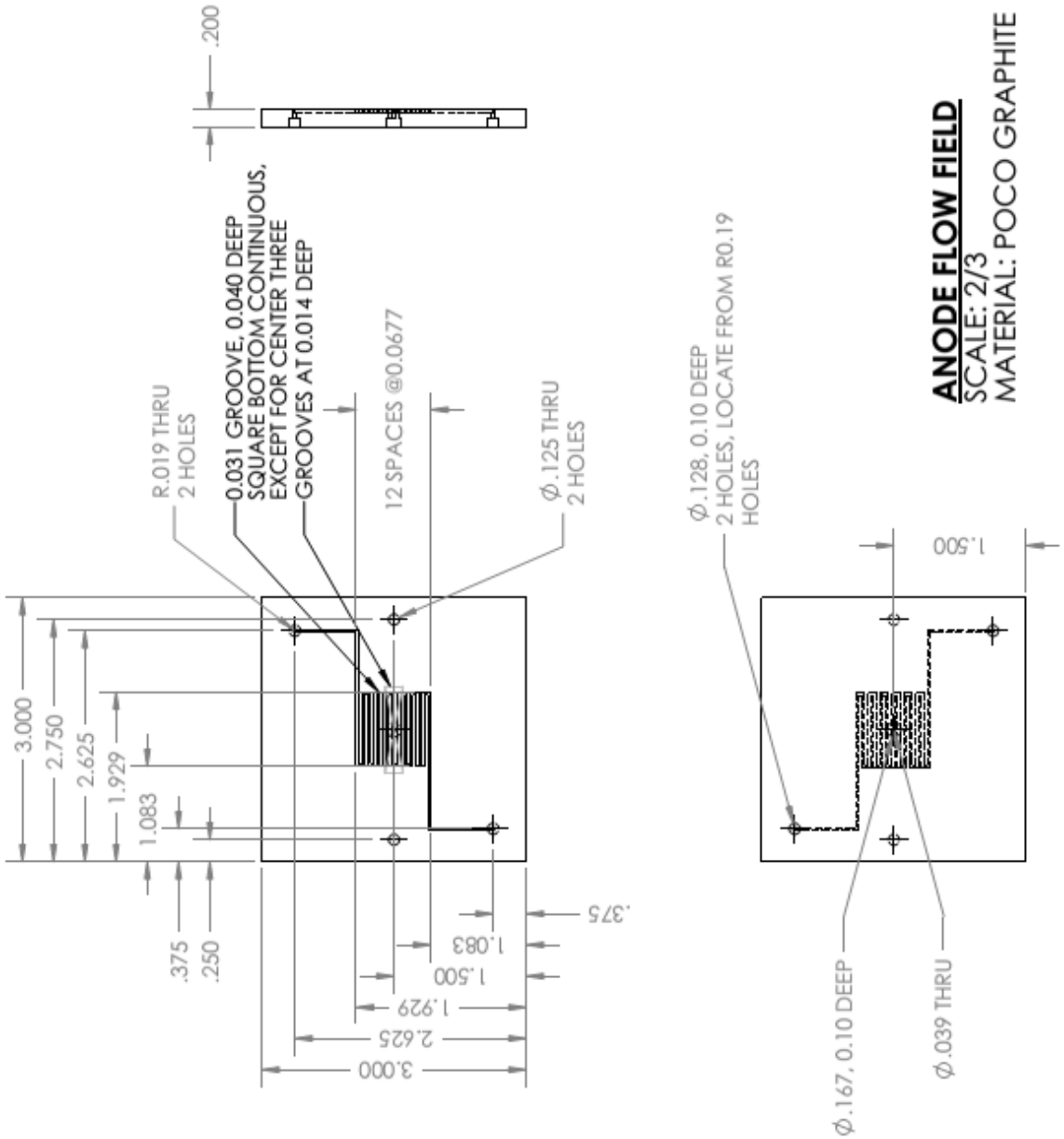

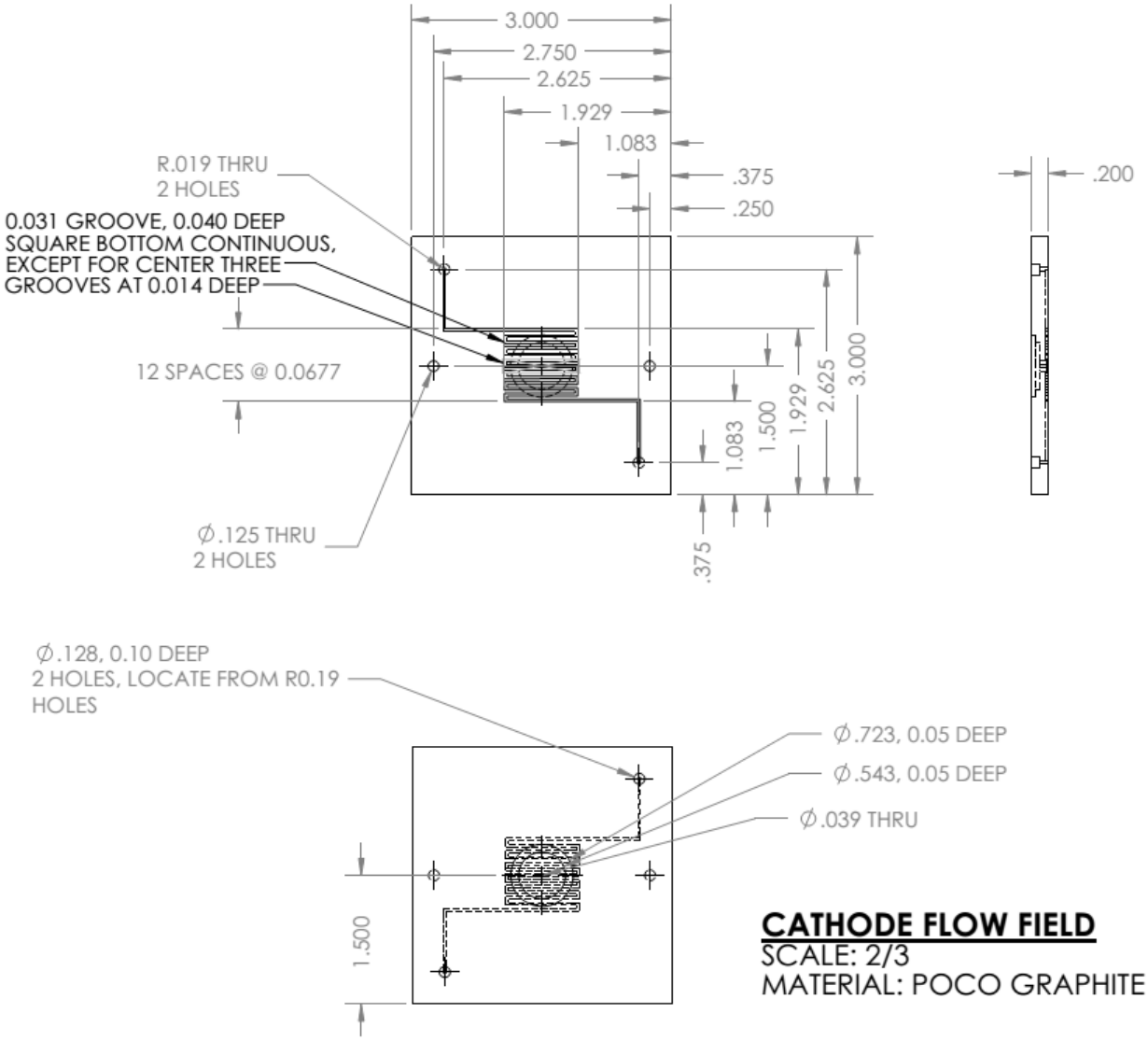

CATHODE FLOW FIELD
SCALE: 2/3
MATERIAL: POCO GRAPHITE

ANODE CURRENT COLLECTOR

SCALE: 2/3

MATERIAL: STAINLESS STEEL (TYPE 420)

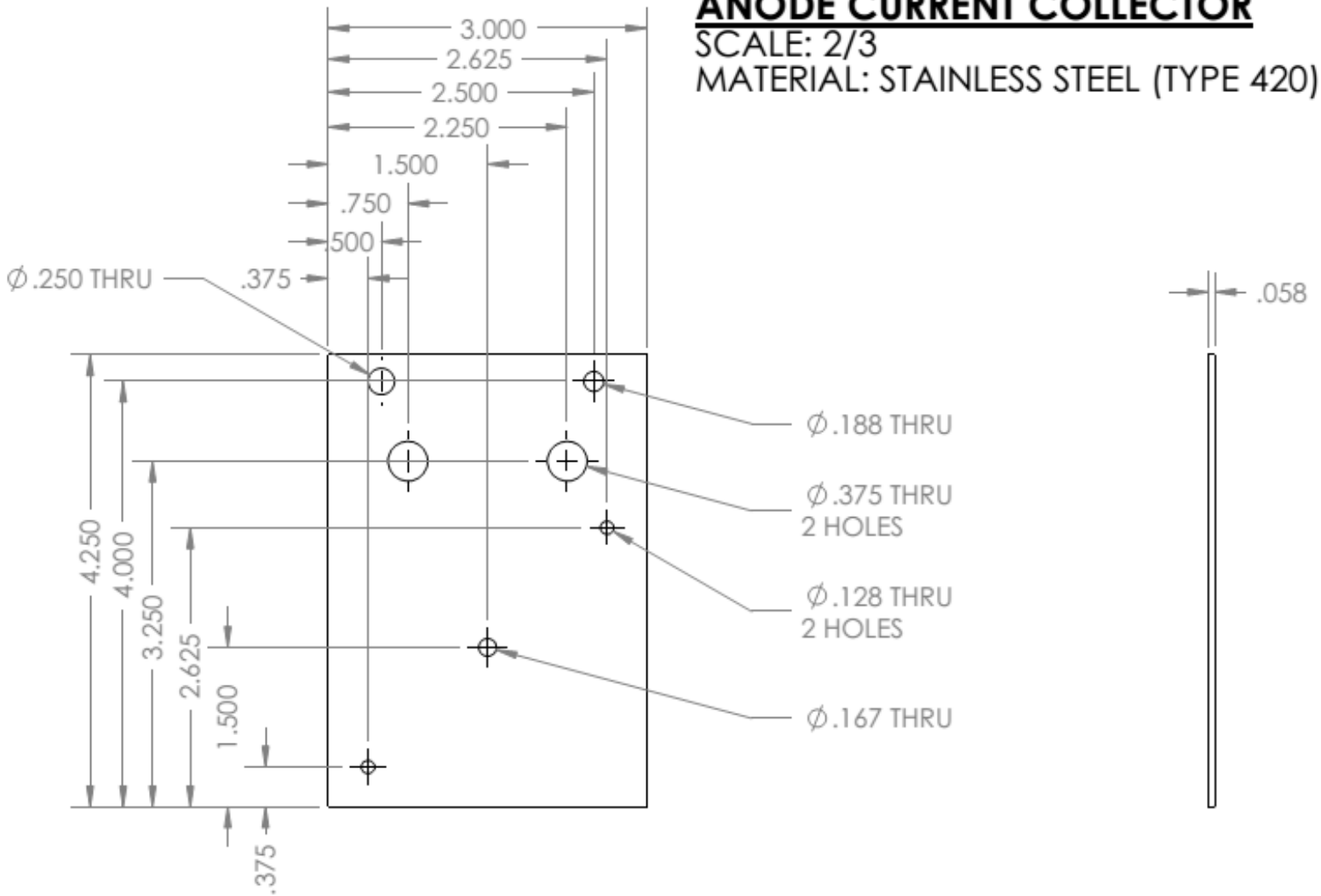

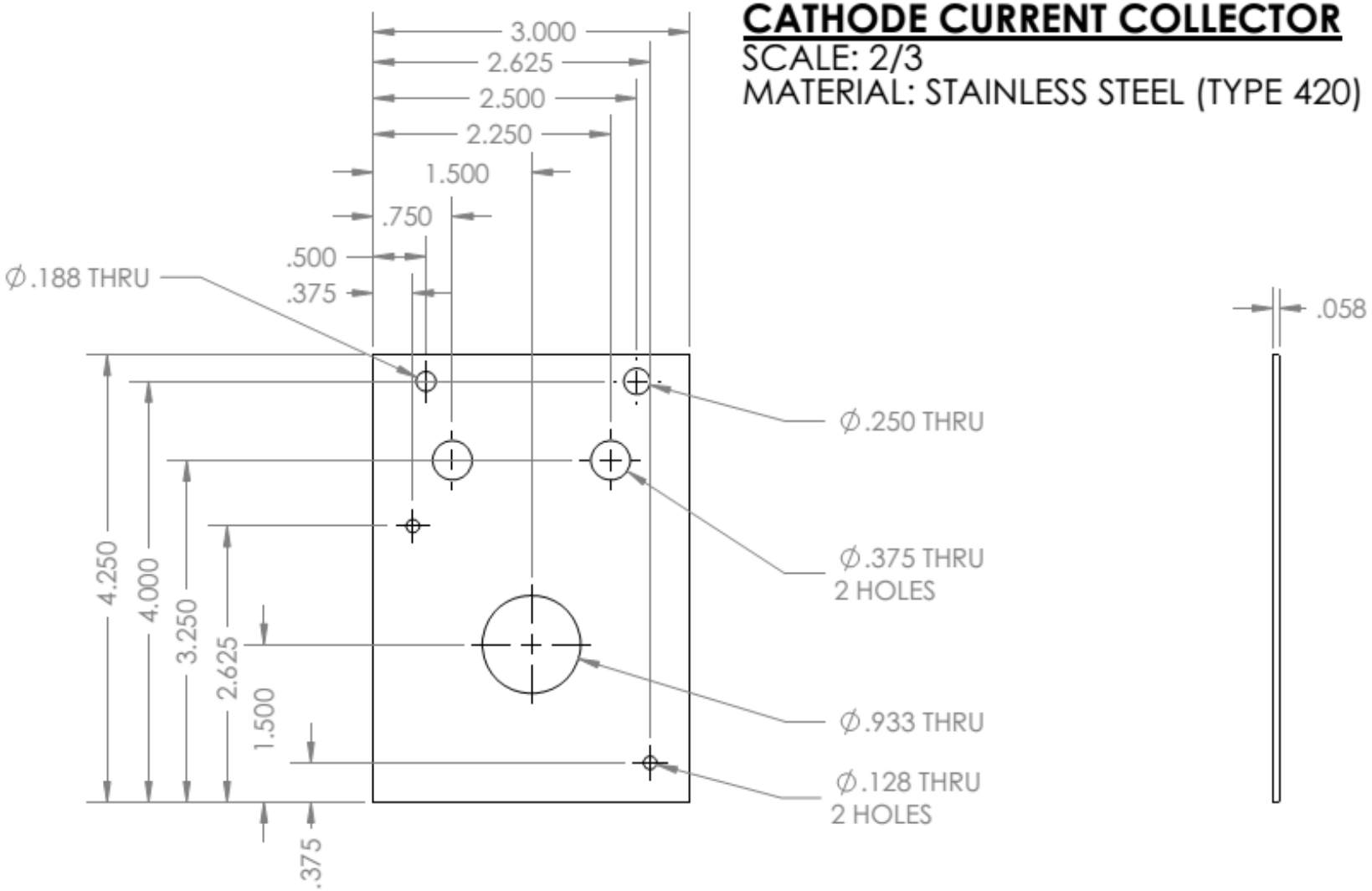
CATHODE CURRENT COLLECTOR
SCALE: 2/3
MATERIAL: STAINLESS STEEL (TYPE 420)
3.000
2.625
2.500
2.250
1.500
.750
.500
.375
Ø.188 THRU
Ø.250 THRU
Ø.375 THRU
2 HOLES
Ø.933 THRU
Ø.128 THRU
2 HOLES
4.250
4.000
3.250
2.625
1.500
.375
.058

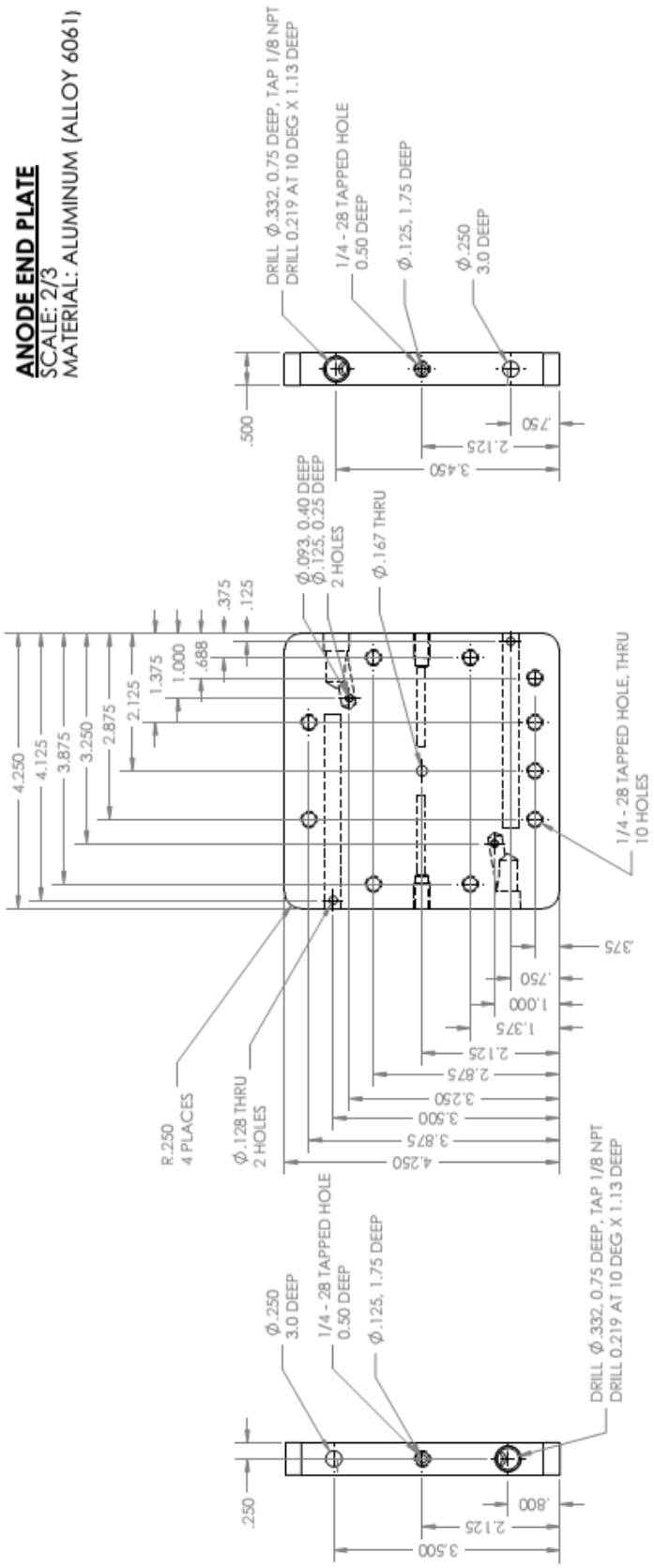
ANODE END PLATE
SCALE: 2/3
MATERIAL: ALUMINUM (ALLOY 6061)
DRILL Ø.332, 0.75 DEEP, TAP 1/8 NPT
DRILL 0.219 AT 10 DEG X 1.13 DEEP
1/4 - 28 TAPPED HOLE
0.50 DEEP
Ø.125, 1.75 DEEP
Ø.250
3.0 DEEP
.500
.750
2.125
3.450
Ø.093, 0.40 DEEP
Ø.125, 0.25 DEEP
2 HOLES
Ø.167 THRU
.375
.125
.688
1.000
1.375
2.125
2.875
3.250
3.875
4.125
4.250
1/4 - 28 TAPPED HOLE, THRU
10 HOLES
.375
.750
1.000
1.375
2.125
2.875
3.250
3.500
3.875
4.250
R.250
4 PLACES
Ø.128 THRU
2 HOLES
Ø.250
3.0 DEEP
1/4 - 28 TAPPED HOLE
0.50 DEEP
Ø.125, 1.75 DEEP
DRILL Ø.332, 0.75 DEEP, TAP 1/8 NPT
DRILL 0.219 AT 10 DEG X 1.13 DEEP
.250
.800
2.125
3.500

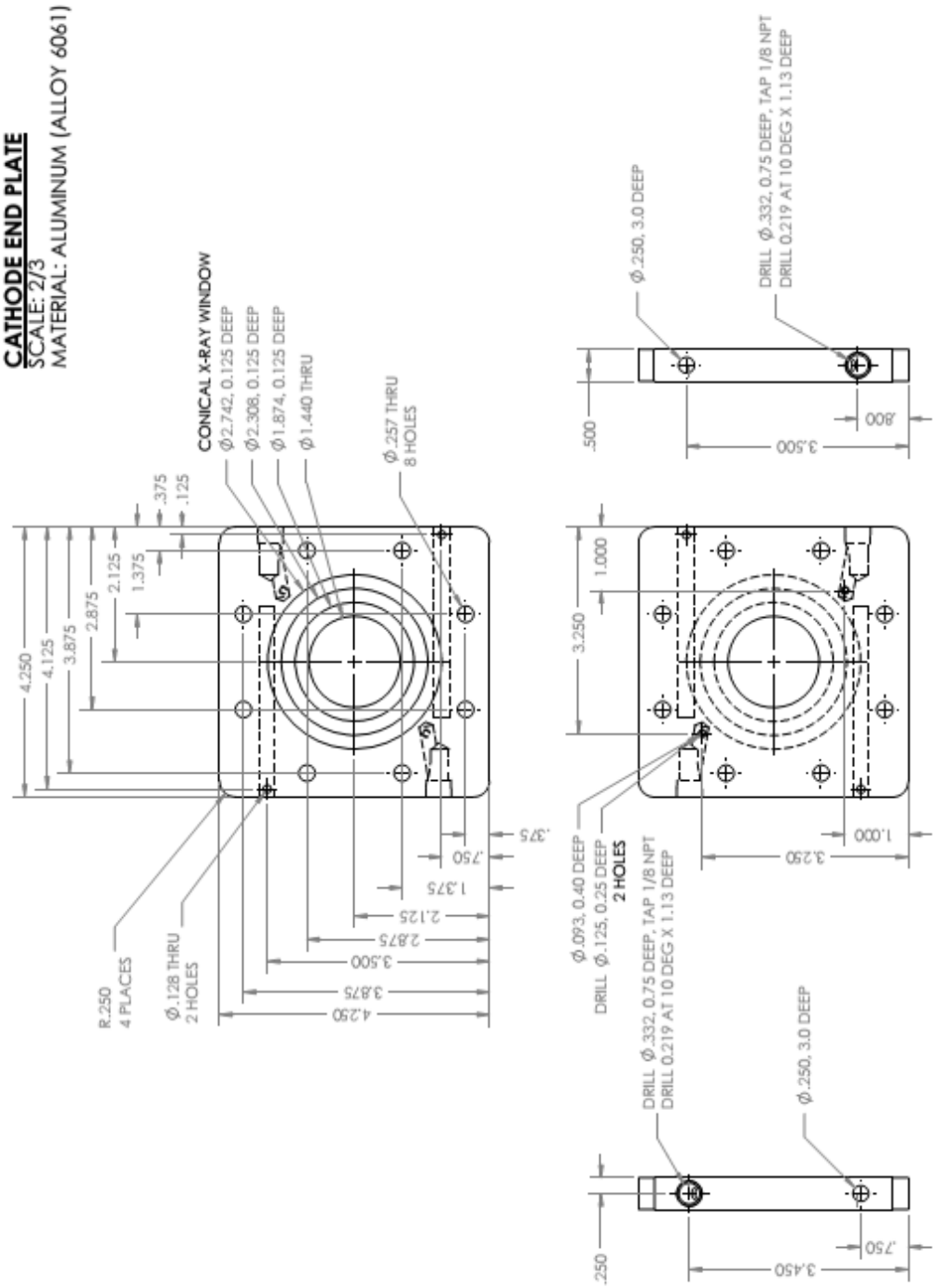
CATHODE END PLATE
SCALE: 2/3
MATERIAL: ALUMINUM (ALLOY 6061)
CONICAL X-RAY WINDOW
Ø2.742, 0.125 DEEP
Ø2.308, 0.125 DEEP
Ø1.874, 0.125 DEEP
Ø1.440 THRU
Ø.257 THRU
8 HOLES
.375
.125
4.250
4.125
3.875
2.875
2.125
1.375
.750
1.375
2.125
2.875
3.500
3.875
4.250
.375
R.250
4 PLACES
Ø.128 THRU
2 HOLES
Ø.250, 3.0 DEEP
DRILL Ø.332, 0.75 DEEP, TAP 1/8 NPT
DRILL 0.219 AT 10 DEG X 1.13 DEEP
.500
.800
3.500
3.250
1.000
1.000
3.250
Ø.093, 0.40 DEEP
DRILL Ø.125, 0.25 DEEP
2 HOLES
DRILL Ø.332, 0.75 DEEP, TAP 1/8 NPT
DRILL 0.219 AT 10 DEG X 1.13 DEEP
Ø.250, 3.0 DEEP
.250
.750
3.450

APPENDIX C

DERIVATION OF CHAPTER 7 X-PARAMETER MODEL EQUATIONS

For the reaction, $Pt + H_2O \overset{eqbm}{\rightleftharpoons} PtO + 2H^+ + 2e^-$, equilibrium can be expressed in terms of chemical potential, μ, as

$$\mu_{Pt} + \mu_{H_2O} = \mu_{PtO} + 2\mu_{H^+} + 2\mu_{e^-} \tag{C.1}$$

where

$$\mu_{Pt} = \mu_{Pt}^0 + RT \cdot \ln\left(\theta_V\right) = \mu_{Pt}^0 + RT \cdot \ln\left(2/3 - \theta_O\right), \tag{C.2}$$

$$\mu_{H_2O} = \mu_{H_2O}^0 + RT \cdot \ln\left(a_{H_2O}\right), \tag{C.3}$$

$$\mu_{PtO} = \mu_{PtO}^0 + RT \cdot \ln\left(\theta_O\right) + \omega_O \theta_O^2, \tag{C.4}$$

$$\mu_{H^+} = \mu_{H^+}^0 + RT \cdot \ln\left(a_{H^+}\right), \tag{C.5}$$

and

$$\mu_{e^-} = -F\Phi\ . \tag{C.6}$$

For simplification, the activity of water and protons $\left(a_{H_2O}, a_{H^+}\right)$ is assumed to be 1. Additionally, O coverage is limited to 2/3 MLs, which was discussed previously in the text. Substituting the above expressions into Equation (C.1) and rearranging yields

$$\left(\mu_{Pt}^0 + \mu_{H_2O}^0 - \mu_{PtO}^0 - 2\mu_{H^+}^0\right) + 2F\Phi - \omega_O\theta_O^2 = RT \cdot \ln\left(\frac{\theta_O}{2/3 - \theta_O}\right), \tag{C.7}$$

and combining the standard chemical potentials yields the standard heat of reaction

$$-\Delta H_{rxn}^0 + 2F\Phi - \omega_O\theta_O^2 = RT \cdot \ln\left(\frac{\theta_O}{2/3 - \theta_O}\right), \tag{C.8}$$

where H refers to enthalpy. Factoring Faraday's constant from the first 2 terms on the left hand side coverts the standard heat of reaction to the standard potential. Rearranging and taking the exponential of both sides yields Equation (6.6).

Considering $Pt + 2H_2O \rightleftarrows PtO_2 + 4H^+ + 4e^-$ on a planar surface, the heat of reaction can be written as the sum of the heats of formation for individual species times the respective stoichiometric coefficients,

$$\Delta H_{rxn} = 4H_{e^-} + 4H^+ + H_{PtO_2} - 2H_2O - HPt \tag{C.9}$$

The heats of formation for platinum and water are equal to constants, c_1 and c_2. The heat of formation of PtO_2 is equal to the sum of a constant and a term representing the adsorption isotherm,

$$H_{PtO_2} = c_3 + \omega_{PtO_2}\left(\sqrt{\theta_{PtO_2}} + 0.1\cdot\theta_{PtO_2}\right) \tag{C.10}$$

The adsorption isotherm was an arbitrary assignment that provided a good fit to experimental data when incorporated with other contributing factors. The heats of formation for protons and electrons, respectively, are written as

$$H_{H^+} = F\Phi_{membrane} \tag{C.11}$$

and

$$H_{e^-} = -F\Phi\,. \tag{C.12}$$

The membrane potential, $\Phi_{membrane}$, is assumed to be 0 in this study. Thus, the heat of reaction can also be written as

$$\Delta H_{rxn} = -4F\Phi + c_3 + \omega_{PtO_2}\left(\sqrt{\theta_{PtO_2}} + 0.1\cdot\theta_{PtO_2}\right) - 2c_2 - c_1. \tag{C.13}$$

The constants can be combined as the standard heat of reaction, which is converted to the standard potential after factoring out Faraday's Constant leaving

$$\Delta H_{rxn} = -4F\left(\Phi - U_6^{\theta}\right) + \omega_{PtO_2}\left(\sqrt{\theta_{PtO_2}} + 0.1\cdot\theta_{PtO_2}\right) = \Delta H_{potential} + \Delta H_{coverage}. \tag{C.14}$$

The activation energy for the anodic and cathodic reactions can be expressed as

$$E_{A,anodic} = E_A^0 + \alpha_{anodic}\Delta H_{potential} + \chi_2\Delta H_{coverage} \tag{C.15}$$

and

$$E_{A,cathodic} = E_{A,anodic} - \Delta H_{rxn} = E_A^0 - \alpha_{cathodic}\Delta H_{potential} - \left(1-\chi_2\right)\Delta H_{coverage}, \tag{C.16}$$

respectively, where α is the transfer coefficient.

Using the Arrhenius expression, the rate equation can initially be expressed as

$$r = k_2 \left[\theta_v a_{H_2O} e^{\left(-\frac{E_{A,anodic}}{RT} \right)} - \theta_{PtO_2} a_{H^+} e^{\left(-\frac{E_{A,cathodic}}{RT} \right)} \right]. \quad \text{(C.17)}$$

Assuming that $\theta_v = a_{H_2O} = a_{H^+} = 1$ and substituting Equations (C.14) - (C.16) into Equation (C.17), the reaction rate becomes Equation (6.7) in the text. The reaction rate for edge sites is derived in the same way except different constants are used to describe the reaction on edge sites and a different adsorption isotherm is assumed

$$H_{PtO_2} = c_4 + \omega_{PtO_2} \left(\sqrt{\theta_{PtO_2}} + 2 \cdot \theta_{PtO_2} \right) \textit{ (Edge Sites).} \quad \text{(C.18)}$$

Furthermore, the amounts of edge sites are approximated as 1/3 the number of face sites for a cuboctahedron with the equivalent volume to a sphere 3 nm in diameter. The volume of a cuboctahedron is calculated as $5/3 \cdot \sqrt{2} a^3$, where a is the cuboctahedron edge length. The number of atoms along the edge of a cuboctahedron, n, is calculated as a divided by the platinum nearest-neighbor distance 2.77 Å. There are 12 corners/vertices on a cuboctahedron and 24 edges of equivalent length. Thus, the total number of edge atoms (including corners) is calculated as $12 + 24(n-2)$. The number of atoms occupying a square face (6 total) is calculated as $(n-2)^2$. For a triangular face (8 total) the number of atoms is calculated as $(n-3)(n-2)/2$. For a cuboctahedron with equivalent volume to a 3 nm sphere, n was rounded to the nearest integer of 7. The ratio of edge + corner atoms to the total amount of surface atoms is 0.36, which is approximated as 1/3 in our model.

APPENDIX D

GPROMS MODELING CODE

D.1 χ-parameter

D.1.1 Variable Types

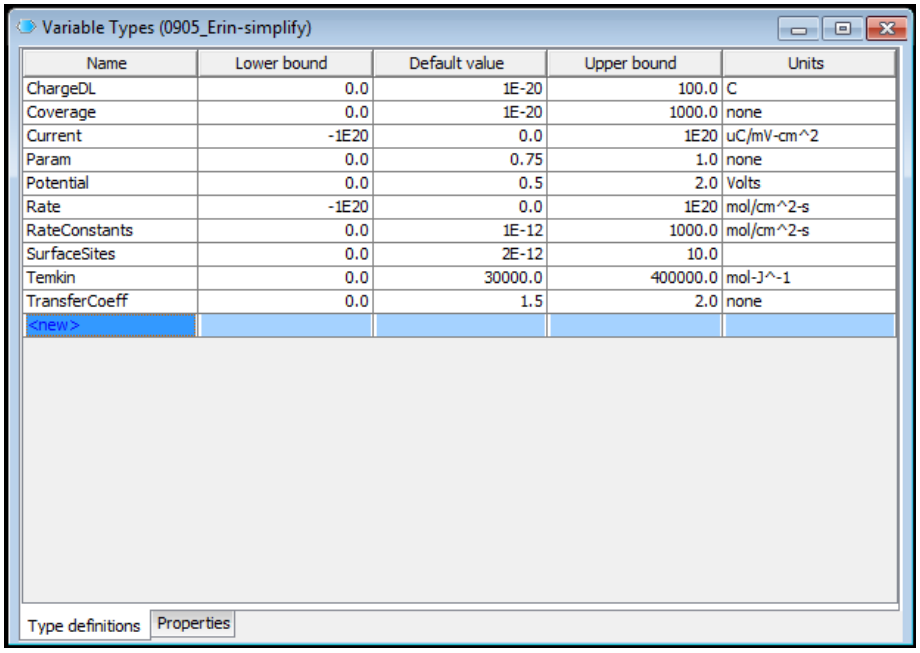

D.1.2 MODEL code

```
PARAMETER
F                                   AS REAL DEFAULT 96487
R_ig                                AS REAL DEFAULT 8.3145
Temp                                AS REAL DEFAULT 298

scan_rate                           AS REAL DEFAULT 0.01

C_dl                                AS REAL DEFAULT 0.00025
Surface_Sites                       AS REAL DEFAULT 210e-6/F
Edge_Sites                          AS REAL DEFAULT Surface_Sites/3

VARIABLE
theta_1,theta_2,theta_3,Sox         AS Coverage
phi,U_1,U_2,U_3                     AS Potential
rate_1,rate_2,rate_3                AS Rate
```

```
i_norm                                      AS Current
Q                                           AS ChargeDL
temkin_1,temkin_2,temkin_3                  AS Temkin
alpha_an2,alpha_an3,alpha_cat2,alpha_cat3   AS TransferCoeff
chi_2,chi_3                                 AS Param
k_2,k_3                                     AS RateConstants


EQUATION
exp(MIN(MAX(F*(phi-U_1)/R_ig/Temp-temkin_1*theta_1^2/R_ig/Temp,-
    7),7))=theta_1/(0.66-theta_1);

rate_2 = k_2*exp((1-chi_2)*temkin_2*(sqrt(theta_2+1e-
    4)+0.1*theta_2)/R_ig/Temp)*(exp(-temkin_2*(sqrt(theta_2+1e-
    4)+0.1*theta_2)/R_ig/Temp)*exp(alpha_an2*F*(phi-U_2)/R_ig/Temp)-
    theta_2*exp(-alpha_cat2*F*(phi-U_2)/R_ig/Temp));

rate_3 = k_3*exp((1-chi_3)*temkin_3*(sqrt(theta_3+1e-
    4)+2*theta_3)/R_ig/Temp)*(exp(-temkin_3*(sqrt(theta_3+1e-
    4)+2*theta_3)/R_ig/Temp)*exp(alpha_an3*F*(phi-U_3)/R_ig/Temp)-theta_3*exp(-
    alpha_cat3*F*(phi-U_3)/R_ig/Temp));

$theta_1 = rate_1/Surface_Sites;
$theta_2 = rate_2/Surface_Sites;
$theta_3 = rate_3/Edge_Sites;

Sox = 2*theta_1 + 4*theta_2 + 4*(Edge_Sites/Surface_Sites)*theta_3;
Q = C_dl*phi;
i_norm = 1000*(2*rate_1*F + 4*rate_2*F + 4*rate_3*F +$Q)/scan_rate;
```

D.1.3 PROCESS code

```
PARAMETER
phi_lo, phi_hi, scan_rate AS REAL

UNIT
E1 AS Erin_thesis_0909

SET
phi_lo      := 0.4;
phi_hi      := 1.2;
scan_rate   := 0.05;

E1.scan_rate  := scan_rate;
```

```
ASSIGN
E1.phi          := phi_lo + scan_rate*time;
E1.temkin_1     := 225000;
E1.temkin_2     := 235000;
E1.temkin_3     := 72000;


E1.U_1          := 0.86;
E1.U_2          := 0.86;
E1.U_3          := 0.595;

E1.alpha_an2    := 1.5;
E1.alpha_an3    := 1.5;
E1.alpha_cat2   := 1.5;
E1.alpha_cat3   := 1.5;
E1.chi_2        := 0.735;
E1.chi_3        := 0.75;

E1.k_2           := 0.5E-12;
E1.k_3           := 0.5E-10;


INITIAL
E1.theta_2       = 0;
E1.theta_3       = 0;


SOLUTIONPARAMETERS
        ReportingInterval := 0.1
        DASolver := "DASOLV" [
                "OutputLevel" := 4
         ]
         IndexReduction := ON


SCHEDULE

## FOR POTENTIAL HOLDS
#SEQUENCE
#   CONTINUE FOR (phi_hi-phi_lo)/(scan_rate)
#RESET
#    E1.phi := phi_hi;
#END
#    CONTINUE FOR 10800
#END
```

```
# FOR SINGLE, TRIANGLE WAVE
SEQUENCE
    CONTINUE FOR (phi_hi-phi_lo)/scan_rate
RESET
    E1.phi := phi_hi - scan_rate*(TIME-(phi_hi-phi_lo)/scan_rate);
END
   CONTINUE FOR (phi_hi-phi_lo)/scan_rate
END
```

D.2 Heterogeneous oxide layer

D.2.1 Variable Types

Variable Types (1105_HeteroOx_thesis)

Name	Lower bound	Default value	Upper bound	Units
Potential	0.0	0.5	2.0	V
Coverage	-100.0	0.5	10000.0	dimensionless
Surf_Sites	0.0	2E-12	10.0	mol/cm^2
Interaction	0.0	30000.0	1000000.0	J/mol
Rate	-1E20	0.5	1E20	mol/cm^2/s
Current	-1E20	0.5	1E20	uC/mV/cm^2
ChargeDL	0.0	1E-20	100.0	C
TransferCoeff	0.0	1.5	4.0	dimensionless
RateConstants	0.0	1E-12	1000.0	1/s
DOS	-5E7	0.5	5E7	J/mol
DisRate	-1E20	0.0	1E20	mol^2/J/cm^2/s
<new>				

Type definitions | Properties

D.2.2 MODEL Code

```
PARAMETER
F                       AS REAL DEFAULT 96487
R                       AS REAL DEFAULT 8.3145
T                       AS REAL DEFAULT 298
scan_rate               AS REAL DEFAULT 0.01
C_dl                    AS REAL DEFAULT 0.00025 #Double layer capacitance

Surface_Sites           AS REAL DEFAULT 210e-6/F
Fraction_Edge           AS REAL DEFAULT 0.36

# Standard potentials
U_1                     AS REAL DEFAULT 0.83
U_2                     AS REAL DEFAULT 0.83
U_3                     AS REAL DEFAULT 0.67

# To characterize distribution
```

```
sig                         AS REAL DEFAULT 14500
sigE                        AS REAL DEFAULT 8700
Lo                          AS REAL DEFAULT -3 * sig
Hi                          AS REAL DEFAULT 3 * sig


DISTRIBUTION_DOMAIN
del_muu                     AS [Lo:Hi] # Change in chemical potential


VARIABLE
x                           AS Distribution(del_muu) of DOS
x_Edge                      AS Distribution(del_muu) of DOS
psi                         AS Distribution(del_muu) of DOS
psi_Edge                    AS Distribution(del_muu) of DOS
dis_rate_2                  AS Distribution(del_muu) of DisRate
dis_rate_3                  AS Distribution(del_muu) of DisRate

phi                                                 AS Potential
theta_OH, theta_PtO2, theta_edge, Sox, S1, S2, S3   ASCoverage
gamma_planar, gamma_edge, gamma_chemi               ASSurf_Sites
omega_OH, omega_PtO2, omega_Edge                    ASInteraction
rate_1, rate_2, rate_3                              ASAS Rate
Pseudocapacitance                                   ASCurrent
Q                                                   ASChargeDL
alpha_an2, alpha_cat2, alpha_an3, alpha_cat3        ASTransferCoeff
k_2, k_3                                            ASRateConstants


EQUATION
theta_PtO2      = integral(del_mu := Lo:Hi; x(del_mu));
theta_edge      = integral(del_mu := Lo:Hi; x_Edge(del_mu));

gamma_planar= (1 - Fraction_Edge)*Surface_Sites;
gamma_edge  = Fraction_Edge*Surface_Sites;
gamma_chemi= exp(-8 * theta_PtO2)*gamma_planar;

gamma_chemi*$theta_OH = (rate_1 - rate_2) - theta_OH * $gamma_chemi;
$x(Lo:Hi)       = dis_rate_2(Lo:Hi)/gamma_planar;
$x_Edge         = dis_rate_3/gamma_edge;

rate_2          = integral(del_mu := Lo:Hi; dis_rate_2(del_mu));
rate_3          = integral(del_mu := Lo:Hi; dis_rate_3(del_mu));

theta_OH        = (1 - theta_OH) * exp(F / R / T * (phi - U_1) - omega_OH * theta_OH ^
                    2 / R / T);
```

```
Q                   = C_dl * phi;

FOR del_mu := Lo to Hi do
dis_rate_2(del_mu) / k_2 = theta_OH * gamma_chemi * psi(del_mu) * exp(-
                           (omega_PtO2 * theta_PtO2 - omega_OH * theta_OH ^ 2) /
                           R /  T + alpha_an2 * F * (phi - U_2) / R / T) - gamma_planar
                           * x(del_mu) * exp(del_mu/R/T - alpha_cat2 * F * (phi - U_2)
                           / R / T);
dis_rate_3(del_mu) / k_3 = gamma_edge * (psi_Edge(del_mu) * exp(-(omega_edge *
                           theta_edge) / R / T + alpha_an3 * F * (phi - U_3) / R / T) -
                           x_edge(del_mu) * exp(del_mu / R / T - alpha_cat3 * F * (phi
                           - U_3) / R / T));
END

Sox     = (gamma_chemi * theta_OH + 4 * gamma_planar * theta_PtO2 + 4 *
            gamma_edge * theta_edge)/Surface_Sites;

# Coverages of OH, PtO2, and edge-PtO2 on a consistent 1 e- (PtOH) basis (just like
Sox).
S1      = gamma_chemi * theta_OH / Surface_Sites ;
S2      = 4*gamma_planar * theta_PtO2 / Surface_Sites ;
S3      = 4*gamma_edge * theta_Edge / Surface_Sites ;

Pseudocapacitance = 1000 * (F * rate_1 + 3 * F * rate_2 + 4 * F * rate_3 + $Q) /
scan_rate;
```

D.2.3 PROCESS Code

```
PARAMETER
phi_lo, phi_hi, scan_rate AS REAL


UNIT
D1 AS Hetero


SET
phi_lo                          := 0.4;
phi_hi                          := 1.15;
scan_rate                       := 0.01;
D1.scan_rate                    := scan_rate;
D1.del_muu                      := [cfdm, 2, 30];
```

```
ASSIGN
#D1.phi                                  := phi_lo + scan_rate * time;
D1.phi                                   := phi_hi - scan_rate * abs(time - (phi_hi -
                                             phi_lo) / scan_rate);
D1.omega_OH                              := 15000;
D1.omega_PtO2                            := 140000;
D1.omega_edge                            := 666667;
D1.alpha_cat2                            := 1.5;
D1.alpha_an2                             := 1.5;
D1.alpha_cat3                            := 1.5;
D1.alpha_an3                             := 2.5;
D1.k_2                                   := 7.35e-2; #1.6E-10;
D1.k_3                                   := 7.81e-3; #1.7e-11;

FOR del_mu           := D1.Lo to D1.Hi do
D1.psi(del_mu)       := 1 / D1.sig / sqrt(2 * 3.14) * exp(-del_mu ^2 / (2 * D1.sig ^2));
D1.psi_edge(del_mu) := 1 / D1.sigE / sqrt(2 * 3.14) * exp(-del_mu ^2 / (2 * D1.sigE
                         ^2));
END

INITIAL
D1.x(D1.Lo:D1.Hi)                        = 0;
D1.xEdge(D1.Lo:D1.Hi)                    = 0;

SOLUTIONPARAMETERS
   ReportingInterval                     := 1.0
   DASolver                              := "DASOLV" [
      "LASolver"                         := "MA28",
       “AbsoluteTolerance”               := 1.0e-7,
      "OutputLevel"                      := 4
   ]
   IndexReduction                        := ON

SCHEDULE
CONTINUE FOR 2 * (phi_hi - phi_lo) / scan_rate;

#Anodic only
#CONTINUE FOR (phi_hi-phi_lo)/scan_rate


#Reduction only
#CONTINUE FOR (phi_hi-phi_lo)/scan_rate


#SEQUENCE
  # CONTINUE FOR (phi_hi-phi_lo)/(scan_rate)
```

```
#RESET
  #  D1.phi := phi_hi;
#END
   # CONTINUE FOR 10800
#END

#SEQUENCE
#    CONTINUE FOR (phi_hi-phi_lo)/scan_rate
#RESET
#    D1.phi := phi_hi - scan_rate*(TIME-(phi_hi-phi_lo)/scan_rate);
#END
#   CONTINUE FOR (phi_hi-phi_lo)/scan_rate
#END
```

APPENDIX E

PYTHON SCRIPTS FOR PDF PROCESSING

The following appendix displays python scripts that were written to rapidly process experimental .gr files using PDFgui.

E.1 2009 Scripts (Argonne National Lab, Beamline 11-ID-B) [CHAPTER 7 data]

E.1.1 Script to determine spdiameter

G:\Fuller Group\Projects\I LatticeStrain_PDF\2009 Argonne - Brian\script.py Friday, September 13, 2013 3:37 PM

```
#!/usr/bin/env python

'''Perform simple refinement of Pt structure to the experimental x-ray PDF.
Save fitted curve, refined structure and results summary.
'''

from diffpy.pdffit2 import PdfFit

# import list of .gr files
import os

data_dir = 'temp_gr-spdia'
results_dir = 'results-spdia'

gr_files = [file for file in os.listdir(data_dir) if file.lower().endswith(".gr")]

results_file = open(results_dir + '\\results.txt' , 'w')
results_file.write("Filename\tLattice Parameter\tScale Factor\tDelta2\tIsotropic
ADP\trw\tSpdiameter\n")

for file in gr_files:
    # Create new PDF calculator object.
    pf = PdfFit()

    # Load data ------------------------------------------------------------------------

    # Load experimental x-ray PDF data

    qmax = 23.0  # Q-cutoff used in PDF calculation in 1/A
    qdamp = 0.0409934410791 # instrument Q-resolution factor, responsible for PDF decay
    qbroad = 0.0139844219837
    pf.read_data(data_dir + '\\' + file,'X',qmax, qdamp)
    pf.setvar('qbroad',qbroad)

    # Load platinum structure, must be in PDFFIT or DISCUS format
    pf.read_struct('Platinum.stru')

    # Configure refinement -------------------------------------------------------------

    # Refine lattice parameters a, b, c.
    # Make them all equal to parameter @10.
    pf.constrain(pf.lat(1), "@10")
    pf.constrain(pf.lat(2), "@10")
    pf.constrain(pf.lat(3), "@10")
    # set initial value of parameter @10
    pf.setpar(10, pf.lat(1))

    #Refine phase scale factor. Right side can have formulas.
    pf.constrain('pscale','@11')
    pf.setpar(11, pf.getvar(pf.pscale()))

    # Refine sharpening factor for correlated motion of close atoms.
    pf.constrain(pf.delta2, 12)
    pf.setpar(12, 3.307)
```

-1-

G:\Fuller Group\Projects\l LatticeStrain_PDF\2009 Argonne - Brian\script.py Friday, September 13, 2013 3:37 PM

```
    # Refine spdiameter
    pf.constrain(pf.spdiameter, 13)
    pf.setpar(13, 28.0)

    # Set all temperature factors isotropic and equal to @14
    for idx in range (1, 5):
        pf.constrain(pf.u11(idx), '@14')
        pf.constrain(pf.u22(idx), '@14')
        pf.constrain(pf.u33(idx), '@14')
    pf.setpar(14, pf.u11(1))

    # Refine ------------------------------------------------------------------------

    pf.pdfrange(1, 2.2, 29.99)
    pf.refine()

    # Save results ------------------------------------------------------------------

    pf.save_pdf(1, results_dir + '\\' + file.rstrip('.gr') + '_refinement.fgr')
    pf.save_struct(1, results_dir + "\\" + file.rstrip('.gr') + "_refinement.rstr")
    pf.save_res(results_dir + "\\" + file.rstrip('.gr') + "_refinement.res")

    lat=pf.getvar(pf.lat(1))
    scale=pf.getvar(pf.pscale())
    delta2=pf.getvar(pf.delta2)
    spdia=pf.getvar(pf.spdiameter)
    u11=pf.getvar(pf.u11(1))
    rw=pf.getrw()


    line="%s\t%f\t%f\t%f\t%f\t%f\t%f\n" % (file,lat,scale,delta2,u11,rw,spdia)
    print line
    results_file.write(line)
results_file.close()
```

E.1.2 Script to lookup spdiameter from results file

G:\Fuller Group\Projects\l LatticeStrain_PDF\r series\get_spdia_from_file.py Friday, September 13, 2013 3:34 PM

```
#!/usr/bin/env python
import os
spdia_results_dir = 'results-rseries-spdiameter'
spdia_file = open(spdia_results_dir + '\\results.txt' , 'r')
dialookup={}
for line in spdia_file:
    if not line.startswith('Filename\t'):
        parts=line.split('\t')
        filename=parts[0]
        dia=parts[5]
        dialookup[filename]=float(dia)
print dialookup
```

E.1.3 Script to determine lattice parameter over varying r-ranges

G:\Fuller Group\Projects\I LatticeStrain_PDF\r series\r-series-script.py Friday, September 13, 2013 3:24 PM

```
#!/usr/bin/env python

'''Perform simple refinement of Pt structure to the experimental x-ray PDF.
Save fitted curve, refined structure and results summary.
'''

from diffpy.pdffit2 import PdfFit


import os

# Generate a lookup dictionary for spdiameter parameter from initial run with rrange 2.2-29.99
spdia_results_dir = 'results-rseries-spdiameter'
spdia_file = open(spdia_results_dir + '\\results.txt' , 'r')
dialookup={}
for line in spdia_file:
    if not line.startswith('Filename\t'):
        parts=line.split('\t')
        filename=parts[0]
        dia=parts[5]
        dialookup[filename]=float(dia)
spdia_file.close()


# import list of .gr files
data_dir = 'temp_gr'
results_dir = 'results-rseries'

gr_files = [file for file in os.listdir(data_dir) if file.lower().endswith(".gr")]

results_file = open(results_dir + '\\results.txt' , 'w')
results_file.write("Filename\tLattice Parameter\tScale Factor\tDelta2\tIsotropic
ADP\tspdiameter (Optimized separately) \trw\tLower Bound R\tUpper Bound R\n")

upperbounds=[3.3,4.36,5.17,10.36,15.18,20.08,25,29.99] # NN: 1,2,3,13, etc
lowerbounds=[2.2,3.3,4.36,5.17,10.36,15.18,20.08]

for rlow in lowerbounds:
    for rhigh in upperbounds:
        if rhigh>rlow:
            for file in gr_files:
                # Create new PDF calculator object.
                pf = PdfFit()

                # Load data
                ------------------------------------------------------------------------

                # Load experimental x-ray PDF data

                qmax = 23.0  # Q-cutoff used in PDF calculation in 1/A
                qdamp = 0.0370411586828 # instrument Q-resolution factor, responsible for PDF
                decay
                qbroad = 0.0174202515977 # From PDFGUI Fit of Nickel: file:
                C:\Users\eredmond3\Desktop\0910APS11IDB\reduced\03032012 pdfgui fits\Nickel.dpp
```

-1-

```
pf.read_data(data_dir + '\\' + file,'X',qmax, qdamp)
pf.setvar('qbroad',qbroad)

# Load platinum structure, must be in PDFFIT or DISCUS format
pf.read_struct('Platinum.stru')

# Configure refinement
----------------------------------------------------------------

# Refine lattice parameters a, b, c.
# Make them all equal to parameter @10.
pf.constrain(pf.lat(1), "@10")
pf.constrain(pf.lat(2), "@10")
pf.constrain(pf.lat(3), "@10")
# set initial value of parameter @10
pf.setpar(10, pf.lat(1))

#Refine phase scale factor. Right side can have formulas.
pf.constrain('pscale','@11')
pf.setpar(11, pf.getvar(pf.pscale()))

# Refine sharpening factor for correlated motion of close atoms.
pf.constrain(pf.delta2, 12)
pf.setpar(12, 3.307)

# Refine spdiameter
#pf.constrain(pf.spdiameter, 13)
#pf.setpar(13, 28.0)

# Fix spdiameter from previously refined value
pf.setvar(pf.spdiameter, dialookup[file])


# Set all temperature factors isotropic and equal to @14
for idx in range (1, 5):
    pf.constrain(pf.u11(idx), '@14')
    pf.constrain(pf.u22(idx), '@14')
    pf.constrain(pf.u33(idx), '@14')
pf.setpar(14, pf.u11(1))

# Refine
----------------------------------------------------------------------------

pf.pdfrange(1, rlow, rhigh)
try:
    pf.refine()

    # Save results
    ----------------------------------------------------------------------

    pf.save_pdf(1, results_dir + '\\' + file.rstrip('.gr') + '_' + str(rlow) +
    '-' + str(rhigh) + '_refinement.fgr')
    pf.save_struct(1, results_dir + "\\" + file.rstrip('.gr') + '_' + str(rlow)
    + '-' + str(rhigh) + "_refinement.rstr")
```

```
                    pf.save_res(results_dir + "\\" + file.rstrip('.gr') + '_' + str(rlow) + '-'
                    + str(rhigh) + "_refinement.res")

                    lat=pf.getvar(pf.lat(1))
                    scale=pf.getvar(pf.pscale())
                    delta2=pf.getvar(pf.delta2)
                    spdia=pf.getvar(pf.spdiameter)
                    ul1=pf.getvar(pf.ul1(1))
                    rw=pf.getrw()


                    line="%s\t%f\t%f\t%f\t%f\t%f\t%f\t%f\n" % (file,lat,scale,delta2,ul1,
                    spdia,rw,rlow,rhigh)
                except:
                    line=file + '\tError, could not converge\n'
                print line
                results_file.write(line)
results_file.close()
```

E.2. 2012 Scripts (Brookhaven National Lab, Beamline X7B) [CHAPTER 7] data

Script for multiphase fit:

G:\Fuller Group\Projects\I LatticeStrain_PDF\Brookhaven 2012\PDFgui\Python\script_withCarbonStruc.py Friday, September 13, 2013 3:50 PM

```
#!/usr/bin/env python
#2012_April-Brookhaven National Lab, Beamline X7B
'''Perform simple refinement of Pt structure to the experimental x-ray PDF.
Save fitted curve, refined structure and results summary.
'''

from diffpy.pdffit2 import PdfFit

# import list of .gr files
import os

qmax_data_dir = 'G:\\Redmond\\reduced\\Samples\\Sum\\Platinum'
data_dir = 'G:\\Redmond\\reduced\\Samples\\Sum\\Platinum\\Stripped'
results_dir = 'G:\\Redmond\\reduced\\Samples\\Sum\\Platinum\\PDFfit_results_spdiameter'

gr_files = [file for file in os.listdir(data_dir) if file.lower().endswith(".gr")]

results_file = open(results_dir + '\\results.txt' , 'w')
results_file.write("Filename\tLattice Parameter Pt\tScale Factor Pt\tDelta2
Pt\tSpdiameter(Angstroms) Pt\tIsotropic ADP Pt\tC Lat\tC-Scale Factor\tC-del2\tC-Spdiameter
(A)\tC_u11_u22\tC_u33\tRw\n")

for file in gr_files:
    # Create new PDF calculator object.
    pf = PdfFit()

    # Load data ------------------------------------------------------------------------

    # Load experimental x-ray PDF data
    gr_file = open(qmax_data_dir + '\\' + file,'r')
    for line in gr_file:
        if line.startswith('qmax ='):
            qmax=float(line[7:])
            break
    gr_file.close()
    # Q-cutoff used in PDF calculation in 1/A
    qdamp = 0.02938296851 # instrument Q-resolution factor, responsible for PDF decay
    qbroad = 3.25081646496e-005
    print data_dir + '\\' + file
    pf.read_data(data_dir + '\\' + file,'X',qmax, qdamp)
    pf.setvar('qbroad',qbroad)

    # Load platinum structure, must be in PDFFIT or DISCUS format
    pf.read_struct('G:\\PDFgui\\Platinum.stru')
    pf.read_struct('G:\\PDFgui\\Graphite.stru')

    # Configure refinement -------------------------------------------------------------
    pf.setphase(1)
    # Refine platinum lattice parameters a, b, c.
    # Make them all equal to parameter @1.
    pf.constrain(pf.lat(1), '@1')
    pf.constrain(pf.lat(2), '@1')
    pf.constrain(pf.lat(3), '@1')
    # set initial value of parameter @1
```

-1-

```
pf.setpar(1, pf.lat(1))

#Refine phase scale factor. Right side can have formulas.
pf.constrain('pscale','@2')
#pf.setpar(2, pf.getvar(pf.pscale()))
pf.setpar(2, 15)

# Refine sharpening factor for correlated motion of close atoms.
pf.constrain(pf.delta2, '@3')
pf.setpar(3, 3.307)

# Refine spdiameter
pf.constrain(pf.spdiameter, '@4')
pf.setpar(4, 10)

# Set all temperature factors isotropic and equal to @5
for idx in range (1, 5):
    pf.constrain(pf.u11(idx), '@5')
    pf.constrain(pf.u22(idx), '@5')
    pf.constrain(pf.u33(idx), '@5')
pf.setpar(5, pf.u11(1))

pf.setphase(2)
# Refine carbon lattice parameters a, b, c.
pf.constrain(pf.lat(1), '@6')
pf.constrain(pf.lat(2), '@6')
pf.constrain(pf.lat(3), '@7')

pf.setpar(6, pf.lat(1))
pf.setpar(7, pf.lat(3))

#Refine phase scale factor. Right side can have formulas.
pf.constrain('pscale','@8')
#pf.setpar(8, pf.getvar(pf.pscale()))
pf.setpar(8, 5)

# Refine sharpening factor for correlated motion of close atoms.
pf.constrain(pf.delta2, '@9')
pf.setpar(9, 3.307)

# Refine spdiameter
pf.constrain(pf.spdiameter, '@10')
pf.setpar(10, 50)

# Set all temperature factors isotropic and equal to @11 and @12
for idx in range (1, 5):
    pf.constrain(pf.u11(idx), '@11')
    pf.constrain(pf.u22(idx), '@11')
    pf.constrain(pf.u33(idx), '@12')
pf.setpar(11, pf.u11(1))
pf.setpar(12, pf.u33(1))

# Refine ----------------------------------------------------------------------
pf.pdfrange(1, 2.2, 3.2)
```

```
    pf.refine()

    # Save results ----------------------------------------------------------------

    pf.save_pdf(1, results_dir + '\\' + file.rstrip('.gr') + '_refinement.fgr')
    pf.save_struct(1, results_dir + "\\" + file.rstrip('.gr') + "_refinement.rstr")
    pf.save_res(results_dir + "\\" + file.rstrip('.gr') + "_refinement.res")

    pf.setphase(1)
    lat=pf.getvar(pf.lat(1))
    scale=pf.getvar(pf.pscale())
    delta2=pf.getvar(pf.delta2)
    spdia=pf.getvar(pf.spdiameter)
    u11=pf.getvar(pf.u11(1))

    pf.setphase(2)
    C_lat=pf.getvar(pf.lat(1))
    C_scale=pf.getvar(pf.pscale())
    C_delta2=pf.getvar(pf.delta2)
    C_spdiameter=pf.getvar(pf.spdiameter)
    C_u11=pf.getvar(pf.u11(1))
    C_u33=pf.getvar(pf.u33(1))

    rw=pf.getrw()


    line="%s\t%f\t%f\t%f\t%f\t%f\t%f\t%f\t%f\t%f\t%f\t%f\t%f\n" % (file,lat,scale,delta2,spdia,
    u11,C_lat,C_scale,C_delta2,C_spdiameter,C_u11,C_u33,rw)
    print line
    results_file.write(line)
results_file.close()
```

E.3 Processing spdiameter for 2012 in operando PDF measurements [Argonne National Lab, 11-ID-B]

G:\Fuller Group\Projects\III Insitu_PDF\PY\script.py Friday, September 13, 2013 3:57 PM

```
#!/usr/bin/env python

'''Perform simple refinement of Pt structure to the experimental x-ray PDF.
Save fitted curve, refined structure and results summary.
'''

from diffpy.pdffit2 import PdfFit

# import list of .gr files
import os

data_dir = 'C:\\Users\\eredmond3\\Desktop\\PY\\temp_gr'
results_dir = 'C:\\Users\\eredmond3\\Desktop\\PY\\results'

gr_files = [file for file in os.listdir(data_dir) if file.lower().endswith(".gr")]

results_file = open(results_dir + '\\results.txt' , 'w')
results_file.write("Filename\tLattice Parameter\tScale
Factor\tDelta2\tSpdiameter(Angstroms)\tIsotropic ADP\tRw\n")

for file in gr_files:
    # Create new PDF calculator object.
    pf = PdfFit()

    # Load data ------------------------------------------------------------------------

    # Load experimental x-ray PDF data

    qmax = 20.0  # Q-cutoff used in PDF calculation in 1/A
    qdamp = 0.0409934410791 # instrument Q-resolution factor, responsible for PDF decay
    qbroad = 0.0139844219837
    pf.read_data(data_dir + '\\' + file,'X',qmax, qdamp)
    pf.setvar('qbroad',qbroad)

    # Load platinum structure, must be in PDFFIT or DISCUS format
    pf.read_struct('C:\\Users\\eredmond3\\Desktop\\PY\\Platinum.stru')

    # Configure refinement -------------------------------------------------------------

    # Refine lattice parameters a, b, c.
    # Make them all equal to parameter @10.
    pf.constrain(pf.lat(1), "@10")
    pf.constrain(pf.lat(2), "@10")
    pf.constrain(pf.lat(3), "@10")
    # set initial value of parameter @10
    pf.setpar(10, pf.lat(1))

    #Refine phase scale factor. Right side can have formulas.
    pf.constrain('pscale','@11')
    pf.setpar(11, pf.getvar(pf.pscale()))

    # Refine sharpening factor for correlated motion of close atoms.
    pf.constrain(pf.delta2, 12)
    pf.setpar(12, 3.307)
```

-1-

```
    # Refine spdiameter
    pf.constrain(pf.spdiameter, 13)
    pf.setpar(13, 28.0)

    # Set all temperature factors isotropic and equal to @14
    for idx in range (1, 5):
        pf.constrain(pf.u11(idx), '@14')
        pf.constrain(pf.u22(idx), '@14')
        pf.constrain(pf.u33(idx), '@14')
    pf.setpar(14, pf.u11(1))

    # Refine ------------------------------------------------------------------------

    pf.pdfrange(1, 1.7, 50.0)
    pf.refine()

    # Save results ------------------------------------------------------------------

    pf.save_pdf(1, results_dir + '\\' + file.rstrip('.gr') + '_refinement.fgr')
    pf.save_struct(1, results_dir + "\\" + file.rstrip('.gr') + "_refinement.rstr")
    pf.save_res(results_dir + "\\" + file.rstrip('.gr') + "_refinement.res")

    lat=pf.getvar(pf.lat(1))
    scale=pf.getvar(pf.pscale())
    delta2=pf.getvar(pf.delta2)
    spdia=pf.getvar(pf.spdiameter)
    u11=pf.getvar(pf.u11(1))
    Rw=pf.getrw()

    line="%s\t%f\t%f\t%f\t%f\t%f\t%f\n" % (file,lat,scale,delta2,spdia,u11,Rw)
    print line
    results_file.write(line)
results_file.close()
```

APPENDIX F

MATLAB SURFACE ENERGY MODELING CODE

File: loop.m

```
c1 = -7.39;          %J/m2, fitting parameter 1
c2 = 5.45E-9;        %J/m, fitting parameter 2
bulk_surf = 1.23;    %J/m2, bulk surface energy


for i = 1:500
    R(i) = i+1;
    D(i) = (2*R(i))/10;
    surface_energy(i) = surf(R(i));
    surf_exp(i)=bulk_surf+c2/(R(i)/10^10);
end


figure(1)
plot(D,surface_energy,'-')
xlabel('particle diameter [=] nm')
ylabel('calculated surface energy [=] J/m^2')
title('Calculated surface energy, Sutton-Chen potential')


figure(2)
plot(D,surf_exp)
xlabel('particle diameter [=] nm')
ylabel('surface energy [=] J/m^2')
title('Experimental surface energy')
```

File: surf.m

```
function G = surf(R)
a = 3.92;
t = 16*pi/3*(R/a)^3;
G=16.0217646*(suchen(R)-t*bulk())/(4*pi*R^2);
```

File: bulk.m

```
function I = bulk()

% number of kth nearest neighbors
l=[12 6 24 12 24 8 48 6 36 24 24 24 72 0 48 12 48 30 72 24 48 24 48 8
84 24 72 48 24 0 96 6 96 48 48 36 120 24 48 24 24 48 120 24 120 0 96 24
108 30];

% constants PCCP
a = 3.9231;         % angstrom, lattice constant
c = 34.408;         % dimensionless parameter
e = 1.9833E-2;      % eV, energy parameter
m = 8;              % positive integer
n = 10;             % positive integer

% Variables for 'for loop'
x = 0;
y = 0;

% Distance, u(k), of each kth shell
j=1:50;
d=sqrt(j*2)/2;
u=d*a;

for k = 1:50
    x = x + (1/2)*((a/u(k))^n)*l(k);
    y = y + ((a/u(k))^m)*l(k);
end

I = (x - c*sqrt(y))*e;
```

File: suchen.m

```
% The overall interaction energy between atoms in a particle of radius
R
function U = suchen(R)

% for interatomic distances spanning from 0 to R
r=0:R/1000:R;

for i = 1:1001
    w(i) = integrand(R,r(i));
end

U=trapz(r,w);
```

File: integrand.m

```
function I = integrand(R,r)

% number of kth nearest neighbors
l=[12 6 24 12 24 8 48 6 36 24 24 24 72 0 48 12 48 30 72 24 48 24 48 8
84 24 72 48 24 0 96 6 96 48 48 36 120 24 48 24 24 48 120 24 120 0 96 24
108 30];

% constants PCCP
c = 34.408;         % dimensionless parameter
e = 1.9833E-2;      % eV, energy parameter
a = 3.92;           % angstrom, lattice constant
n = 10;             % positive integer
m = 8;              % positive integer

% Variables for 'for loop'
x = 0;
y = 0;

% Distance, u(k), of each kth shell
j=1:50;
d=sqrt(j*2)/2;
u=d*a;

for k = 1:50
    alpha = pi-2*real(asin((R^2-u(k)^2-r^2)/(2*u(k)*r)));
    x = x + (1/2)*((a/u(k))^n)*l(k)*(1-(sin(alpha/4))^2);
    y = y + ((a/u(k))^m)*l(k)*(1-(sin(alpha/4))^2);
end

I = (x - c*sqrt(y))*e*(4/a^3)*4*pi*r^2;
```

APPENDIX G

PYTHON SCRIPTS FOR PROCESSING ELECTROCHEMICAL DATA

For data smoothing

```
import numpy
import pylab
import os
def smooth(x,window_len=11,window='hanning'):

    """smooth the data using a window with requested size.

    This method is based on the convolution of a scaled window with the
signal.
    The signal is prepared by introducing reflected copies of the
signal
    (with the window size) in both ends so that transient parts are
minimized
    in the begining and end part of the output signal.

    input:
        x: the input signal
        window_len: the dimension of the smoothing window; should be an
odd integer
        window: the type of window from 'flat', 'hanning', 'hamming',
'bartlett', 'blackman'
            flat window will produce a moving average smoothing.

    output:
        the smoothed signal

    example:

    t=linspace(-2,2,0.1)
    x=sin(t)+randn(len(t))*0.1
    y=smooth(x)

    see also:

    numpy.hanning, numpy.hamming, numpy.bartlett, numpy.blackman,
numpy.convolve
    scipy.signal.lfilter

    TODO: the window parameter could be the window itself if an array
instead of a string
    NOTE: length(output) != length(input), to correct this: return
y[(window_len/2-1):-(window_len/2)] instead of just y.
    """

    if x.ndim != 1:
        raise(ValueError, "smooth only accepts 1 dimension arrays.")

    if x.size < window_len:
```

```
        raise(ValueError, "Input vector needs to be bigger than window
size.")


    if window_len<3:
        return x


    if not window in ['flat', 'hanning', 'hamming', 'bartlett',
'blackman']:
        raise(ValueError, "Window is on of 'flat', 'hanning',
'hamming', 'bartlett', 'blackman'")

    # reflects data
    s=numpy.r_[x[(window_len-1)/2:0:-1],x,x[-1:-(window_len+1)/2:-1]]

    #print(len(s))
    if window == 'flat': #moving average
        w=numpy.ones(window_len,'d')
    else:
        w=eval('numpy.'+window+'(window_len)')

    y=numpy.convolve(w/w.sum(),s,mode='valid')
    return y

directory = "G:\\Fuller Group\\Projects\\II OxideGrowth_Model\\Kinetic
Studies on MEAs\\CMEA_212_A0.3_C0.3-
20130225\\InitialCharacterization\\"
results_directory = directory + "Smoothed\\"

CV_files = [file for file in os.listdir(directory) if
file.startswith("iniCV") and file.endswith(".txt")]

for filename in CV_files:
    # open 'r'ead only file
    CV_file = open(directory+filename, 'r')
    results_file = open(results_directory + 'Smoothed_' + filename,
'w')
    results_file.write("Current(A)\tPotential(V)\tTime(s)\tSmoothed
Current (A)\n")

    # Pre-defining arrays that you can do operations on (hence
numpy.array([]))
    current = numpy.array([])
    potential = numpy.array([])
    time = numpy.array([])

    CV_file.readline()

    for line in CV_file:
        rows = line.split('\t')
        current = numpy.append(current,float(rows[0]))
        potential = numpy.append(potential,float(rows[1]))
        time = numpy.append(time,float(rows[2]))

    CV_file.close()
```

```
    smooth_current = smooth(current,45)

    #print(current.size)
    #print(smooth_current.size)

    for index in range(current.size):
        line = "%f\t%f\t%f\t%f\n" %
(current[index],potential[index],time[index],smooth_current[index])
        results_file.write(line)

    results_file.close()

    #pylab.plot(potential,current)
    #pylab.plot(potential,smooth_current)
    #pylab.show()
```

For separating ECA data (lower potentials)

```
import numpy
import pylab
import os

# A. Where to find the file I want to import
directory = "D:\\Fuller Group\\Projects\\II OxideGrowth_Model\\Kinetic
Studies on MEAs\\CMEA_212_A0.3_C0.3-
20130225\\25CPotentialSweepsECA\\ECA - 25C\\LastCycle_ECA - 25C\\"
results_directory = "D:\\Fuller Group\\Projects\\II
OxideGrowth_Model\\Kinetic Studies on MEAs\\CMEA_212_A0.3_C0.3-
20130225\\25CPotentialSweepsECA\\ECA - 25C\\LastCycle_ECA -
25C\\Results\\"
results_file = open(results_directory + 'results.txt', 'w')
results_file.write("Filename\tOrder No.\tq(ADS)[Coloumbs]\tECA(ADS)
[m2(Pt)/g(Pt)]\tq(DES) [Coloumbs]\tECA(DES) [m2(Pt)/g(Pt)]\tCrossover
Current (A)\n")

ECA_files = [file for file in os.listdir(directory) if
file.startswith("LastCyc") and file.endswith(".txt")]

subplot_counter = 0

for filename in ECA_files:
    if filename.find('(') == -1:
        order_no =0
    else:
        order_no =
int(filename[filename.find('(')+1:filename.find(')')])+1

    # open 'r'ead only file
    ECA_file = open(directory+filename, 'r')

    # D. Pre-defining arrays that you can do operations on (hence
numpy.array([]))
    time = numpy.array([])
    potential = numpy.array([])
    current = numpy.array([])

    # E. Importing values from file in A. to pre-defined arrays in D.
    ECA_file.readline()

    for line in ECA_file:
        try:
            rows = line.split('\t')
            time = numpy.append(time, float(rows[0]))
            potential = numpy.append(potential, float(rows[1]))
            current = numpy.append(current, float(rows[2]))
        except:
            print('Skipping line: ' + line + ' in file: ' + filename)
            continue

    # F. Close file
    ECA_file.close()

    # G. Calculating ECA - ADSORPTION REGION
```

```
    index_LPL_ads = current[455:525].argmax()+450
    index_450 = abs(potential[:500]-0.45).argmin()
    index_400 = abs(potential[:500]-0.40).argmin()
    I_ads_base = numpy.average(current[index_450:index_400+1])
    q_ads =
numpy.trapz(current[:index_LPL_ads+1],time[:index_LPL_ads+1])-
I_ads_base*(time[index_LPL_ads]-time[0])
    ECA_ads = abs(q_ads/(210e-6)/0.3/25/10)

    #H. Calculating ECA - DESORPTION REGION
    n = potential.size
    index_400des = abs(potential[500:n]-0.40).argmin()+500
    index_450des = abs(potential[500:n]-0.45).argmin()+500
    I_des_base = numpy.average(current[index_400des:index_450des+1])
    index_LPL_des = abs(current[480:550]-I_des_base).argmin()+480
    q_des =
numpy.trapz(current[index_LPL_des:index_400des+1],time[index_LPL_des:in
dex_400des+1])-I_des_base*(time[index_400des]-time[index_LPL_des])
    ECA_des = abs(q_des/(210e-6)/0.3/25/10)

    #I. Crossover
    I_x = (I_des_base - I_ads_base)/2+I_ads_base

    # H. Writing Data to File
    row="%s\t%f\t%f\t%f\t%f\t%f\t%f\n" %
(filename,order_no,q_ads,ECA_ads,q_des,ECA_des,I_x)
    results_file.write(row)

    # I. Plotting Commands
    subplot_counter = subplot_counter + 1

    Figure_1 = pylab.figure(1,figsize=(22,17))
    Figure_1.suptitle('ECA - 25 C: Integrated Areas on Current (I) vs
Potential (V vs RHE) Curve')
    pylab.subplot(8,9,subplot_counter)
    pylab.subplots_adjust(left = 0.08, right = 0.95, wspace = 0.15,
hspace = 0.15)
    pylab.plot(potential,current,color = 'k')

pylab.fill_between(potential[index_400:index_LPL_ads+1],current[index_4
00:index_LPL_ads+1],I_ads_base,color='#4682b4')

pylab.fill_between(potential[index_LPL_des:index_400des+1],current[inde
x_LPL_des:index_400des+1],I_des_base,color= '#b0c4de')
    ax = pylab.gca()
    ax.xaxis.set_visible(False)
    ax.yaxis.set_visible(False)
    pylab.title(filename, fontsize=6)
    Figure_1.savefig('D:\\Fuller Group\\Projects\\II
OxideGrowth_Model\\Kinetic Studies on MEAs\\CMEA_212_A0.3_C0.3-
20130225\\25CPotentialSweepsECA\\ECA - 25C\\LastCycle_ECA -
25C\\ECAareas_25C.png')

results_file.close()
pylab.show()
```

For finding last cycle of ECA data

```
import numpy
import pylab
import os

# A. Where to find the file I want to import
directory = "G:\\Fuller Group\\Projects\\II OxideGrowth_Model\\Kinetic
Studies on MEAs\\CMEA_212_A0.3_C0.3-
20130225\\25CPotentialSweepsECA\\ECA - 25C\\"
results_directory = "G:\\Fuller Group\\Projects\\II
OxideGrowth_Model\\Kinetic Studies on MEAs\\CMEA_212_A0.3_C0.3-
20130225\\25CPotentialSweepsECA\\ECA - 25C\\LastCycle_ECA - 25C\\"


Sweep_files = [file for file in os.listdir(directory) if
file.startswith("ECA") and file.endswith(".txt")]

subplot_counter = 0

for filename in Sweep_files:
    # open 'r'ead only file
    Sweep_file = open(directory+filename, 'r')
    results_file = open(results_directory + 'LastCyc_' + filename, 'w')
    results_file.write("Time(s)\tPotential(V)\tCurrent(A)\n")

    # D. Pre-defining arrays that you can do operations on (hence
numpy.array([]))
    time = numpy.array([])
    potential = numpy.array([])
    current = numpy.array([])

    # E. Importing values from file in A. to pre-defined arrays in D.
    Sweep_file.readline()

    for line in Sweep_file:
        rows = line.split('\t')
        time = numpy.append(time, float(rows[0]))
        potential = numpy.append(potential, float(rows[1]))
        current = numpy.append(current, float(rows[2]))

    # F. Close file
    Sweep_file.close()

    # G. Initial ASSIGNMENT of n
    n = potential.size - 10

    # H. Searching for maximum using iterative 100 steps backward.
While potential(small window) is NOT EQUAL to potetial(big window)
    #    n is redefined as n - 100 for each iteration. When the max
potentials are equal, then I will have found the range where my
    #    maximum value resides.
    while potential[n-10:n].max() != potential[n-20:n+10].max():
        n = n - 10

    # I. Reporting INDEX value of max - must add (n-200) to get the
real index (otherwise will start array at 0 index).
```

```
    last_cycle_end = potential[n-20:n+10].argmax() + (n-20)


    # J. Same concept as H - J to find 2nd to last max, giving me the
indices of the last cycle. I know what my potential profile looks like.
    n = last_cycle_end - 10

    while potential[n-10:n].max() != potential[n-20:n+10].max():
        n = n - 10

    last_cycle_begin = potential[n-20:n+10].argmax() + (n-20)


    # K. Writing file
    for index in range(last_cycle_begin,last_cycle_end):
        line = "%f\t%f\t%f\n" %
(time[index],potential[index],current[index])
        results_file.write(line)

    results_file.close()

    # L. Plotting Commands
    subplot_counter = subplot_counter + 1

    Figure_1 = pylab.figure(1,figsize=(22,17))
    Figure_1.suptitle('Potential Profile')
    pylab.subplot(8,9,subplot_counter)
    pylab.subplots_adjust(left = 0.08, right = 0.95, wspace = 0.15,
hspace = 0.15)

pylab.plot(time,potential,'bo',time[last_cycle_begin:last_cycle_end],po
tential[last_cycle_begin:last_cycle_end],'r')
    ax = pylab.gca()
    ax.xaxis.set_visible(False)
    ax.yaxis.set_visible(False)
    #pylab.xlabel('time (s)')
    #pylab.ylabel('potential (V vs RHE)')
    pylab.title(filename, fontsize=6)
    Figure_1.savefig('G:\\Fuller Group\\Projects\\II
OxideGrowth_Model\\Kinetic Studies on MEAs\\CMEA_212_A0.3_C0.3-
20130225\\25CPotentialSweepsECA\\ECA - 25C\\LastCycle_ECA -
25C\\PotProfile_25C.png')

    Figure_2 = pylab.figure(2,figsize=(22,17))
    Figure_2.suptitle('CV - Last Cycle')
    pylab.subplot(8,9,subplot_counter)
    pylab.subplots_adjust(left = 0.08, right = 0.95, wspace = 0.15,
hspace = 0.15)

pylab.plot(potential[last_cycle_begin:last_cycle_end],current[last_cycl
e_begin:last_cycle_end])
    ax = pylab.gca()
    ax.xaxis.set_visible(False)
    ax.yaxis.set_visible(False)
    #pylab.xlabel('potential (V vs RHE)')
    #pylab.ylabel('current (A)')
    pylab.title(filename, fontsize=6)
```

```
    Figure_2.savefig('G:\\Fuller Group\\Projects\\II
OxideGrowth_Model\\Kinetic Studies on MEAs\\CMEA_212_A0.3_C0.3-
20130225\\25CPotentialSweepsECA\\ECA - 25C\\LastCycle_ECA -
25C\\CVLastCyc_25C.png')

pylab.show()
```

Separating cycling data (upper potential limit)

```
import numpy
import pylab
import scipy.integrate as numint
import os

# A. Where to find the files I want to import and where I want to store
the results file
directory = "G:\\Fuller Group\\Projects\\II OxideGrowth_Model\\Kinetic
Studies on MEAs\\CMEA_212_A0.3_C0.3-
20130225\\25CPotentialSweepsECA\\Sweep - 25C\\LastCycle_Sweep - 25C\\"
results_file = open(directory + 'SweepResults_25C.txt', 'w')
results_file.write("LPL [V]\tUPL[V]\tScan Rate [mV/s]\tOrder
No.\tq(ADS)[Coloumbs]\tECA(ADS) [m2(Pt)/g(Pt)]\tq(DES)
[Coloumbs]\tECA(DES) [m2(Pt)/g(Pt)]\tCrossover Current
(A)\tq0.8\tq0.85\tq0.90\tq0.95\tq1.0\tq1.15\tq_anoTOT\tq_cat\n")

# B. What files to proces in directory
Sweep_files = [file for file in os.listdir(directory) if
file.startswith("LastCyc") and file.endswith(".txt")]


# C. LOOPING

subplot_counter = 0

for filename in Sweep_files:
# i. Splitting filename into parts for Excel File
    parts = filename.split('_')
    LPL = float(parts[1][3:])
    UPL = float(parts[2][3:])
    NU = float(parts[3][2:])
    order_no = float(parts[4][:3])

# ii. Open 'r'ead only file containing ALL cycles (from A.)
    Sweep_file = open(directory + filename, 'r')

# iii. Pre-defining arrays that you can do operations on (hence
numpy.array([]))
    time = numpy.array([])
    potential = numpy.array([])
    current = numpy.array([])

# iv. Importing values from file in A. to pre-defined arrays in (iii).
    Sweep_file.readline()

    for line in Sweep_file:
        try:
            rows = line.split('\t')
            time = numpy.append(time, float(rows[0]))
            potential = numpy.append(potential, float(rows[1]))
            current = numpy.append(current, float(rows[2]))
        except:
            print('skipping line:' + line + 'in file:' + filename)
            continue

    Sweep_file.close()
```

```
# v. Splitting data into Anodic and Cathodic Data Sets
    Split_point = potential.argmin()
# ----------------------------------------------------
    time_cat = time[:Split_point+1]
    potential_cat = potential[:Split_point+1]
    current_cat = current[:Split_point+1]
# ----------------------------------------------------
    time_ano = time[Split_point:]
    potential_ano = potential[Split_point:]
    current_ano = current[Split_point:]

# vi. Pre-defining q values and max indices for CATHODIC SWEEP
(index_catUPL) and ANODIC SWEEP (index_anoUPL)
    q_ads = 0
    ECA_ads = 0
    q_des = 0
    ECA_des = 0
    q_800 = 0
    q_850 = 0
    q_900 = 0
    q_950 = 0
    q_1000 = 0
    q_1150 = 0
    index_catUPL = potential_cat.argmax()
    index_anoUPL = potential_ano.argmax()

# vii. REDUCTION CALCS [qred and ECA ads]
    if potential[Split_point] < 0.2:
        n = time_cat.size
        index_LPL_ads = current_cat[n-5:n].argmax()+(n-5)
        index_450 = abs(potential_cat-0.45).argmin()
        index_400 = abs(potential_cat-0.40).argmin()
        I_ads_base = numpy.average(current_cat[index_450:index_400+1])
# ----------------------------------------------------------------------
----------------------------------------------------------------
        q_ads = numpy.trapz(current_cat[index_400:index_LPL_ads+1]-
I_ads_base,time_cat[index_400:index_LPL_ads+1])
        ECA_ads = abs(q_ads/(210e-6)/0.3/25/10)
        q_cat = abs(numpy.trapz(current_cat[index_catUPL:index_400+1]-
I_ads_base,time[index_catUPL:index_400+1]))
    else:
        index_505 = abs(potential_cat-0.51).argmin()
# ----------------------------------------------------------------------
----------------------------------------------------------------
        q_cat = abs(numpy.trapz(current_cat[index_catUPL:index_505+1]-
current_cat[index_505],time[index_catUPL:index_505+1]))

# viii. OXIDATION CALCS [ECA des and I_x]
    if potential[Split_point] < 0.2:
        index_400des = abs(potential_ano-0.40).argmin()
        index_450des = abs(potential_ano-0.45).argmin()
        I_des_base =
numpy.average(current_ano[index_400des:index_450des+1])
        index_LPL_des = abs(current_ano[:10]-I_des_base).argmin()
        I_x = (I_des_base - I_ads_base)/2+I_ads_base
```

```
# ------------------------------------------------------------------
------------------------------------------------------------------
        q_des = numpy.trapz(current_ano[index_LPL_des:index_400des+1]-
I_des_base,time_ano[index_LPL_des:index_400des+1])
        ECA_des = abs(q_des/(210e-6)/0.3/25/10)
        q_ano =
numint.cumtrapz(current_ano[index_400des:index_anoUPL+1]-
I_des_base,time_ano[index_400des:index_anoUPL+1])
        space = q_ano.size
        q_tot = q_ano[space-1]
        if potential_ano[index_anoUPL] > 1.13:
            q_1150 = q_ano[abs(potential_ano[index_400des:] -
1.15).argmin()-1]
        if potential_ano[index_anoUPL] > 0.98:
            q_1000 = q_ano[abs(potential_ano[index_400des:] -
1.0).argmin()-1]
        if potential_ano[index_anoUPL] > 0.93:
            q_950 = q_ano[abs(potential_ano[index_400des:] -
0.95).argmin()-1]
        if potential_ano[index_anoUPL] > 0.88:
            q_900 = q_ano[abs(potential_ano[index_400des:] -
0.90).argmin()-1]
        if potential_ano[index_anoUPL] > 0.83:
            q_850 = q_ano[abs(potential_ano[index_400des:] -
0.85).argmin()-1]
        if potential_ano[index_anoUPL] > 0.78:
            q_800 = q_ano[abs(potential_ano[index_400des:] -
0.80).argmin()-1]
    else:
        index_505des = abs(potential_ano-0.51).argmin()
        I_x = (current_ano[index_505des]-
current_cat[index_505])/2+current_cat[index_505]
        q_ano =
numint.cumtrapz(current_ano[index_505des:index_anoUPL+1]-
current_ano[index_505des],time_ano[index_505des:index_anoUPL+1])
        space = q_ano.size
        q_tot = q_ano[space-1]
        if potential_ano[index_anoUPL] > 1.13:
            q_1150 = q_ano[abs(potential_ano[index_505des:] -
1.15).argmin()-1]
        if potential_ano[index_anoUPL] > 0.98:
            q_1000 = q_ano[abs(potential_ano[index_505des:] -
1.0).argmin()-1]
        if potential_ano[index_anoUPL] > 0.93:
            q_950 = q_ano[abs(potential_ano[index_505des:] -
0.95).argmin()-1]
        if potential_ano[index_anoUPL] > 0.88:
            q_900 = q_ano[abs(potential_ano[index_505des:] -
0.90).argmin()-1]
        if potential_ano[index_anoUPL] > 0.83:
            q_850 = q_ano[abs(potential_ano[index_505des:] -
0.85).argmin()-1]
        if potential_ano[index_anoUPL] > 0.78:
            q_800 = q_ano[abs(potential_ano[index_505des:] -
0.80).argmin()-1]

# ix. Writing Data to File
```

```
print(LPL,UPL,NU,order_no,q_ads,ECA_ads,q_des,ECA_des,I_x,q_800,q_850,q
_900,q_950,q_1000,q_1150,q_tot,q_cat,sep='\t',file=results_file)

# x. Plotting Commands
    subplot_counter = subplot_counter + 1
    Figure_1 = pylab.figure(1, figsize = (22,17))
    Figure_1.suptitle('Sweeps @ 25C: Integrated Areas on Current (I) vs
Potential (V vs RHE) Curves')
    pylab.subplot(8,9,subplot_counter)
    pylab.plot(potential_cat,current_cat,color = 'r')
    pylab.plot(potential_ano,current_ano,color='k')
    if potential[Split_point] < 0.2:

pylab.fill_between(potential_cat[index_400:index_LPL_ads+1],current_cat
[index_400:index_LPL_ads+1],I_ads_base,color ='#b0c4de')

pylab.fill_between(potential_ano[index_LPL_des:index_400des+1],current_
ano[index_LPL_des:index_400des+1],I_des_base,color = '#4682b4')

pylab.fill_between(potential_ano[index_400des:index_anoUPL+1],current_a
no[index_400des:index_anoUPL+1],I_des_base,color = '#5f9ea0')

pylab.fill_between(potential_cat[index_catUPL:index_400+1],current_cat[
index_catUPL:index_400+1],I_ads_base,color ='#b0e0e6')
    else:

pylab.fill_between(potential_ano[index_505des:index_anoUPL+1],current_a
no[index_505des:index_anoUPL+1],current_ano[index_505des],color =
'#5f9ea0')

pylab.fill_between(potential_cat[index_catUPL:index_505+1],current_cat[
index_catUPL:index_505+1],current_cat[index_505],color ='#b0e0e6')
    ax = pylab.gca()
    ax.xaxis.set_visible(False)
    ax.yaxis.set_visible(False)
    pylab.title(filename, fontsize=6)
    Figure_1.savefig('G:\\Fuller Group\\Projects\\II
OxideGrowth_Model\\Kinetic Studies on MEAs\\CMEA_212_A0.3_C0.3-
20130225\\25CPotentialSweepsECA\\Sweep - 25C\\LastCycle_Sweep -
25C\\IntAreas_25C.png')


results_file.close()
pylab.show()
```

Separating last cycle of cycling data

```
import numpy
import pylab
import os

# A. Where to find the file I want to import
directory = "E:\\Fuller Group\\Projects\\II OxideGrowth_Model\\Kinetic
Studies on MEAs\\CMEA_212_A0.3_C0.3-
20130225\\25CPotentialSweepsECA\\Sweep - 25C\\"
results_directory = "E:\\Fuller Group\\Projects\\II
OxideGrowth_Model\\Kinetic Studies on MEAs\\CMEA_212_A0.3_C0.3-
20130225\\25CPotentialSweepsECA\\Sweep - 25C\\LastCycle_Sweep - 25C\\"


Sweep_files = [file for file in os.listdir(directory) if
file.startswith("LPL") and file.endswith(".txt")]

subplot_counter = 0

for filename in Sweep_files:
    # open 'r'ead only file
    Sweep_file = open(directory+filename, 'r')
    results_file = open(results_directory + 'LastCyc_' + filename, 'w')
    results_file.write("Time(s)\tPotential(V)\tCurrent(A)\n")

    # D. Pre-defining arrays that you can do operations on (hence
numpy.array([]))
    time = numpy.array([])
    potential = numpy.array([])
    current = numpy.array([])

    # E. Importing values from file in A. to pre-defined arrays in D.
    Sweep_file.readline()

    for line in Sweep_file:
        rows = line.split('\t')
        time = numpy.append(time, float(rows[0]))
        potential = numpy.append(potential, float(rows[1]))
        current = numpy.append(current, float(rows[2]))

    # F. Close file
    Sweep_file.close()

    # G. Initial ASSIGNMENT of n
    n = potential.size - 10

    # H. Searching for maximum using iterative 100 steps backward.
While potential(small window) is NOT EQUAL to potetial(big window)
    #    n is redefined as n - 100 for each iteration. When the max
potentials are equal, then I will have found the range where my
    #    maximum value resides.
    while potential[n-10:n].max() != potential[n-20:n+10].max():
        n = n - 10

    # I. Reporting INDEX value of max - must add (n-200) to get the
real index (otherwise will start array at 0 index).
    last_cycle_end = potential[n-20:n+10].argmax() + (n-20)
```

```
    # J. Same concept as H - J to find 2nd to last max, giving me the
indices of the last cycle. I know what my potential profile looks like.
    n = last_cycle_end - 10

    while potential[n-10:n].max() != potential[n-20:n+10].max():
        n = n - 10

    last_cycle_begin = potential[n-20:n+10].argmax() + (n-20)


    # K. Writing file
    for index in range(last_cycle_begin,last_cycle_end):
        line = "%f\t%f\t%f\n" %
(time[index],potential[index],current[index])
        results_file.write(line)

    results_file.close()

    # L. Plotting Commands
    subplot_counter = subplot_counter + 1

    Figure_1 = pylab.figure(1)
    Figure_1.suptitle('Potential Profile')
    pylab.subplot(8,9,subplot_counter)
    pylab.subplots_adjust(left = 0.08, right = 0.95, wspace = 0.15,
hspace = 0.15)

pylab.plot(time,potential,'bo',time[last_cycle_begin:last_cycle_end],po
tential[last_cycle_begin:last_cycle_end],'r')
    ax = pylab.gca()
    ax.xaxis.set_visible(False)
    ax.yaxis.set_visible(False)
    #pylab.xlabel('time (s)')
    #pylab.ylabel('potential (V vs RHE)')
    pylab.title(filename, fontsize=6)

    Figure_2 = pylab.figure(2)
    Figure_2.suptitle('CV - Last Cycle')
    pylab.subplot(8,9,subplot_counter)
    pylab.subplots_adjust(left = 0.08, right = 0.95, wspace = 0.15,
hspace = 0.15)

pylab.plot(potential[last_cycle_begin:last_cycle_end],current[last_cycl
e_begin:last_cycle_end])
    ax = pylab.gca()
    ax.xaxis.set_visible(False)
    ax.yaxis.set_visible(False)
    #pylab.xlabel('potential (V vs RHE)')
    #pylab.ylabel('current (A)')
    pylab.title(filename, fontsize=6)

pylab.show()
```

Determining the pseudocapacitance (i_norm)

```
import numpy
import pylab
import scipy.integrate as numint
import os

# A. Where to find the files I want to import and where I want to store
the results files
directory = "G:\\Fuller Group\\Projects\\II OxideGrowth_Model\\Kinetic
Studies on MEAs\\CMEA_212_A0.3_C0.3-
20130225\\25CPotentialSweepsECA\\Sweep - 25C\\LastCycle_Sweep - 25C\\"
results_directory = directory + 'I_norm\\'

# B. What files to proces in directory
Sweep_files = [file for file in os.listdir(directory) if
file.startswith("LastCyc") and file.endswith(".txt")]

order   = numpy.array([])
q_des   = numpy.array([])
ECA_results = open('G:\\Fuller Group\\Projects\\II
OxideGrowth_Model\\Kinetic Studies on MEAs\\CMEA_212_A0.3_C0.3-
20130225\\25CPotentialSweepsECA\\ECA - 25C\\LastCycle_ECA -
25C\\Results\\results.txt', 'r')
ECA_results.readline()
for line in ECA_results:
    try:
        rows = line.split('\t')
        order = numpy.append(order, float(rows[1]))
        q_des = numpy.append(q_des, float(rows[4]))
    except:
        print('skipping line:' + line + 'in results file')
        continue

ECA_results.close()

# C. LOOPING

subplot_counter = 0

for filename in Sweep_files:
    results_file = open(results_directory + 'Norm_' + filename, 'w')
    results_file.write("Time(s)\tPotential(V)\tCurrent(A)\tNormalized
Current Density (uC/mV-cm^2)\n")

    # i. Splitting filename into parts for Excel File
    parts = filename.split('_')
    LPL = float(parts[1][3:])
    UPL = float(parts[2][3:])
    NU = float(parts[3][2:])
    order_no = int(parts[4][:3])

    # ii. Open 'r'ead only file containing ALL cycles (from A.)
    Sweep_file = open(directory + filename, 'r')

    # iii. Pre-defining arrays that you can do operations on (hence
numpy.array([]))
    time = numpy.array([])
```

```
    potential = numpy.array([])
    current = numpy.array([])

    # iv. Importing values from file in A. to pre-defined arrays in
(iii).
    Sweep_file.readline()
    for line in Sweep_file:
        try:
            rows = line.split('\t')
            time = numpy.append(time, float(rows[0]))
            potential = numpy.append(potential, float(rows[1]))
            current = numpy.append(current, float(rows[2]))
        except:
            print('skipping line:' + line + 'in file:' + filename)
            continue
    Sweep_file.close()

    index_order = abs(order - order_no).argmin()
    q_value = q_des[index_order]

    # v. Splitting data into Anodic and Cathodic Data Sets
    Split_point = potential.argmin()
    # -----------------------------------------------------
    time_cat = time[:Split_point+1]
    potential_cat = potential[:Split_point+1]
    current_cat = current[:Split_point+1]
    # -----------------------------------------------------
    time_ano = time[Split_point:]
    potential_ano = potential[Split_point:]
    current_ano = current[Split_point:]

    # vi. Scan Rate
    Nu = (potential_ano[-6]-potential_ano[5])/(time_ano[-6]-
time_ano[5])

    # vii. I_x Calculations
    if potential[Split_point] < 0.2:
        index_450 = abs(potential_cat-0.45).argmin()
        index_400 = abs(potential_cat-0.40).argmin()
        I_ads_base = numpy.average(current_cat[index_450:index_400+1])
        index_400des = abs(potential_ano-0.40).argmin()
        index_450des = abs(potential_ano-0.45).argmin()
        I_des_base =
numpy.average(current_ano[index_400des:index_450des+1])
        I_x = (I_des_base - I_ads_base)/2+I_ads_base
    else:
        index_505 = abs(potential_cat-0.51).argmin()
        index_505des = abs(potential_ano-0.51).argmin()
        I_x = (current_ano[index_505des]-
current_cat[index_505])/2+current_cat[index_505]

    # viii. Corrected Current Array
    I_corrected = current - I_x

    # ix.
    i_norm = I_corrected*(210e-6)*1000/Nu/q_value
```

```
    # x. Writing Data to File
    for index in range(i_norm.size):
        line = "%f\t%f\t%f\t%f\n" %
(time[index],potential[index],current[index],i_norm[index])
        results_file.write(line)

    # x. Plotting Commands
    # Figure_1 = pylab.figure(1)
    # if potential[abs(potential_ano-1.15).argmin()] < 0.1:
        # pylab.plot(potential,i_norm,color = 'k')
        # pylab.xlabel('Potential (V vs RHE)')
        # pylab.ylabel('Norm. Current Density (uC/mV-cm^2)')
        # pylab.title('UPL = 1.15')
    # Figure_2 = pylab.figure(2)
    # if potential[abs(potential_ano-1.0).argmin()] < 0.1:
        # pylab.plot(potential,i_norm,color = 'k')
        # pylab.xlabel('Potential (V vs RHE)')
        # pylab.ylabel('Norm. Current Density (uC/mV-cm^2)')
        # pylab.title('UPL = 1.0')


results_file.close()
pylab.show()
```